DISSERTATION

MEASUREMENT OF THE TOTAL FLUX AVERAGED NEUTRINO INDUCED NEUTRAL CURRENT ELASTIC SCATTERING CROSS SECTION WITH THE T2K PI-ZERO DETECTOR

Submitted by

Daniel Ruterbories

Department of Physics

In partial fulfillment of the requirements

For the Degree of Doctor of Philosophy

Colorado State University

Fort Collins, Colorado

Spring 2014

Doctoral Committee:

Advisor: Bruce E. Berger

Norman Buchanan
Kevin Lear
Robert Wilson

Copyright by Daniel Ruterbories 2014
All Rights Reserved

ABSTRACT

MEASUREMENT OF THE TOTAL FLUX AVERAGED NEUTRINO INDUCED NEUTRAL CURRENT ELASTIC SCATTERING CROSS SECTION WITH THE T2K PI-ZERO DETECTOR

Tokai-to-Kamioka (T2K) is a second generation accelerator neutrino oscillation experiment. T2K uses a high intensity proton beam produced at the Japan Proton Accelerator Research Complex (J-PARC) incident on a carbon target and focused with three magnetic horns to produce a high intensity and nearly pure muon neutrino beam with a peak energy of 600 MeV at a 2.5° off axis angle. The muon neutrino beam travels 295 km across Japan to the Super Kamiokande (SK) water Cherenkov detector in the Kamioka mine. The neutrino beam is also sampled by a complex of near detectors 280 m downstream of the carbon target located both on and off the beam axis. These detectors measure the neutrino beam before neutrino oscillations occur to provide input constraints to oscillation searches using SK.

The off-axis near detector, ND280, is a composite detector made up of a tracker section and a Pi-Zero detector (PØD), all surrounded by an electromagnetic calorimeter. The entire detector is enclosed in a dipole magnet with a field of 0.2 T. The primary purpose of the tracker section is to measure neutrino induced charged current events characterized by the production of muons. The PØD is primarily designed to detect electromagnetic showers and to measure interactions on water through the use of a removable water target. In addition to these measurements, the ND280 detector is also used to study the cross sections of neutrino interactions on the various materials in the detectors. Limited knowledge of the cross sections in this neutrino energy regime are an important source of systematic error in neutrino oscillation measurements.

This thesis presents a measurement of one neutrino interaction channel in the PØD, neutral current elastic scattering (NCE). In this process a neutrino elastically scatters off a

proton or neutron in the target nucleus producing a proton or neutron with higher energy. The signature of this process is a single proton track. A particle identification algorithm (PID) was developed to suppress the dominant muon background. Using this algorithm in conjunction with a Michel electron veto the flux averaged absolute cross section is measured to be $<\sigma>_{\text{flux}} = 2.24\times10^{-39}\frac{\text{cm}^2}{\text{nucleon}} \pm 0.07(\text{stat.})\ ^{+0.53}_{-0.63}(\text{sys.})$.

TABLE OF CONTENTS

ABSTRACT ii
LIST OF TABLES vii
LIST OF FIGURES xv
Chapter 1 Introduction 1
Chapter 2 Neutrino Scattering and Oscillations 11
2.1 Neutrino Scattering 13
2.1.1 Cross Section Calculation 14
2.1.2 Neutrino Generator: NEUT 16
2.2 Neutrino Oscillations 18
Chapter 3 T2K Experimental Setup 21
3.1 T2K Beam line 21
3.1.1 Neutrino Beam Line 23
3.1.2 Neutrino Flux 24
3.2 T2K Near Detector Complex 28
3.2.1 INGRID On-Axis Detector 29
3.2.2 ND280 Off-Axis Detector 29
3.2.3 Pi-Zero Detector 36
3.2.4 Multi-Pixel Photon Detectors 40
3.3 T2K Far Detector 43
Chapter 4 Previous NCE Measurements 45
4.1 Early Cross Section Measurement at BNL 47
4.1.1 External Neutron Contamination 48
4.1.2 In-Detector backgrounds 48
4.1.3 Results 50
4.2 BNL E734 52
4.2.1 Experimental Setup 52
4.2.2 Signal Definition 54
4.2.3 Backgrounds 54
4.2.4 Results 55
4.3 MiniBooNE 56
4.3.1 Experimental Setup 56
4.3.2 Signal Definition 57
4.3.3 Event Selection 58
4.3.4 External Neutron Background 60
4.3.5 Results 62
Chapter 5 Analysis Tool Development 68
5.1 PØD Reconstruction 68
5.1.1 Hit Preparation 69
5.1.2 Track Reconstruction 70
5.2 Parametric Track Treatment 73
5.3 PID Algorithm 74

5.4 Momentum Reconstruction Algorithm 82
5.5 Neutron Clustering Algorithm 84
5.6 Charge Threshold Correction 84
Chapter 6 Event Selection 88
6.1 Event selection cuts 94
6.1.1 Data and Beam Quality 94
6.1.2 Single 3-D Track 97
6.1.3 Fiducial Volume 97
6.1.4 Containment 97
6.1.5 PID on the Track End 99
6.1.6 PID on Track Front 101
6.1.7 Michel Electron 101
6.1.8 Final NCE Sample 106
6.1.9 PID Cut Optimization 113
Chapter 7 Systematics 119
7.1 Detector and Reconstruction Systematics 120
7.2 Physics Systematics 138
7.2.1 Reweight Method 139
7.2.2 Cross-section Model Uncertainties 140
7.2.3 Outside Background Estimation 159
7.3 Beam Flux 170
7.3.1 Evaluation Methods 170
7.3.2 Flux systematic 173
Chapter 8 Cross Section Extraction 181
8.1 Flux-Averaged absolute cross section 181
8.1.1 Cross Section Calculation Validation 184
Chapter 9 Conclusion 189
Bibliography 196

LIST OF TABLES

4.1 Internal backgrounds and methods to remove and/or estimate their contribution to the final sample in the HPB experiment. 49
4.2 Ratio of neutral current to charged current elastic(quasi-elastic) scattering cross section as seen in [68] 51
4.3 Event hypothesis likelihood categories used in MiniBooNE reconstruction. 59
4.4 Event selection background breakdown in the MiniBooNE sample. 61

5.1 PID MPV and Gaussian sigma parameters by bin number 79
5.2 Areal density of various materials in the PØD 83

6.1 Event selection event yields by cut progression. The first line, pre-selection, corresponds to events reconstructed as a single 3-D track with good beam and data quality flags. 90
6.2 Event selection after all cuts broken down by FSI topologies and categorized with the fiducial volume taken into account for all targets as well as the top three nuclear targets. There are a total 3730.63 events selected in the p.o.t. normalized MC. The outside PØD category has been scaled by the external scaling factor found in Section 7.2.3. 94
6.3 Event selection after all cuts broken down by FSI topologies and categorized without the fiducial volume taken into account for all targets as well as the top three nuclear targets. This means interactions are only categorized by their FSI category, removing an outside the fiducial volume category. The difference seen between the outside PØD events in Table 6.2 and this outside category is a small fraction of outside events are categorized as anti-ν, this is $\sim$10 events in the all category. There are a total 3730.63 events selected in the p.o.t. normalized MC. The outside PØD category has been scaled by the external scaling factor found in Section 7.2.3. 95
6.4 Event selection after all cuts broken down by interaction channel. Only channels which yield 50 or more events are shown. The first section shows the 3 dominant channels, NCE on neutron and proton and CCQE. The next section contains the dominant NC channels. The final section contains the dominant CC channel. These events account for 3532.67 events out of a total 3730.63. The external background events are shown because the analysis will constrain external events with data meaning the physics systematics will only be applied to background events which are not external. All event rates are p.o.t. normalized. The external background category has been scaled by the external scaling factor found in Section 7.2.3. 96

7.1 Systematics table for flux-averaged cross-section with water in the PØD. The statistical error is included for reference. 120
7.2 PID parameter values derived from data and MC. 123
7.3 Comparison of MC constants to the Data constants, $1 - \frac{\text{MC}}{\text{Data}}$. 124

7.4 Optimized cut positions for the MC derived PID distribution and data derived PID distribution. 124
7.5 Default road following parameter values and the variation used with the associated systematic error 132
7.6 Michel tagging efficiency a similar event selection found in Section 5.3 with an additional cut using the NCE analysis PID to ensure a high purity muon-like sample. 138
7.7 Systematics table of cross-section model uncertainty with central values and 1σ variations 141
7.8 Pion FSI parameter sets used for FSI study, found in [90]. These parameters sets correspond to the last 16 bins found in Figure 7.35. 156
7.9 The p.o.t. normalized event rates for the signal and background categories. Each category has the number of primary neutrons associated with the reconstructed particle. 161
7.10 Primary particle breakdown for the external backgrounds in the NCE selection. 165
7.11 Primary particle breakdown for clusters found by the clustering algorithm. 165

8.1 Central values estimated by NEUT MC scaled to exposed 9.918×10^{19} for the FSI topology. The events used in this calculation only come from the MC prediction except for the external events which are scaled by the data constraint. Events are scaled to data p.o.t.. 183
8.2 Run 1+2 water-in cross section final FSI topological cross section. 184

LIST OF FIGURES

1.1 Feynman diagram of the two NCE interaction channels. Elastic scattering off protons (left) and off neutrons (right). 2
1.2 True interaction type to FSI topology breakdown in the PØD fiducial volume with water in the PØD prior to event selection. True interactions on Y axis and FSI on X axis. Event rates are not normalized to a specific number of protons on target (p.o.t.). Use only for relative rates of various processes. 5
1.3 True interaction event rates in the PØD fiducial volume with water in the PØD prior to event selection. Event rates are not normalized to p.o.t. Use only for relative rates of various processes. 6
1.4 FSI topology event rates in the PØD fiducial volume with water in the PØD prior to event selection. Event rates are not normalized to p.o.t. Use only for relative rates of various processes. 7

2.1 Width of the Z-peak for 2,3,4 "active" neutrinos [23]. 13
2.2 NCE diagram scattering off a free quark. The neutrino starts with 4-momentum k and the quark with p. After scattering the neutrino has 4-momentum k' and the quark p'. 14

3.1 General experimental layout of T2K. [47] 21
3.2 Beam bunching structure of the T2K beam. Timing of the neutrino induced NCE events in the PØD. Includes running with only six bunches during Run 1 (spring 2010) and eight bunches during Run 2 (fall 2010, spring 2011). 22
3.3 POT delivered as a function of time as well as protons per pulse increase over time. Data points are from Run 1 (spring 2010), Run 2 (fall 2010, spring 2011), Run 3 (spring 2012), and Run 4 (fall 2012, spring 2013). A good spill refers to a spill where information about the number of protons and the timing is measured and recorded. [52] 23
3.4 Aerial photo of the J-PARC showing the various accelerators. North is towards the bottom of the photo. [53] 24
3.5 The T2K neutrino beam line (top) and beam line monitors (bottom). [47] 25
3.6 The effect of the focusing magnet horns on the flux at SK. Predicted ν_μ flux at SK for horn currents of 0, 205, and 250 kA (top). Ratio of flux compared to the predicted nominal flux with 250 kA running (bottom). [54] 26
3.7 T2K flux prediction at 295 km at three different off(on)-axis angles compared to the ν_μ survival probability. [54] 27
3.8 Energy of the decay neutrino from pion decay at 0, 2, 2.5, and 3 degrees off-axis from the parent pion direction. 28
3.9 Layout of all 17 INGRID modules. The beam center is located at the center of the cross. The two axis of the detector span 11 m and have 7 modules each. There are two off-axis modules to measure the symmetry of the beam as well as a proton module located at the beam center. [47] 30

3.10 Blow up view of the components making up a INGRID detector module. The black outer portions are the veto regions while the inner portion of the detector is a set of scintillator and iron sandwiches. [47] 31
3.11 Layout of the off-axis ND280 detector. [47] 32
3.12 Layout of a TPC module. [47] 34
3.13 PID distribution for the TPC. [47] 35
3.14 Monte Carlo prediction of the momentum reconstruction resolution as a function of the momentum. The dashed line is the design requirements specified for the construction of the TPC. [61] 35
3.15 Schematic view of the PØD showing the four major SuperPØDules as well as the XZ/YZ readout planes and inactive materials. [64] 37
3.16 Breakdown of the parts in the MPPC connector (left) and combined (right). [64] .. 38
3.17 The LIS cavity on the opposite side of the WLS fibers. The exposed portion of WLS fiber is illuminated by a 400 nm UV LED using the LIS system. [64] 38
3.18 Stability of the LIS system broken down by the average signal detected per pulser box on a flash by flash basis for all 10 amplitude settings. [64] 39
3.19 Stability of the LIS system over a three week period broken down by pulser box. [64]40
3.20 Close-up view of the MPPC pixels and view of the ceramic housing. [58] 41
3.21 MPPC response to multiple pulses from an LED. The individual photon peaks are visible up to 7 photons. The first peak corresponds to the noise pedestal. [58] .. 42
3.22 Overall correlated noise, from crosstalk, afterpulsing effects, as a function of the over-voltage tested at various temperatures. [58] 42
3.23 MPPC photon detection efficiency for a 515 nm photon as a function of the over-voltage and tested at various temperatures. [58] 43
3.24 Example event display of a single muon-like ring event in SK. [47] 44
3.25 Example event display of a single electron-like ring event in SK. [47] 44

4.1 The detector used by the HPW group. The full detector is shown on the left and a calorimeter module on the right. [67] 46
4.2 Expected difference in time between neutrino beam arrival and front and side entering neutrons from neutrino events in the surrounding concrete. [68] 50
4.3 Corrected event rate as a function of reconstructed Q^2 for the $\nu_\mu + p^+ \rightarrow \nu_\mu + p^+$ interaction. For reference the equivalent charged current interaction is shown. At the time of this experiment parameters associated with the WS-GIM model were under study and as a result the expectation from the model as a function of the $\sin^2\theta_w$ are shown for values of 0.4, 0.28, and 0.2. [68] 51
4.4 The BNL E734 detector setup with a detail inset of the target and tracking section of the detector used in the NCE analysis. [4] 53
4.5 Flux averaged differential cross section as a function of reconstructed Q^2 for both the neutrino and anti-neutrino analyses. The flux normalization was determined from the CCQE interaction measurement. The theoretical predictions on the plot use an M_A of 1.06 $\frac{\text{GeV}}{\text{c}^2}$ and a $\sin^2\theta_w$ of 0.220. [4] 55
4.6 Predicted flux at MiniBooNE broken down by neutrino species. [12] 57
4.7 Schematic view of the MiniBooNE detector. [12] 58

4.8 Rejection of electrons due to cosmic events outside of beam timing causing reconstructed events during the beam window. [5] 60
4.9 Final event sample after all cuts are applied binned by kinetic energy and using a 4.2 m fiducial volume in MiniBooNE. [5] 61
4.10 Dirt sample breakdown and selection criteria. [5] 62
4.11 Dirt sample correction factors with the piecewise fit. The error bars on the Z and R samples are statistical errors. The error on the kinetic energy sample uses the uncertainty introduced by the optical model, the largest detector systematic. [5] ... 63
4.12 Flux averaged differential cross section with respect to reconstructed Q^2. [5] 64
4.13 The ratio of the differential cross section for NCE to CCQE. [5] 65
4.14 The ratio of the differential cross section for NCE to CCQE including NCE(CCQE)-like backgrounds as signal. [5] 66

5.1 Flow of the PØD reconstruction algorithm, starting with the calibrated hits, through the tracking reconstruction, shower reconstruction, and finally Michel decay tagging. 69
5.2 Length vs angle phase space coverage by Parametric (red) and Kalman (black) fit tracks. 74
5.3 Examples of how muon-like particles cross scintillation planes. The most common node is two hits as seen on the left. Higher angle tracks produce higher number of hits per node as seen in the center. Some tracks can produce single hits if the particle passes through the the point of the triangular bar as seen on the right. 75
5.4 Expected energy loss as a function of $\beta\gamma$. As can be seen in the Bethe region when the particle has a lower than the minimum ionizing particle (MIP) momentum the energy loss increases significantly while there is only a modest increase in energy loss as the momentum of the particle increases above the MIP region. [83] .. 76
5.5 MC particle prediction for the sand muon data selection. 76
5.6 Data sand muon charge deposition binned from the end of the track. 78
5.7 MC sand muon charge deposition binned from the end of the track. 79
5.8 Stopping particle charge deposition at the end of the track for data (top) and MC (bottom) for tracks starting and stopping within the fiducial volume. 80
5.9 PID parameter fits for data sand muons. 81
5.10 Uncorrected hit charges (left) and corrected hit charges (right). Data hit charges are in black and MC hit charges in red. 85

6.1 Track type broken down by FSI interaction type and fitter used. Over 1324.56 events in the NCE sample ends up being fit with the parametric fitter. Only 1013.76 events are reconstructed with the Kalman fitter. This distribution contains all single reconstructed tracks. 91
6.2 Selection efficiency (top) and purity (bottom) by selection cut. 92
6.3 NCE events broken down by the highest energy proton. Some events are actually the result of a higher energy neutron converting to a proton, where the primary proton energy is low or 0 (not found). There is a clear kinetic energy threshold in the PØD of ∼125 MeV. 93

6.4 Starting position for all single track events broken down by interaction type before the FV cut. 98
6.5 True neutrino energy spectrum by interaction type for single tracks after the fiducial volume cut. 99
6.6 Soft containment position cuts by interaction type. The data/beam quality, single track, and fiducial volume cuts have been applied. 100
6.7 PID pull distributions for the end of the track by interaction type, Kalman (top) and Parametric (bottom). All cuts up to the PID end cut have been applied. 102
6.8 Track kinetic energy (top) and angle (bottom) by interaction type. All cuts including the PID end cut have been applied. 103
6.9 PID pull distributions for the beginning of the track by interaction type, Kalman (top) and Parametric (bottom). All cuts up to the PID on the track front have been applied. The outside scaling factor (See Section 7.2.3) has been applied to the outside and sand backgrounds. 104
6.10 Track kinetic energy (top) and angle (bottom) by interaction type after the all cuts up to and including PID Beg. cut have been applied. The outside scaling factor (See Section 7.2.3) has been applied to the outside and sand backgrounds. 105
6.11 Number of Michel clusters by interaction type with all cuts but the Michel cut applied. The outside scaling factor (See Section 7.2.3) has been applied to the outside and sand backgrounds. 106
6.12 Track kinetic energy (top) and angle (bottom) by interaction type for the final event selection. The outside scaling factor (See Section 7.2.3) has been applied to the outside and sand backgrounds. 107
6.13 Track kinetic energy (top) and angle (bottom) by interaction type for the final Kalman track event selection. The outside scaling factor (See Section 7.2.3) has been applied to the outside and sand backgrounds. 108
6.14 Track kinetic energy (top) and angle (bottom) by interaction type for the final Parametric track event selection. The outside scaling factor (See Section 7.2.3) has been applied to the outside and sand backgrounds. 109
6.15 Comparison of track angle reconstruction to the true primary particle angle: Kalman (left) and Parametric (right). The distribution mean and sigma: $\bar{x} = -1.66$ degrees RMS = 14.69 degrees (left) and $\bar{x} = -2.02$ degrees RMS = 22.5 degrees (right). 110
6.16 Track energy reconstruction performance based on the primary particle energy for Kalman tracks: truth - reconstruction (left) and 1-$\frac{\text{Reconstruction}}{\text{Truth}}$ (right). The distribution mean and sigma for protons plus neutrons: $\bar{x} = 49.55$ MeV RMS = 205.1 MeV (left) and $\bar{x} = 2.3\%$ RMS = 12.1% (right). The distribution mean and sigma for protons only: $\bar{x} = -6.45$ MeV RMS = 142.9 MeV (left) and $\bar{x} = -1.2\%$ RMS = 9.2% (right). 111
6.17 Track energy reconstruction performance based on the primary particle energy for Parametric tracks: truth - reconstruction (left) and 1-$\frac{\text{Reconstruction}}{\text{Truth}}$ (right). The distribution mean and sigma for protons plus neutrons: $\bar{x} = 81.16$ MeV RMS = 219.2 MeV (left) and $\bar{x} = 4.98\%$ RMS = 13.1% (right). The distribution mean and sigma for protons only: $\bar{x} = 14.9$ MeV RMS = 180.4 MeV (left) and $\bar{x} = 0.32\%$ RMS = 11.2% (right). 112

6.18 The p.o.t. normalized selected signal events versus purity phase space for PID optimization. Each point is for a single PID End + Begining cut combination. This plot shows the possible selection purity and number of signal events selected for these combinations. The optimized cut positions are shown with a +. 114
6.19 Efficiency × Purity: Kalman tracks optimized to be (12,4) (top) and Parametric tracks optimized to be (3,0.5) (bottom). The labeled points are the optimized positions using the Efficiency × Purity metric. 115
6.20 Efficiency × Purity × Purity: Kalman tracks optimized to be (13,4.5) (top) and Parametric tracks optimized to be (3,1) (bottom). The labeled points are the optimized positions using the Efficiency × Purity × Purity metric. 116
6.21 Kalman track selection signal events with optimized points (13,4.5,713.418) and (12,4,730.795) (top) and purity with optimized points (13,4.5,0.448) and (12,4,0.441) (bottom) for PID optimization. 117
6.22 Parametric track selection signal events with optimized points (3,1,987.263) and (3,0.5,1000.31) (top) and purity with optimized points (3,1,0.490) and (3,0.5,0.484) (bottom) for PID optimization. 118

7.1 Vertex resolutions, X (top) and Y (bottom), for a contained single track sample which starts in the fiducial volume. 122
7.2 Full selected event versus purity phase space for MC Constants. Optmized cut points for both optimization definitions are shown with a +..... 125
7.3 Efficiency×Purity: Kalman tracks (10.5,4) (top) and Parametric tracks (2.5,0.5) (bottom) for MC Constants. Labeled points are the optimized cut position using the efficiency×purity metric. 126
7.4 Efficiency×Purity×Purity: Kalman tracks (13,5) (top) and Parametric tracks (3,1) (bottom) for MC Constants. Labeled points are the optimized cut position using the efficiency×purity×purity metric. 127
7.5 Kalman track selection signal events (13,5,711.343) and (10.5,4,744.899) (top) and purity (13,5,0.45) and (10.5,4,0.43) (bottom) for MC Constants. 128
7.6 Parametric track selection signal events (3,1,976.558) and (2.5,0.5,1007.84) (top) and purity (3,1,0.49) and (2.5,0.5,0.48) (bottom) for MC Constants. 129
7.7 Measured cross-section for nominal data derived constants (black) and MC derived constants (red). 130
7.8 Fractional change in cross-section with respect to the nominal data driven method. 131
7.9 Number of selected events for MC (red) and data (black). On the x-axis is the parameter variation for the width, angle and layer parameters. 134
7.10 Difference in MC and data total event rate response for reconstruction parameter variations. On the x-axis is the parameter variation for the width, angle and layer parameters. 134
7.11 Predicted selection efficiency for reconstruction parameter variations. On the x-axis is the parameter variation for the width, angle and layer parameters. 135
7.12 Predicted number of background events for reconstruction parameter variations. On the x-axis is the parameter variation for the width, angle and layer parameters. 135
7.13 Cross-section values for reconstruction parameter variations; all variations (left) and only 1× modification variations (right). 136

7.14 Fractional change in the cross-section by parameter variation. On the x-axis is the parameter variation for the width, angle and layer parameters. The final systematic values are pulled from this plot. The 1x variations are used. 136
7.15 M_A^{QE} T2KReweight parameter variation and fractional change in the cross section. 142
7.16 M_A^{Res} T2KReweight parameter variation and fractional change in the cross section. 143
7.17 Spectral function T2KReweight parameter variation and fractional change in the cross section. 143
7.18 Fermi momentum T2KReweight parameter variation and fractional change in the cross section. 144
7.19 CC resonant production low energy normalization T2KReweight parameter variation and fractional change in the cross section. 144
7.20 CC resonant production high energy normalization T2KReweight parameter variation and fractional change in the cross section. 145
7.21 CCQE low energy normalization T2KReweight parameter variation and fractional change in the cross section. 146
7.22 CCQE medium energy normalization T2KReweight parameter variation and fractional change in the cross section. 146
7.23 CCQE high energy normalization T2KReweight parameter variation and fractional change in the cross section. 147
7.24 CC DIS normalization T2KReweight parameter variation and fractional change in the cross section. 147
7.25 CC ν_e normalization T2KReweight parameter variation and fractional change in the cross section. 148
7.26 CC coherent normalization T2KReweight parameter variation and fractional change in the cross section. The truncation at -2 and -3 sigma is to avoid negative cross sections since the variation for this parameter is 100%. 148
7.27 NC π^0 normalization T2KReweight parameter variation and fractional change in the cross section. 149
7.28 Other NC normalization T2KReweight parameter variation and fractional change in the cross section. 149
7.29 NC π^+ normalization T2KReweight parameter variation and fractional change in the cross section. 150
7.30 NC coherent normalization T2KReweight parameter variation and fractional change in the cross section. 150
7.31 NCE M_A^{QE} Shape Only T2KReweight parameter variation and fractional change in the cross section. 151
7.32 W shape T2KReweight parameter variation and fractional change in the cross section. 152
7.33 Pionless delta decay T2KReweight parameter variation and fractional change in the cross section. 152
7.34 Variation in the calculated cross section for all parameter sets. Only the last 16 bins are used in the systematic. The first bin is the nominal cross section. 155
7.35 Fractional change of the cross section with respect to the nominal cross section. Only the last 16 bins are used in the systematic. The first bin is the nominal cross section. 155

7.36 Distribution of truth matched primary particles' energy after the full event selection. All particles are matched by the highest charge contributor at the downstream end of the track. 157
7.37 GEANT validation plot of neutrons on carbon total scattering cross section. [91] . 159
7.38 GEANT validation plot of neutrons on lead total scattering cross section. [91] 160
7.39 GEANT validation plot of neutrons on carbon inelastic scattering cross section. [91] 160
7.40 GEANT validation plot of neutrons on lead inelastic scattering cross section. [91] 161
7.41 Scaling factor fit result with full systematic and statistical errors for various charge thresholds. 163
7.42 Cluster position binned in Z. A large shape difference is visible in the USEcal (Z<-3000 mm). The MC has been normalized to data above 3000 mm to amplify the shape difference in the USEcal. 164
7.43 Input histogram into the fit. Y position of clusters. 166
7.44 Input histogram with scaling factor applied after the fit. Y position of clusters. ... 166
7.45 Distribution of 10000 throws with the best fit external background scaling factor (top) and fit error (bottom). 168
7.46 Tracks passing the NCE event selection starting in the USEcal without external background scaling (top) and with scaling (bottom). 169
7.47 T2K beam flux fractional errors at ND280 by neutrino species [54]. 171
7.48 NCE Selection binned in neutrino energy. 172
7.49 Fractional change in the selection efficiency for all beam flux throws. 175
7.50 Fractional change in the total background for all beam flux throws. The background is partially estimated by the MC and measured by data. 176
7.51 Fractional change in cross section measured using variations in the background estimation, the flux, and the selection efficiency. The number of selected event input uses the MC prediction. The estimated error via this method is $-22.5\%, +17.5\%$. 177
7.52 Fractional change in cross section measured using variations in the background estimation, the flux, and the selection efficiency. The number of selected event input is from data. The estimated error via this method is +17.5%, -21.5%. 178
7.53 Total number of selected events for each flux throw (left) and the fractional change in the number of selected events with respect to the nominal number of selected events (right). 179
7.54 Fractional change in cross section measured using variations in the number of selected events. The estimated error via this method is $\pm 20.7\%$. 180

8.1 The points represent the selection efficiency as a function of true neutrino energy. The overlaid histogram is a scaled histogram of all NCE events in the fiducial volume. The efficiency is the selected number of NCE events divided by the total predicted NCE signal in a given true neutrino energy bin. 182
8.2 NEUT predicted generator level cross section for true NCE interactions with full neutrino energy range (top) and zoomed (bottom). 185
8.3 Tuned NuMu flux from the 11bv3.2 flux files for Run 1+2 (top) and the nominal 11a flux (bottom). 186

8.4 Predicted flux-averaged generator level cross section using the nominal and tuned fluxes on various targets. The Boron NEUT prediction was empty. 187

9.1 Breakdown of the flux averaged absolute cross section per nucleon as predicted by NEUT for different elemental targets using the T2K and MiniBooNE flux predictions. [54] [12]. 192
9.2 The points show a comparison of the flux averaged absolute cross section per nucleon using a carbon target as predicted by NEUT. Scaled T2K and MiniBooNE flux predictions are shown for shape comparisons of the experiment's respective flux. [54] [12] 192
9.3 Ratio of the normalized MiniBooNE to T2K flux. 193
9.4 Q^2 as a function of the neutrino energy given the T2K flux. 194
9.5 Q^2 as a function of the neutrino energy when the ratio of the MiniBooNE to T2K flux is applied. 194
9.6 Comparison of the T2K Q^2 distribution and the Q^2 distribution when the MiniBooNE to T2K flux ratio is applied. 195

Chapter 1

Introduction

The analysis presented in this dissertation investigates the flux averaged absolute cross section of neutrino-nucleon neutral current elastic scattering. Historically the neutral current elastic (NCE) scattering process was used to probe the Glashow-Weinberg-Salam (GWS) model [1] [2] [3]. The GWS model combines the electromagnetic and weak forces in the form of a gauge theory. Weak decays, such as beta decay or muon decay, were used to probe the low energy region of the GWS model, but higher energy probes were needed. In NCE scattering the incoming neutrino scatters off either a neutron or proton in the target nucleus transferring some energy to the nucleon as shown in Figure 1.1. The NCE process provides a method to directly probe weak interactions at higher energies. For instance, the NCE process, in combination with its charged current (CC) equivalent, CC quasi-elastic (CCQE), was used [4] to measure one of the fundamental free parameters in the GWS model, θ_w, also known as the weak or Weinberg angle.

The measurement of NCE scattering probes the dominant neutral current interaction channel at Tokai-to-Kamioka's (T2K) peak beam energy of $\sim$ 600 MeV. The two most recent measurements of this interaction channel were made by the BNL 734 [4] and MiniBooNE [5] experiments. In these measurements the cross section measured was exclusively the proton channel (BNL734) or the sum of the proton and neutron channels (MiniBooNE). Both of these measurements were made using the NCE interaction mode as defined by their respective neutrino generators, the simulation programs that use models to predict neutrino event rates, and not by the particles predicted to exit the target nucleus. Both reported a differential cross section with respect to the square of the momentum transferred, Q^2, based on the kinetic energy of the highest energy proton or sum of all visible protons for BNL 734 and MiniBooNE respectively. The NCE measurement in the pi-zero detector (PØD) will differ from these measurements by investigating NCE as defined by the particles exiting the nucleus.

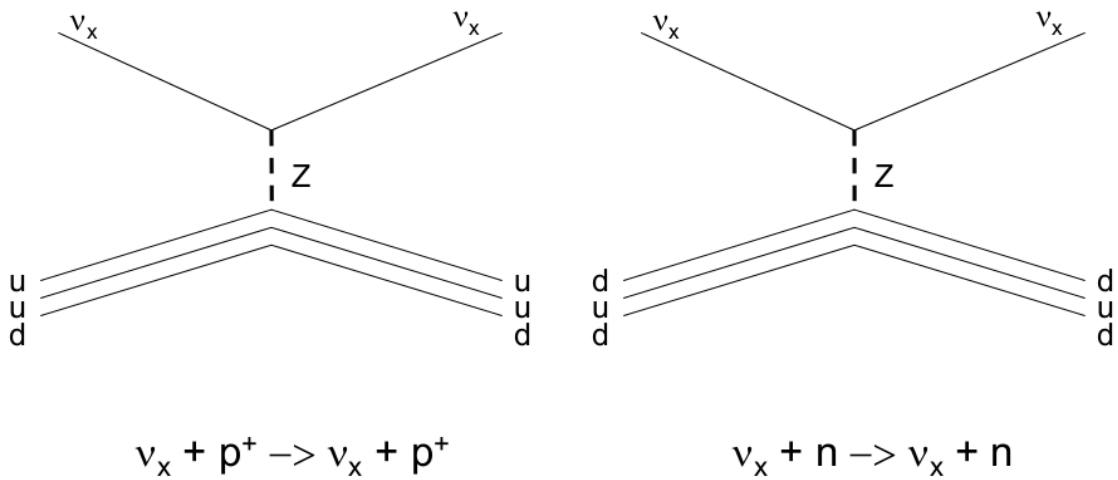

Figure 1.1: Feynman diagram of the two NCE interaction channels. Elastic scattering off protons (left) and off neutrons (right).

The measurement described in this dissertation will focus on a flux averaged absolute cross section, but future iterations of the analysis will investigate the cross section as a function of the proton angle, which has not been done before, as well as kinetic energy of the proton which is related to the Q^2 measured in BNL 734 and MiniBooNE. It should be noted the tools used to select the NCE topology can also be used for more exotic physics searches where either NCE or recoil particles are the signal. These include studies such as sterile neutrino searches using neutrino universality and combinations of the near and far detector event rates in T2K similarly to MINOS [6]; beam induced light dark matter where the unseen dark matter particle knocks off nucleons [7] [8]; and non-zero form factors $F^s_{1(2)}$ which are thought to come from the strange quark content of the nucleon [9] [10] [11] [5].

While the initial NCE interaction is simulated as scattering off a single independent bound or unbound nucleon, targets in the PØD are complex nuclei which obfuscate the initial interaction via final state interactions (FSI). For instance, if the true neutrino interaction is an elastic scattering event off a neutron, with FSI this neutron can re-interact with the target nucleus and produce extra nucleons, or never exit the nucleus. From the point of view of the detector any particle that doesn't exit the nucleus never existed. Because of FSI, some interaction types, for instance NCπ^0, can produce an observable NCE event through final state processes like pion absorption, charge exchange, or pionless delta decay. To try to avoid model-dependent mapping back to the true interaction through the model of FSI in NEUT, the neutrino generator simulation program used in T2K the measurement, this dissertation will focus on observable topologies.

The signal definition for this analysis will be any event in which a ν_μ type neutrino and at least one nucleon exits the nucleus in the fiducial volume, defined in Section 3.2.3. No mesons, other leptons, or gammas greater than 50 MeV are allowed in the final state. The gamma threshold is introduced to allow for nuclear excitation gammas while removing the small number(<1%) of NC gamma events from the signal category. In the cases where a neutron exits the nucleus, the event can be identified by the protons produced through

secondary interactions in the detector material. For this event to be considered a signal event, the initial interaction and secondary interaction must have occurred in the fiducial volume.

To understand the effect of FSI a matrix of true interaction to FSI topologies is provided. Figure 1.2 shows the true NEUT interaction mode, Y-axis, and the observable topologies on the X-axis for all event types predicted by NEUT in the fiducial volume of the PØD. Due to the nature of NCE, which is sensitive to nucleon type and number, each topology is further broken into four ejected nucleon categories: single proton, single neutron, multi-nucleon, no nucleons. It should be noted that there is a bug in NEUT that causes some CC events to end up in the NCE event pool even though they should not be counted as NCE events. These events are "Pauli blocked" events, or events where the resulting nucleon from the neutrino interaction is below the Fermi energy of the nucleus, where the event still undergoes Δ-absorption resulting in ejected nucleons. These events should have been discarded by NEUT. Unfortunately these events end up appearing as events where there are no mesons and no electrons/muons/taus in the final state but nucleons are present. As a result, these events are incorrectly identified as NCE events despite originally being a CC interaction. This sub sample enters the analysis at the 1% level which is well-covered by the systematic errors. A fix for this bug has already been applied to NEUT and future iterations of this analysis will not see these events in the MC.

Figure 1.3 breaks down the events by true neutrino interaction type. According to NEUT 39.1% of all true events are CCQE and 16.7% are NCE. Figure 1.4 breaks the events down by FSI topologies, dependent on the type and number of nucleons. According to the NEUT FSI prediction, 45.1% of interactions are CCQE with any number of nucleons and 19.2% are NCE with any number of nucleons (including zero nucleons).

In this analysis the event selection centers on selecting single proton tracks contained within the active region of the PØD while removing other particles from background processes reconstructed as single tracks. The most dominant interaction channel, charged cur-

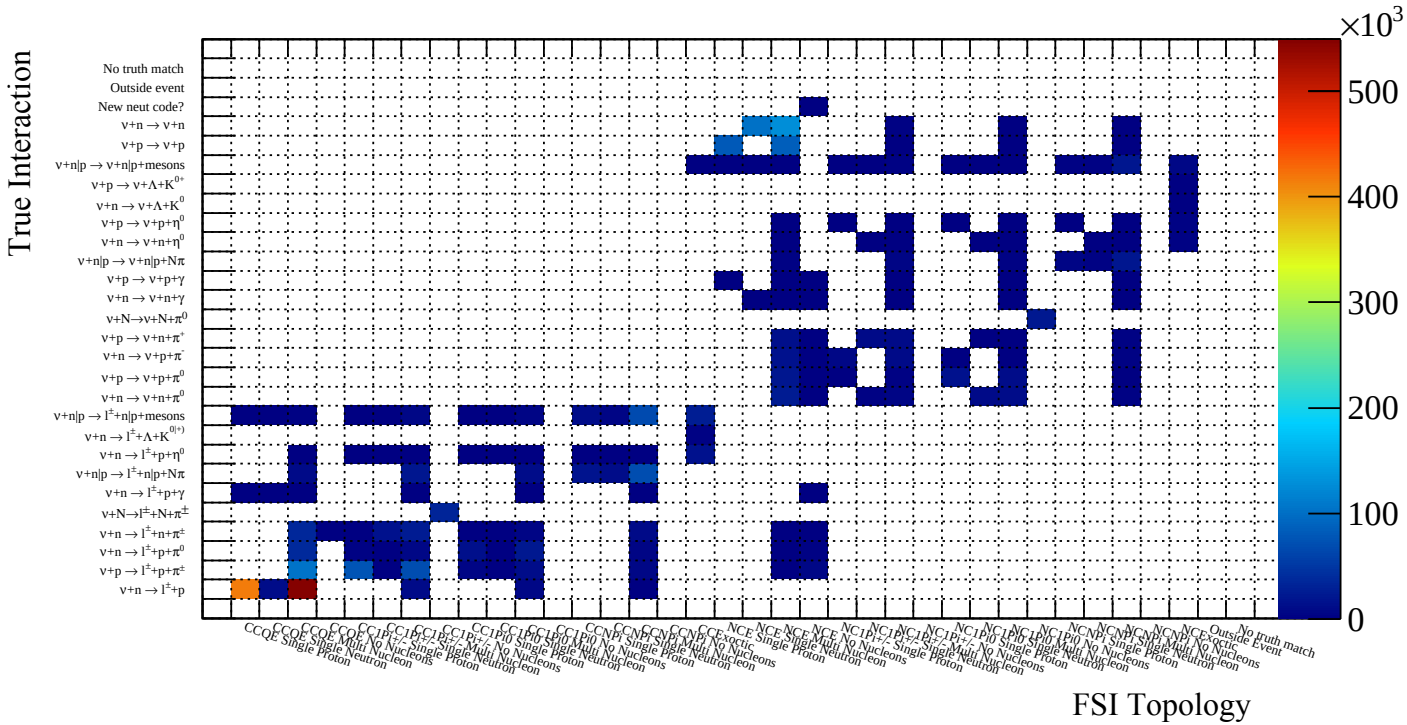

Figure 1.2: True interaction type to FSI topology breakdown in the PØD fiducial volume with water in the PØD prior to event selection. True interactions on Y axis and FSI on X axis. Event rates are not normalized to a specific number of protons on target (p.o.t.). Use only for relative rates of various processes.

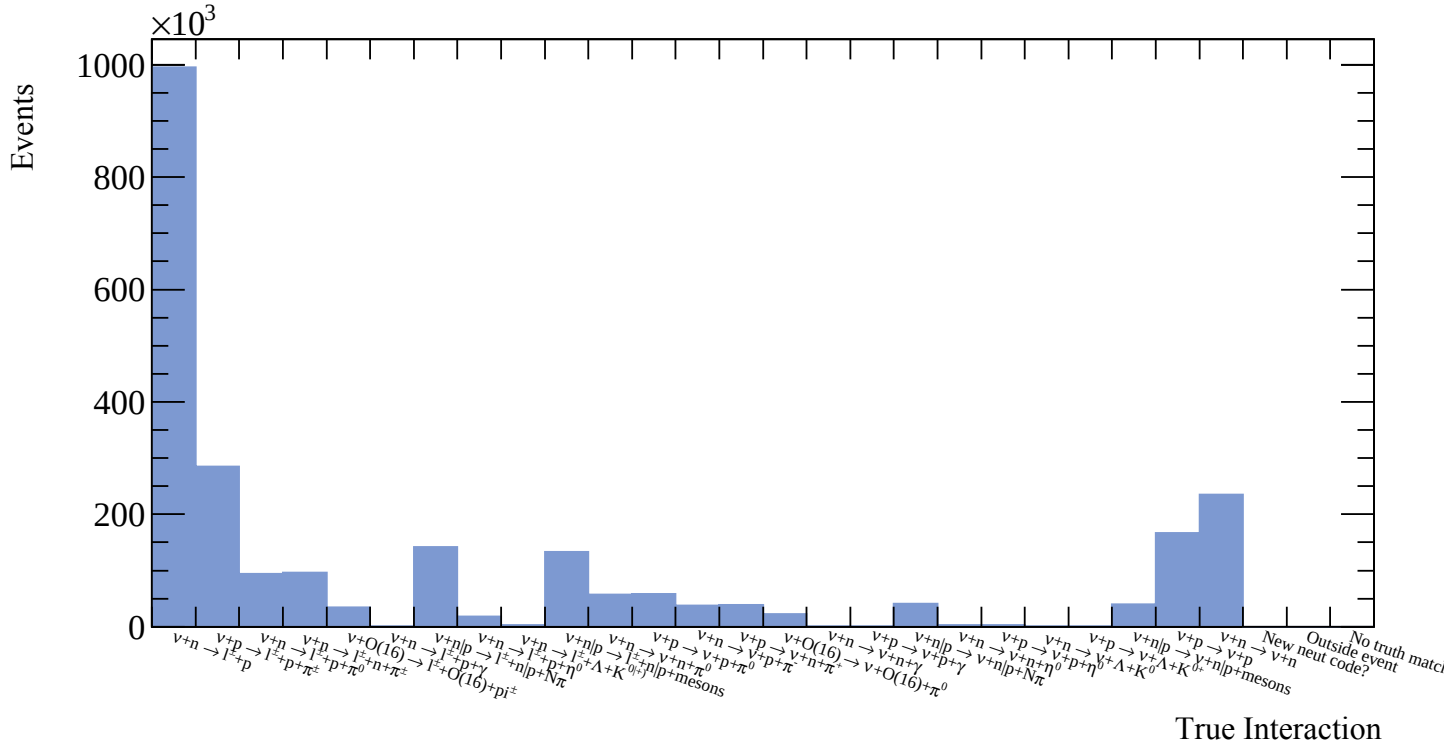

Figure 1.3: True interaction event rates in the PØD fiducial volume with water in the PØD prior to event selection. Event rates are not normalized to p.o.t. Use only for relative rates of various processes.

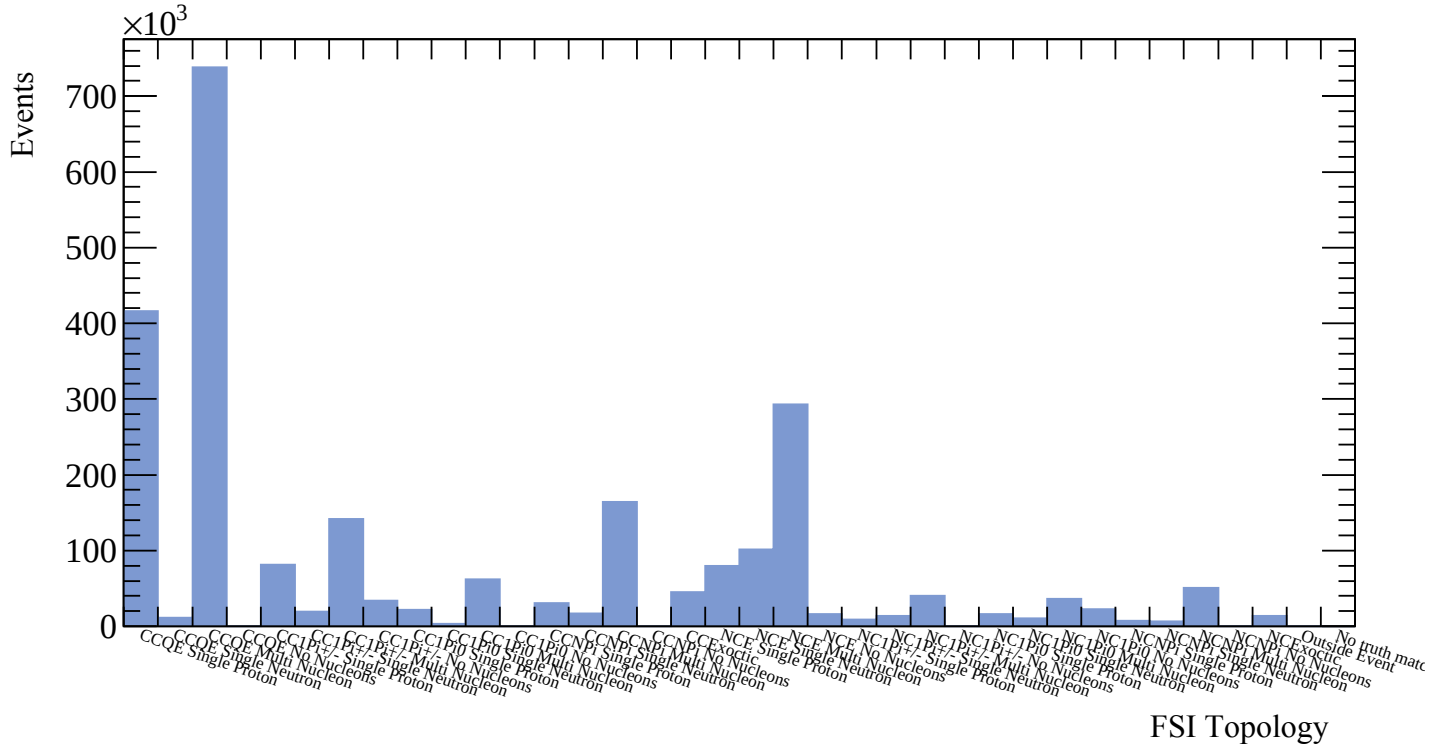

Figure 1.4: FSI topology event rates in the PØD fiducial volume with water in the PØD prior to event selection. Event rates are not normalized to p.o.t. Use only for relative rates of various processes.

rent quasi-elastic (CCQE) scattering, is also the largest background. These events tend to contain a long muon track with or without a reconstructable proton track or are events where the muon and proton are back-to-back and are reconstructed as a single track.

The dissertation is broken down into nine different chapters. Chapter 2 describes the physics behind neutrino scattering and oscillations. In addition a description of the NEUT neutrino generator and relevant models used by the generator to produce the event rate predictions is provided.

Chapter 3 describes the T2K experimental setup. Emphasis is placed on the pi-zero detector (PØD) and the beam line.

Chapter 4 describes NCE cross section measurements from earlier experiments. These experiments used the NCE interaction to detect the existence of the Z^0. The chapter provides a detailed description of the BNL 734 and MiniBooNE experimental apparatuses and results. The MiniBooNE experiment provides the largest sample of NCE events to date and as a result provides fine-grained results in Q^2 phase space.

Chapter 5 provides a description of the analysis tools required to measure the NCE process using the PØD. This includes a description of the PØD reconstruction algorithm, special treatment of tracks resulting from the secondary parametric track fitter, the development of the particle identification algorithm used to discriminate protons from muons, a momentum reconstruction algorithm, and tools developed to deal with a low charge threshold simulation issue.

Chapter 6 provides the event selection criteria chosen to select the final physics sample used to extract the cross section. This description includes tables of the final physics sample broken down by both the neutrino generator level definition, to understand the initial sample before the interaction of the particles in the target nucleus, also known as final state interactions (FSI), as well as after. A description of how the PID cut locations were optimized is also provided.

Chapter 7 describes all the relevant systematic error analyses. This includes a description of detector, reconstruction, cross section model, final state interactions, secondary interactions, and beam flux uncertainty propagated to the final cross section result. In the beam flux systematic error analysis section a description of different evaluation methods is provided.

Chapter 8 describes the method used to calculate the final flux averaged absolute cross section. A description of the NEUT cross section defined by topology (after final state interactions) as well as before FSI is provided.

The final chapter provides a description of the final cross section result, possible future expansions of the analysis, and two comparisons to the MiniBooNE result. Because the signal definition in the T2K result is different from the MiniBooNE result, as well as the flux and kinematic acceptance, which result in different efficiency corrections, a direct comparison is not possible. Despite these issues a comparison can be made by making several assumptions. First, the MiniBooNE collaboration provides their flux estimation [12]. Taking the MiniBooNE flux and applying NEUT's cross section model a comparison of the flux averaged cross section before final state interactions can be done. Secondly, a comparison can be done by restricting the Q^2 phase space. This will help minimize the impact of the efficiency correction used in the present analysis.

The analysis described in this dissertation is only a portion of the contributions I made to the T2K experiment. My initial contributions to the experiment started with the design of the analysis software used to perform quality tests on the ∼12,000 multi-pixel photon counters (MPPC) allocated for use in the PØD. This project included analysis of the dark spectrum, which is affected by the thermal noise and correlated noise inherent to the device, as well as the response to varying light levels from a pulsed LED. The purposes of these tests were to identify sensors with unusually high noise levels and/or low or high response to the pulsed LED. I also helped with the construction of modules, also known as PØDules, and water target bags as well as connecting the MPPCs to the readout electronics.

Once the PØD was shipped to Japan I helped do the initial check of the electronic readout and detector response using the light injection calibration system. I also helped with the installation of the detector into the ND280 basket, connection of the power and cooling systems, connection of the DAQ and cosmic triggering systems, as well as the installation of the light injection calibration system. During this period I helped with the checkout and commissioning of the detector and calibration system in preparation for the first running in early 2009. I also wrote the commissioning manual and analysis scripts necessary to check out the detector after shutdown periods. This analysis software includes a method to finely tune the individual readout channels so the detector has a uniform response.

My initial analysis was investigating neutrino induced CCπ^0, which was plagued by efficiency issues in reconstructing the low energy photons seen in the π^0 decay, but eventually morphed into the NCE analysis described in this dissertation. This change in analysis came about because of studies I did to help understand why the calibrations early on in the T2K experiment were not properly accounting for time variation from run period to run period. During these studies I discovered the signature of enough protons to perform an NCE analysis before it was generally considered viable. These studies eventually lead to the development of the particle identification algorithm used in the NCE analysis. These studies were also used to help understand the charge scale of the detector for the NCπ^0 systematic studies, although the final method used in the NCπ^0 analysis was different. I also helped with the development of analysis software and methods. Specifically, I developed the algorithms and analysis methods described in Chapter 5 as well as the development of an event display. All these methods, especially the particle identification and event display, have been used by numerous analyses in the PØD.

Chapter 2

Neutrino Scattering and Oscillations

The Standard Model is the theory which explains the the existence of particles and how they interact through the electromagnetic, weak and strong forces. The theory is based on the local gauge of SU(3)×SU(2)×U(1). The results described in this dissertation are described by the combination of SU(2)×U(1), also known as the electro-weak theory based on the GWS model. The SU(3) portion corresponds to the strong interactions developed in quantum chromodynamics (QCD). In all there are 12 fundamental particles, called fermions. These are broken down into two groups, the quarks and the leptons. The quarks come in three generations corresponding to up/down, charm/strange, and top/bottom. The quarks are charged particles with a charge of $\frac{1}{3}e$ for the up, charm, and top quarks, where e is the charge of the electron. The other three quarks have a charge of $-\frac{2}{3}e$. In the lepton sector there are also three generations, sometimes referred to as flavors. These are the electron, muon, and tau flavors. The neutrino is found in the lepton sector of the Standard Model. The flavor, or generation of neutrino, is defined by the flavor of lepton resulting from an interaction with the $W^{\pm}$, see Section 2.1.

Interactions between fundamental particles are moderated by different gauge bosons due to local gauge symmetry breaking. The electromagnetic force is moderated by the photon. The weak force is moderated by the W^{+}, W^{-}, and Z^{0} bosons. The strong force is moderated by the gluon, which carries the "color" charge. In total there are 12 gauge bosons (8 gluons, W^{+}, W^{-}, Z^{0}, and the photon). The $W^{\pm}$ and Z^{0} bosons are experimentally measured to have mass. However, in a local gauge theory the bosons need to be massless to allow for gauge invariance. To get around this the Higgs mechanism was introduced, which provides mass to the heavy gauge bosons via spontaneous symmetry breaking [13] [14] [15]. This was theorized to result in the Higgs boson which was recently discovered at the Large Hadron Collider (LHC) [16] [17].

The neutrino was first introduced by Wolfgang Pauli, in a letter sent to L. Meitner and the participants of the Tubingen conference (original [18] and translated [19]), to explain how beta decay, $n \rightarrow p^+ + e^- + \bar{\nu_e}$, conserved energy and angular momentum. It took another 26 years for the anti-electron neutrino to be experimentally verified by the Reines-Cowan neutrino experiment at Savannah River [20]. The muon-type neutrino was discovered by an experiment lead by Leon M. Lederman, Melvin Schwartz and Jack Stienberger [21]. In addition to the discovery of the muon-type neutrino, this experiment provided the foundation for how modern neutrino beams are produced. The final active flavor was confirmed by the DONUT experiment at Fermi National Laboratory in 2000 [22].

The number of active neutrinos, or neutrinos that couple to the Z^0 and $W^\pm$ bosons, is well constrained by precision measurements of the partial width of the Z^0 from e^+e^- collider experiments. The most precise measurements of the invisible partial width, thought to be due to active neutrino flavors, was done with four experiments at the LEP collider. The final result combining these four experiments finds the number of active neutrinos to be 2.984±0.008, see Figure 2.1 [23].

Because the neutrino is a neutral lepton it only interacts via the weak force. In the standard model the electromagnetic and weak forces are combined in the GWS model which results in the gauge bosons $W^\pm$, Z^0, and the photon. The weak interaction allows for the coupling of the $W^\pm$ and Z^0 with quarks and anti-quark ($q\bar{q}$) or leptons and anti-lepton ($l\bar{l}$) pairs. As a result, neutrinos interact with both electrons and nucleons in matter, although weakly. Interactions that are moderated by the $W^\pm$ are referred to as charged current since there is charge exchanged in the interaction. Similarly, interactions with the Z^0 are referred to as neutral current due to the lack of charge exchange.

Modern experiments like T2K, see Chapter 3, are designed to measure another neutrino phenomena, neutrino oscillation. These types of experiments require an understanding not only of how neutrinos propagate, but also how they interact with matter. The analysis

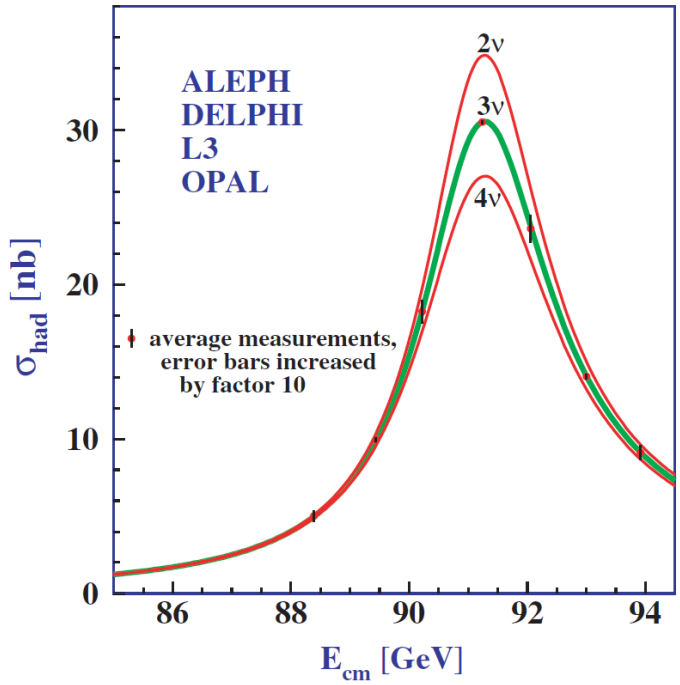

Figure 2.1: Width of the Z-peak for 2,3,4 "active" neutrinos [23].

presented in Chapters 5–8 measures the cross section, or probability of an interaction, of neutral current elastic scattering.

2.1 Neutrino Scattering

Neutrino experiments studying the oscillation of neutrino flavor states need predictions of the event rates of interaction modes of neutrinos scattering off complex nuclei. In the simple diagrams the neutrino may be scattering off a single nucleon. This isn't as simple as the fundamental neutrino-quark weak interaction. To predict the event rates of various interaction modes the cross section as a function of neutrino energy is calculated and multiplied with the predicted neutrino beam flux. In this section a general description of how a cross section is calculated, the specific simulation program used in T2K, and a more detailed description of NCE will be presented.

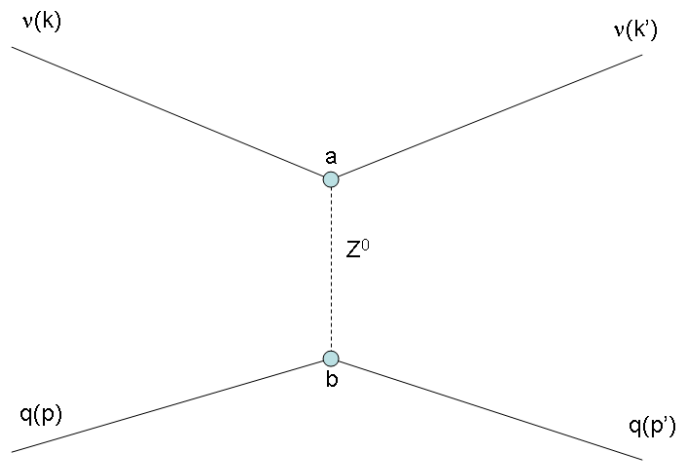

Figure 2.2: NCE diagram scattering off a free quark. The neutrino starts with 4-momentum k and the quark with p. After scattering the neutrino has 4-momentum k' and the quark p'.

2.1.1 Cross Section Calculation

In practice, to calculate the cross section of various processes the lowest level Feynman diagrams are produced first, with the higher order diagrams used as corrections. In the case of the NCE channel the tree level diagram is shown in Figure 1.1. In this diagram the neutrino is scattered off a proton or neutron. This diagram is already more complicated than the most basic diagram where the neutrino would only be scattering off an up or down quark. To get around this, as will be seen in the next section, a set of form factors are used to describe the scattering off the set of quarks. The general procedure for calculating the cross section can be seen in scattering off a free quark.

The first step in calculating the cross section is to calculate the matrix element, also known as the amplitude, directly from Figure 2.2. This calculation depends on the lepton vertex "a" and quark vertex "b" coupled by the Z propagator. This results in the matrix

element Equation 2.1,

$$M = \frac{g_z^2}{8(m_z c)^2}[\bar{u}(k')\gamma^\mu(1-\gamma^5)u(k)][\bar{u}(p')\gamma^\mu(c_V - c_A\gamma^5)u(p)] \tag{2.1}$$

Typically in an experiment the spins of the incoming and outgoing particles are random. Therefore the magnitude square of the matrix element is averaged over the incoming spins and summed over all the possible exiting spins resulting in the average magnitude square or $< |M|^2 >$. Casimir's trick [24],

$$\sum_{\text{all spins}} [\bar{u}(a)\Gamma_1 u(b)][\bar{u}(a)\Gamma_2 u(b)]^* = Tr[\Gamma_1(\not{p}_b + m_b c)\bar{\Gamma}_2(\not{p}_a + m_a c)] \tag{2.2}$$

is applied to the square of the matrix element twice. The resulting averaged magnitude squared of the matrix element is seen in Equation 2.3,

$$\begin{aligned} < |M|^2 > = \frac{1}{2}(\frac{g_z}{m_z c})^4[&(c_V + c_A)^2(p_k \cdot p_p)(p_{k'} \cdot p_{p'}) + (c_V - c_A)^2(p_k \cdot p_{p'})(p_p \cdot p_{k'}) \\ &- (mc)^2(c_V^2 - c_A^2)(p_k \cdot p_{k'})] \end{aligned} \tag{2.3}$$

Once the matrix element is calculated the differential cross section is calculated using the golden rule for the scattering of two particles [24],

$$d\sigma = |M|^2 \frac{\hbar^2 S}{4\sqrt{(p_k \cdot p_p)^2 - (m_k m_p c^2)^2}} \frac{c\ d^3 p_{k'}}{(2\pi)^3 2E_{k'}} \frac{c\ d^3 p_{p'}}{(2\pi)^3 2E_{p'}} \delta^4(p_k + p_p - p_{k'} - p_{p'}) \tag{2.4}$$

where S is a statistical term to account for double counting events with two or more identical particles. This formula can then be evaluated in various reference frames (center-of-momentum or laboratory) to get the appropriate four-vector inner products. For instance, in the center-of-momentum frame $\bar{p_k} = -\bar{p_p}$ which will modify the $\delta^4(p_k + p_p - p_{k'} - p_{p'})$ to become $\delta(E_k + E_p - E_{k'} - E_{p'})\delta(-\bar{p}_{k'} - \bar{p}_{p'})$. The final form,

$$\frac{d\sigma}{d\cos\theta_{CM}} = \frac{4}{\pi}(\hbar c)^2 \left[\frac{g_z}{2M_Z c^2}\right]^4 E^2(c_V^2 + c_A^2 + c_V c_A) \tag{2.5}$$

is derived by integrating over the appropriate delta functions in the center-of-momentum frame.

2.1.2 Neutrino Generator: NEUT

To simulate the interaction of neutrinos in the near detector as well as the far detector the NEUT neutrino generator [25] is used. Historically NEUT was developed to simulate atmospheric neutrino interactions in the original Kamiokande experiment. NEUT has also been used in the K2K, SciBooNE, and T2K experiments. Because of this the original program simulates neutrino interactions from tens of MeV to hundreds of TeV on numerous nuclei including water, hydrogen, carbon, and iron and other elements found in the detectors. The NEUT program simulates numerous interaction channels ranging from quasi-elastic channels, resonant pion, deep inelastic scattering, coherent pion interactions as well as kaon and eta production.

Specifically for the results of this dissertation, NEUT uses the Llwellyn-Smith model [26] of quasi-elastic interactions scattering off free nucleons and is expanded to include nuclear effects via a Fermi gas model of independent nucleons in the nucleus by the Smith and Moniz model [27]. The axial vector and vector components of the nucleon are assumed to be of the dipole form with an axial vector mass of 1.2 GeV/c^2 to match the results of the MiniBooNE CCQE cross section measurement [28] [29] as well as the K2K result [30].

The equation for NCE using the Llwellyn-Smith model is seen in Equation 2.7,

$$\frac{d\sigma}{dQ^2} = \frac{M^2 G^2 \cos^2\theta_c}{8\pi E_\nu^2}[A(q^2) \mp B(q^2)\frac{(s-u)}{M^2} + C(q^2)\frac{(s-u)^2}{M^4}] \tag{2.6}$$

with,

$$
\begin{aligned}
(s-u) &= 4ME_\nu + q^2 - m_l^2 \\
A &= \frac{(m_l^2 - q^2)}{4M^2}[(4 - \frac{q^2}{M^2})|F_A|^2 - (4 + \frac{q^2}{M^2})|F_V^1|^2 - \frac{q^2}{M^2}|\xi F_V^2|^2(1 + \frac{q^2}{4M^2}) \\
&- \frac{4q^2 ReF_V^{1*}\xi F_V^2}{M^2} + \frac{q^2}{M^2}((4 - \frac{q^2}{M^2})|F_A^3|^2 - \frac{m_l^2}{M^2}(|F_V^1 + \xi F_V^2|^2 + |F_A + 2F_P|^2 \\
&+ (\frac{q^2}{M^2} - 4)(|F_V^3|^2 + |F_P|^2))] \qquad (2.7) \\
B &= -\frac{q^2}{M^2}ReF_A^*(F_V^1 + \xi F_V^2) - \frac{m_l^2}{M^2}Re[(F_V^1 + \frac{q^2}{4M^2}\xi F_V^2)^* F_V^3 - (F_A + \frac{q^2 F_P}{2M^2})^* F_A^3 \\
C &= \frac{1}{4}(|F_A|^2 + |F_V^1|^2 - \frac{q^2}{M^2}|\frac{\xi F_V^2}{2}|^2 - \frac{q^2}{M^2}|F_A^3|^2
\end{aligned}
$$

The "$-$" corresponds to neutrinos and "$+$" to anti-neutrinos. The q^2 seen in the formula is the square of the momentum transfer defined in Equation 2.8,

$$Q^2 = -q^2 = (k - k`)^2 \qquad (2.8)$$

using the Feynman diagram in Figure 2.2. The form factors, $F_v^{1,2,3}$ and F_A, are used to describe the the nuclear target material, which is an extended charged target. The form factor F_A is typically given the dipole form [5],

$$F_A(q^2) = \frac{g_a}{(1 + \frac{Q^2}{M_A^2})^2} \qquad (2.9)$$

The axial mass, M_A is an experimentally measured quantity using electron and neutrino scattering experiments. In addition, the ξ variable, with a value of the difference of the anomalous magnetic moments of the protons and neutron, is used by Llwellyn-Smith so that $F_V^2(0) = 1$ by construction under the conserved vector current hypothesis. The final variables in 2.7 are the nucleon mass, M, and the energy of the neutrino, E_ν. Approximations can be made to reduce the formula, specifically the mass of the lepton (m_l) is essentially zero

compared to the mass of the nucleon and second class currents (F_A^3) are assumed to be small. This will reduce the equation to the form seen in the appendix of the MiniBooNE NCE paper [5].

To simulate the effects of the propagation of the nucleons out of the nuclear medium of the target NEUT uses a cascade model. A cascade model takes the relevant particle, in the case of NEUT the hadrons, steps the particle a small step spatially, calculates if the particle interacted and if not continues to take small steps. If the particle interacts the daughter particles are subject to the cascade model. Once all the particles have reached the edge of the nucleus the information is passed on to the rest of the Monte Carlo. Pions, nucleons, etas, and kaons are treated differently depending on the energy region and what experimental scattering data is available. Each of the particles is subject to elastic and inelastic scattering, charge exchange, absorption, and particle creation.

2.2 Neutrino Oscillations

Neutrino oscillations were first proposed by Pontecorvo [31] in the form of neutrino to anti-neutrino oscillations. This proposal provided the foundation upon which Maki, Nakagawa, and Sakata [32] expanded the idea that neutrinos of one flavor (electron, muon, tau) can oscillate into another flavor. The first indication of this effect came from the Davis experiment in the Homestake mine [33]. The Davis experiment measured the flux of electron neutrinos from the sun and found there to be a deficit when compared to the predicted rate based on Bahcall's solar model [34]. At the time it was clear there was a problem, but it wasn't clear the problem was with the understanding of neutrinos or the solar model used to predict the neutrino flux from the sun. This became known as the solar neutrino problem.

This problem persisted until the Sudbery Neutrino Observatory (SNO) [35] made a measurement looking at the neutral current interaction mode of solar neutrinos. By measuring the neutral current interactions SNO made an integrated measurement of all the neutrino

flavors instead of the flavor specific charged current measurements [36]. The result of the measurement agreed with Bahcall's model of the sun and the expected neutrino flux. This indicated the flux of neutrinos was correct, but a fraction of them were showing up as a different flavor in the detector.

The first conclusive measurement of neutrino oscillations came from the SK experiment. From the measurement of the angular distribution of atmospheric neutrinos it was shown the upward neutrinos from the other side of the Earth were suppressed compared to the downward neutrinos [37].

Neutrino oscillations can occur if the propagation eigenstate differs from the flavor eigenstate measured in neutrino scattering experiments. This can be described by the transformation of the mass eigenstates into the flavor eigenstates via a unitary matrix,

$$|\nu_{e,\mu,\tau}>= U_{(e,\mu,\tau)i}|\nu_i> \tag{2.10}$$

The parameterization of the unitary matrix results in 3 angles (θ_{12},θ_{13},θ_{23}) and 3 phases (δ_{CP} and two Majorana phases that are possibly non-zero if neutrinos are Majorana particles), see Equation 2.11,

$$U = \begin{pmatrix} c_{12}c_{13} & s_{12}c_{13} & s_{13}e^{-i\delta} \\ -s_{12}c_{23} - c_{12}s_{23}s_{13}e^{i\delta} & c_{12}c_{23} - s_{12}s_{23}s_{13}e^{i\delta} & s_{23}c_{13} \\ s_{12}s_{23} - c_{12}c_{23}s_{13}e^{i\delta} & -c_{12}s_{23} - s_{12}c_{23}s_{13}e^{i\delta} & c_{23}c_{13} \end{pmatrix} \times \begin{pmatrix} 1 & 0 & 0 \\ 0 & e^{i\frac{\alpha_{21}}{2}} & 0 \\ 0 & 0 & e^{i\frac{\alpha_{31}}{2}} \end{pmatrix} \tag{2.11}$$

where c_{ij} and s_{ij} represent $\cos\theta_{ij}$ and $\sin\theta_{ij}$. This mixing matrix can be used to predict the probability of oscillation or survival of flavors. To do this the time propagation operator is used on the initial flavor state to propagate the state to $t > 0$, see Equation 2.12.

$$|\nu_i, x, t > 0>= e^{ip_i x}e^{-iE_i t}|\nu_i, x = 0, t = 0> \tag{2.12}$$

To get the probability that the $\alpha \rightarrow \beta$ under relativistic conditions ($p >> m_i$ and $E \sim p$)

the amplitude is squared, see Equation 2.13.

$$P_{\alpha\to\beta} = |<\nu_\beta|\nu_\alpha>|^2 = |U^*_{\alpha i}U_{\beta i}e^{-i\frac{m_i^2 L}{2E}}|^2 \tag{2.13}$$

Expanding this out the probabilities for both survival, $P_{\alpha\to\alpha}$, and flavor change, $P_{\alpha\to\beta}$, can be evaluated.

Neutrino oscillation parameters have been extensively probed using a variety of experimental setups, but can be broken down into three general groups based on the oscillation parameters of interest. The first of these groups uses neutrinos originating from cosmic rays or accelerator based neutrino sources. This group measures θ_{23} and $|\Delta m^2_{23}|$. Experiments in this group made precision measurements of these parameters including KEK-to-Kamioka (K2K) [38], Super Kamiokande (SK) [39], Main Injector Neutrino Oscillation Experiment (MINOS) [40], and Tokai-to-Kamioka (T2K) [41].

The second group uses reactor and accelerator sources to measure θ_{13} and eventually probe δ_{CP}. Experiments in this group include (Double) Chooz, MINOS, T2K, RENO, and Daya Bay. In 2012 Daya Bay [42] and later RENO [43] released results looking for the disappearance of the anti-electron neutrino, confirming θ_{13} was non-zero, opening the window to measure charge parity violation via δ_{CP}. T2K measured the appearance of electron type neutrinos from a muon type neutrino beam [44], further confirming a non-zero θ_{13}.

The last group uses reactor and solar neutrinos. This group measures θ_{12} and Δm^2_{21}. Experiments in this group include Kamioka Liquid Scintillator Antineutrino Detector (KamLAND), SNO, and SK. Using reactor sources in Japan KamLAND has produced a three flavor oscillation analysis [45] providing constraints on θ_{12}, Δm^2_{21}, and θ_{13}. Using solar neutrinos SK provides measurements of the solar oscillation parameters [46].

Chapter 3

T2K Experimental Setup

The Tokai-to-Kamioka (T2K) [47] experiment, see Figure 3.1, is a second generation long baseline neutrino oscillation experiment sited in Japan. T2K is based on the experience from the KEK-to-Kamioka (K2K) [48] [49] [50] experiment, also based in Japan. The T2K experiment uses a high intensity proton source at the Japan Proton Accelerator Research Complex (J-PARC), to produce an intense highly pure ν_μ beam which is pointed towards the Super-Kamionkande (SK) [51] far detector 295 km away. The beam parameters and baseline were optimized to provide a narrow band beam with a peak energy of ∼600 MeV to maximize the probability of the appearance of ν_e oscillated from the ν_μ neutrinos in order to measure θ_{13}. T2K is also designed to measure the disappearance of ν_μ due to the oscillation of the ν_μ into other flavors. As a result, T2K will make precision measurements of θ_{23} and Δm^2_{23} with a precision of $\delta(\sin^2 2\theta_{23}) \sim 0.01$ and $\delta(\Delta m^2_{23}) \sim 10^{-4}\text{eV}^2$.

3.1 T2K Beam line

To meet the physics goals of the T2K experiment a high intensity, highly pure ν_μ beam is required. A new beam complex, J-PARC, was constructed near the eastern coast of Japan to produce an intense off-axis beam. Protons are accelerated up to 30 GeV (design of the main ring is for 50 GeV) and separated into a spill of eight (six during Run 1) bunches separated

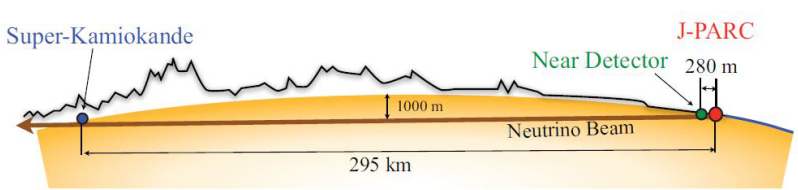

Figure 3.1: General experimental layout of T2K. [47]

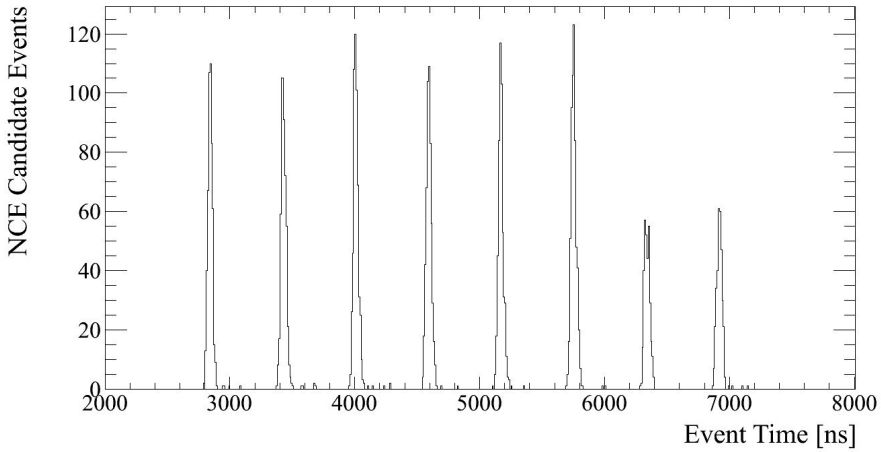

Figure 3.2: Beam bunching structure of the T2K beam. Timing of the neutrino induced NCE events in the PØD. Includes running with only six bunches during Run 1 (spring 2010) and eight bunches during Run 2 (fall 2010, spring 2011).

by 581 ns. Figure 3.2 shows the bunch structure of the beam using the timing of the NCE neutrino events in the PØD. The repetition rate of the beam has been increasing and was 0.4 Hz by the end of Run 4 (0.32 Hz during Run 1). Over the course of running from 2010 until 2013 the beam power has been increased from ∼40 kW to ∼220 kW and delivered 6.4×10^{20} protons on target (POT). Figure 3.3 shows the integrated total POT over the full running periods up to summer 2013 as well as the increase in protons per pulse over time, setting a new world record of $\sim 1.2 \times 10^{14}$ protons per pulse. The design of the accelerator complex is for a mega-watt class beam with facilities upgraded over time and with a goal to provide T2K with 7.8×10^{21} POT.

Figure 3.4 shows the overall layout of the beam complex. The proton beam originates at the ion source on the north end of the linear accelerator (LINAC) accelerating H^- ions up to 180 MeV (design acceleration of 400 MeV). The beam is then fed into a rapid cycling synchrotron (RCS) and accelerated up to 3 GeV after the electrons are stripped from the proton. To produce the neutrino beam, the beam is then injected into the main ring and accelerated up to 30 GeV (design acceleration of 50 GeV). In a single turn the beam is

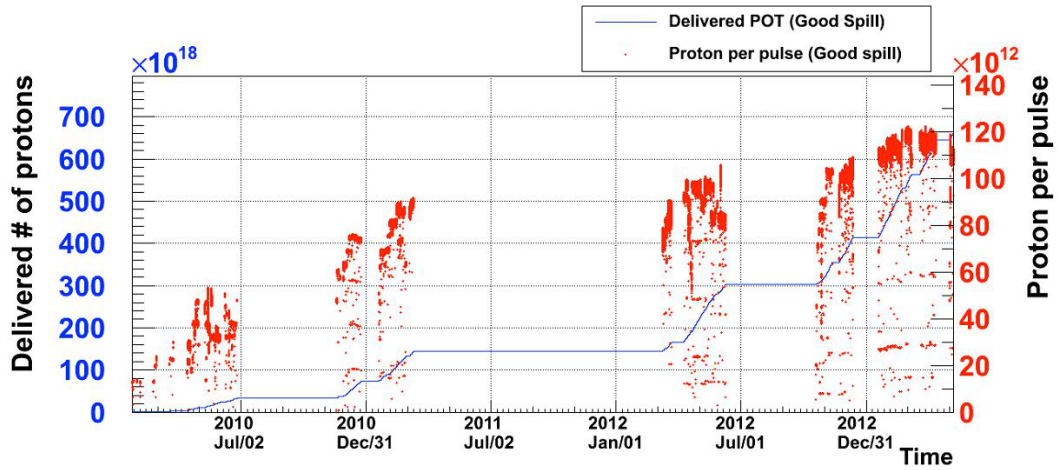

Figure 3.3: POT delivered as a function of time as well as protons per pulse increase over time. Data points are from Run 1 (spring 2010), Run 2 (fall 2010, spring 2011), Run 3 (spring 2012), and Run 4 (fall 2012, spring 2013). A good spill refers to a spill where information about the number of protons and the timing is measured and recorded. [52]

then passed through various beam monitoring instruments and impinged on a cooled carbon target located in the first of three magnetic focusing horns.

3.1.1 Neutrino Beam Line

Figure 3.5 shows the beam line monitors and infrastructure from the main ring to the target station. In this section of the beam line the beam is monitored by 50 beam loss monitors, 19 segmented secondary emission monitors (SSEMs), 21 electrostatic monitors (ESMs), and 5 current transformers (CTs). These monitors provide a measurement of the total number of protons impinged on the target with an uncertainty of 2%.

T2K uses a carbon target housed inside the first of three magnetic horns. Each magnetic horn is run in a pulsed mode at 250 kA providing a 1.7 T field to focus the resulting mesons from the proton-carbon interactions. The purpose of the horns is to increase the flux of neutrinos seen at SK. Figure 3.6 shows the predicted effect of having the horns run at 0,

Figure 3.4: Aerial photo of the J-PARC showing the various accelerators. North is towards the bottom of the photo. [53]

205, and 250 kA. At the peak energy of ∼600 MeV there is a factor of ∼17 increase in flux by running with 250 kA compared to 0 kA. In addition to an increase in flux, the horns can be used to select either positive or negative pions (kaons) by changing the polarity of the horns. By doing this a predominately ν_μ beam or a mostly $\bar{\nu_\mu}$ beam can be created.

The focused mesons are projected 96 m through a helium filled decay pipe and are terminated in a beam dump. A muon monitor just downstream of the beam dump is used to monitor the beam intensity and direction on a bunch-by-bunch basis using an ionization chamber array and silicon PIN photo diode array. Downstream of the muon monitor there is a nuclear emulsion detector used to measure the absolute flux and momentum of the muons.

3.1.2 Neutrino Flux

The T2K flux [54] is predicted using a variety of in situ monitors and external dedicated hadron experiments such as NA61 [55] [56]. The T2K experiment utilizes the off-axis effect to produce a beam peaked at ∼600 MeV while suppressing the high energy tail which would produce neutral current backgrounds in the far detector, see Figure 3.7. The off-axis angle

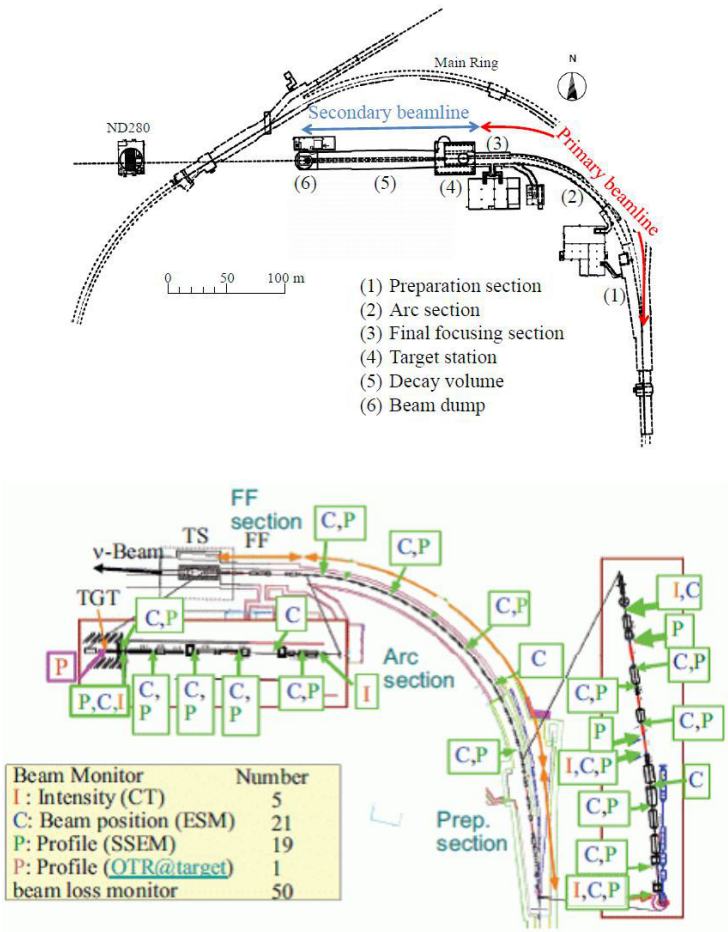

Figure 3.5: The T2K neutrino beam line (top) and beam line monitors (bottom). [47]

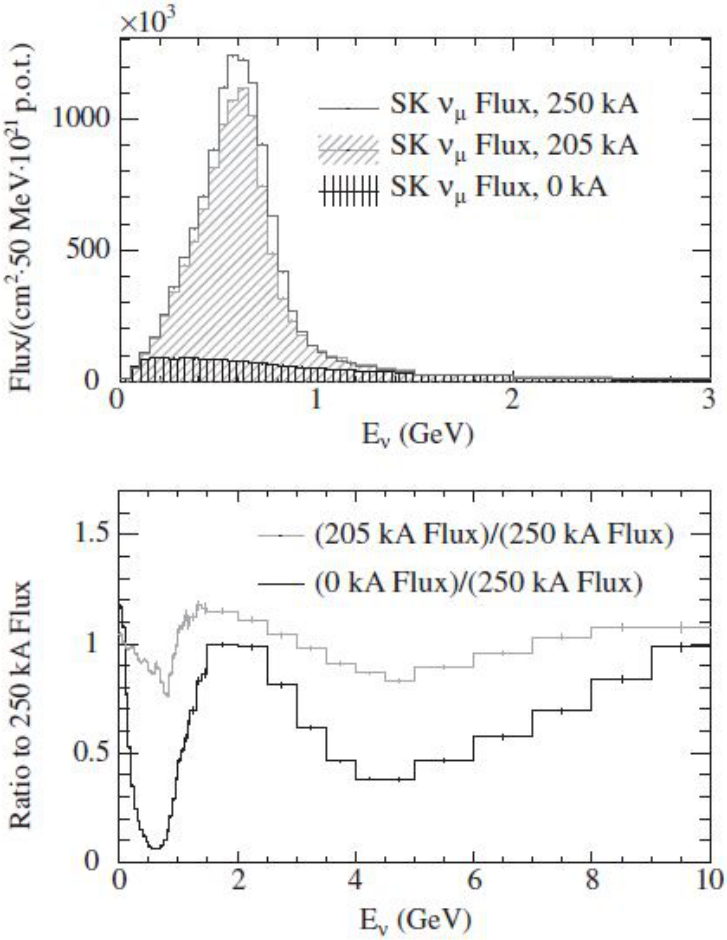

Figure 3.6: The effect of the focusing magnet horns on the flux at SK. Predicted ν_μ flux at SK for horn currents of 0, 205, and 250 kA (top). Ratio of flux compared to the predicted nominal flux with 250 kA running (bottom). [54]

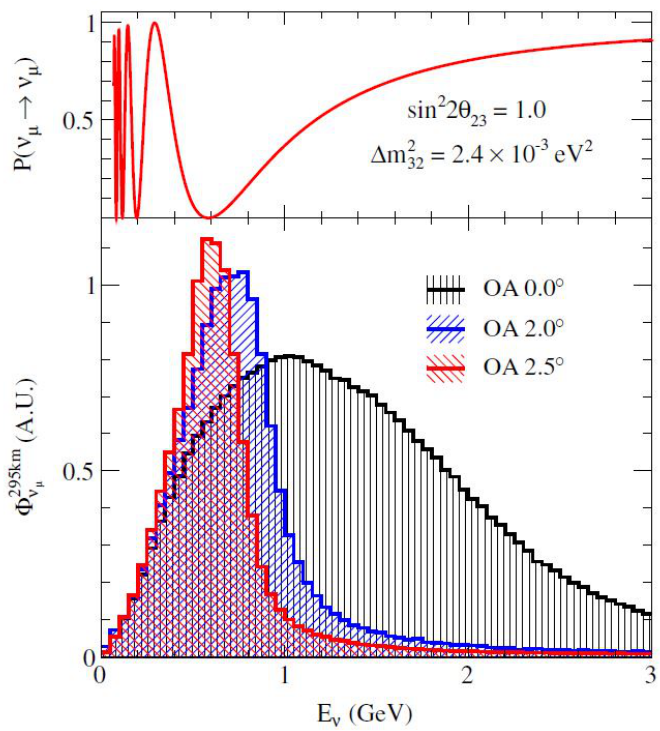

Figure 3.7: T2K flux prediction at 295 km at three different off(on)-axis angles compared to the ν_μ survival probability. [54]

can be tuned to provide the required peak energy given the baseline of the experiment. The survival probability of the ν_μ with a $\sin^2(2\theta_{23})$ of 1.0 and Δm^2_{23} of $2.4{\times}10^{-3}$eV^2 is shown.

The off-axis effect is the result of the conservation of momentum and energy in the decay of charged pions and kaons produced by the proton carbon collisions. Taking the decay of pions as an example, $\pi^+ \to \mu^+ + \nu_\mu$, four momentum must be conserved, thus, $P^\lambda_{\pi^+} = P^\lambda_{\mu^+} + P^\lambda_{\nu_\mu}$, where λ is the four-vector index. Rearranging this equation, squaring both sides, and solving for the energy of the neutrino a relationship between the energy of neutrino, the energy of the pion, and the angle between the pion and neutrino is derived,

$$E_\nu = \frac{m_\pi^2 - m_\mu^2}{2(E_\pi - \sqrt{E_\pi^2 - m_\pi^2}\cos(\theta_{\pi\nu}))} \tag{3.1}$$

This relationship can be used to determine the maximum energy of the neutrino given an

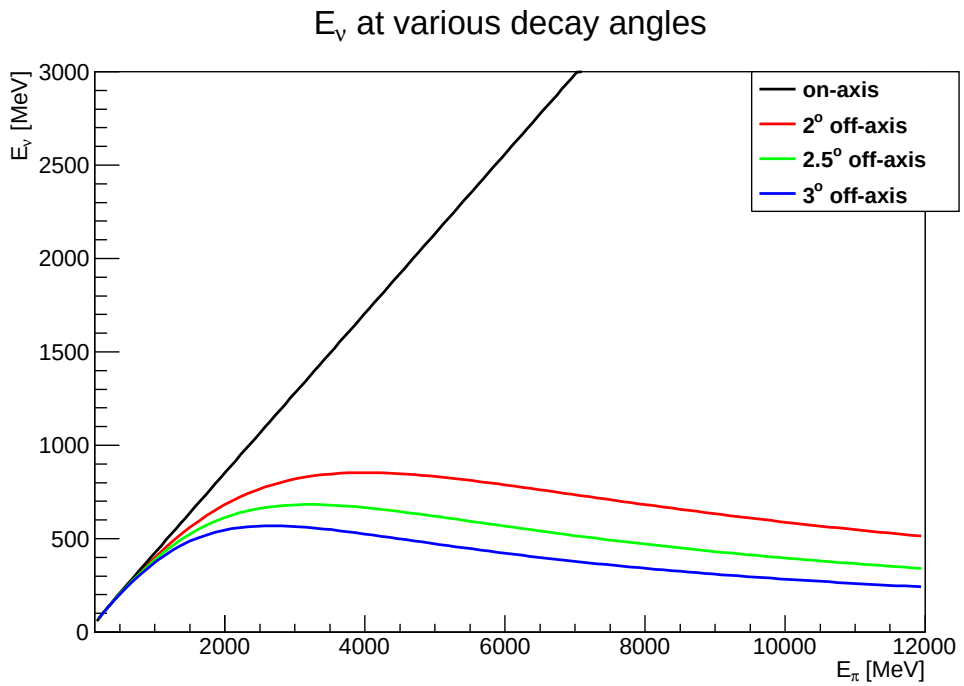

Figure 3.8: Energy of the decay neutrino from pion decay at 0, 2, 2.5, and 3 degrees off-axis from the parent pion direction.

off-axis angle. Figure 3.8 shows the energy spectrum of the neutrino for various off-axis angles and pion energies.

3.2 T2K Near Detector Complex

In order to constrain beam parameters and cross sections which have an effect on the oscillation analyses of T2K, a set of detectors were constructed in the unoscillated beam. This section describes the on-axis Interactive Neutrino Grid (INGRID) and the off-axis ND280 detector. In addition, a description of the Hamamatsu multi-pixel Photon Counters (MPPCs) [57] [58], which are used by all the scintillator detectors in T2K is provided.

3.2.1 INGRID On-Axis Detector

The INGRID [59], see Figure 3.9, is the on-axis detector used to detect the muons, and protons in the proton module, from charged current interactions. The purpose of the detector in terms of the flux constraints in the oscillation measurements is to monitor and measure the beam normalization and spatial distributions. INGRID is made up of 14 modules in the form of a cross with seven modules vertically and seven horizontally. In addition, there are two modules off-axis to measure the symmetry of the beam. Each of these modules is composed of a sandwich of 9 iron and 11 scintillation planes. The readout planes are then enclosed in scintillator vetoes, see Figure 3.10. An additional module composed of finer scintillation planes is used to study CCQE interactions with a visible proton, as well as other topologies needing finer sampling.

3.2.2 ND280 Off-Axis Detector

The ND280 off-axis detector is designed to sample the initial conditions of the neutrino beam at the same off-axis angle as SK. The detector is made up by several sub-detectors designed to measure various neutrino interactions relevant to the systematics associated with the oscillation analyses. The entire detector is enclosed in the refurbished UA1 magnet which provides a 0.2 T magnetic field along the X-axis of the detector geometry, see Figure 3.11. The magnetic field allows for particle charge identification as well as momentum measurements via the curvature of the detected track. The side muon range detector (SMRD) is located within the magnet yoke. Surrounding the inner detectors is a set of electromagnetic calorimeters (ECals). The two detectors located inside the ECals are the pi-zero detector (PØD) and the tracker, which is made up of alternating fine grained detectors (FGDs) and time projection chambers (TPCs).

The purpose of the ND280 off-axis detector is to constrain the uncertainties associated with the flux prediction and cross section models by measuring the rate of events. The

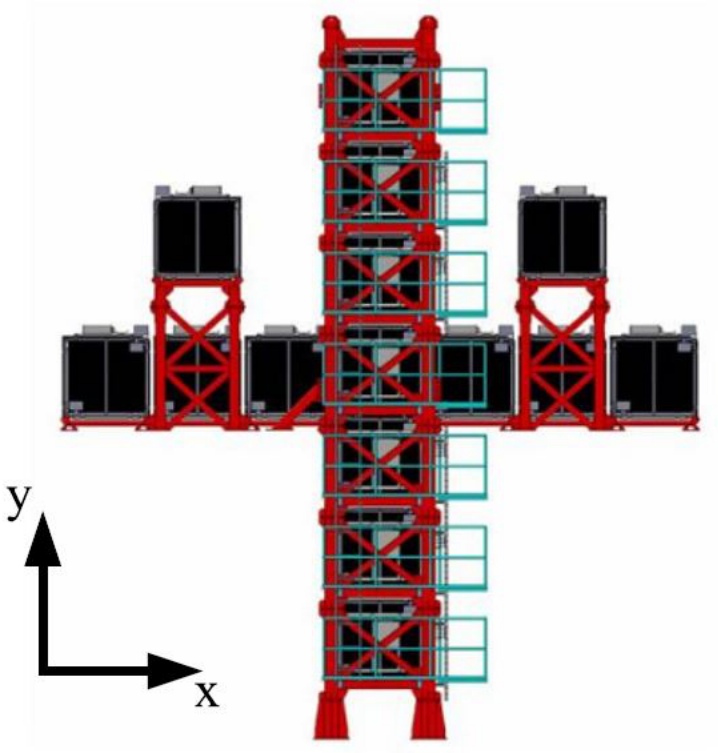

Figure 3.9: Layout of all 17 INGRID modules. The beam center is located at the center of the cross. The two axis of the detector span 11 m and have 7 modules each. There are two off-axis modules to measure the symmetry of the beam as well as a proton module located at the beam center. [47]

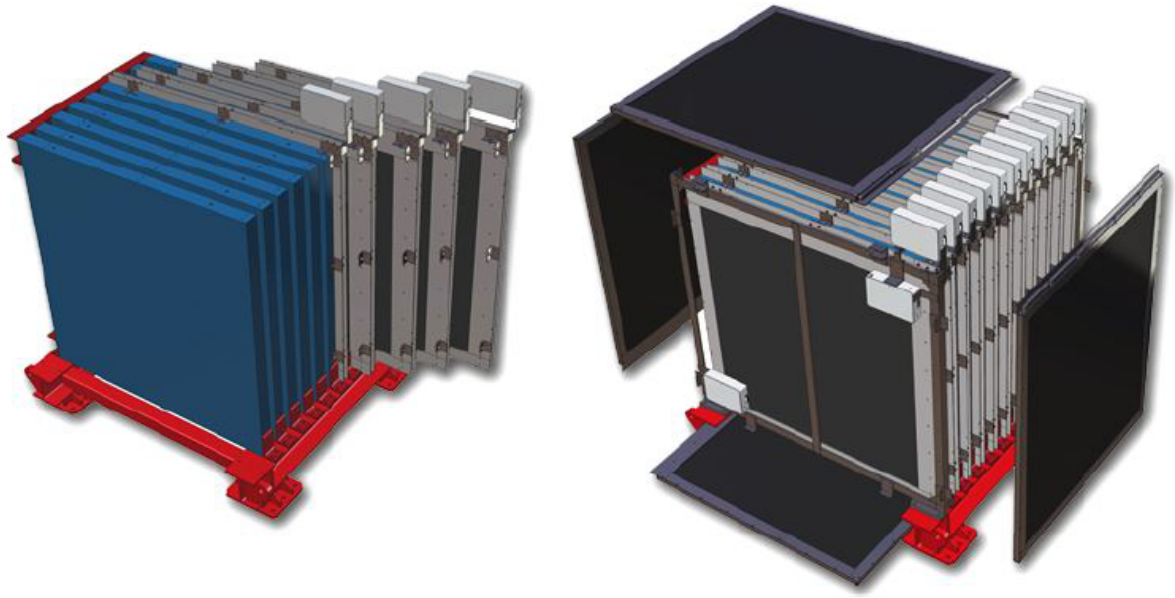

Figure 3.10: Blow up view of the components making up a INGRID detector module. The black outer portions are the veto regions while the inner portion of the detector is a set of scintillator and iron sandwiches. [47]

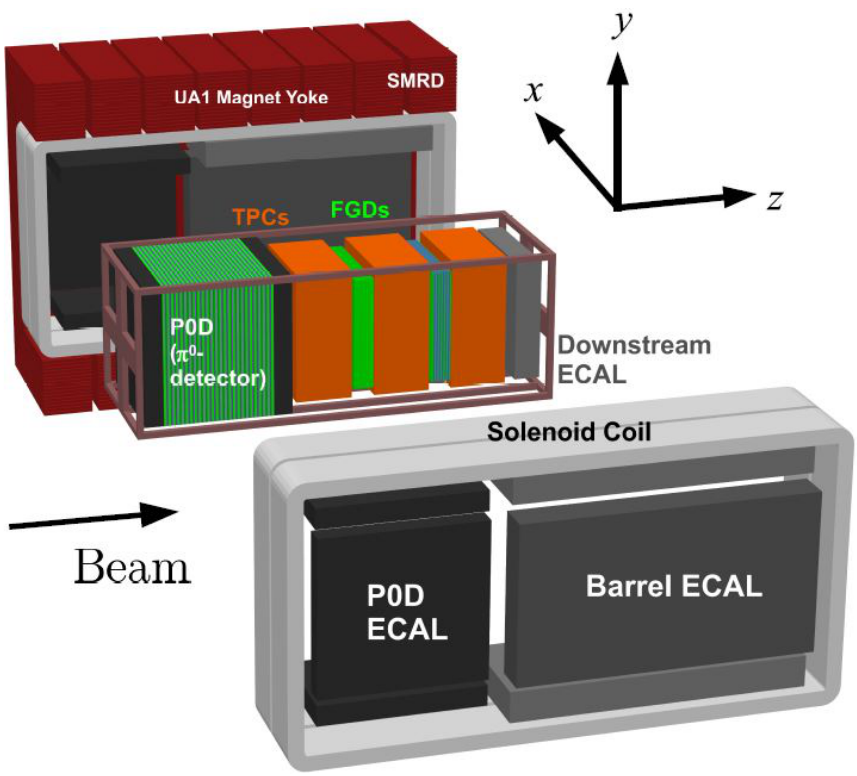

Figure 3.11: Layout of the off-axis ND280 detector. [47]

idea is by combining the external information of the flux prediction, including constraints from the NA61 experiment and beam monitors, as well as external cross section data fits to the NEUT generator with the measured event rate at ND280 detector will reduce the error on the predicted number of unoscillated events at the far detector. By combining all this information in the form of an ND280 likelihood the error at the far detector due to the flux and some cross section models is reduced. An example of this can be seen in the recent T2K appearance paper [44] where the fractional error on the number of ν_e signal events due to beam flux and the near detector is estimated to be 2.9% for $\sin^2 2\theta_{13} = 0.1$ and 25.9% without the near detector constraint.

3.2.2.1 Tracker Detector

The tracker section of the ND280 detector is designed to reconstruct the charge and momentum of particles from charged current interactions. The tracker is made up of two types of detectors, the FGD and TPC. In total there are two FGDs sandwiched between three TPCs.

The two FGDs [60] are configured differently in order to provide a carbon and carbon plus water neutrino target. The upstream FGD is a fully active detector/target composed entirely of layers of alternating scintillation bars. The downstream FGD is composed of the same scintillator bar layers sandwiching inactive water target regions. This allows the tracker region to measure neutrino interactions off of carbon, the typical target used in past measurements, and water that will allow for direct constraints on neutrino interactions on the SK target material.

The upstream FGD has a total of 30 readout layers composed of 192 bars for a total of 5760 channels. Each bar is instrumented with a wavelength shifting fiber coupled to an MPPC. The downstream FGD uses the same bar geometry and readout, but has six 2.5 cm water targets in between 14 layers of scintillator, giving 2688 readout channels.

The three TPCs [61], see Figure 3.12, are low pressure detectors designed to precisely measure the track position, with a design resolution of 0.7 mm, and provide dE/dx based particle identification along with momentum reconstruction using the curvature of the track by drifting ionization electrons to readout planes. The TPCs use a gas mixture chosen for the optimal balance of drift speed and diffusion. The TPCs are readout using micromegas [61] readout pads. Using the timing of the drift and the pattern measured by the micromegas pads the full 3D reconstruction of a track can occur. Using the momentum and energy loss per unit distance of the detected particle the TPC can differentiate between different particle types. In Figure 3.13, the points represent the measured energy loss versus momentum. The

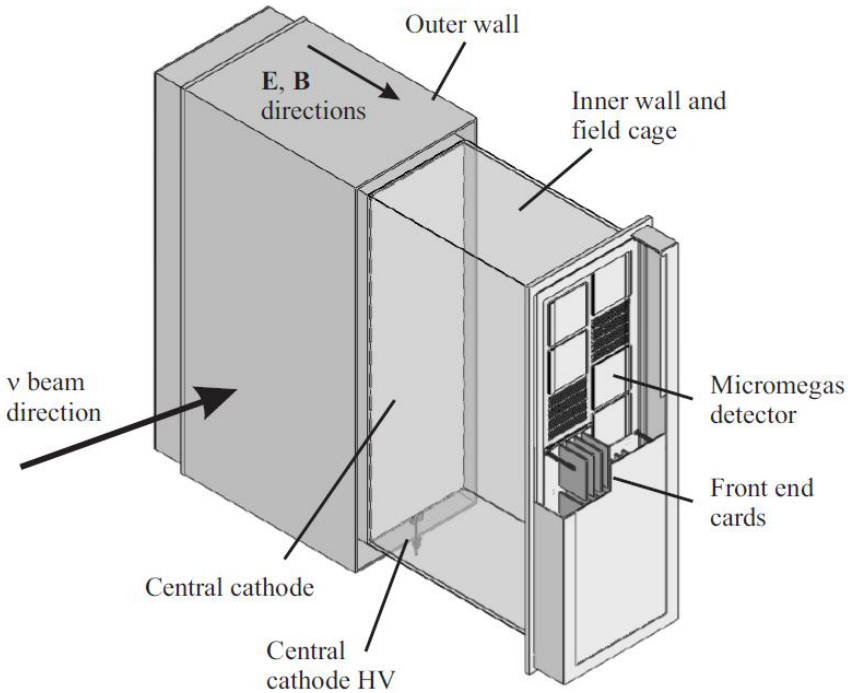

Figure 3.12: Layout of a TPC module. [47]

curves on the plot show the expected energy loss versus momentum for different particle types. The TPC has an estimated momentum reconstruction resolution $\sigma_{p_\perp}/p_\perp$ of 4–12% depending on the momentum of the particle, see Figure 3.14. As can be seen from Figure 3.14, the MC performance is better than the design specification, depicted by the dashed line.

3.2.2.2 Electromagnetic Calorimeters

The tracker and PØD are surrounded by a series of ECals [62] designed to provide containment of electromagnetic showers as well as particle identification. In all there are three separate ECal regions, the "PØDECal" surrounding the PØD, the "tracker ECal" surrounding the FGDs and TPC, and the downstream ECal providing containment at the downstream end of the tracker. Each ECal is made up of scintillating bars with wavelength-shifting fibers coupled to either one MPPC, in the case of the ECal surrounding the PØD, or two MPPCs to provide readout at both ends of the bar.

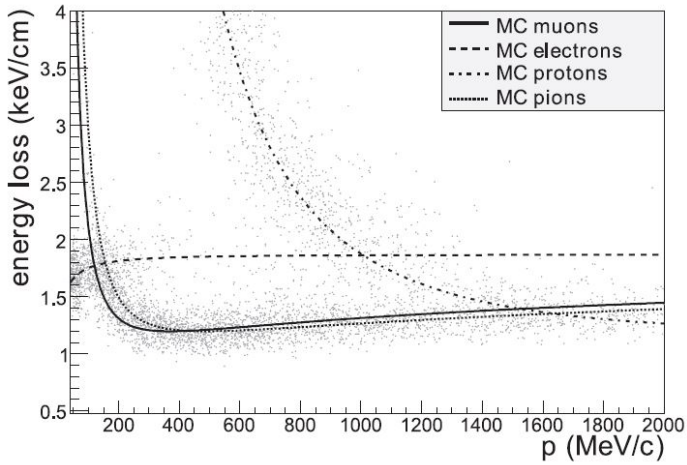

Figure 3.13: PID distribution for the TPC. [47]

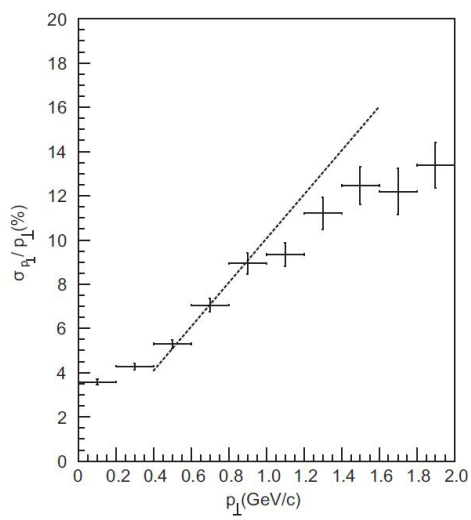

Figure 3.14: Monte Carlo prediction of the momentum reconstruction resolution as a function of the momentum. The dashed line is the design requirements specified for the construction of the TPC. [61]

3.2.2.3 Side Range Muon Detector

The SMRD [63] was designed to provide momentum reconstruction for the high energy muons originating from neutrino interactions in the central part of the magnet. Scintillation bars are located within the flux return of the magnet and read out via MPPCs coupled to wavelength-shifting fibers.

3.2.3 Pi-Zero Detector

The PØD [64] was designed to measure two important backgrounds, which result in large uncertainties on the background estimation, for the oscillation analysis: the uncertainty of π^0 production from neutral current π^0 neutrino interactions on water and the uncertainty on the normalization of the ν_e component in the beam. The PØD is a sampling calorimeter detector made up of four major regions, an upstream electromagnetic calorimeter (USECal), upstream water target (USWT), central water target (CWT), and a downstream Ecal (CECal). Each region is referred to as a SuperPØDule. Each SuperPØDule is made up of the primary building block of the active region of the detector, a PØDule. Each PØDule is constructed of an XZ and YZ readout plane encapsulated in a light-tight cover. The PØD contains a total of 40 PØDules. A cut away version of the PØD can be seen in Figure 3.15.

The USECal is composed of PØDules sandwiching steel/lead/steel radiators (identified as lead in Figure 3.15), starting with a scintillator readout plane on the upstream end. This SuperPØDule consists of seven PØDules and seven radiator planes. The USWT is composed of PØDules sandwiching brass/water planes. In all, the USWT has 13 PØDules and 13 brass/water planes. The CWT is of similar design to the USWT, with 13 PØDules, but only 12 brass/water planes. The CECal is the same as the USECal, with the SuperPØDule having a scintillator readout at the downstream end.

The scintillation target of the PØD is composed of 10400 triangular bars. The height of a bar from tip to base is 17 mm and is 33 mm wide. The bore holes are placed 8.5 mm above

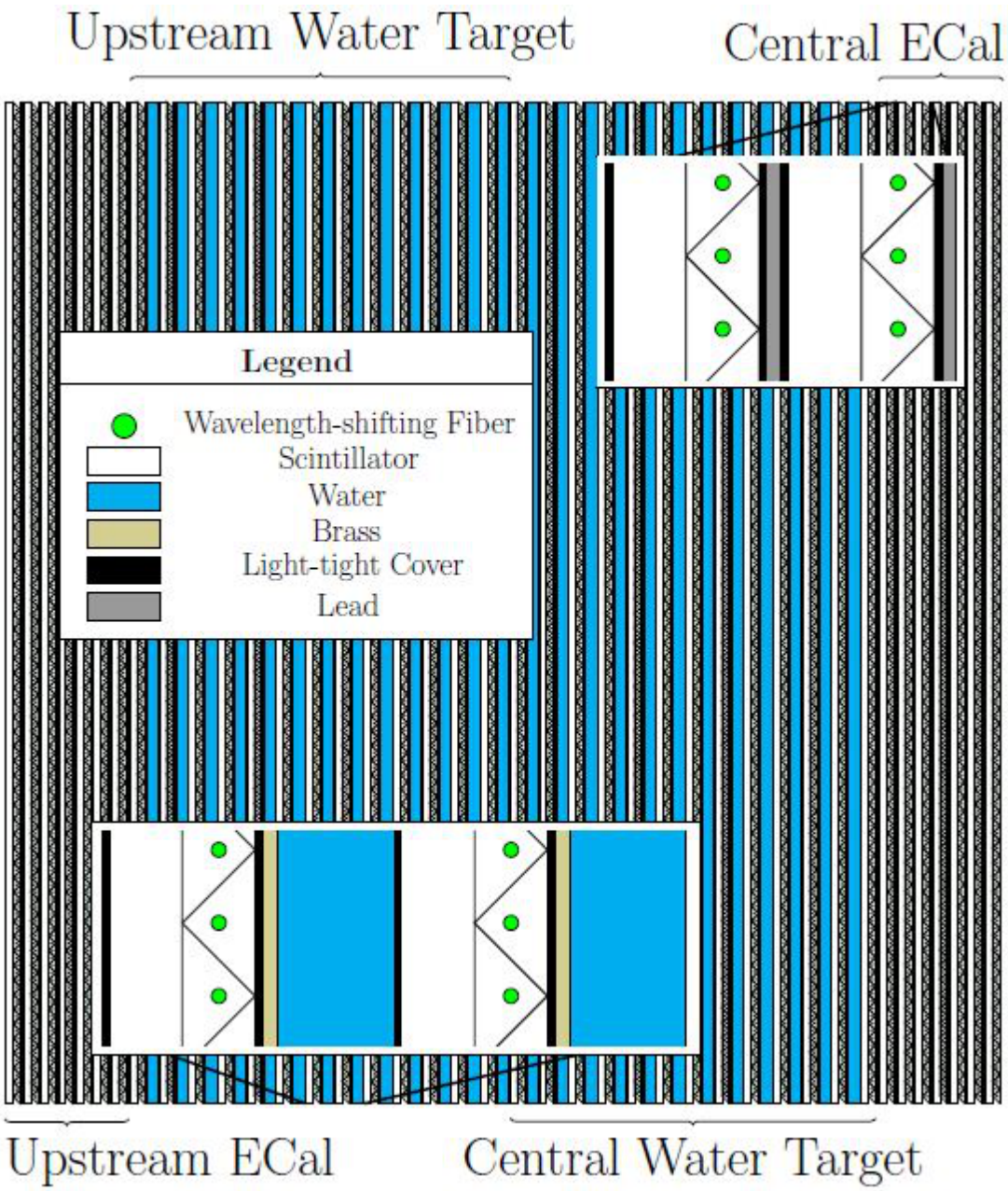

Figure 3.15: Schematic view of the PØD showing the four major SuperPØDules as well as the XZ/YZ readout planes and inactive materials. [64]

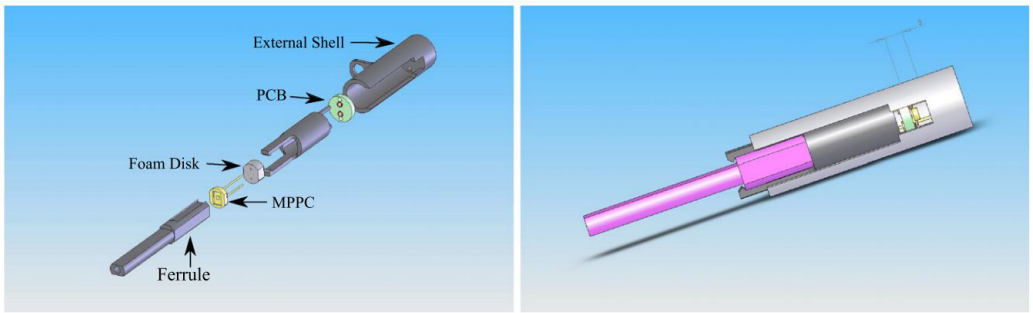

Figure 3.16: Breakdown of the parts in the MPPC connector (left) and combined (right). [64]

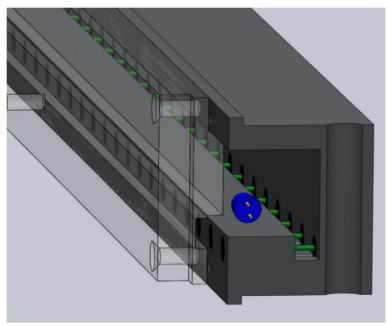

Figure 3.17: The LIS cavity on the opposite side of the WLS fibers. The exposed portion of WLS fiber is illuminated by a 400 nm UV LED using the LIS system. [64]

the base of the triangle. The bars were extruded with a TiO_2 coating to increase the photon capture efficiency. The XZ projection is composed of 126 bars while the YZ projection is constructed with 134 bars. This give the PØD an active readout XY region of 2103 mm by 2239 mm.

The PØD is readout via wavelength-shifting (WLS) fibers installed in a bore hole within the triangular scinitillator bars. Each WLS fiber is coupled to the MPPC via a custom connector shown in Figure 3.16. The other side of the WLS fiber is mirrored with 5 mm of the fiber exposed in the light injection system (LIS) cavity, shown in Figure 3.17.

The light injection system is designed to flash all 10400 channels with a light intensity from a few PE to hundreds of PE. This range covers the expected full range of physics signals. The purpose of the system is to monitor the WLS fiber and readout electronics for variations

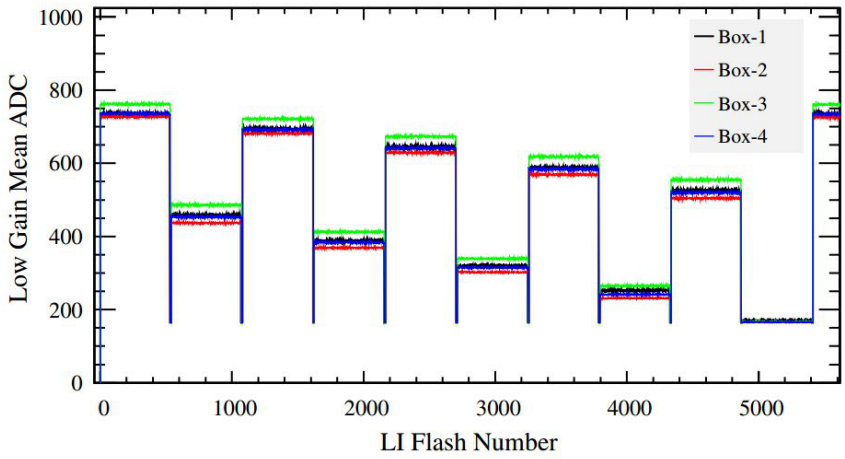

Figure 3.18: Stability of the LIS system broken down by the average signal detected per pulser box on a flash by flash basis for all 10 amplitude settings. [64]

and degradations over the lifetime of the experiment. The LIS is triggered interspersed with the beam triggers and other calibration triggers. The triggers are setup to allow the LIS to cycle through 10 different amplitudes per hour with 500 flashes per setting. This gives a full amplitude scan every hour.

The LIS is composed of four pulser boxes using pulsers from the MINOS experiment [65]. Each box is connected to 20 XY or YZ readout planes by a 60 cm shielded cable. Each readout plane is illuminated by a pair of back-to-back 400 nm UV LEDs. The stability from flash to flash over an entire pulser box is shown in Figure 3.18. The stability over time for each pulser is shown in Figure 3.19.

The fiducial volume used by PØD analyses is designed to exploit the PØD's ability to run with and without water. To ensure water is always present in the fiducial volume the +Y coordinate is partially dictated by how much water the water target bags can hold. In the end the fiducial volume was decided by the PØD NuE and PØD NCπ^0 analyses. The analysis described in chapters 5-8 uses the same definition to leverage the fiducial mass calculation used by these analyses. The Z boundaries actually remove part of a PØDule on the upstream side of the USWT and the downstream side of the CWT. Each XZ and

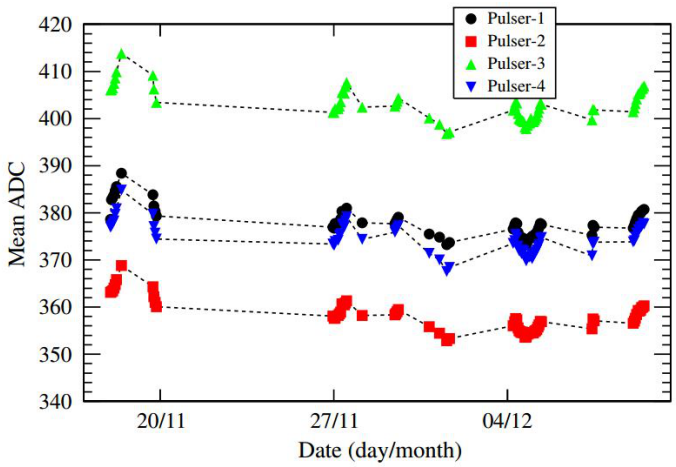

Figure 3.19: Stability of the LIS system over a three week period broken down by pulser box. [64]

YZ plane is ∼20 mm in Z, which means the upstream Z cut removes the XZ readout plane while the downstream Z cut removes the YZ readout plane. This provides an active layer for vetoing exiting or entering particles.

3.2.4 Multi-Pixel Photon Detectors

T2K is the first high energy physics experiment to use the MPPC in place of PMTs on a large scale. The MPPC used by T2K is a customized version of a commercial Hamamatsu MPPC. The active region of the sensor is broken down into 667 pixels on a 1.3 by 1.3 mm surface, see Figure 3.20. The MPPC was chosen because of its relatively low cost, insensitivity to magnetic fields, and the ability to couple directly to the wavelength shifting fibers used in the readout. The typical MPPC delivered to T2K has a breakdown voltage of ∼70V and is run with an over-voltage of 1-2 V depending on the detector. Although the sensors operate in Geiger mode, the sensors provide single photon counting ability at room temperature due to the pixelated structure. Each pixel of the MPPC is ∼50 μm by ∼50 μm. Figure 3.21 shows the response of a sensor to a pulsed LED light. Each of the peaks corresponds to a different number of pixels activated during a pulse.

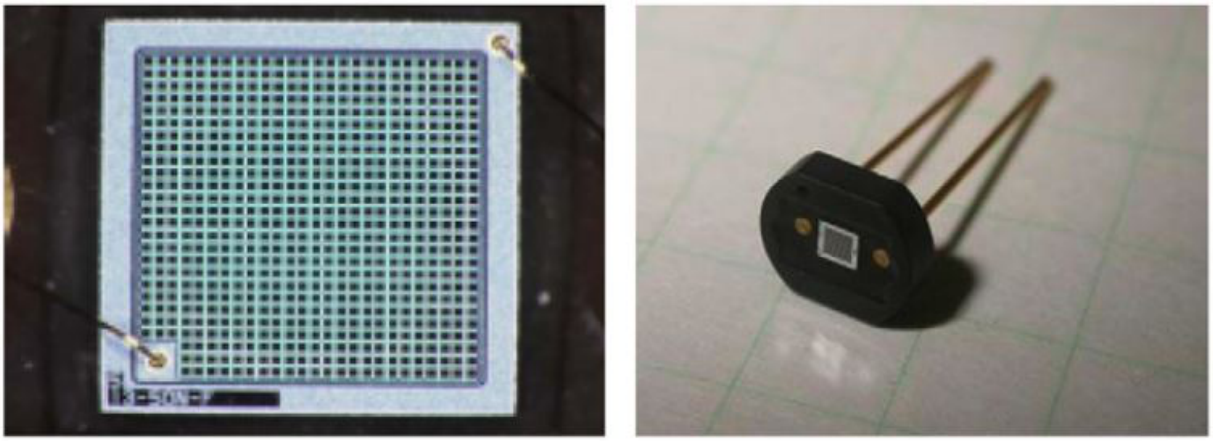

Figure 3.20: Close-up view of the MPPC pixels and view of the ceramic housing. [58]

The number of pixels fired isn't necessarily just from the LED photons, but also from effects inherent to the sensor. The thermal dark noise of the MPPC is ∼1 MHz. In addition to thermal dark noise the MPPC is susceptible to crosstalk between pixels, where a photon produced by the avalanche in one pixel can fire a neighboring pixel and start another avalanche. In addition to crosstalk and thermal noise, the sensor can be fired by afterpulsing. Afterpusling occurs when a trapped electron in the silicon causes a delayed re-activation of a pixel usually resulting in the accumulation of charge equivalent to a partial PE. This happens because afterpulsing usually occurs during the recharging of the pixel. Typically these two effects are combined into a single probability called the correlated noise probability. Figure 3.22 shows the correlated noise probability as a function of the over-voltage, tested at different temperatures.

The MPPC has a photon detection efficiency (PDE) which depends on the over-voltage applied. As seen in Figure 3.23, the PDE ranges from 5-40%. In the regions of 1 to 1.6 V over-voltage the response is approximately linear with a slope of 1.5% per 0.1 V.

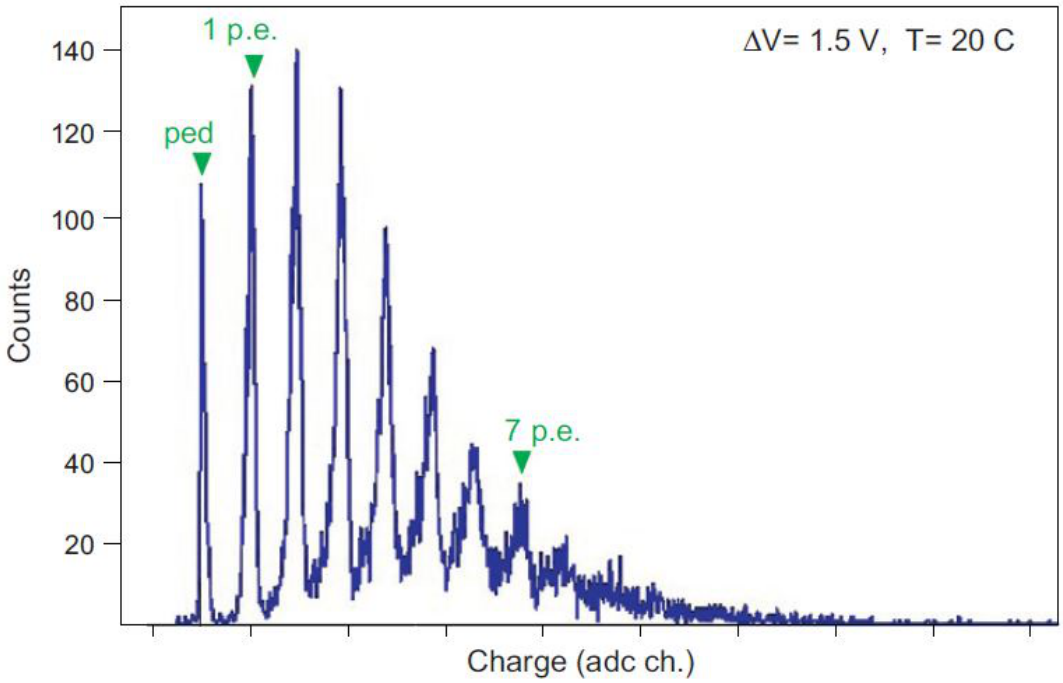

Figure 3.21: MPPC response to multiple pulses from an LED. The individual photon peaks are visible up to 7 photons. The first peak corresponds to the noise pedestal. [58]

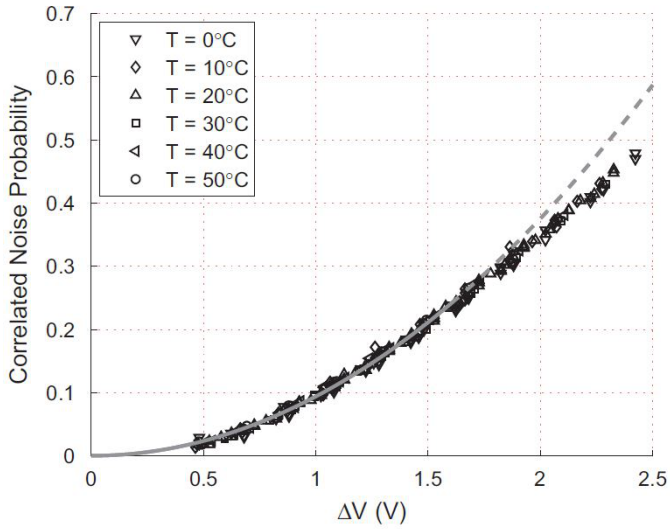

Figure 3.22: Overall correlated noise, from crosstalk, afterpulsing effects, as a function of the over-voltage tested at various temperatures. [58]

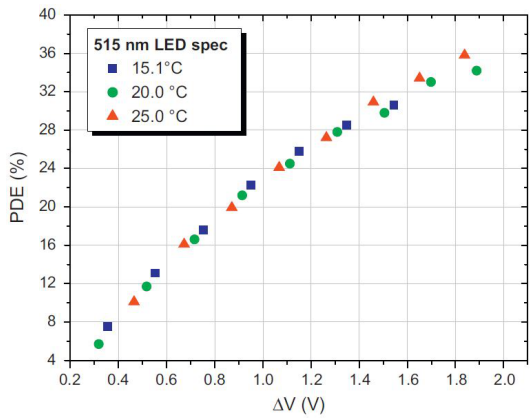

Figure 3.23: MPPC photon detection efficiency for a 515 nm photon as a function of the over-voltage and tested at various temperatures. [58]

3.3 T2K Far Detector

To measure the oscillated neutrino beam T2K uses the Super-Kamiokande(SK) [51] water Cherenkov detector. SK holds 50 kt of purified water with a fiducial volume of 22.5 kt. It is read out by 13,014 PMTs. Of the 13,014 PMTs, 11129 50-cm PMTs face inward and 1885 20-cm PMTs face outward. The inward facing PMTs are optically separated from the outward facing PMTs to provide a target volume, referred to as the inner detector (ID), and a veto region referred to as the outer detector (OD). The OD PMTs are attached to 60 cm by 60 cm wavelength shifting plates to increase the photon detection efficiency.

The primary signal for the oscillation analyses is CCQE events. The signature for the appearance analysis is a single electron-like ring. For the disappearance analysis the signature is a single muon-like ring. The protons from the CCQE interactions are typically below Cherenkov threshold. Due to the relatively higher muon mass compared to the electron mass the visible ring from a muon is sharper due to less scattering. The electron produces an electromagnetic shower through pair production that results in scattering which produces multiple overlaid cones of light. This in turn produces a “fuzzy” ring. Examples of a muon-like ring and electron-like ring can be found in figures 3.24 and 3.25 respectively.

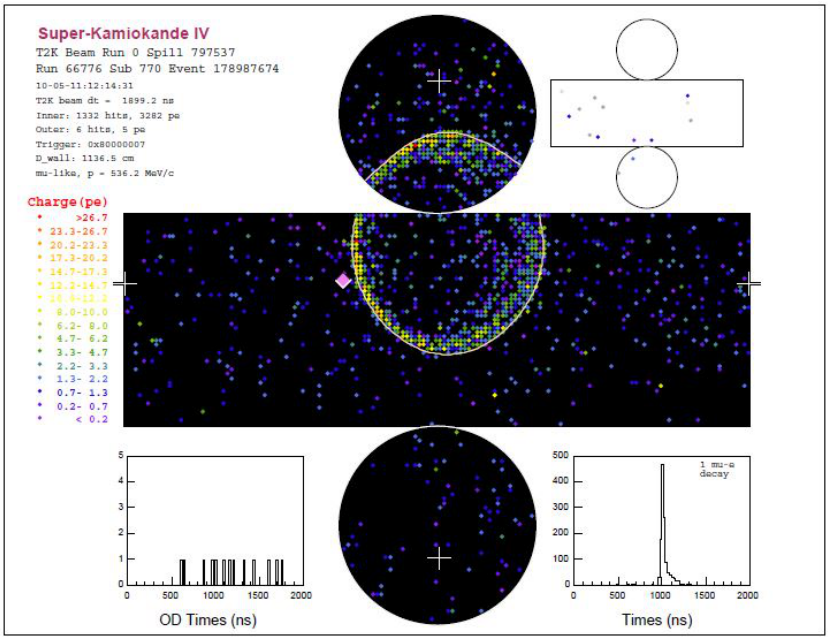

Figure 3.24: Example event display of a single muon-like ring event in SK. [47]

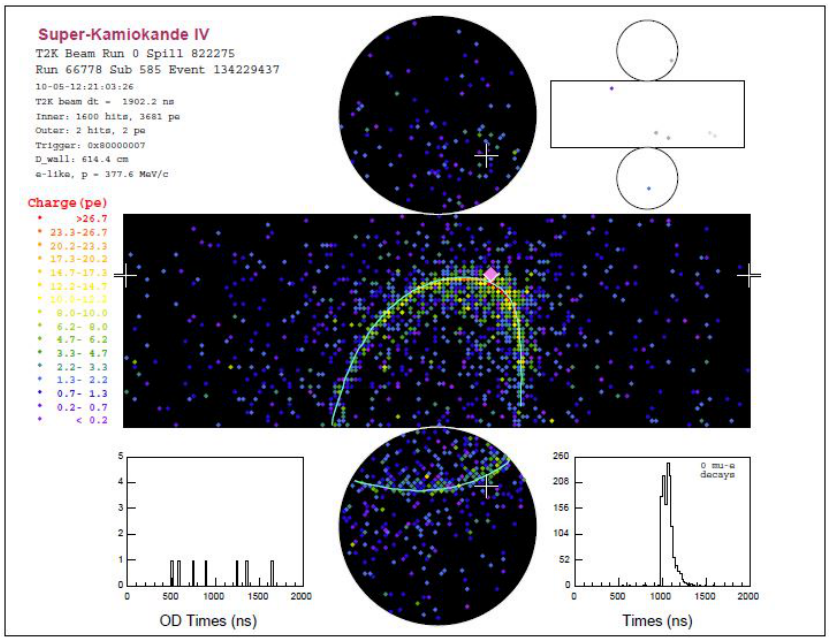

Figure 3.25: Example event display of a single electron-like ring event in SK. [47]

Chapter 4

Previous NCE Measurements

Compared to the CCQE neutrino-nucleus interaction channel the NCE channel is not often measured. CCQE is usually measured by experiments because this is the typical channel used to measure neutrion oscillation due to the detection of the flavor of the neutrino via the charged lepton. The resulting lepton in the CCQE interaction is a charged particle visible in the detector while the resulting lepton in the NCE interaction is a neutrino which is invisible to the detector. This difference is due to the exchange of a Z^0 boson in the NC interactions instead of a $W^{\pm}$ in the CC interaction. Using the kinematics of the visible lepton, more information is available experimentally than in a neutral current process. Even though the resulting lepton isn't visible in an NCE interaction, measurements of the kinematics of the hadronic system as well as the overall cross section can provide powerful measurements to investigate the nuclear form factors used to model the hadronic component of neutrino interactions.

The NCE interaction channel was first observed in 1976 by the Columbia, Illinois, Rockefeller (CIR) [66] and Harvard, Pennsylvania, Wisconsin (HPW) [67] collaborations using a neutrino beam located at Brookhaven National Laboratory (BNL).

The CIR group carefully considered backgrounds to the elastic signal, mostly concerned about neutron backgrounds which produce the signature single straight proton-like track by producing secondary protons within the target volume of the detector. The CIR group used a detector comprised of 21 6-by-6 ft aluminum spark chamber/scintillation counter sandwiches as well as five 8-by-8 ft range chambers to measure the momentum of the muons. To remove the neutron backgrounds they used time of flight measurements as well as geometric arguments related to the geometry of neutron induced proton events to remove the external backgrounds. In addition to the neutron background, they also studied the effects of

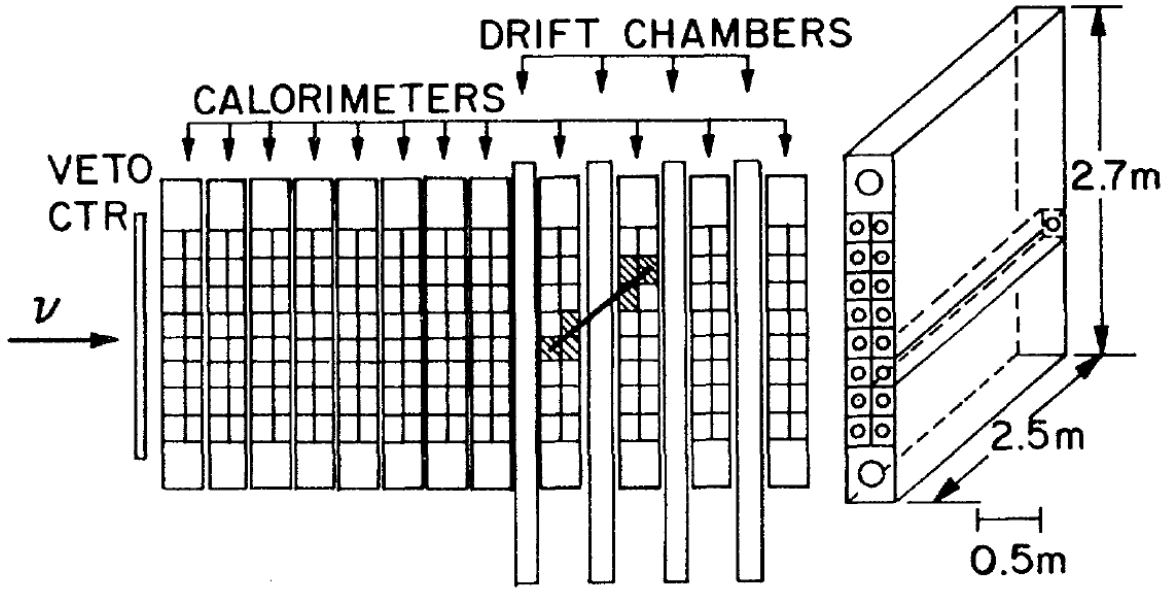

Figure 4.1: The detector used by the HPW group. The full detector is shown on the left and a calorimeter module on the right. [67]

misidentified CCQE events where the muon was of a very high angle and not reconstructed. They also studied pion events that appeared as signals via strong interactions with nucleons in the detector. After their estimated background subtraction they estimated 19(21) signal events depending on the isospin of the pion interaction between the nucleons and pions, either $\frac{1}{2}$ or $\frac{3}{2}$ respectively. The final statistical significance of their measurements were 4.4σ and 5.1σ respectively. In addition, they compared the NCE to CCQE cross sections and found a ratio of 0.23 ± 0.09, with only statistical errors reported.

The HPW group was also concerned about neutron induced backgrounds in their analysis. The detector was composed of 12 calorimeter modules, each with 16 small cells viewed by PMTs. At the downstream end of the detector there were four drift chambers sandwiched between the calorimeters as seen in Figure 4.1. The detector utilized the upstream calorimeters as well as a liquid scintillator veto to tag events from front and side entering particles. In all the detector used 33 tons of liquid scintillator as a target. Their analy-

sis used contained tracks which had charge deposition consistent with a proton. They also removed delayed events from the final sample as these were likely due to neutrons from interactions upstream of the detector. A kinematic cut of 150 MeV kinetic energy was required for an proton candidate to be considered. They also considered multi-particle events such as $\nu_\mu + p^+ \rightarrow \nu_\mu + p^+ + \pi^0$ and $\nu_\mu + n \rightarrow \nu_\mu + p^+ + \pi^-$ where the pion track doesn't exit the vertex cell or the π^0 isn't detected. They estimated this background by looking at multi-particle events and extrapolating the event rate down to regions in kinematic phase space where the particle track would be smaller than the size of a detector cell. After all selection cuts were applied they measured 30 events with a total estimated background of 7 events. In addition, they also compared the NCE to CCQE cross sections and found a ratio of 0.17 ± 0.05 including only statistical errors.

An early measurement of the NCE cross section as well as a ratio with CCQE was done by Harvard-Pennsylvania-BNL in 1979 [68]. These measurements were further improved at BNL including the BNL E734 experiment [4], which is the experiment modern NCE cross section measurements are generally compared to. In sections 4.1, 4.2, and 4.3 we present a description of the BNL experimental measurements as well the most recent measurement from MiniBooNE. All of these experiments have anti-neutrino and neutrino results, but only the neutrino results will be summarized.

4.1 Early Cross Section Measurement at BNL

In this secction we describe the NCE measurement done by Harvard-Pennsylvania-BNL (HPB) in 1979 [68]. This measurement used a higher statistical sample combining a previous sample [69] with additional running and an upgraded detector. This measurement used a similar detector configuration used by the HPW group to detect elastic scattering. The measurement includes checks to understand beam related neutrons as well as neutrons from neutrino interactions from the concrete shielding in the detector hall. In addition, estimations

of the neutrino induced backgrounds within the detector including neutrino-neutron elastic scattering were investigated.

4.1.1 External Neutron Contamination

Multiple studies were performed to understand the external neutron contamination seen in the selected sample. To understand beam related neutrons a comparison of the expected bunch structure from CCQE events was compared to the NCE sample. No events were outside of the expected timing window of ∼50 ns. Neutrons from neutrino events were expected to have an average β of 0.6. By comparing the ToF of these neutrons with the distances from the concrete near the detector a comparison of the event sample timing and the delayed time of the external neutrons with this β is seen in Figure 4.2. To understand the side entering neutrons, the worst case scenario (shortest distance) was assumed. In addition, they investigated the position distribution of the events transverse to the beam as well as along the beam direction to look for distortions consistent with external neutron events. They also investigated the 2D distribution of the kinetic energy versus angle to understand the event distribution in bands of neutrino energy and the lack of low energy protons at low angles, events likely to come from external neutrons. All of these studies show no or very little contamination.

4.1.2 In-Detector backgrounds

There were a few types of neutrino induced backgrounds originating from within the detector. These typically came from neutral current resonant pion production where the pions and/or daughter particles were not visible or from low energy charge current events which were low energy muons and pions. Table 4.1 lists these backgrounds and the estimation and removal methods used.

Table 4.1: Internal backgrounds and methods to remove and/or estimate their contribution to the final sample in the HPB experiment.

Interaction	**Estimation/removal method**
$\nu_\mu + n \rightarrow \nu_\mu + p^+ + \pi^-$ $\nu_\mu + p^+(n) \rightarrow \nu_\mu + p^+(n) + \pi^0$	Compared to Gargamelle and scaled by CCQE rates. Studies of pion absorption were performed as well looking at vertex activity.
$\nu_\mu + p^+ \rightarrow \nu_\mu + n + \pi^+$ $\nu_\mu + n \rightarrow \mu^- + p^+$	Michel decay tag (∼60% efficient upstream and ∼35% downstream) Corrected for spatial coincidence which removed NCE events
$\nu_\mu + n \rightarrow \nu_\mu + n$	Generate uniform distribution over detector, correct by NCE-n to NCE-p^+ cross section ratio NCE off of n(p) FSI nuclear cascade model for both $p \rightarrow n$ and $n \rightarrow p^+$ cases

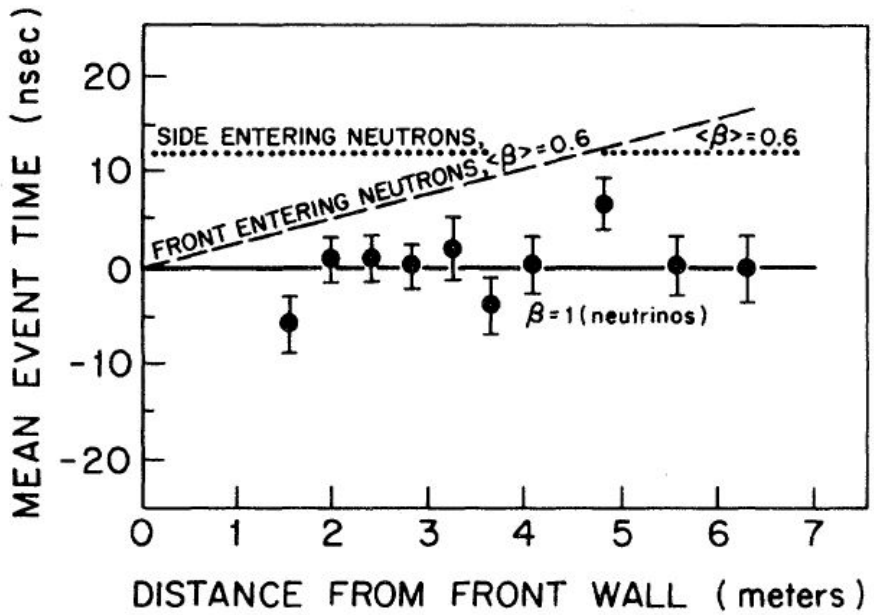

Figure 4.2: Expected difference in time between neutrino beam arrival and front and side entering neutrons from neutrino events in the surrounding concrete. [68]

4.1.3 Results

There were multiple results from this experiment including differential event rates, cross section ratios, and tests of the WS-GIM model. Figure 4.3 shows the event yield as a function of the reconstructed Q^2. The event yield is corrected for the acceptance of the measurement as well as the flux which was normalized to the CCQE selection. The various curves represent different values of $\sin^2\theta_w$, which at the time was being evaluated along with other parameters in the WS-GIM model.

In addition to the differential event rate, the ratio of neutral to charged current cross sections was taken and found to be 0.11±0.015, which was compatible with the previous measurements at the time, shown in Table 4.2. As will be seen in Section 4.2, this ratio has changed over time as the understanding of neutrino interactions became more well understood.

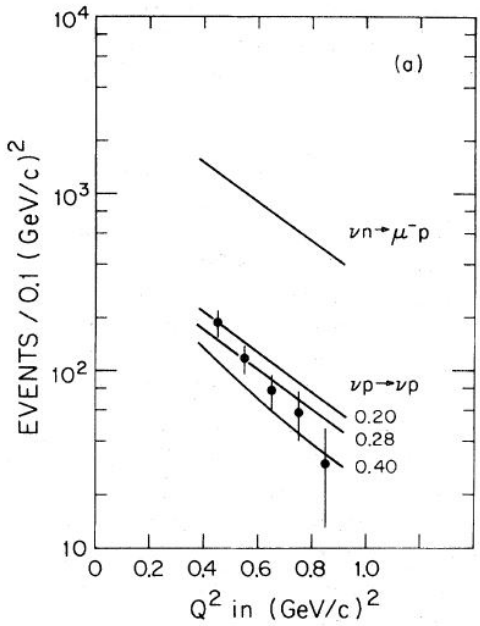

Figure 4.3: Corrected event rate as a function of reconstructed Q^2 for the $\nu_\mu + p^+ \to \nu_\mu + p^+$ interaction. For reference the equivalent charged current interaction is shown. At the time of this experiment parameters associated with the WS-GIM model were under study and as a result the expectation from the model as a function of the $\sin^2\theta_w$ are shown for values of 0.4, 0.28, and 0.2. [68]

Table 4.2: Ratio of neutral current to charged current elastic(quasi-elastic) scattering cross section as seen in [68]

Experiment	$\frac{\nu_\mu+p^+\to\nu_\mu+p^+}{\nu_\mu+n\to\mu^-+p^+}$
CIB (1981) [69]	0.11±0.03
Gargamelle (1978) [70]	0.12±0.06
Aachen-Padova (1980) [71]	0.10±0.03
This experiment	0.11±0.015

4.2 BNL E734

The BNL E734 experiment [4] was the first experiment to produce an absolute cross section measurement looking specifically for $\nu_\mu + p^+ \rightarrow \nu_\mu + p^+$ and $\bar{\nu}_\mu + p^+ \rightarrow \bar{\nu}_\mu + p^+$. Prior to this measurement searches for NCE interactions had been performed, but only acceptance corrected event rates were reported. Unlike the MiniBooNE measurement described in Section 4.3, the BNL E734 result specifically looked at the neutrino-proton scattering considering the neutrino-neutron scattering a background to the measurement. The final result of this measurement was an absolute differential cross section of the neutrino and anti-neutrino scattering as a function of the Q^2 of the interaction. In addition to the cross section measurement the BNL experiment also produced a NCE/CCQE cross section ratio which is still used in the NEUT generator prediction for NCE in T2K, a precision measure of $\sin^2\theta_w$ and the axial-vector mass M_A which were of interest at the time of the experiment.

4.2.1 Experimental Setup

The BNL E734 detector was a 170 metric tonne detector exposed to a horn focused neutrino or anti-neutrino beam. There were three major sections to the detector, a high-resolution target and tracking section, a shower containment system, and a muon spectrometer. Figure 4.4 shows the full detector as well as a blowup view of the target and tracking sections of the detector. For the NCE analysis only the high resolution target and tracking module was used as the protons were usually contained within this portion of the detector. The tracking section of the detector was composed of 112 sub-modules made up of a combination of liquid scintillator cells and crossed planes of proportional drift tubes (PDT). Each sub-module was composed of 16 liquid scintillator cells and 54 PDTs for a total of 1892 cells and 12096 PDTs. The purpose of the liquid scintillator cells was to provide timing information at the nanosecond scale as well as charge deposition information. The PDTs

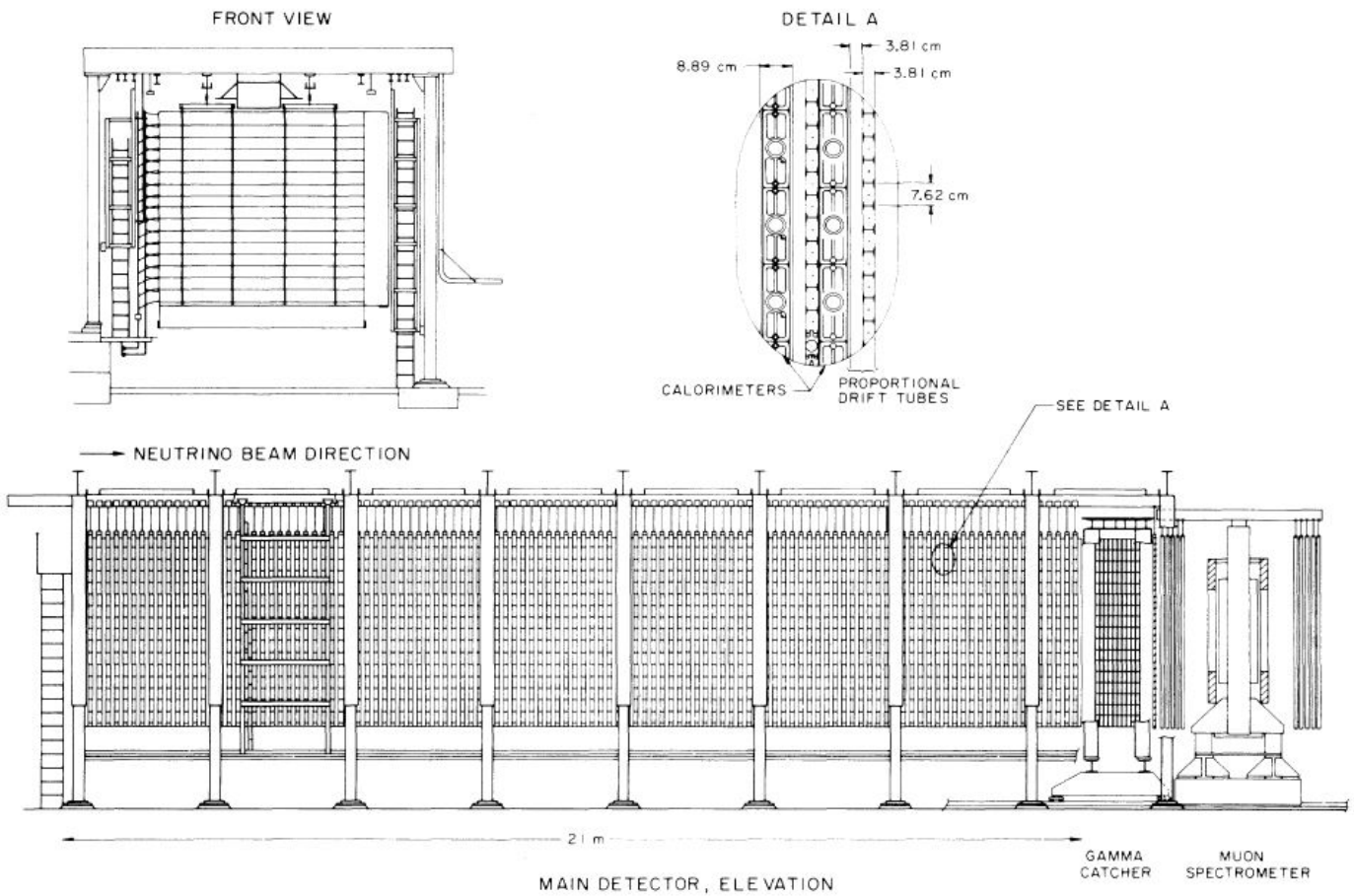

Figure 4.4: The BNL E734 detector setup with a detail inset of the target and tracking section of the detector used in the NCE analysis. [4]

were used to provide 1.5 mm spatial resolution information as well as charge deposition information. The downstream portion of the detector contained a shower containment system, which was a liquid scintillator/lead sandwich, as well as a muon spectrometer which used a dipole magnet and PDTs to measure the momentum of the outgoing muons/anti-muons from CC interactions.

4.2.2 Signal Definition

BNL E734 measured the neutral current elastic scattering, but only the proton channel. The signal was defined before final state interactions, although the MC simulation used incorporated nucleon-nucleon re-interactions in the target nucleus. As with the previous measurement in Section 4.1, the neutron channel was considered a background.

4.2.3 Backgrounds

Similar to previous experiments, BNL E734 was concerned with external neutrons from the beam and neutrino interactions, as well as low energy pion and charged current events. As before, see Section 4.1, a TOF study was performed to ensure that there were no out of time events with respect to the beam timing structure. This ensured there were no neutrons due to interaction in the beam target. To reduce the neutrino induced neutron backgrounds from external dead material, the fiducial volume was reduced to $\sim$19% of the total target mass. To better remove low energy events with muons, pions and neutral particles, a vertex activity study was performed to look for extra energy deposition near the vertex of the event, and in a spherical area around the vertex to identify signatures from neutral particles.

MC predictions were used to estimate the backgrounds for subtraction. A higher purity selection was used to verify the validity of the background subtraction method. This higher purity selection used a stricter vertex activity cut than the standard analysis.

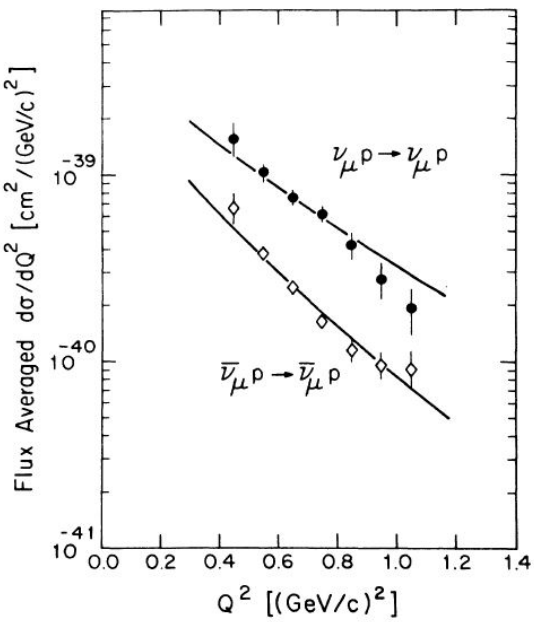

Figure 4.5: Flux averaged differential cross section as a function of reconstructed Q^2 for both the neutrino and anti-neutrino analyses. The flux normalization was determined from the CCQE interaction measurement. The theoretical predictions on the plot use an M_A of 1.06 $\frac{\text{GeV}}{\text{c}^2}$ and a $\sin^2\theta_w$ of 0.220. [4]

4.2.4 Results

As with the result described in Section 4.1, the BNL E734 data were fit for various electroweak parameters as well as neutrino and anti-neutrino differential cross sections and cross section ratios. Figure 4.5 shows the neutrino differential cross section. The event rate was efficiency corrected. The flux normalization was determined using the charged current quasi-elastic measurement. The neutral current to charged current quasi-elastic cross section was also measured to be 0.153 ± 0.007 (stat.) ± 0.017 (syst.). This ratio is used in T2K's NEUT MC, see Section 2.1.2, to predict the event rate of the proton elastic scattering interaction channel.

4.3 MiniBooNE

MiniBooNE [72] is a short baseline neutrino oscillation experiment designed to investigate the LSND anomaly [73]. In addition to investigating neutrino oscillation phenomena, the experiment undertook an extensive neutrino cross section measurement program leveraging the large number of neutrino interactions in the fiducial volume. To date the experiment has measured about 90% of the total neutrino interaction rate by various exclusive channels including, CCQE [28] [29], CCπ^+ [74] [75], CCπ^0 [76], NCπ^0 [77] [78], and NCE [5], and is continuing to make measurements using anti-neutrino data with 83% of the interaction rate covered by measurements of CCQE [79],NCE [80],NCπ^0 [77], and the wrong sign component of their beam [81]. The final NCE result using neutrino data measures the absolute differential cross section with respect to the reconstructed Q^2 for NCE and NCE-like interactions. Additionally, ratios between the NCE and CCQE differential cross sections were performed for both the NCE and NCE-like and CCQE and CCQE-like samples.

4.3.1 Experimental Setup

The MiniBooNE detector [72] is a spherical 12.2 meter diameter Cherenkov detector located in the Booster Neutrino Beam (BNB) at Fermi National Labratory. MiniBooNE is filled with 800 tons of mineral oil. The beam line uses a 8.89 GeV/c proton beam impinged on a beryllium target to produce a highly pure ν_μ beam. The resulting mesons produced by proton interactions in the target are focused using a toroidal magnet field produced by the focusing horn. The focused charged mesons are then allowed to propagate into an air-filled decay pipe. The resulting neutrinos from decays of the mesons then propagate through a beam dump 50 m downstream of the target and finally through 474 m of dirt to ensure no beam particles such as neutrons can get to the detector. The resulting neutrino beam has a mean energy of $\sim$ 800 MeV. The predicted flux can be seen in Figure 4.6.

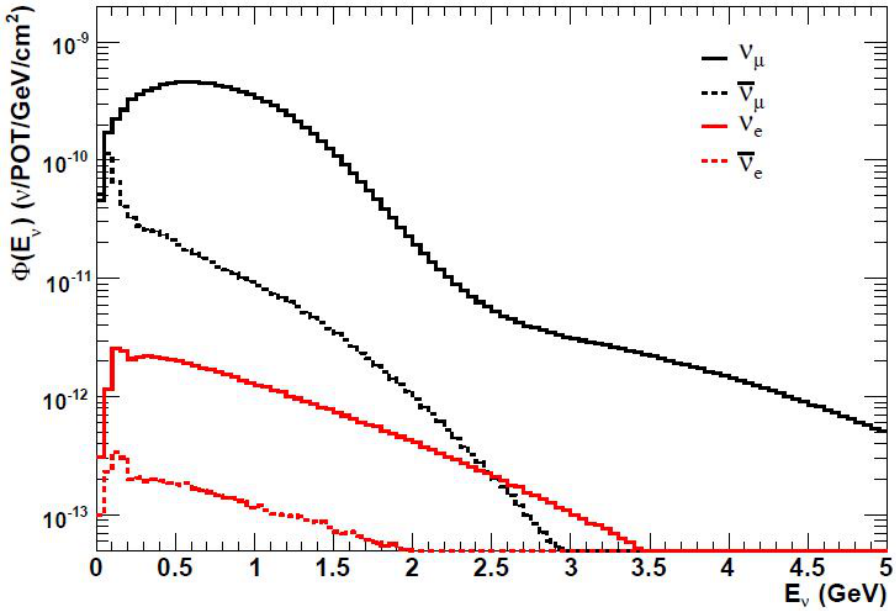

Figure 4.6: Predicted flux at MiniBooNE broken down by neutrino species. [12]

The MiniBooNE detector is read out by 1520 PMTs. The detector is divided into two independent regions where 1280 PMTs read out an inner signal region which has a radius of 5.75 m while the outer veto region, with a thickness of 0.35 m, is read out by 240 back-to-back PMTs mounted tangentially to the barrier between the two regions. A schematic view of the detector can be seen in Figure 4.7.

4.3.2 Signal Definition

Unlike the BNL experiments previously described, the signal in MiniBooNE was defined as elastic scattering events where a proton is visible. This allows for both the $\nu_\mu + p^+ \rightarrow \nu_\mu + p^+$ and $\nu_\mu + n \rightarrow \nu_\mu + n$ interaction channels as long as the neutron re-interacts in the detector and produces a visible proton, or FSI effects produce enough visible protons to be selected by the event selection. The MiniBooNE measurement defined two categories for NCE, a true (generator level) NCE referred to as NCE and an NCE-like definition which corresponds to a background which comes from non-NCE true events, but the particles

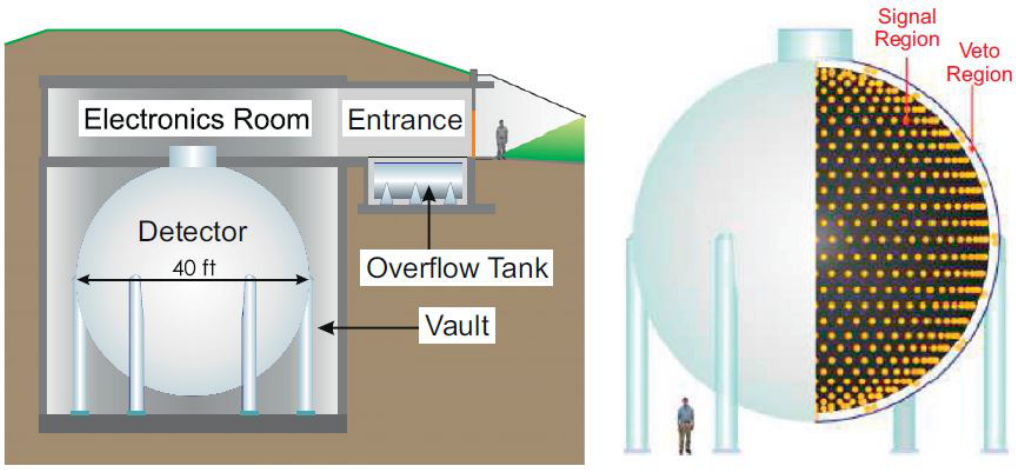

Figure 4.7: Schematic view of the MiniBooNE detector. [12]

after FSI are only nucleons. In principle this means in the primary measurement category, NCE, resonant pion production with the absorption of the pion, or pion-less delta decay will produce an irreducible background as the exiting topology is indistinguishable from true NCE events.

4.3.3 Event Selection

The event reconstruction used in MiniBooNE utilized time and charge information from all of the PMTs, as well as the reconstructed position and direction of particles, to come up with an event maximum likelihood. In total MiniBooNE uses six event hypothesis, see Table 4.3. Since, for instance, the single proton and single muon event hypothesis are single particles, likelihood ratios between such event hypothesis allows for particle identification. To select the NCE sample MiniBooNE implemented the seven cuts listed below:

1. Single sub event where a sub event is defined as at least 10 PMT hits with no more than 10 ns between consecutive hits

2. No more than 6 hits from the veto region PMTs

3. At least 24 hits from the signal volume PMTs

Table 4.3: Event hypothesis likelihood categories used in MiniBooNE reconstruction.

Event Hypothesis	**Description**
Single proton	NCE, NCE-like event
Single muon	CCQE, CCQE-like from ν_μ
Single electron	CCQE, CCQE-like from ν_e
Single π^0	NCπ^0 production
Muon and π^+	CCπ^+ production from ν_μ
Muon and π^0	CCπ^0 production from ν_μ

4. Coincident with the beam timing window

5. Reconstructed proton kinetic energy must be less than 650 MeV

6. Log-likelihood ratio of the single electron and single proton event hypothesis must be less than 0.42

7. Energy dependent fiducial volume cut

   - FV radius $<$ 4.2m for reconstructed kinetic energy $<$ 200 MeV
   - FV radius $<$ 5.0m for reconstructed kinetic energy $>$ 200 MeV

Each of these cuts has a particular purpose. A NCE-like event should only leave a single sub-event as opposed to an event with a pion or muon event where there would be two sub-events, one for the muon or pion and one for the decay products. The veto hit cut is applied to ensure contained events, for more accurate energy reconstruction, as well as vetoing external entering events. At least 24 hits are required for a well-reconstructed event. The selection rejects events with a reconstructed kinetic energy greater than 650 MeV (Q^2 >1.22 GeV^2) due to the reduced signal to background ratio in this region. In order to reduce backgrounds not associated with the beam, mostly Michel electrons from cosmic muons, the log-likelihood ratio is taken between the proton and electron event hypothesis, see Figure 4.8. The final cut is a kinetic energy dependent fiducial volume cut. This cut is implemented to control

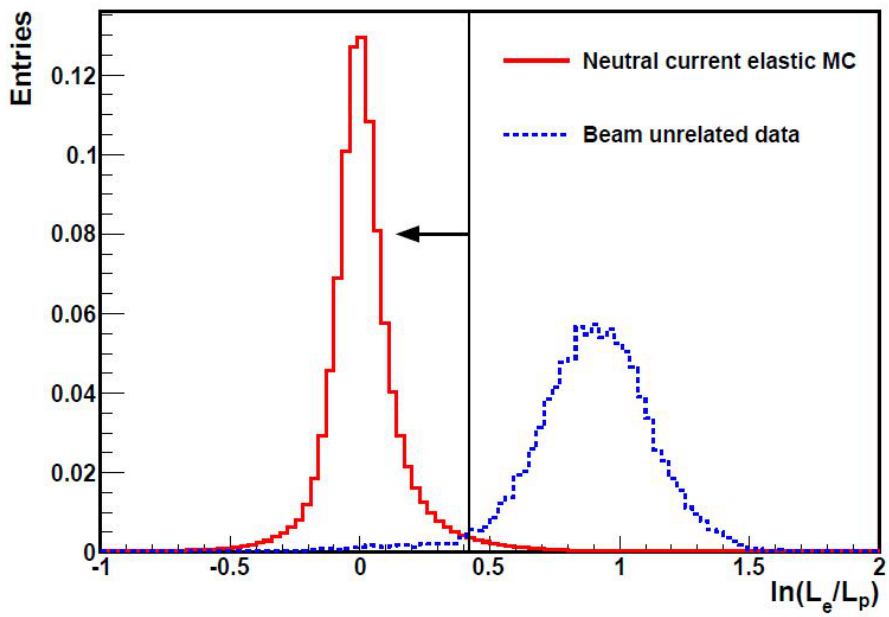

Figure 4.8: Rejection of electrons due to cosmic events outside of beam timing causing reconstructed events during the beam window. [5]

the number of events, typically lower kinetic energy protons, caused by external neutrons from the neutrino interactions in the upstream dirt outside the detector.

After all cuts have been applied a total of 94,531 events are selected, the largest sample of NCE events to date. The selection efficiency is estimated to be 35% with a purity of 65%. The selection backgrounds are broken down into categories shown in Table 4.4. The final event selection binned by kinetic energy with the predicted backgrounds from MC is shown in Figure 4.9.

4.3.4 External Neutron Background

To constrain the neutron background MiniBooNE extracted three dirt-neutron enriched samples using a slightly modified set of cuts. The dirt-neutron contamination of the physics sample originates from neutrino interactions in the upstream wall of the detector hall. These interactions produce neutral particles that enter the fiducial volume and produce proton-like

Table 4.4: Event selection background breakdown in the MiniBooNE sample.

Background category	**Description**
NCE-Like(15%)	Events where the topology seen by the detector is NCE, but the primary interaction is not i.e. NC resonant pion production with no pion in the final state
External Neutrons(10%)	Events where a visible proton are produced by neutrons from neutrino events outside the detector
Others(10%)	Mostly CC events, but have some NC pion, beam unrelated (0.5%) and anti-neutrino NCE events

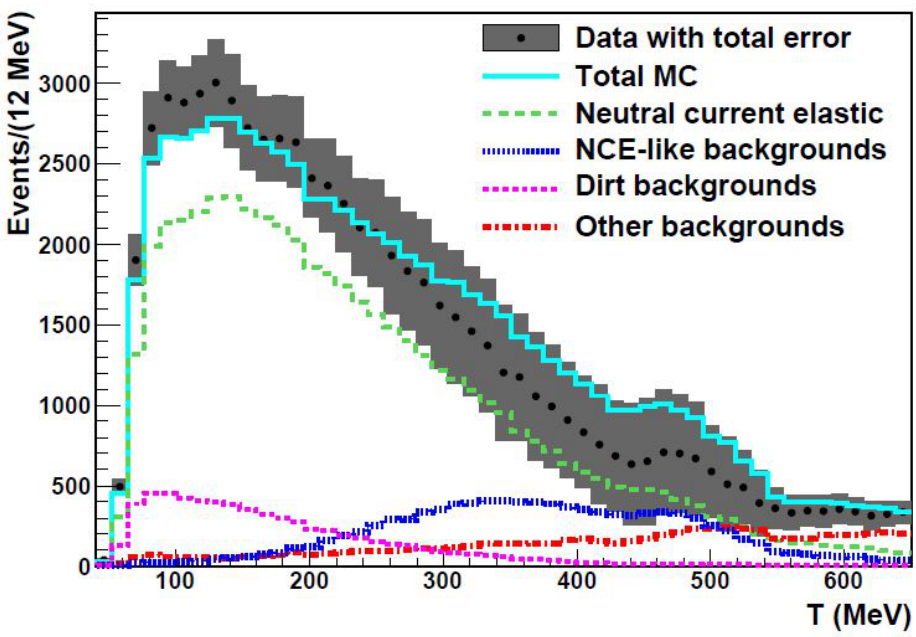

Figure 4.9: Final event sample after all cuts are applied binned by kinetic energy and using a 4.2 m fiducial volume in MiniBooNE. [5]

Sample name	Purpose of the sample	Cuts : $Precuts+$	Dirt fraction (%)
NCE	NCE sample (dirt-reduced)	$R_{fiducial}(T)$	13.4
Dirt–Z	Fit dirt from Z (dirt-enhanced)	3.8 m $< R <$ 5.2 m	27.8
Dirt–R	Fit dirt from R (dirt-enhanced)	$Z < 0$ m	34.3
Dirt–E	Fit dirt from energy (dirt-enhanced)	3.8 m $< R <$ 5.2 m and $Z < 0$ m	37.6

Figure 4.10: Dirt sample breakdown and selection criteria. [5]

signitures. To select these samples the nominal NCE sample cuts described in 4.3.3 are used except for the fiducial volume cut (cut 7). Using cuts 1-6 as a preselection, three different samples were selected with emphasis on the radial distribution of events (R) , the distribution of events along the beam direction (Z) and reconstructed kinetic energy (E). The cuts used to derive these samples and the fraction of dirt content are found in Figure 4.10.

Each of these samples was then fit in a similar way to extract a correction for the MC. For the Z and R samples the distributions were broken down into bins of kinetic energy. For each of these kinetic energy bins a correction factor was calculated using the data to MC ratio. The E sample is fit similarly to get a bin-by-by correction factor. The resulting correction factor, as a function of the reconstructed kinetic energy, can be seen in Figure 4.11. To correct the MC dirt prediction, these three distributions are fit together with a piecewise function where the points are fit linearly below 300 MeV and as a constant above 300 MeV as seen in Figure 4.11. The piecewise function is then applied to the MC dirt event prediction on a kinetic energy bin-by-bin basis. There is $\sim$ 30% reduction in the integrated predicted dirt background as a result of this correction applied to the MC.

4.3.5 Results

To make these measurements, the crucial external neutron background, see Section 4.3.4, was constrained by data. For all other backgrounds the MC predicted number is used to purity correct the number of events. The primary NCE measurement is an absolute flux averaged differential cross section with respect to the reconstructed Q^2, see Figure 4.12.

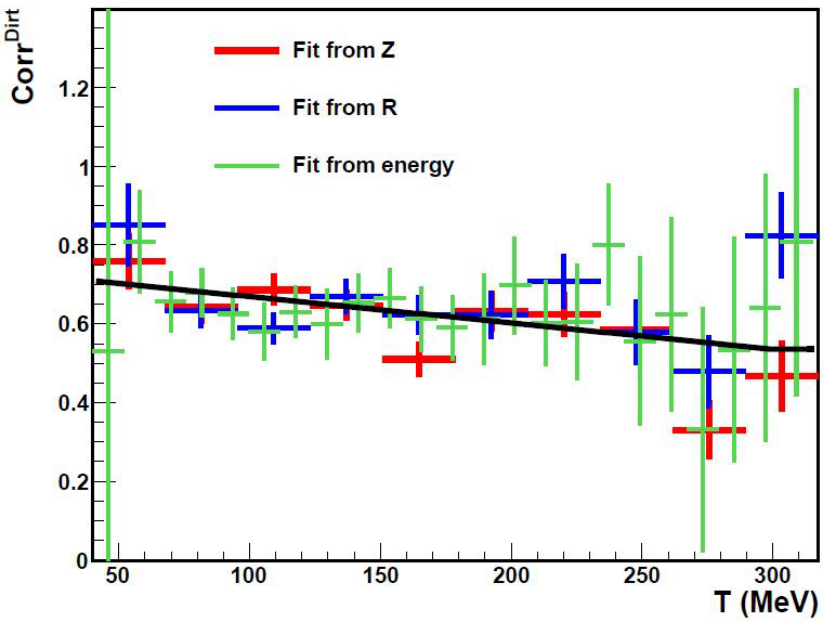

Figure 4.11: Dirt sample correction factors with the piecewise fit. The error bars on the Z and R samples are statistical errors. The error on the kinetic energy sample uses the uncertainty introduced by the optical model, the largest detector systematic. [5]

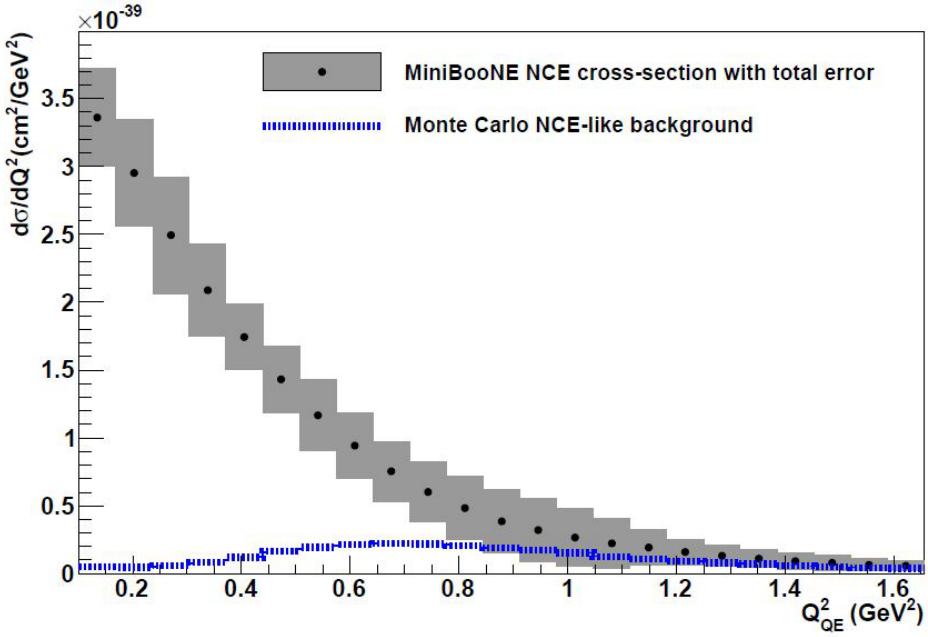

Figure 4.12: Flux averaged differential cross section with respect to reconstructed Q^2. [5]

Unlike the BNL experiments, where the event Q^2 was determined by the reconstructed kinetic energy of the proton track (typically the highest energy proton in the event), MiniBooNE can estimate the total proton energy deposition for all protons in the event as it is proportional to the total scintillation light seen in the event. Because of this, the reconstructed Q^2 is defined as,

$$Q^2 = 2m_p \Sigma T_p \tag{4.1}$$

using the same stationary target assumption as in the BNL measurements.

The differential cross section is then compared to the CCQE differential cross section, where the Q^2 is estimated with the same assumption referred to as Q^2_{QE}, in the form of a ratio of NCE to CCQE, see Figure 4.13 or NCE-like to CCQE-like (including NCE(CCQE)-like backgrounds), see Figure 4.14. In each of the plots there are two MC predictions using different input parameter sets. The black solid curve has a value of $M_A = 1.23$ GeV/c^2 and a Pauli Blocking value of 1.022. The dotted blue curve was produced using an $M_A = 1.35$ GeV/c^2 and a Pauli Blocking value of 1.007. These parameters are used to vary the shape and overall

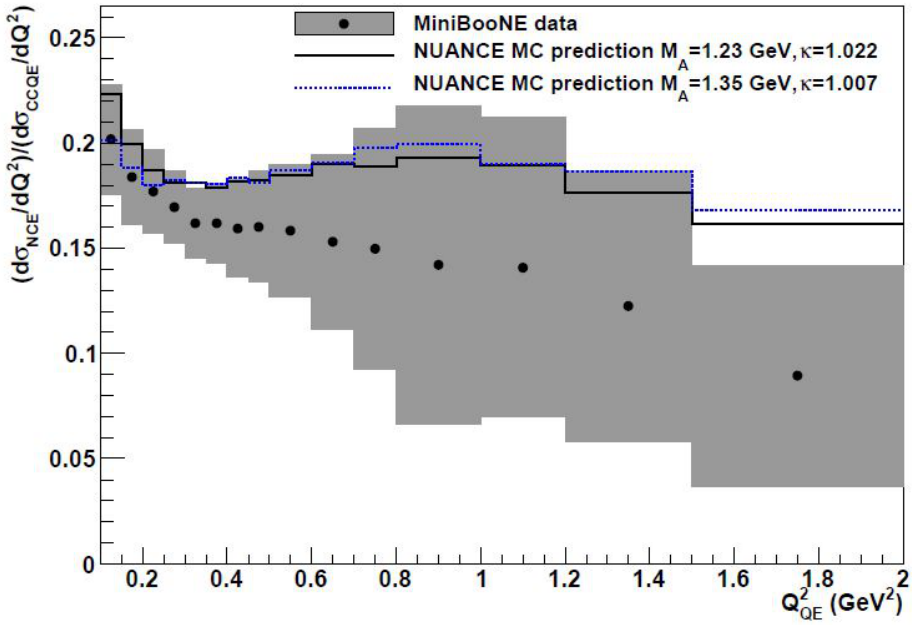

Figure 4.13: The ratio of the differential cross section for NCE to CCQE. [5]

normalization of the cross section. The gray color represents the statistical and systematic errors added in quadrature without the flux error. As can be seen the majority of the bins agree both with the value predicted by BNL E734 of 0.153±0.007±0.017 as well as the MC prediction, except in the cases of the highest and lowest Q^2 bin. Neither of these regions were covered by the BNL E734 result. There are differences larger than the total error between the MC prediction and the measured rate between the NCE-like and CCQE-like samples above 0.6 GeV^2.

The BNL 734 measurement represents the most precise NCE cross section measurement using a tracking detector. The signal definition for this measurement differs from the goals of modern experiments which desire to define cross sections by the observable particles in the detector to avoid potential biases using the MC prediction of the primary interactions before final state interactions. At the time of this experiment it was thought the CCQE interaction channel was well understood and as a result used to determine the normalization of the neutrino flux. With the measurement of CCQE in MiniBooNE [28] there is tension

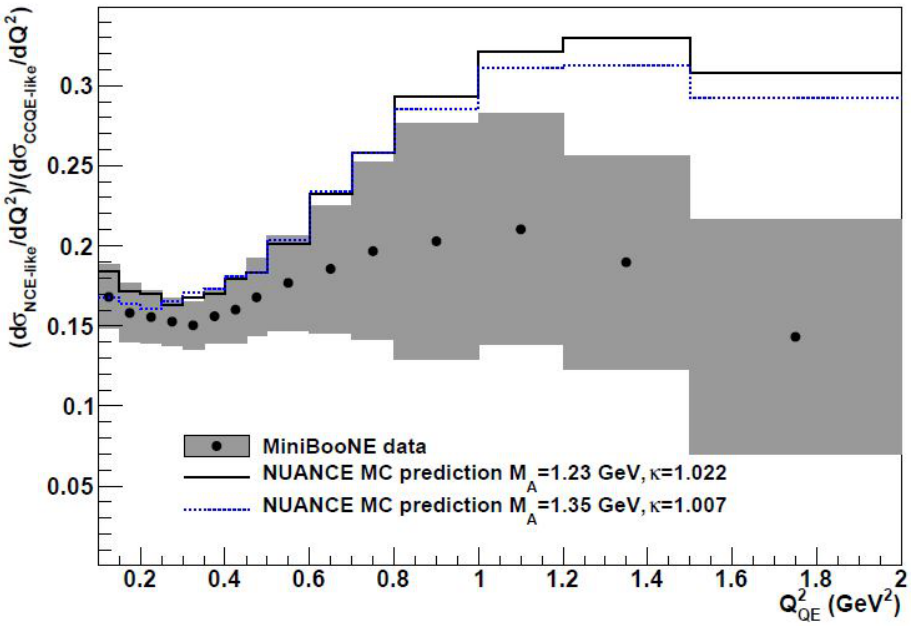

Figure 4.14: The ratio of the differential cross section for NCE to CCQE including NCE(CCQE)-like backgrounds as signal. [5]

between their results and the earlier NOMAD result [82] in the few GeV region. The tension is present because any simple cross section model which varies parameters like M_A cannot explain both datasets simultaneously. This tension calls into question the validity of the normalization of the flux used in the BNL 734 cross section result.

The MiniBooNE measurement represents the most detailed NCE cross section result with a finely binned differential cross section result ranging in Q^2 from 0.1 to 1.6 GeV^2. In addition, MiniBooNE measures the ratio of CCQE to NCE and CCQE-like to NCE-like events. In the CCQE-like to NCE-like ratio there are discrepencies between the MC prediction and the measured value beyond 1 sigma total errors above 0.6 GeV^2. This difference could be of interest in the continuing efforts to understand the CCQE process in the context of neutrino oscillation experiments.

The T2K measurement presented in this dissertation represents the foundation of an analysis program to try and understand the BNL 734 results using a modern experiment

where the neutrino flux is constrained by dedicated experiments. In addition, future T2K results should attempt to understand the CCQE-like to NCE-like ratio and determine if T2K sees a similar result to MiniBooNE.

Chapter 5

Analysis Tool Development

This chapter describes all the tools that were developed specifically for the NCE analysis. These tools have been provided as a general tools for other PØD based analyses to use. To better understand the context of these tools a description of the PØD reconstruction algorithm is given in Section 5.1. Because of the poor PØD reconstruction performance for protons a different particle identification algorithm (PID) was developed independent of the default reconstruction PID algorithm. This PID algorithm, see Section 5.3, is of particular interest to the CCQE and CCπ^+ groups both of which need to either accept or reject protons, muons, or pions. Because the PØD reconstruction doesn't currently attempt to reconstruct the energy of particles in the detector, it is left up to the analyzer to make this energy estimation. For the NCE analysis a robust algorithm using the expected energy loss in various materials in the PØD was developed, see Section 5.4. To understand the flux of external neutrons, an important background to the analysis, a neutron clustering algorithm was developed to detect neutron scattering in the detector. A description of the neutron clustering algorithm can be found in Section 5.5. Certain systematic differences concerning the low charge energy threshold simulation were discovered and a description of methods to mitigate this issue can be found in Section 5.6

5.1 PØD Reconstruction

The PØD reconstruction algorithm was developed with the general idea of producing a single "final" result which was available to global reconstruction, which combines multiple sub-detector reconstruction results together. Because of this general philosophy certain types of assumptions have to be made when producing the final particles presented to the global reconstruction. A flow chart of the overall reconstruction algorithm can be seen in Figure 5.1.

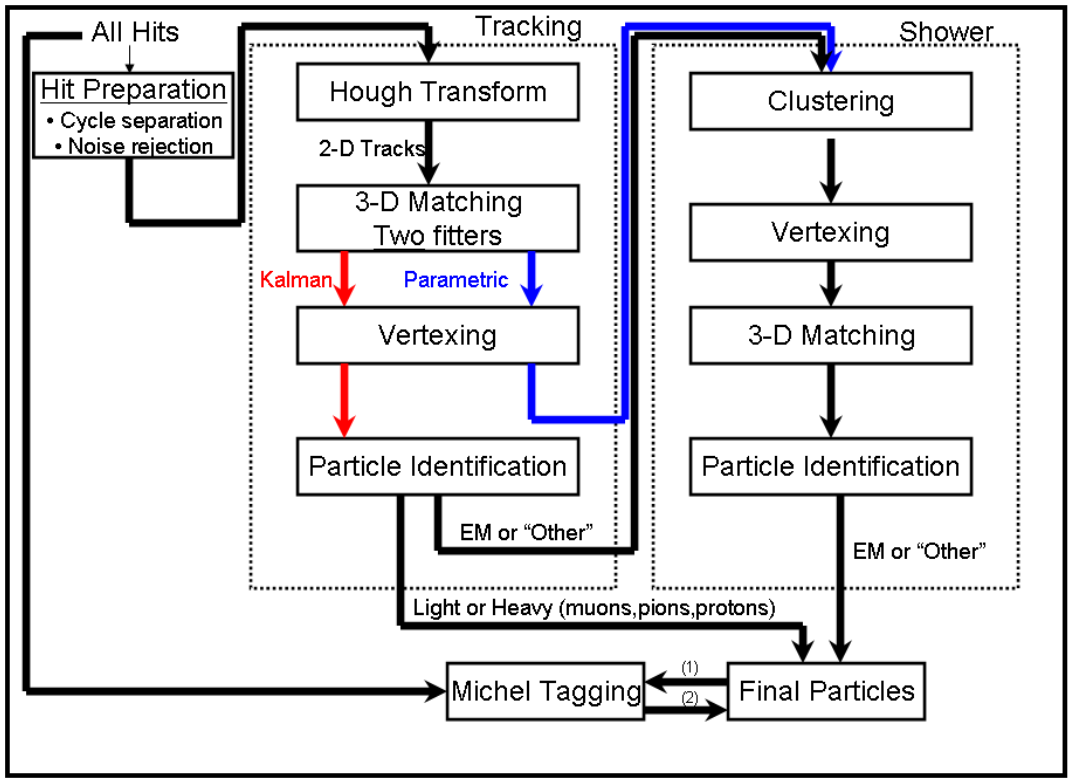

Figure 5.1: Flow of the PØD reconstruction algorithm, starting with the calibrated hits, through the tracking reconstruction, shower reconstruction, and finally Michel decay tagging.

PØD reconstruction has four separate regions of reconstruction: the hit preparation, track reconstruction, shower reconstruction, and Michel decay tagging. For the purposes of this analysis the output of the shower reconstruction is ignored.

5.1.1 Hit Preparation

The input hits are all hits which are recorded by the DAQ system. This means the hits must meet a charge threshold imposed by the readout hardware of ∼25 ADC counts above the nominal pedstal charge. By meeting this charge requirement, a time stamp is issued to the hit. The PØD reconstruction requires all hits to have a valid TDC value. Since the electronics integrate the charge in 23 individual time cycles (integration cycles), the first step

in the reconstruction is to break down the hits into 23 groups defined by the cycle number. The hit cleaning algorithm is applied to each of the 23 groups of hits.

Within each group of hits the hits have three criteria applied to them: hit charge greater than 15 PE, hit charge is greater than 7 PE with a neighbor in the same view (XZ or YZ) within 30 ns and 10 cm, or the hit has a neighbor within 30 ns and 3.5 cm. If any one of these criteria is met the hit is saved and passed onto the tracking portion of the reconstruction. In order to initiate the reconstruction at all a cycle must have at least 5 hits. which pass the criteria above.

5.1.2 Track Reconstruction

The track reconstruction algorithm takes the cleaned hits and attempts to produce any number of 2-D and 3-D tracks using a Hough transform, two fitters, and particle identification.

5.1.2.1 Hough Transform

The initial track seeds are produced using a Hough transform to identify hits in a line. The Hough transform is applied to each of the two views (XZ and YZ) independently to produce a 2-D track. A Hough transform is a coordinate transformation which applies various straight lines of varying slopes to each of the hits and calculates the perpendicular distance from the line to the origin. Once this has been done to all hits the intersection of the curves for each hit on the distance versus angle (slope) space specifies the seed state. At least 4 hits must be present in the view to run the Hough transform. Once the track seed has been produced the track is extended layer by layer via a road following algorithm which looks for hits upstream and downstream of the track seed in a width of 60 mm with an angular tolerance of 1.5 radians for particle scattering.

5.1.2.2 3-D Matching and Fitting

Once the 2-D track seeds are produced they are matched to tracks from the other view. All permutations are all allowed and tracks are allowed to be used multiple times to account for tracks that appear on top of each other in one view but can be resolved in the other. Once the 3-D matching is done one of two fitters is applied to the track to get the final track parameters. The first of these fitters is a Kalman filter method which uses each of the scintillation planes as a measurement to interatively fit over the length from the track. The Kalman filter begins at the downstream end of the track and moves upstream layer by layer. Once the filter reaches the upstream end of the track the filter continues to fit from the upstream position back to the downstream position. When the fit is complete each scintillation layer is provided with a "node", a grouping of hits which provide position, time, charge and direction information. All tracks are asssumed to be going downstream. If the track is of too high of an angle or is too short to provide enough layers (minimum of 6) to measure a second fitter is applied.

The second fitter is a simple linear fit over the hits which provides a general direction and position of the tracks. This fitter doesn't provide nodes per scintillation layer, as the Kalman filter does, but instead provides one node for each hit in the track.

5.1.2.3 Vertexing

The vertexing algorithm takes combinations of all the tracks and projects the tracks to the point of closest approach. Using the uncertainty in the position and time of the tracks to produce an uncertainty in the point's uncertainty in time and space, the vertex is considered possible if the spatial variance in less than 50 cm and the time variance is less 40 ns. This is done for all tracks to come up with possible vertices. The vertices are then clustered if they are consistent to less than 40 ns and 20 cm in space. This process continues until all vertices are clustered into a best candidate and no more track combinations are possible. Only a single vertex is allowed per integration window.

5.1.2.4 Particle identification

The PØD reconstruction PID algorithm is a likelihood based PID with probability distribution function (PDF) inputs from particle gun studies. The particle gun studies used muons and electrons to investigate the charge asymmetry in adjacent XZ/YZ readout layers, the charge asymmetry in adjacent PØDules, the number of layers with no hits, and the fraction of charge in the last 5 readout planes of the reconstructed track. These values were then used in the likelihood to produce a score corresponding to the most likely particle type. The PØD reconstruction PID doesn't use any quantity which is dependent on the absolute charge to avoid being subject to charge differences between MC and data. The PID has a light track, heavy track, EM-like, and "other" category at the tracking stage. The light track category is the muon/pion like category while the heavy track is reserved for proton-like particles. The EM and other categories are passed on to the showering reconstruction algorithm which has its own PID categories. All tracks fit with the parametric fitter are automatically given an "other" PID and passed onto the shower reconstruction.

5.1.2.5 Michel decay tagging

Since the Michel electron resulting from muon decay is a low energy shower, delayed after an event with a lifetime of 2.2 μs, the algorithm takes all hits prior to hit preparation as an input. The Michel electron tagging algorithm then takes the final particle objects and uses a time-space clustering algorithm to look for coincident clusters of hits near the particle. The PØD reconstruction algorithm uses two different tagging algorithms that look for clusters in a slightly different manner.

The first of these algorithms, TP0DTagMuonDecay, is an older algorithm which uses an X,Y,Z,T search. Unlike the other algorithm, TP0DTagMuonDecay searches along the entire length of the reconstruction object. The second algorithm, TP0DMuonDecayTag, is a newer algorithm which uses X,Y,Z,T search but only searches around the downstream portion of the object and only searches the upstream portion if no candidates are found. Due to the

large data/MC differences discovered in TP0DMuonDecayTag this algorithm is not used in the NCE analysis.

5.2 Parametric Track Treatment

A secondary fitter was introduced into the PØD reconstruction algorithm to increase reconstruction efficiency for high angle tracks that only cross a small number of readout planes. This fitter is only used if the Kalman filter fails or the input criteria to be fit by the Kalman filter is not met. For instance, tracks that cross less than six readout planes (minimum number of planes for a Kalman fit), equivalent to three PØDules, are fit with a straight line approximation in each view which is then combined into a 3-D track. The minimum number of readout planes for the line approximation is two readout planes in each view and a minimum of 10 hits.

Figure 5.2 shows the length versus track angle phase space for Parametric and Kalman tracks. Parametric tracks cover the short and/or high angular regions while Kalman tracks cover the longer lower angle regions. The primary difference between the output of the two algorithms is instead of a single node per readout plane, as is done with the primary Kalman filter, parametrically fit tracks have a node per hit which results on average two nodes per readout plane, which is the result of the triangular bars used in the PØD, see Figure 5.3. The PID algorithm, described in Section 5.3, works on the node charges and as a result, will produce incorrect PID values for tracks from the secondary fitter. To correct for the difference in node definitions another algorithm was introduced to combine hits from a single readout plane into a single node. For each parametrically-fit track, the algorithm loops over all the hits and combines hits in each readout plane into a charge-average position with a single charge. By modifing how the information is stored in the parametrically-fit tracks, the PID algorithm is applied in the same fashion for both types of fit tracks. While the output of this algorithm has been designed to be structurally the same as Kalman fit tracks,

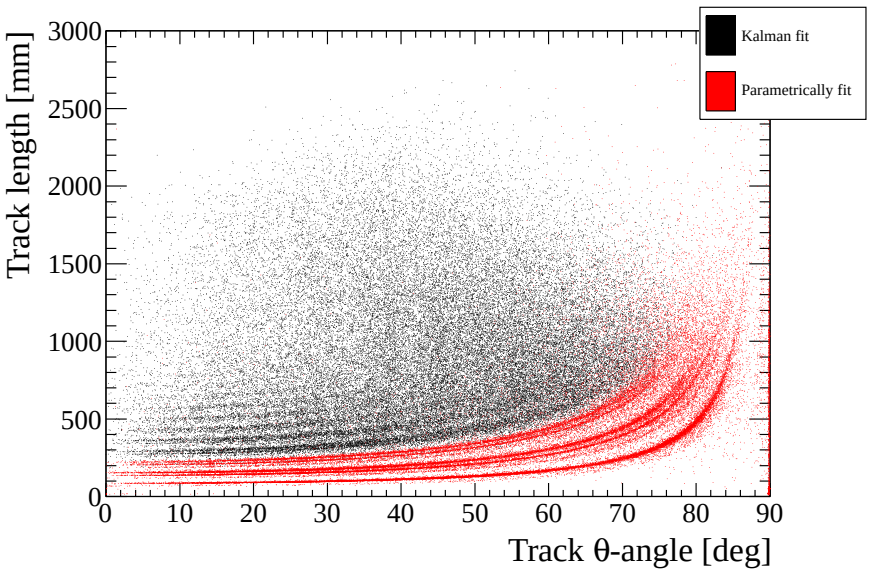

Figure 5.2: Length vs angle phase space coverage by Parametric (red) and Kalman (black) fit tracks.

the nodes are still different due to the fitting method and as a result the analysis treats the tracks from each fitter slightly differently.

5.3 PID Algorithm

The primary purpose of the PID algorithm is to differentiate between muons from CC type interactions and signal protons from NCE type interactions. The algorithm is based on the large charge deposition difference between stopping muon/pions and protons due to the large mass difference of the particles. This is due to the primary energy deposition mechanism coming from ionization in the Bethe-Bloch region of $\sim 0.1 < \beta\gamma <\sim 700$, see Figure 5.4.

The constants used for the PID are derived from stopping particles entering the upstream face of the PØD water-in data. These particles are almost all muons, although there is a small component of protons and other particles entering from interactions in the upstream

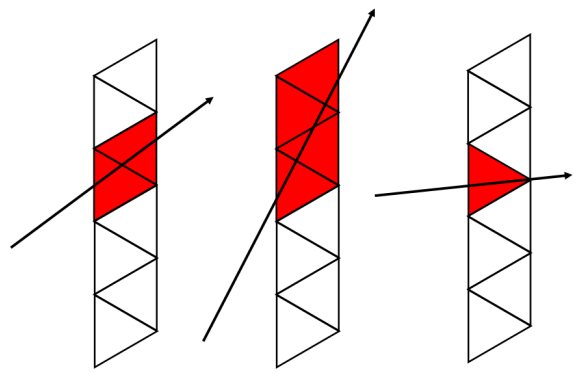

Figure 5.3: Examples of how muon-like particles cross scintillation planes. The most common node is two hits as seen on the left. Higher angle tracks produce higher number of hits per node as seen in the center. Some tracks can produce single hits if the particle passes through the the point of the triangular bar as seen on the right.

magnet yoke and solenoid. Figure 5.5 shows the particle breakdown of tracks entering the front face of the PØD in Monte Carlo. The particle composition is 75% muons, 7% protons, and 18% others, which are almost all electrons. The event selection for the upstream entering muon data set, referred to as sand muons, used to generate the PID constants is:

1. Good PØD/Magnet data quality and beam spill flags
2. Single reconstructed vertex in the PØD during a beam bunch related integration window
3. Single 3-D track with light track PID from the standard PØD reconstruction algorithm
4. Upstream node should have a Z position less than -3250 mm
   (The first upstream PØDule)
5. Track length >= 1 meter
6. Downstream end of the track should be at least 200 mm from the active edges in X,Y and Z to ensure containment

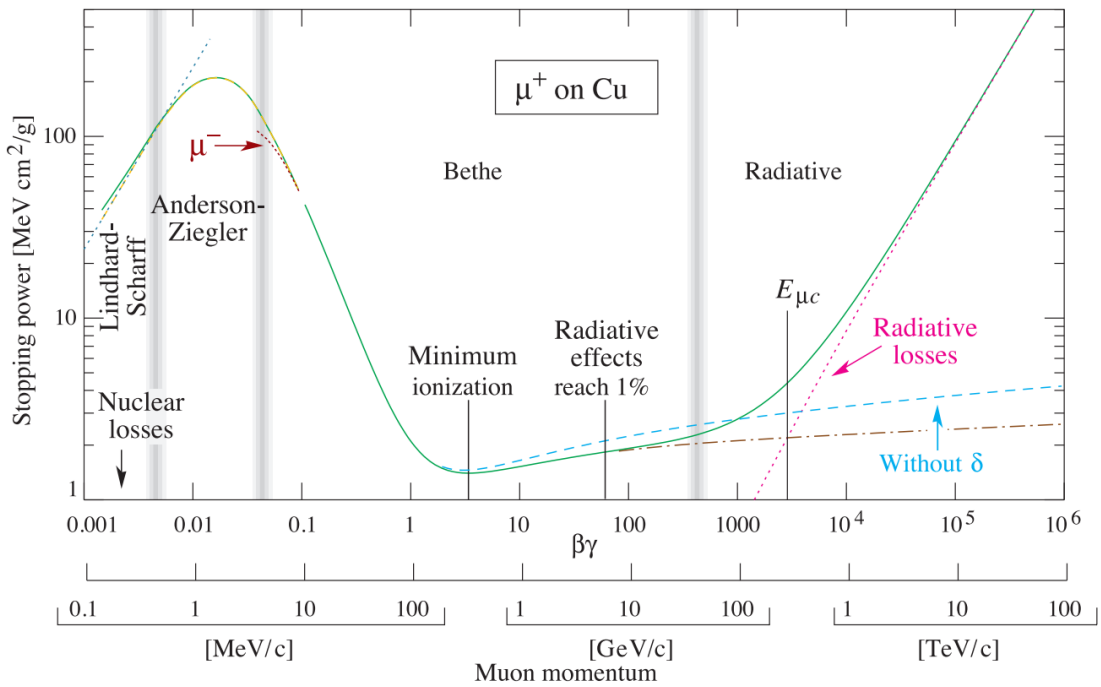

Figure 5.4: Expected energy loss as a function of $\beta\gamma$. As can be seen in the Bethe region when the particle has a lower than the minimum ionizing particle (MIP) momentum the energy loss increases significantly while there is only a modest increase in energy loss as the momentum of the particle increases above the MIP region. [83]

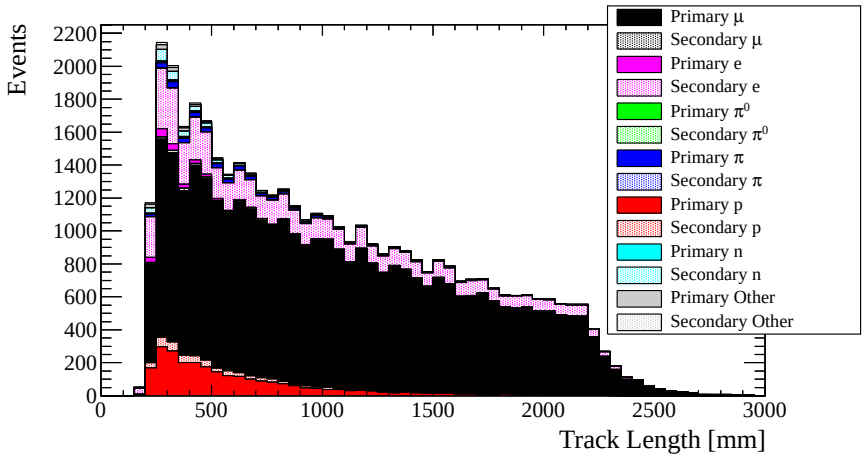

Figure 5.5: MC particle prediction for the sand muon data selection.

The events selected should primarily be muon-like particles reconstructed in the most upstream PØDule and contained at least 20 cm from the edges of the PØD. This containment definition means the tracks can stop in either ECal as well as the water target. The reason this is allowed is because the primary analysis will also allow tracks to stop in either ECal as well as the water target and as a result the PID needs to be sensitive to the differing geometries.

The length requirement was introduced to reduce non-muon particle contamination. This will reduce the exposure of the PID to systematic differences between data and MC relative particle populations.

For each reconstructed track the path length corrected node charges,

$$E_{Dep,corrected} = E_{Dep,node} \times \cos(\theta)_{node} \tag{5.1}$$

are histogrammed as a function of the distance from the end of the track. To avoid distance binning effects, which would result in low statistics in some bins, a distance bin width of 67.1 mm was chosen. This distance corresponds to the minimum distance between PØDules in the water target. While the binning is appropriate for the water target region, it is 25 mm too wide for tracks which stop in the ECal regions. This may reduce the effectiveness of the PID in the ECal region. A more complex PID algorithm which accounts for the differing readout distance at the ECal–WT boundary may be necessary in the future, but as can be seen later the purity of this PID is not an issue as the final sample achieves a high proton purity.

As can be seen in Figures 5.6 (data) and 5.7 (MC), there is a clear stopping particle signature for the sand muon sample. Looking at tracks which start and stop within the PØD fiducial volume, the stopping signitures of the protons and muon-like particles can be seen in data and MC in Figure 5.8. The particles depositing energy in the lower band correspond to muon or pions or other particles of similar mass while the upper band comes

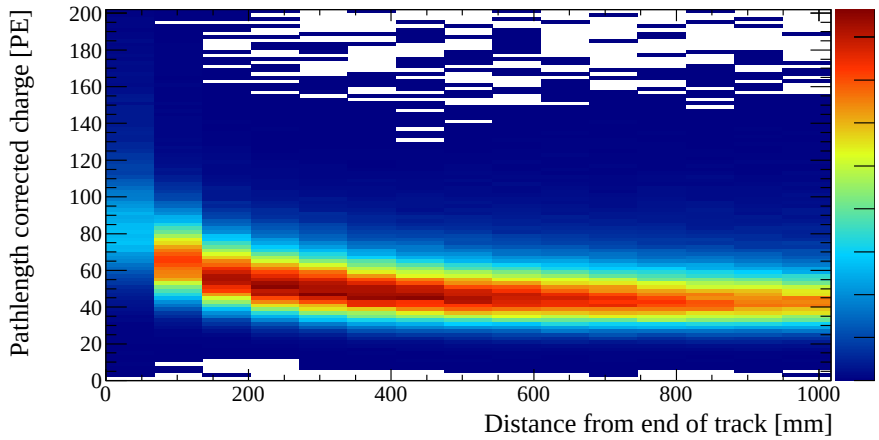

Figure 5.6: Data sand muon charge deposition binned from the end of the track.

from protons. The difference in the charge deposition between the lower band and upper bands allows for the construction of the PID.

To extract the constants used in the PID the first six distance bins are used. These bins were chosen to encompass the portions of the track where protons and muon are most distinguishable. This constrains the usable length of the track for PID purposes to a maximum of 410 mm, although smaller lengths can be used resulting in the PID only using a portion of the six distance bins. The length of the track is calculated by summing up the distances between nodes. Each of these bins is then fit with a Landau $\otimes$ Gaussian function. The implementation of the Landau $\otimes$ Gaussian is based off the LandGau.C example found in CERN's ROOT fit tutorial documentation [84]. The Landau used in this function uses the CERNLIB approximation which has a shifted most probable value(MPV). The MPV is corrected for the final output of the fit.

The full set of fit parameters can be found in Figure 5.9 for the water-in configuration. A summary of the extracted PID parameter values can be seen in Table 5.1 where the central values are the values used by the algorithm.

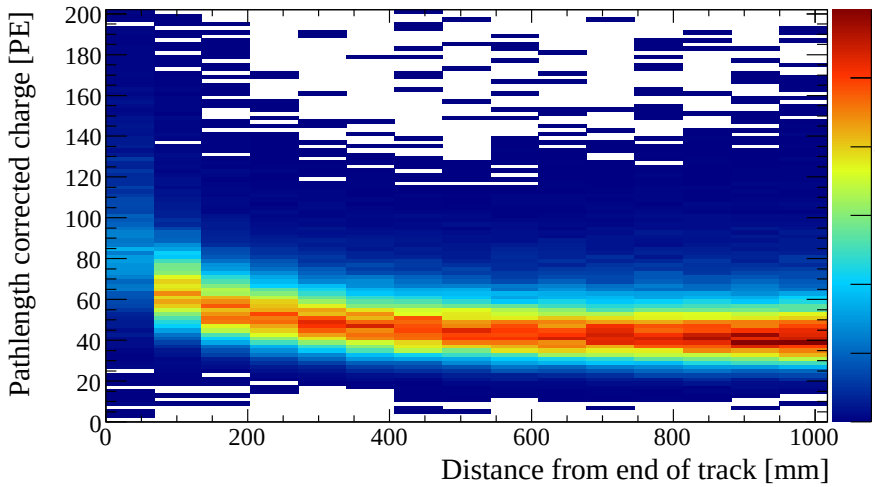

Figure 5.7: MC sand muon charge deposition binned from the end of the track.

Table 5.1: PID MPV and Gaussian sigma parameters by bin number

Bin number	Muon MPV	Gaussian Sigma
1	78.91	15.91
2	64.54	13.60
3	55.58	11.15
4	51.61	10.84
5	49.12	10.45
6	47.27	10.34

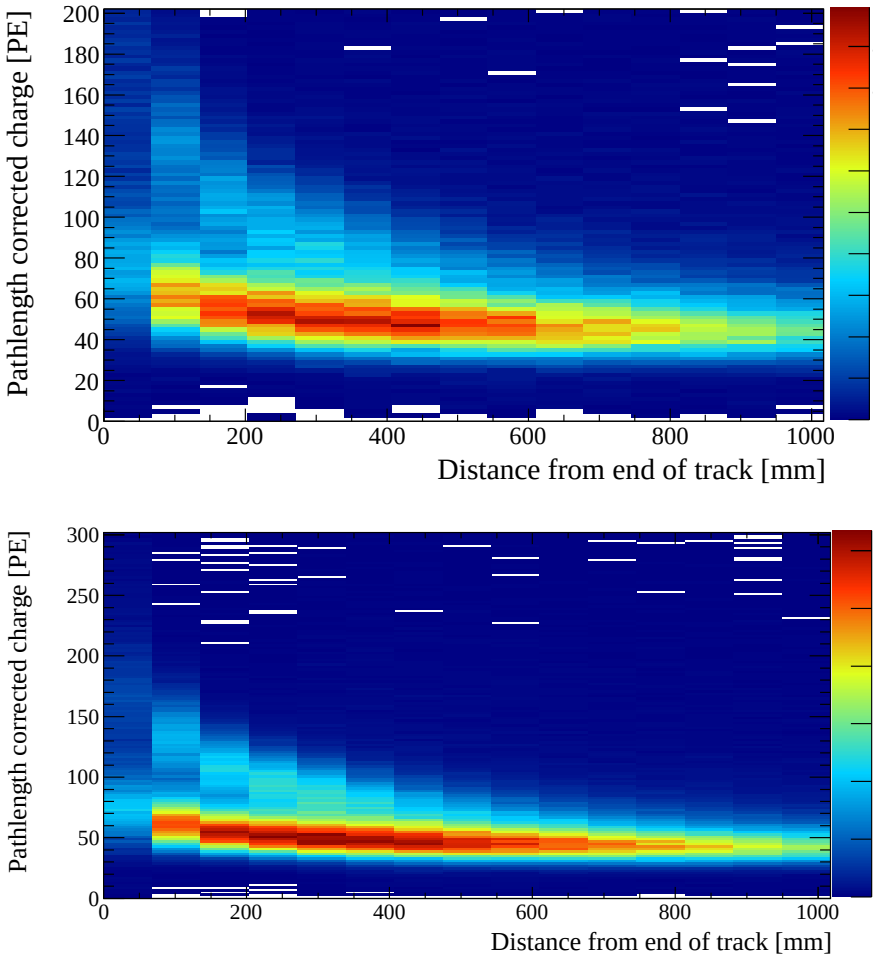

Figure 5.8: Stopping particle charge deposition at the end of the track for data (top) and MC (bottom) for tracks starting and stopping within the fiducial volume.

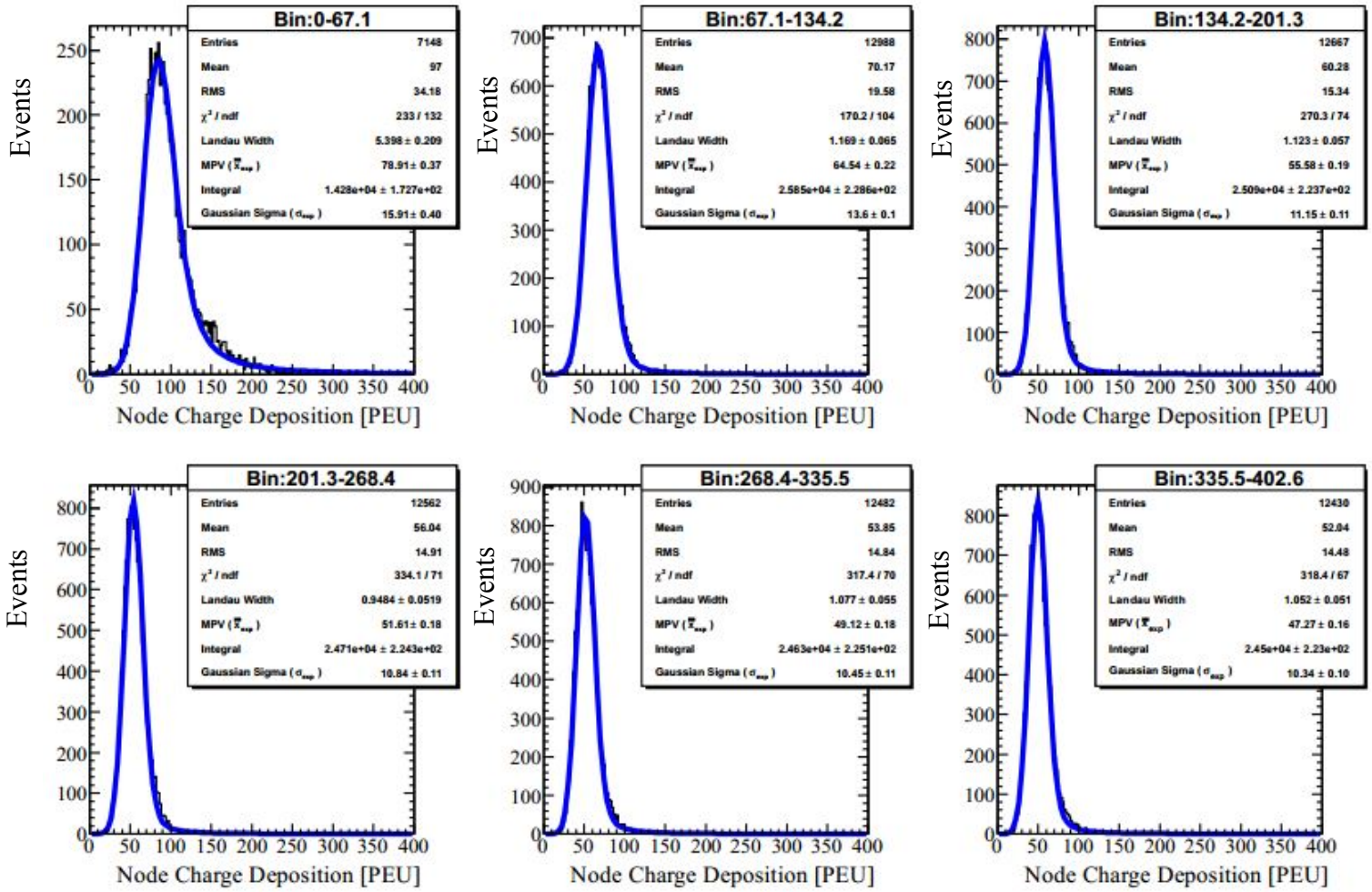

Figure 5.9: PID parameter fits for data sand muons.

Once the PID parameters are extracted the PID can be applied to either the upstream or downstream portion of the track. Using Equation 5.2,

$$Pull_{PID} = \sum_{node=0}^{node=N \text{and} \Delta X <= 410mm} \frac{Q_{measure} - \bar{Q}_{exp,\Delta Xbin}}{\sigma_{exp,\Delta Xbin}} \tag{5.2}$$

a pull is calculated for the track's region of interest where the length used can be up to 410 mm. In general the pull should be centered at zero for stopping muons. Particles with heavier energy deposition will end up on the positive side of the pull while MIPs will end up on the negative side of the distribution. The variables in the equation are: distance from the end of the track (ΔX), the path length corrected charge ($Q_{measure}$), and the expectation values given the distance from the end of the track ($\bar{Q}_{exp,\Delta Xbin}$, and $\sigma_{exp,\Delta Xbin}$). The constants extracted from fits to sand muon data are applied to both MC and data events in the same fashion.

5.4 Momentum Reconstruction Algorithm

Another algorithm introduced by this analysis reconstructs the momentum of the track under the assumption it was created by a proton. Information about both the track direction and materials traversed is used to reconstruct the momentum. Protons in the reconstructable momentum regions predominately deposit energy via ionization radiation according to the Bethe-Bloch equation, Equation 5.3.

$$-\frac{dE}{dx} = Kz^2 \frac{Z}{A} \frac{1}{\beta^2} \left[\frac{1}{2} \ln \frac{2m_e c^2 \beta^2 \gamma^2 T_{max}}{I^2} - \beta^2 - \frac{\delta(\beta\gamma)}{2} \right] \text{with } T_{max} = \frac{2m_e c^2 \beta^2 \gamma^2}{1 + 2\gamma \frac{m_e}{M} + (\frac{m_e}{M})^2} \tag{5.3}$$

As the particle reaches lower momenta other processes start to dominate. To correctly account for multiple energy deposition processes the analysis uses energy deposition values from NIST's PSTAR database [85].

Table 5.2: Areal density of various materials in the PØD

P0D Region	Material	Areal Density [$\frac{g}{cm^2}$]	Uncertainty [$\frac{g}{cm^2}$]
PØDules Skin	Polystyrene	0.144	0.024
Brass radiator	Copper	1.088	0.032
Glue	Epoxy	0.034	0.0072
Water Target Boundary	HDPE	0.597	0.048
Water Bags	HDPE	0.00323	0.00003
ECal Steel	Iron	0.36	0.042
ECal Pb Radiator	Lead	3.924	0.058
Water Target	Water	2.733	0.023
Scintillator	Polystyrene	1.72	0.003

To reconstruct the momentum the algorithm takes small steps in areal density, 0.05 $\frac{g}{cm^2}$ per step, from the downstream end of the track to the upstream end. The total amount of areal density traversed for a given material is corrected by the $\cos(\theta)$ of the track. This effectively means the higher the angle of the track, the more material the track will traverse. Materials traversed are kept in the order found in the detector to account for different energy deposition curves which occur in the materials. To get the areal densities and their uncertainties values from [86] were used. The calculated areal densities for various materials in the PØD can be found in Table 5.2.

Currently the algorithm uses copper curves to estimate the energy loss in brass. Typical brass is composed of an alloy of copper and zinc with possible additions of ∼1–5% other metals. Copper and zinc are adjacent elements in the periodic table with similar mean excitation energy, from [87], 322 eV and 330 eV. Because of these similarities the assumption of copper only brass should have a small effect. Regardless, this issue will be investigated in the future when the differential cross section with respect to Q^2 or T_p is evaluated. At the same time a feasibility study using FGD produced backwards-going protons will be done.

If it is determined there are enough backward going protons a cross check using TPC1's momentum measurement can be performed to check the momentum reconstruction in the PØD. Performance of the current algorithm using just copper constants can be seen in later figures after the event selection is explained, Figures 6.16 and 6.17 for Kalman and Parametric tracks respectively.

5.5 Neutron Clustering Algorithm

In order to better understand the external background a data driven method was needed. The method described in Section 7.2.3 required the creation of a new reconstruction algorithm which is not in the standard ND280 software. The algorithm is a standard density clustering method which uses all hits before the standard reconstruction objects are made. The clustering algorithm looks for spatially correlated hits which are <70 mm apart. The algorithm uses an iterative brute force approach to search all possible adjacent hits, which means the algorithm can produce clusters of varying shapes and sizes. In order for a cluster to be formed at least 2 hits must be found. The final clusters created by this algorithm are only 2-dimensional. An attempt at the creation of 3-dimensional clusters was introduced, but these clusters would need more understanding as this would introduce a "purity" of good matches versus bad matches which would complicate the analysis.

5.6 Charge Threshold Correction

A large discrepancy between the low charge threshold in the MC and data was discovered by the π^0 group. This issue was thought to manifest itself in a large difference in shower reconstruction efficiency for low energy showers, although this hasn't been verified to be the sole cause. This issue can manifest itself in two samples in the NCE analysis: the Michel tagging efficiency and the neutron clustering algorithm, see Section 7.2.3, used to derive a data constraint on external backgrounds.

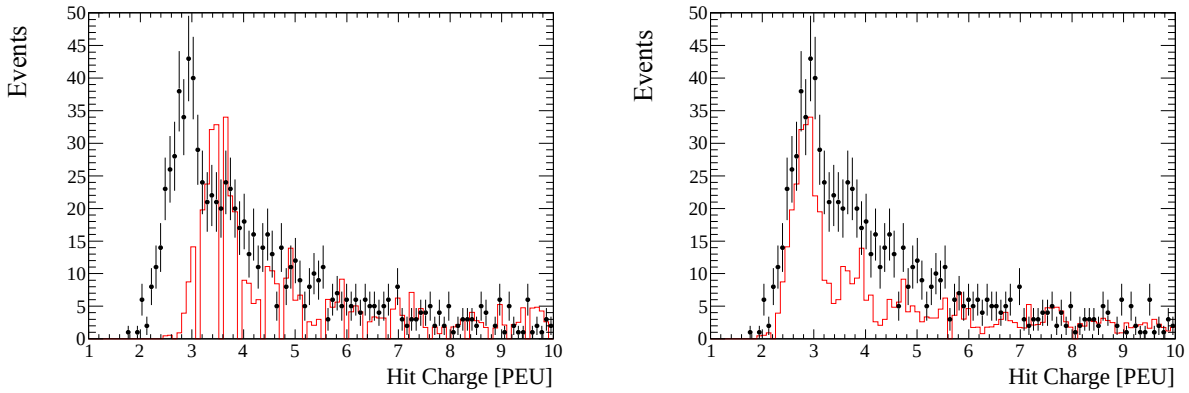

Figure 5.10: Uncorrected hit charges (left) and corrected hit charges (right). Data hit charges are in black and MC hit charges in red.

To fix the issue the cause was first identified by the calibration group. The TripT electronics have a TDC discriminator circuit which gives timestamps for hits above a predefined ADC threshold. The PØD is tuned to run with a gain of 11 ADC counts per PE and TDC discriminator level appropriate for a 2.5 PE threshold or 27.5 ADC counts above pedestal. Only hits with a valid TDC are used in the reconstruction. The discriminator level in the MC was observed to be 3 PE, or 20% higher than the data. The root cause was determined to come from a difference in how the MC hits were modeled in the electronics simulation and subsequently in the hit calibration. The gain of the PØD was set to 10.5 ADC counts per PE in the electronics simulation while the gain was not matched in the calibration. The gain was applied as 9.9 ADC counts in the TMPPCGainDummyMethod class while the linearity correction was set to 10.76 ADC counts/V in the TMPPCLinCalibMethod class. According to the calibration group this results in a 20% change in the MC charge scale. This effectively means for low charge hits the MC hit charge is 20% higher than an equivalent hit in data. As a result, lower hit charges could pass the threshold in MC. Figure 5.10 shows the before and after MC hit charge correction for the low hit charges found in a set of neutron clusters (see Section 7.2.3). To correct for this issue the most valid method is to rerun the entire MC with these input variables corrected, but unfortunately this was not feasible for the timescale of

this analysis. A second method was devised to correct for the differing threshold. By scaling the MC hit charges down by 20% and reapplying a threshold, the MC/data difference can be corrected.

The Michel tagging algorithms both use an area search algorithm that looks for a certain number of hits above a specific charge threshold. These hits are at least 100 ns later than the reconstructed object. The method used to correct for charge threshold effects rescales the hit charges in the Michel clusters and counts the number of hits that should have been rejected by the charge threshold and see if the number of hits left over is above the number of hits required to be a valid Michel cluster. TagMuonDecay requires at least two hits in a cylinder surrounding the reconstruction object which have a hit charge of at least 4.5 PE. MuonDecayTag requires only a single hit in a sphere near the end or beginning of the reconstruction object, but the hit charge must be greater than 8 PE.

Upon investigating the effect of the charge threshold correction on the Michel tagging algorithms it was determined MuonDecayTag was susceptible to systematics which were not evaluated, specifically noisy channels in data which are not rejected or simulated as well as outside backgrounds. Based on the large data/MC difference this algorithm has been dropped from the analysis chain and only the more robust TagMuonDecay algorithm is used.

The neutron clustering algorithm introduced cannot be corrected in the same manner as the Michel tagging algorithms for two reasons. The first issue stems from the fact the neutron cluster construction isn't just an area search requiring a specific number of hits within a specific volume. The neutron clustering algorithm instead takes a seed hit and searches for neighboring hits 70 mm from the seed hit. If a hit is found, that hit is added to the pool and additional hits are searched for near the new hits until no new hits are found. As a result, if a hit that should have been removed by the electronics threshold, was in the middle of a pattern which caused the cluster to be formed a simple counting of the hits above a new threshold wouldn't account for all systematic differences. The second issue stems from how PØD reconstruction initiates the reconstruction and cleans dark noise

hits. PØD reconstruction applies a cleaning algorithm to the input hit list. This cleaning algorithm saves all hits above 15 PEU, hits with charge >7 PEU and a neighbor within 10 cm and 30 ns, and hits which are neighbors within 3.5 cm and 30 ns. If at least 5 hits pass this algorithm in a given integration window the reconstruction is initiated. The problem with the cleaning algorithm and minimum number of hits requirements is these are coupled to the charge threshold simulation issue. In addition, the neutron clustering algorithm requires only two hits for a 2-D cluster. To avoid unintended threshold simulation issues the algorithm takes all input hits as candidates and any threshold are applied in the cluster analysis. The charge threshold was also modified to ensure stability of the result. More information on this study can be found in Section 7.2.3.

Chapter 6

Event Selection

The event sample is selected using a set of seven cuts designed to identify proton tracks from a large background of muons. The decision was made to use an intermediate reconstruction object in PØD reconstruction. Unlike the rest of the PØD analyses so far, see [88] and [89], this analysis does not use the standard final reconstruction algorithm objects. The NCE analysis instead uses the tracking stage of the reconstruction, taking the "TP0DTrackRecon" algorithm as the "final" result. This algorithm result is just prior to the PØD reconstruction PID. A description of the reconstruction can be found in Section 5.1.

The standard PØD reconstruction PID (not to be confused with the NCE analysis PID) doesn't attempt to treat Parametric tracks. As a result, tracks fit by the parametric fitter are just passed onto the shower reconstruction. If the results of the standard reconstruction PID is used 50% (1325 out of 2338 reconstructed NCE events) of the NCE sample gets assigned a shower-like PID and are reconstructed as a shower. To avoid a reduction in efficiency the NCE analysis doesn't used the standard PID algorithm.

Figure 6.1 breaks down all single track events before the standard PØD reconstruction PID is applied, by fitter type (parametric or Kalman) and by FSI interaction category. Using the intermediate reconstruction objects, which are all tracks, an event selection can use the full reconstructed NCE event sample.

Shown below is the cut flow used for the event selection:

1. Data quality and beam quality checks
    - Magnet + PØD data quality and beam flags are good
2. Single 3-D track reconstructed with "TP0DTrackRecon" algorithm in the beam window
3. Most upstream reconstructed node is within the fiducial volume

- This is the standard fiducial volume definition for PØD analyses
- -836 mm<=X<=764 mm, -871 mm<=Y<=869 mm,
  -2969 mm<=Z<=-1264 mm

4. Downstream reconstructed node is at least 10 mm from the active edge of the PØD

5. Stopping muon hypothesis pull applied to the end of the track

   - $Pull_\mu > 12.5$ for Kalman fit tracks
   - $Pull_\mu > 3$ for parametrically fit tracks

6. Stopping muon hypothesis pull applied to the beginning of the track

   - $Pull_\mu > 4.25$ for Kalman fit tracks
   - $Pull_\mu > 0.75$ for parametrically fit tracks

7. No Michel cluster associated with the track using the TagMuonDecay algorithm

The performance of these cuts is summarized by the selection efficiency and purity by cut in Figure 6.2, with the cut by cut event yields in Table 6.1. Because the Kalman and Parametric tracks are mutually exclusive event samples the sum of the two event selections is used. The final sample has a purity, see Equation 6.1, of 45.96% and a selection efficiency, see Equation 6.2, of 13.74%.

$$\text{Purity} = \frac{\text{Total number of selected NCE events}}{\text{Total number of selected events}} \tag{6.1}$$

$$\text{Efficiency} = \frac{\text{Total number of selected NCE events}}{\text{Total number of NCE events in the fiducial volume}} \tag{6.2}$$

The low efficiency is after all reconstruction and detector thresholds. Effectively this efficiency is the result of the fact the vast majority of the protons produced in NCE interactions are below the detector threshold, see Figure 6.3 where the highest energy proton is plotted

Table 6.1: Event selection event yields by cut progression. The first line, pre-selection, corresponds to events reconstructed as a single 3-D track with good beam and data quality flags.

Cut	**Data Events**	**MC Events**	**Comments**
Pre-Selection	385851	441715	
Fiducial Volume	32273	348349	
Containment	19470	20454.5	
PID on end of track	6153	6680.83	
PID on beg. of track	4605	4370.21	Outside bkg scaling factor applied
Michel	3936	3730.63	Outside bkg scaling factor applied

for the total NCE selection and the selected proton is shown in red. Events resulting from neutron conversions can result in events selected with a low energy primary proton.

If one looks at how well the selection does after these thresholds, the selection has a ∼75% selection efficiency. To understand how the event selection breaks down by various definitions including FSI, true generator interaction, and target nuclei, a set of tables has been provided using flux corrected and p.o.t. corrected MC event rates. The first table, Table 6.2, investigates the FSI defined events based on the fiducial volume boundary. This allows for an understanding of the observable interaction types inside and outside the fiducial volume. The second table, Table 6.3, investigates the FSI defined events based only on their observable topology. By breaking the events down by observable topologies a sense of the relative sizes of the topologies can be determined. The third table, Table 6.4, provides the events as classified by the true interaction channel before FSI effects occur. This table helps with understanding if all the physics systematics evaluated later are actually done properly. All these tables also provide a breakdown of the three dominant nuclear targets; carbon, oxygen, and copper.

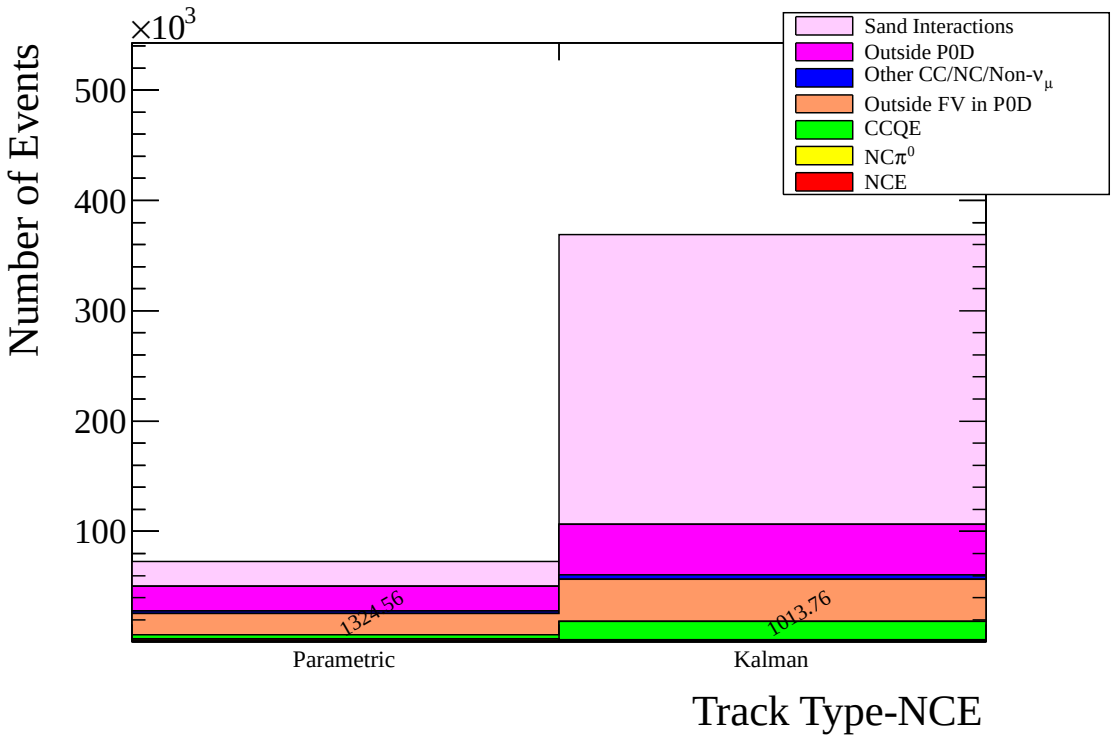

Figure 6.1: Track type broken down by FSI interaction type and fitter used. Over 1324.56 events in the NCE sample ends up being fit with the parametric fitter. Only 1013.76 events are reconstructed with the Kalman fitter. This distribution contains all single reconstructed tracks.

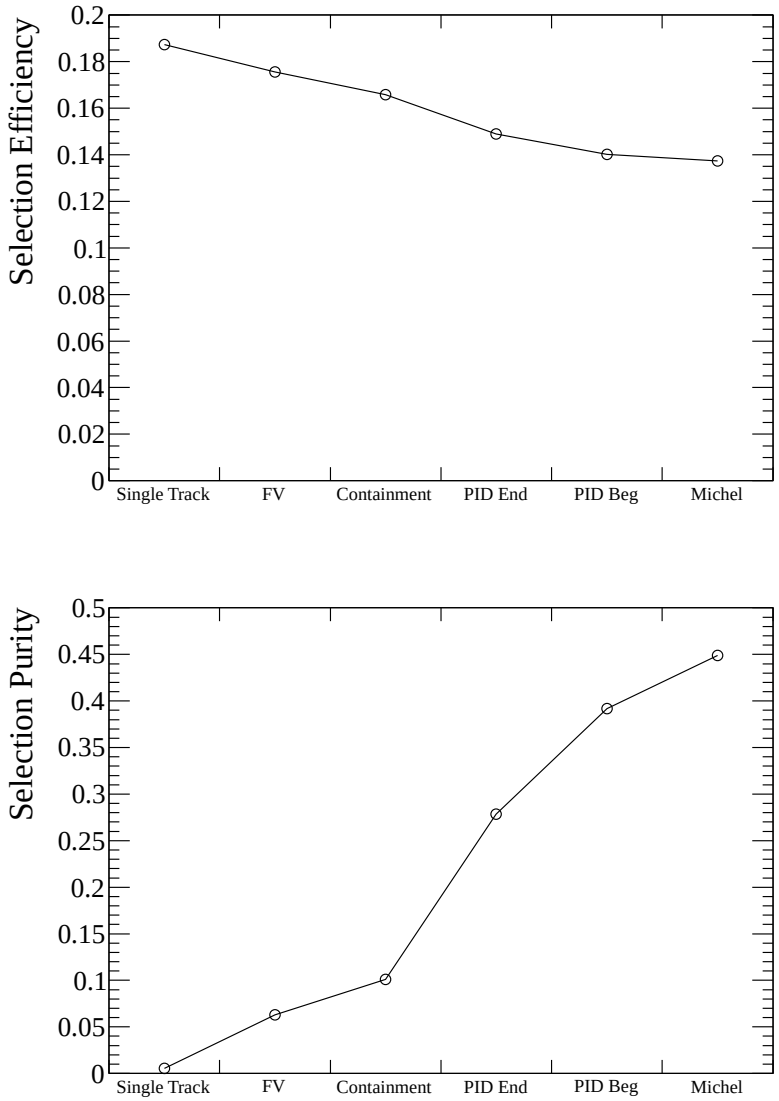

Figure 6.2: Selection efficiency (top) and purity (bottom) by selection cut.

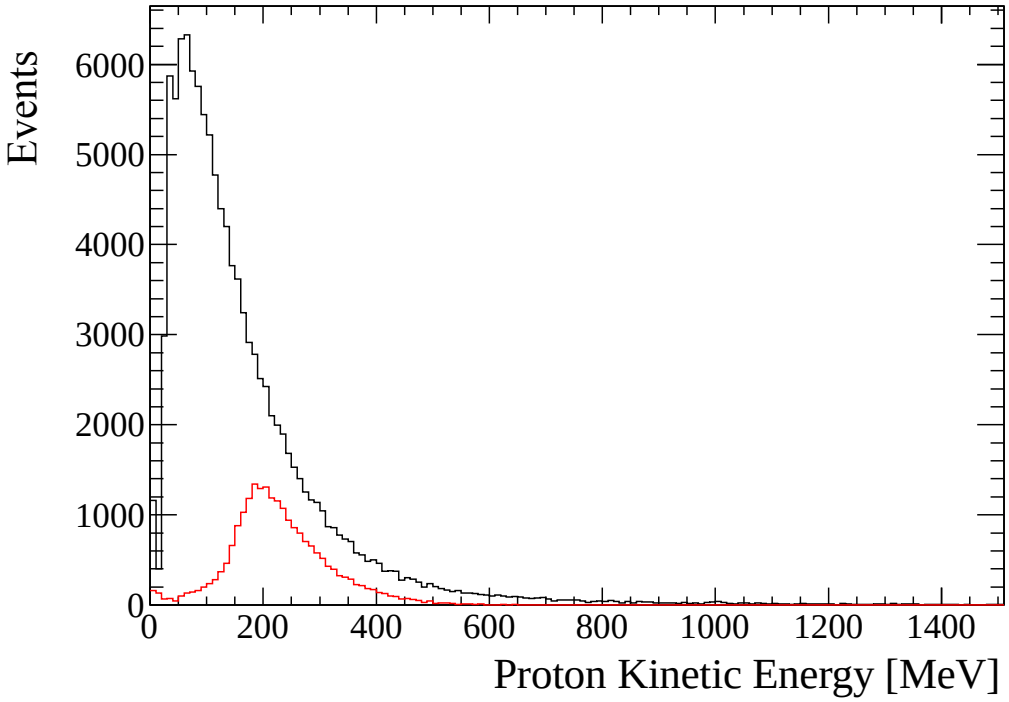

Figure 6.3: NCE events broken down by the highest energy proton. Some events are actually the result of a higher energy neutron converting to a proton, where the primary proton energy is low or 0 (not found). There is a clear kinetic energy threshold in the PØD of ∼125 MeV.

Table 6.2: Event selection after all cuts broken down by FSI topologies and categorized with the fiducial volume taken into account for all targets as well as the top three nuclear targets. There are a total 3730.63 events selected in the p.o.t. normalized MC. The outside PØD category has been scaled by the external scaling factor found in Section 7.2.3.

FSI Category	**All Targets**	**Carbon**	**Oxygen**	**Copper**
NCE	1714.69	729.87	521.16	214.82
CCQE	578.07	273.49	196.68	92.70
NCπ^0	157.12	70.87	33.79	12.46
Other	425.82	196.68	130.76	51.42
Outside FV in PØD	346.09	130.182	37.83	22.39
Outside PØD	508.84	4.44	175.79	0
Total	3730.63	1405.53	1096.01	393.79

.

6.1 Event selection cuts

6.1.1 Data and Beam Quality

To ensure the data analyzed is of the proper quality the beam and data quality groups provide a set of flags and numbers for analyzers to determine good data. For this analysis the beam data quality requires an event with proper spill p.o.t. value from the final current transformer (CT) readout in the secondary beamline and good beam spill flag, meaning the beam DAQ was live and readout the spill. The p.o.t. is summed up over all events run over to determine the total POT used in the final analysis. Since this is a PØD only analysis, all events analyzed have a good PØD data quality flag as well as a good magnet flag (the magnetic field is well defined at 0.2 T) to ensure the detector was performing within tolerances and the magnetic field was well defined. There is a global ND280 data quality flag, but this flag is sensitive to other detector problems which do not affect the quality of events analyzed by this analysis.

Table 6.3: Event selection after all cuts broken down by FSI topologies and categorized without the fiducial volume taken into account for all targets as well as the top three nuclear targets. This means interactions are only categorized by their FSI category, removing an outside the fiducial volume category. The difference seen between the outside PØD events in Table 6.2 and this outside category is a small fraction of outside events are categorized as anti-ν, this is $\sim$10 events in the all category. There are a total 3730.63 events selected in the p.o.t. normalized MC. The outside PØD category has been scaled by the external scaling factor found in Section 7.2.3.

FSI Category	**All Targets**	**Carbon**	**Oxygen**	**Copper**
NCE	1885.31	791.15	537.97	226.51
CCQE	671.11	314.20	210.96	100.45
CC Other	145.04	61.61	36.31	12.11
NC Other	355.44	165.62	94.10	38.85
Outside PØD	499.06	4.44	169.80	0
Anti-ν	93.19	28.25	22.32	7.16
ν_e	81.49	40.26	24.55	8.72
Total	3730.63	1405.53	1096.01	393.79

Table 6.4: Event selection after all cuts broken down by interaction channel. Only channels which yield 50 or more events are shown. The first section shows the 3 dominant channels, NCE on neutron and proton and CCQE. The next section contains the dominant NC channels. The final section contains the dominant CC channel. These events account for 3532.67 events out of a total 3730.63. The external background events are shown because the analysis will constrain external events with data meaning the physics systematics will only be applied to background events which are not external. All event rates are p.o.t. normalized. The external background category has been scaled by the external scaling factor found in Section 7.2.3.

Interaction	**NEUT Code**	**Total**	**Signal**	**Total Bkg**	**External Bkg**
$\nu_x + n \rightarrow \nu_x + n$	52	506.11	333.99	172.13	55.09
$\nu_x + p^+ \rightarrow \nu_x + p^+$	51	955.48	909.93	45.55	5.89
$\nu_x + n \rightarrow x^- + p^+$	1	514.79	0	514.79	34.98
$\nu_x + p^+ \rightarrow \nu_x + p^+ + \pi^0$	32	281.17	167.08	114.09	9.22
$\nu_x + n \rightarrow \nu_x + n + \pi^0$	31	196.21	102.96	93.26	24.11
$\nu_x + n \rightarrow \nu_x + p^+ + \pi^-$	33	167.50	73.81	93.69	10.30
$\nu_x + p^+ \rightarrow \nu_x + n + \pi^+$	34	150.66	89.38	61.28	16.35
$\nu_x + N \rightarrow \nu_x + N + N\pi$	41	79.72	10.11	69.61	19.05
$\nu_x + p^+ \rightarrow x^- + p^+ + \pi^+$	11	299.58	18.43	281.15	22.26
$\nu_x + N \rightarrow x^- + N + mesons$	26	121.02	0	121.02	118.79
$\nu_x + n \rightarrow x^- + n + \pi^+$	13	104.33	3.36	100.97	54.80
$\nu_x + N \rightarrow x^- + N + N\pi$	21	74.16	0	74.16	60.07
$\nu_x + n \rightarrow x^- + p^+ + \pi^0$	12	82.55	3.81	78.74	19.52

6.1.2 Single 3-D Track

A single 3-D track from the "TPØDTrackRecon" algorithm is required for this analysis. The hypothesis is that the single track corresponds to a reconstructed proton. Unlike most PØD analyses, this analysis uses an intermediate reconstruction algorithm output due to efficiency losses from the track PID introduced used in PØD reconstruction.

6.1.3 Fiducial Volume

Future advancements in this analysis will look at interactions on water which constrains the allowed interaction region to regions of the PØD with water. As a result the choice in X, Y, and Z directions is partially dictated by where water is guaranteed to be. A standard PØD water target fiducial volume was determined by the PØD group. The upstream Z cut removes the X readout layer from the upstream PØDule in the water target while the downstream Z cut removes the Y readout layer from the most downstream PØDule in the water target. The XY cut was determined to allow the largest fiducial volume, but still guarantee the water level is above the top fiducial volume (+Y). The reconstructed vertex distribution and cut values can be seen in Figure 6.4. The Z binning in Figure 6.4 corresponds to 40 PØDules in position. After the fiducial volume cut, the dominant background is CCQE with small portions coming from other NC and CC processes as well as outside backgrounds as seen in the true neutrino energy spectrum in Figure 6.5.

6.1.4 Containment

A 'soft' containment requirement is implemented to remove edge effects from tracks with downstream ends near the edge of the active region of the PØD. This soft containment cut removes all tracks which deposit charge on the outer most readout channel in either X,Y or Z, defined as 10 mm from the active edge defined in the geometry. Distributions of the X,Y and Z cut positions can be seen in Figure 6.6.

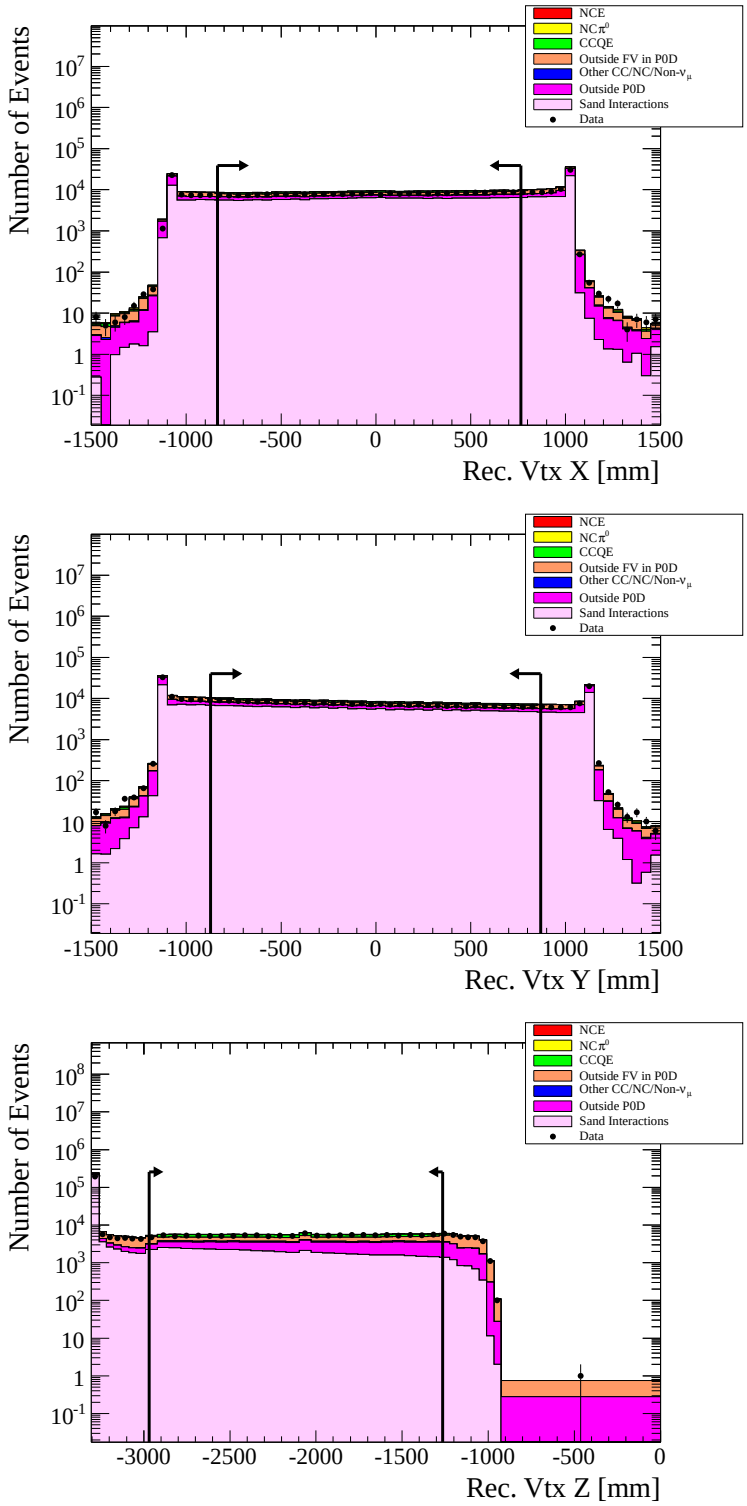

Figure 6.4: Starting position for all single track events broken down by interaction type before the FV cut.

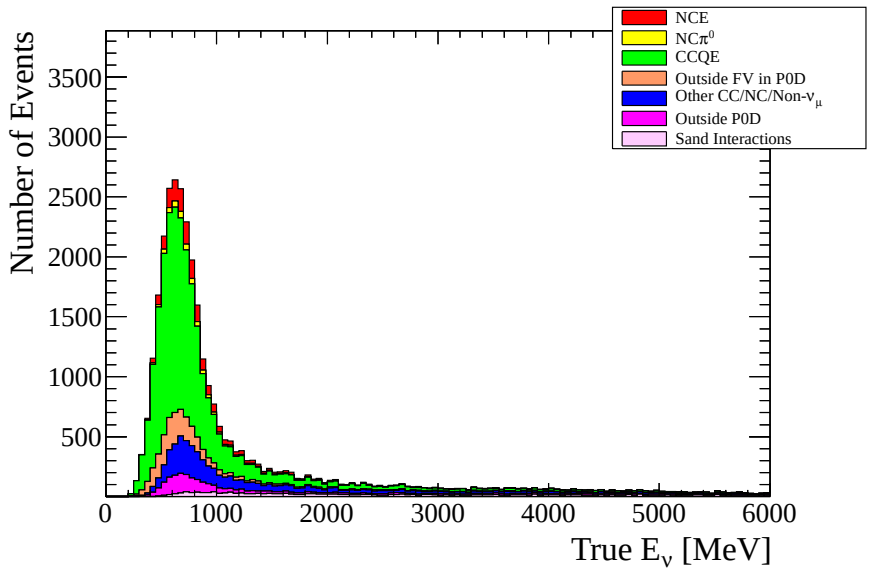

Figure 6.5: True neutrino energy spectrum by interaction type for single tracks after the fiducial volume cut.

This cut removes the most obvious exiting tracks, but some tracks can escape out of the PØD through inactive regions such as the water bags. The primary method to ensure a contained track selection comes from the PID cut (see next cut) on the end of the track. Since the PID uses a stopping muon hypothesis, exiting tracks tend to end up with a negative pull due to the MIP-like charge deposition.

6.1.5 PID on the Track End

The single most dominant background to this analysis is CCQE reconstructed as a single track. The CCQE background enters the single track sample as either a forward going muon with no visible (to the PØD) proton, a back-to-back muon/proton, or a high angle muon which exits the PØD through inactive regions. In order to remove the CCQE backgrounds with a reconstructed muon present, an efficient and pure PID algorithm has been developed. Using the downstream portion of the track the node charge is compared with the expected stopping muon charge deposition and a pull value is computed, see Section 5.3. Due to the

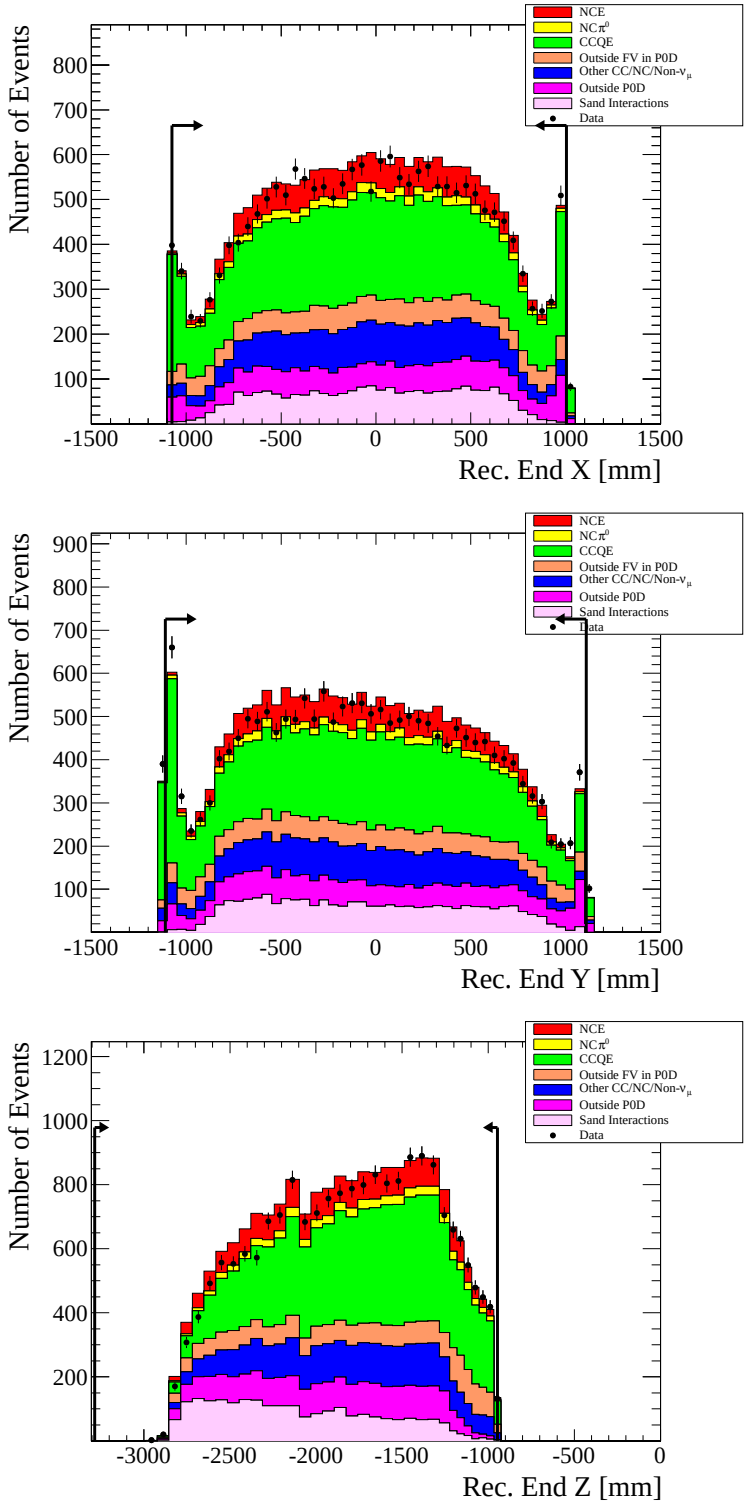

Figure 6.6: Soft containment position cuts by interaction type. The data/beam quality, single track, and fiducial volume cuts have been applied.

differing treatment of Kalman and Parametric tracks a different cut value is required. The PID for both Kalman and Parametric tracks can use up to the last 410 mm of the track, but is limited to 50% of the track length to minimize confusion on back-to-back tracks. The PID distributions for both track types can be seen in Figure 6.7. After this cut is applied the track kinetic energy can be estimated since almost all the tracks are contained. The track kinetic energy estimation and angle are histogrammed in Figure 6.8.

See Section 6.1.9 for specifics on how the PID cut positions were determined.

6.1.6 PID on Track Front

The CCQE background that is left over after applying the PID to the end of the track has a component where instead of the muon propagating downstream it is scattered upstream and a proton is ejected downstream. This cut uses the same PID algorithm as the previous cut but applied to the start of the track. The pull distributions for both Kalman and Parametric tracks are seen in Figure 6.9. The track's kinematic variables after this cut can be seen in figure 6.10.

6.1.7 Michel Electron

While almost all of the CCQE background has been removed (97.5%) some muons were not reconstructed due to high angles or low momentum. To try and remove these events a Michel tag was employed. The PØD reconstruction package employs two different Michel tagging algorithms based on position time clustering. The overall efficiency of the Michel taggers is 53.6(49.3)% for data(MC) with the cleanest muon samples, see Section 7.1.0.4. Individally the taggers have an efficiency of 43.4(42.1)% for the TagMuonDecay algorithm and (47.7)(44.3)% for the MuonDecayTag algorithm for data(MC).

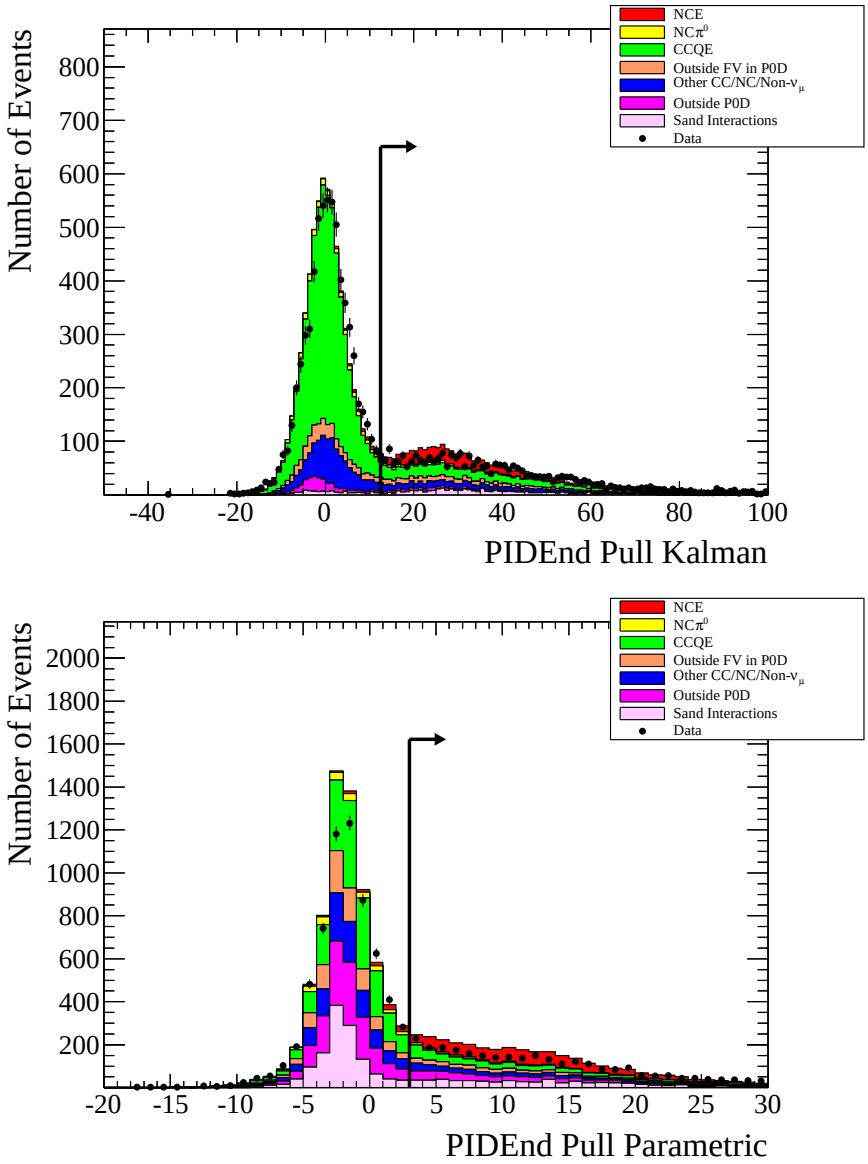

Figure 6.7: PID pull distributions for the end of the track by interaction type, Kalman (top) and Parametric (bottom). All cuts up to the PID end cut have been applied.

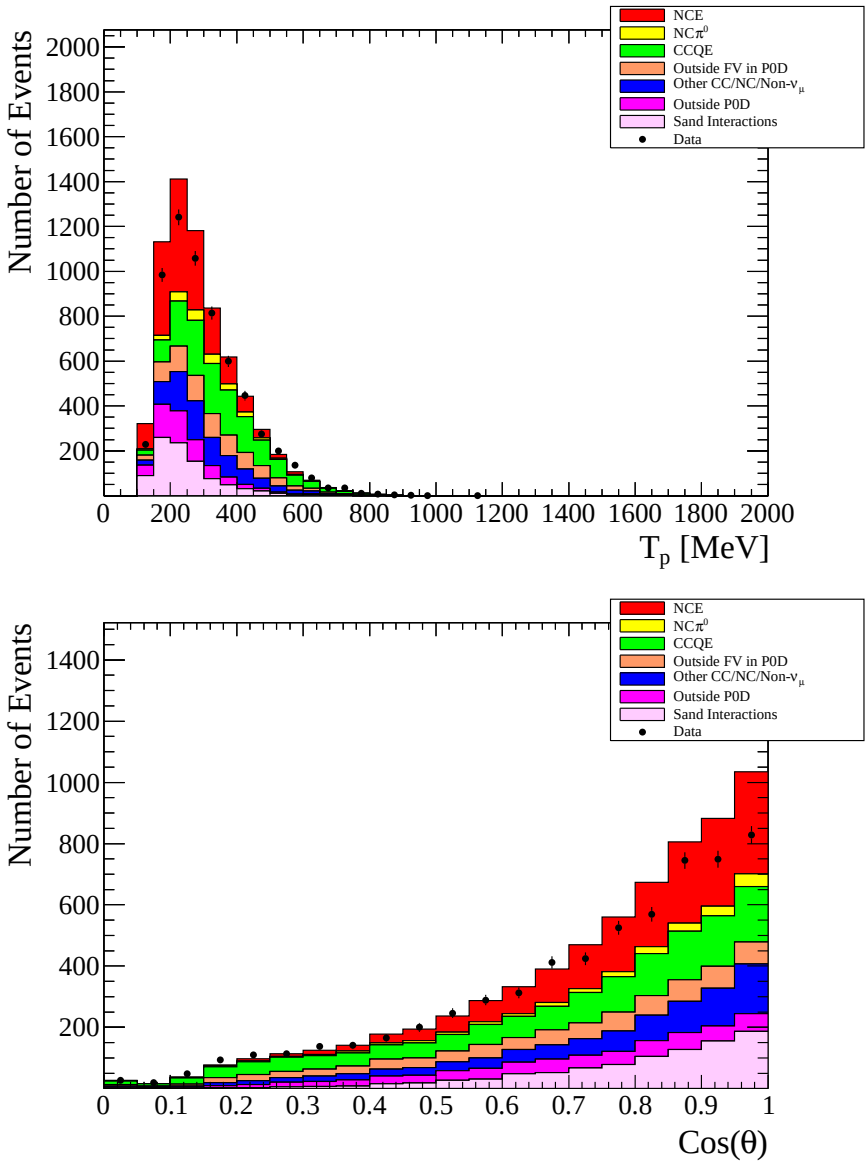

Figure 6.8: Track kinetic energy (top) and angle (bottom) by interaction type. All cuts including the PID end cut have been applied.

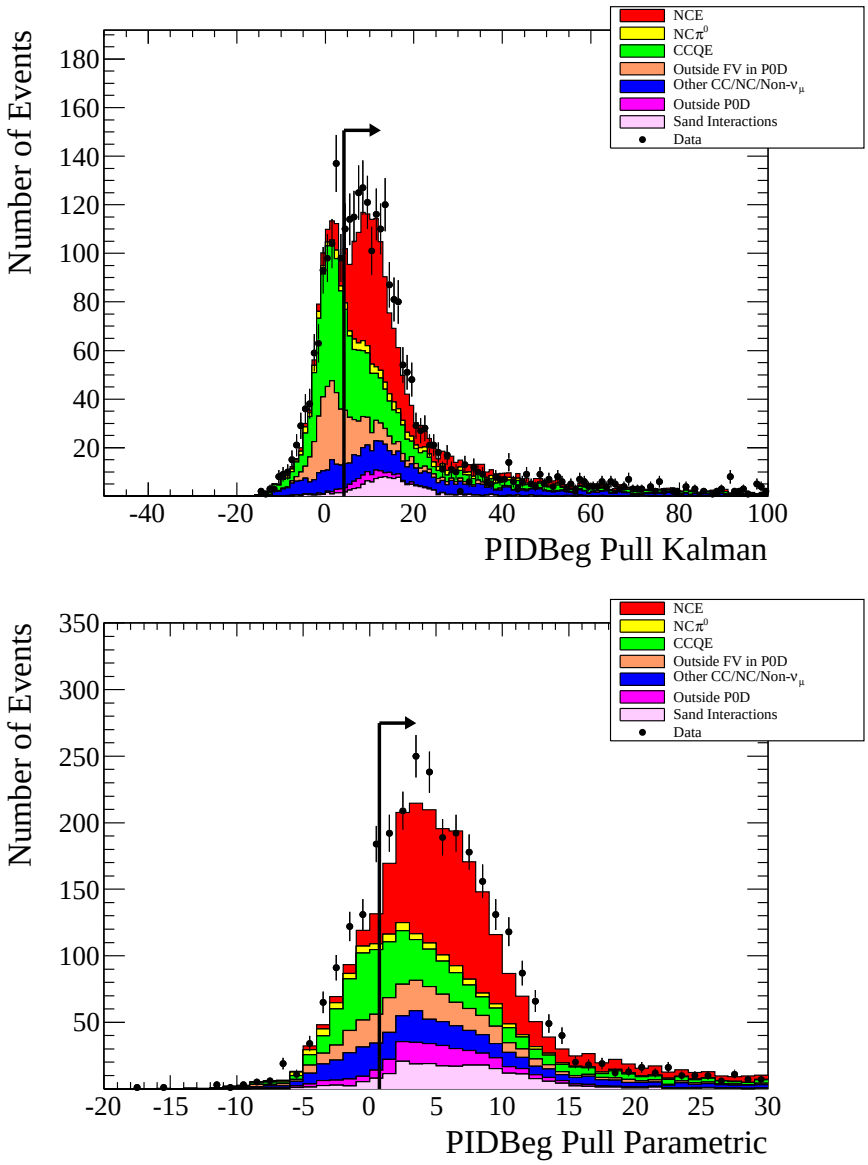

Figure 6.9: PID pull distributions for the beginning of the track by interaction type, Kalman (top) and Parametric (bottom). All cuts up to the PID on the track front have been applied. The outside scaling factor (See Section 7.2.3) has been applied to the outside and sand backgrounds.

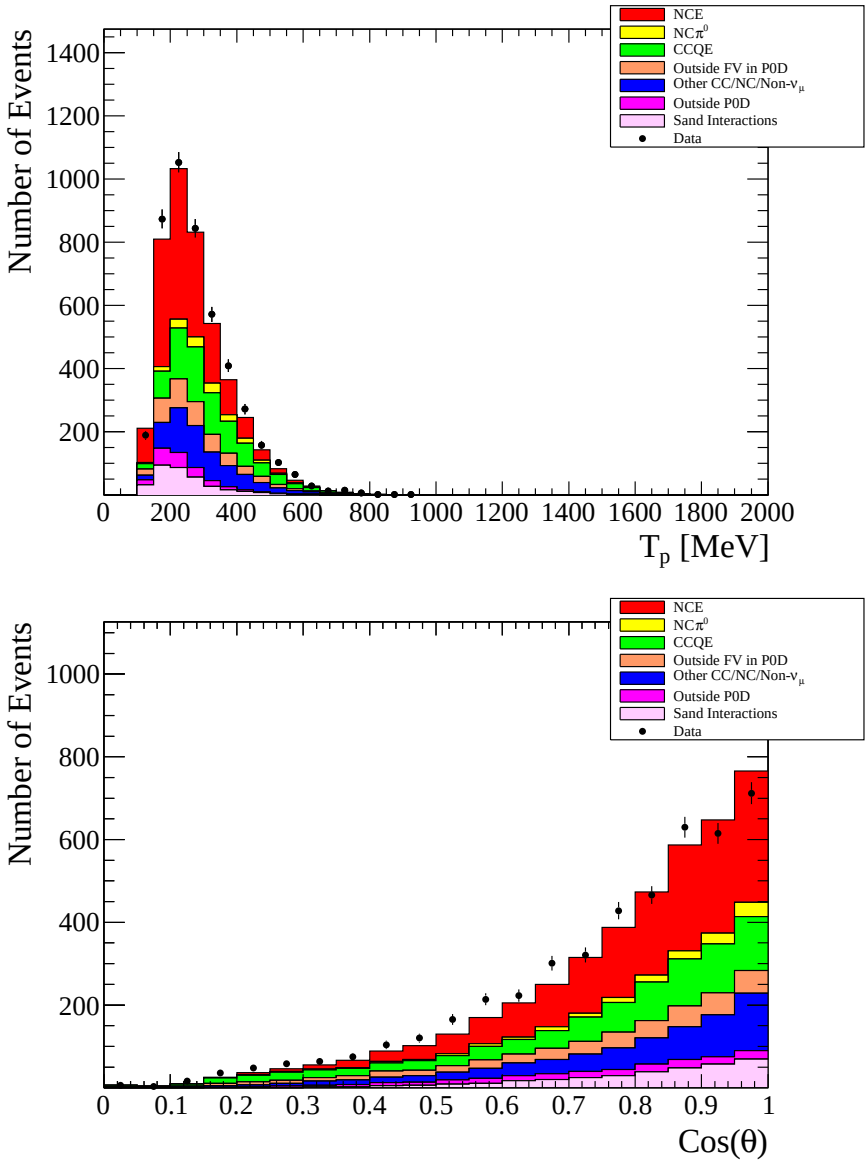

Figure 6.10: Track kinetic energy (top) and angle (bottom) by interaction type after the all cuts up to and including PID Beg. cut have been applied. The outside scaling factor (See Section 7.2.3) has been applied to the outside and sand backgrounds.

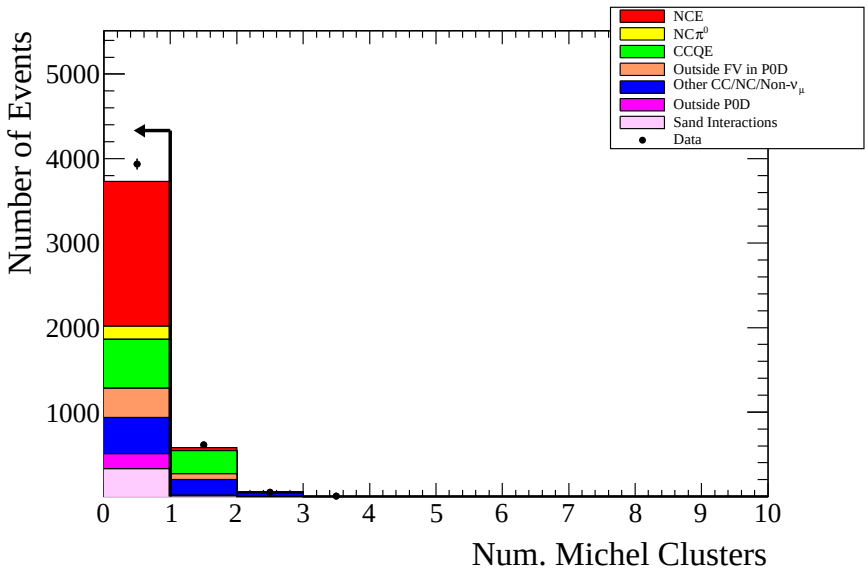

Figure 6.11: Number of Michel clusters by interaction type with all cuts but the Michel cut applied. The outside scaling factor (See Section 7.2.3) has been applied to the outside and sand backgrounds.

From the point of view of this analysis either algorithm is potentially valid but due to large data/MC differences for the MuonDecayTag algorithm only the TagMuonDecay algorithm is used. Only events that have no associated Michel clusters are allowed, as seen in Figure 6.11.

6.1.8 Final NCE Sample

The kinematic description of the final NCE sampe can be seen in Figure 6.12. The final samples have also been broken down by Kalman tracks, see Figure 6.13, and Parametric tracks, see Figure 6.14. The performance of the angular reconstruction can be seen in Figure 6.15 and the energy reconstruction performance in Figures 6.16 and 6.17. The final event sample has 3936 selected events in data, with the MC predicting 1714.69 NCE and 2015.94 background events, with a selection purity of 45.96% and efficiency of 13.74%.

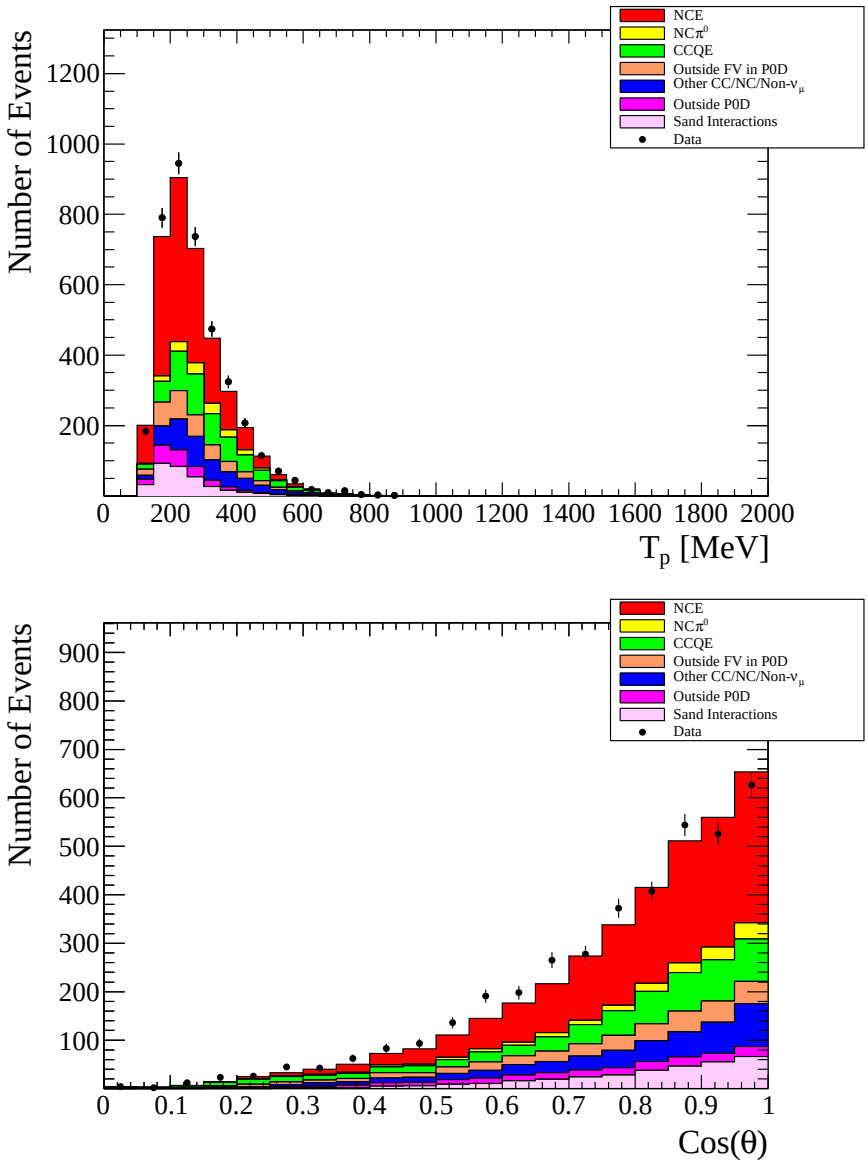

Figure 6.12: Track kinetic energy (top) and angle (bottom) by interaction type for the final event selection. The outside scaling factor (See Section 7.2.3) has been applied to the outside and sand backgrounds.

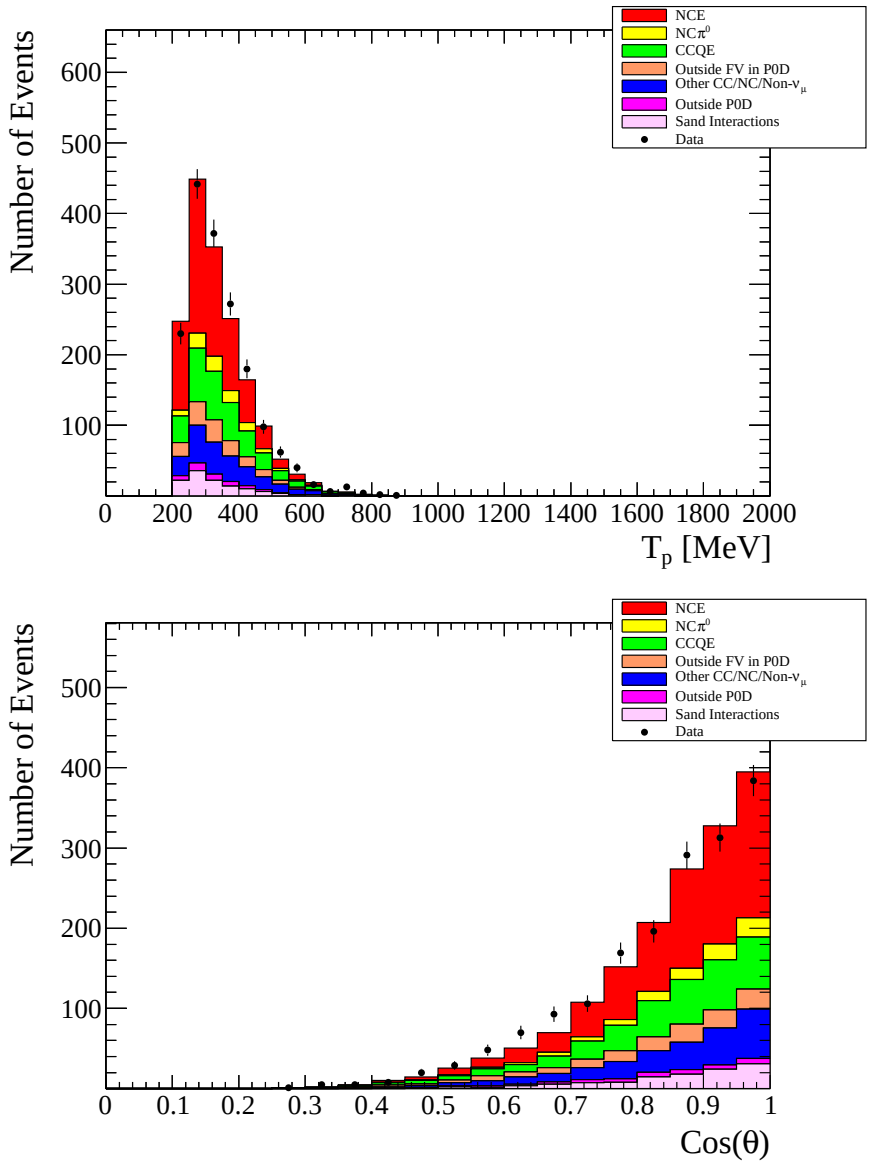

Figure 6.13: Track kinetic energy (top) and angle (bottom) by interaction type for the final Kalman track event selection. The outside scaling factor (See Section 7.2.3) has been applied to the outside and sand backgrounds.

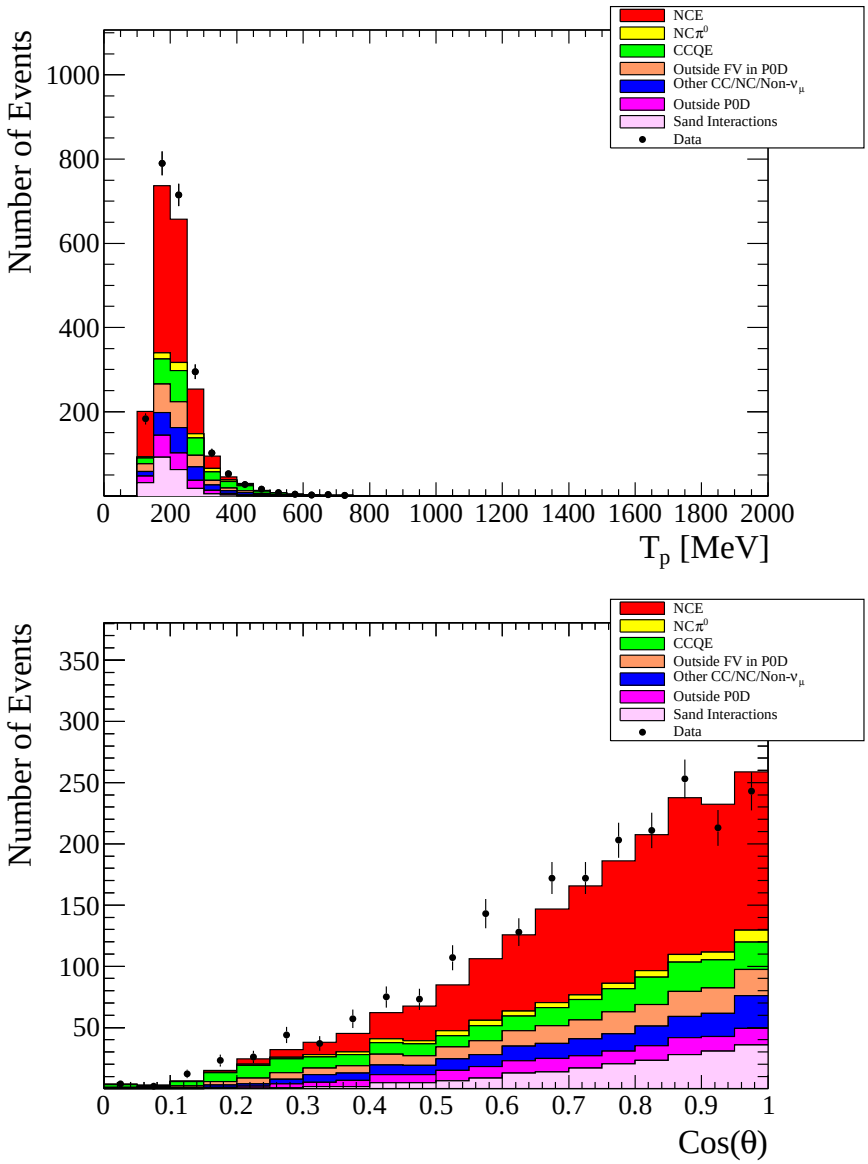

Figure 6.14: Track kinetic energy (top) and angle (bottom) by interaction type for the final Parametric track event selection. The outside scaling factor (See Section 7.2.3) has been applied to the outside and sand backgrounds.

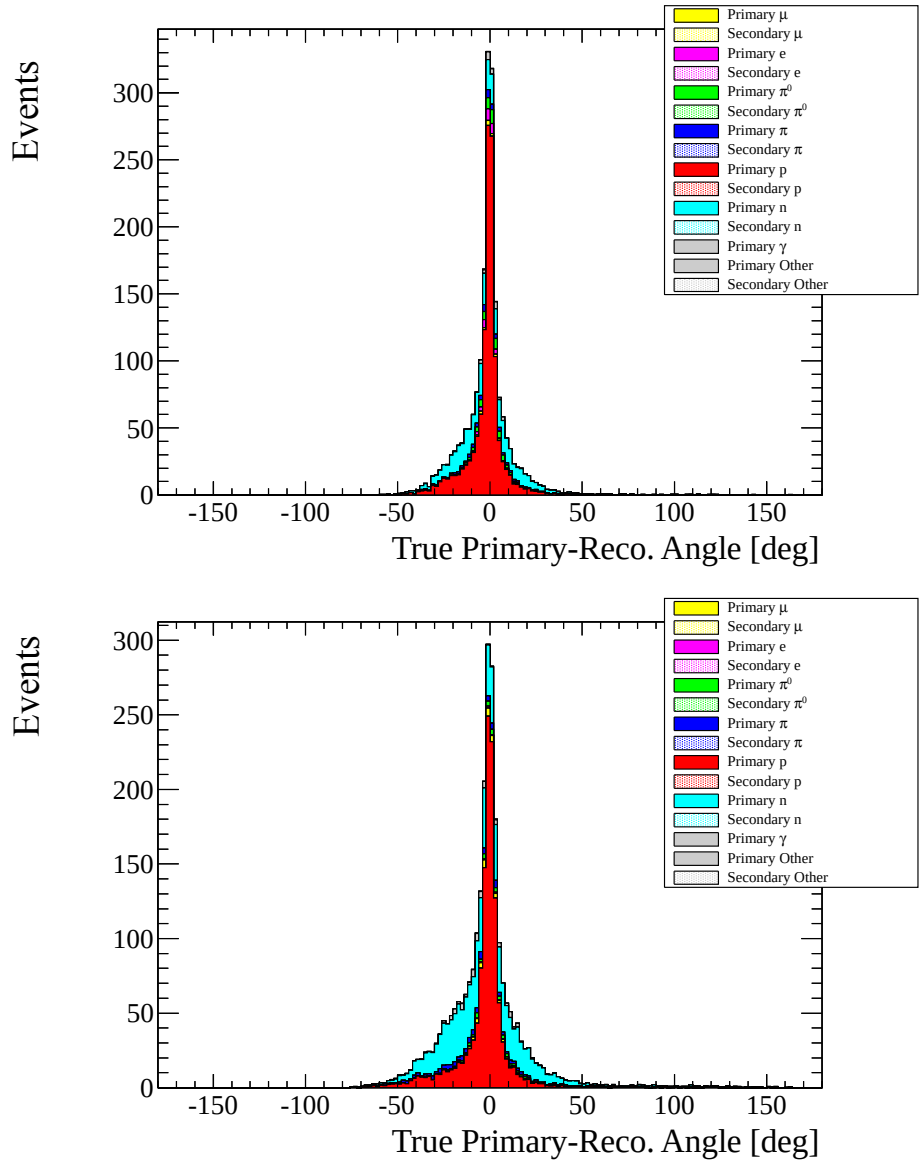

Figure 6.15: Comparison of track angle reconstruction to the true primary particle angle: Kalman (left) and Parametric (right). The distribution mean and sigma: $\bar{x} = -1.66$ degrees RMS = 14.69 degrees (left) and $\bar{x} = -2.02$ degrees RMS = 22.5 degrees (right).

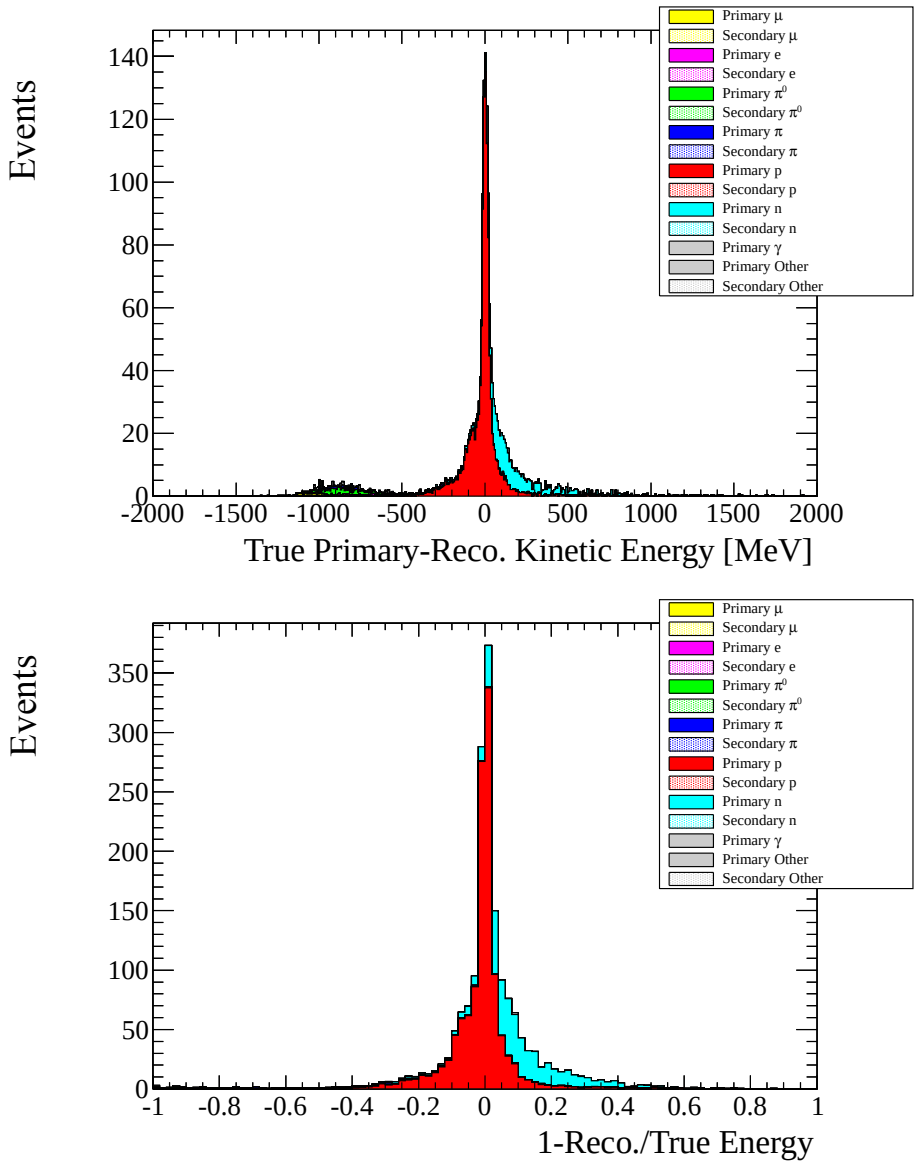

Figure 6.16: Track energy reconstruction performance based on the primary particle energy for Kalman tracks: truth - reconstruction (left) and 1-$\frac{\text{Reconstruction}}{\text{Truth}}$ (right). The distribution mean and sigma for protons plus neutrons: $\bar{x}$ = 49.55 MeV RMS = 205.1 MeV (left) and $\bar{x}$ = 2.3% RMS = 12.1% (right). The distribution mean and sigma for protons only: $\bar{x} = -6.45$ MeV RMS = 142.9 MeV (left) and $\bar{x} = -1.2\%$ RMS = 9.2% (right).

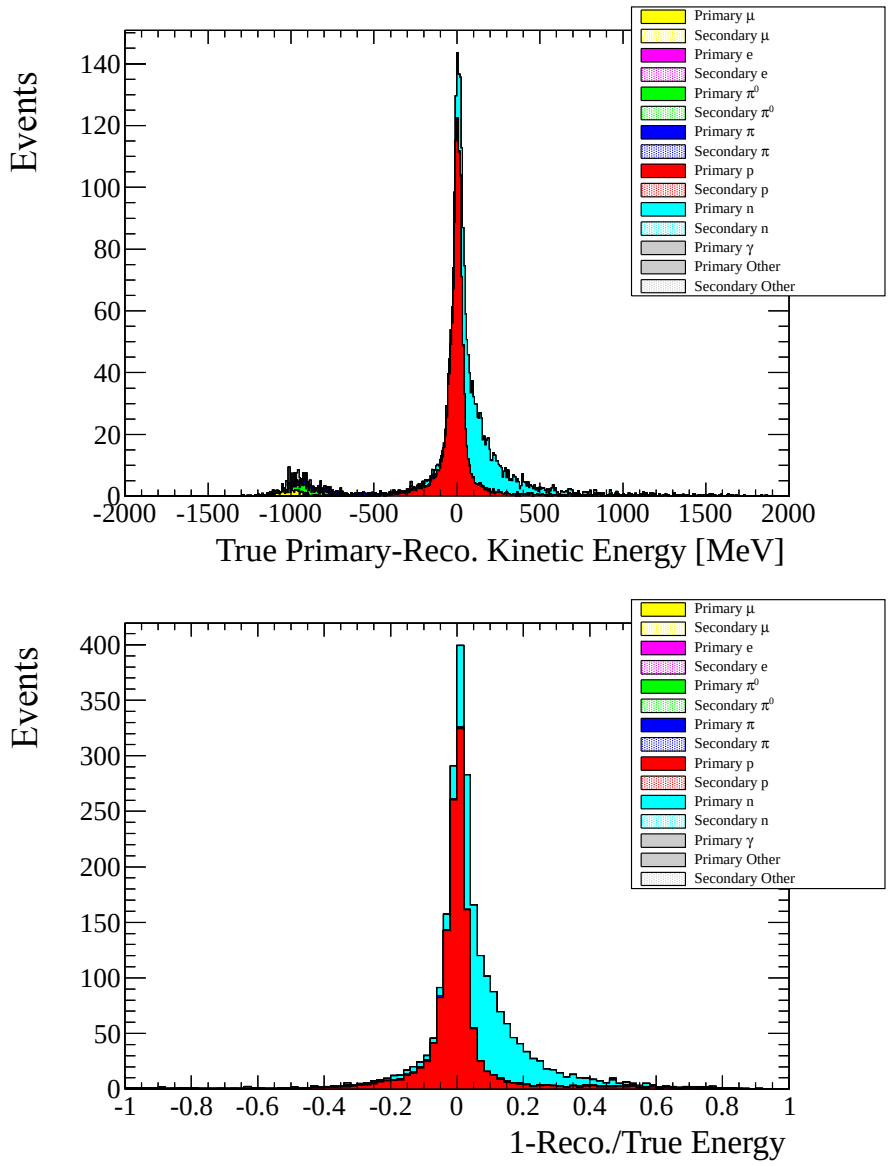

Figure 6.17: Track energy reconstruction performance based on the primary particle energy for Parametric tracks: truth - reconstruction (left) and 1-$\frac{\text{Reconstruction}}{\text{Truth}}$ (right). The distribution mean and sigma for protons plus neutrons: $\bar{x}$ = 81.16 MeV RMS = 219.2 MeV (left) and $\bar{x}$ = 4.98% RMS = 13.1% (right). The distribution mean and sigma for protons only: $\bar{x}$ = 14.9 MeV RMS = 180.4 MeV (left) and $\bar{x}$ = 0.32% RMS = 11.2% (right).

6.1.9 PID Cut Optimization

The PID related cuts for both Kalman and Parametric tracks were optimized by varying the cuts over a wide range of values. Looking at two different optimization criteria an optimal cut value for the end and beginning of the track cuts was determined. The selection metrics efficiency $\times$ purity and efficiency $\times$ purity $\times$ purity for flux reweighted events were investigated for beam MC only. The purpose of the second metric is to investigate if the analysis can get a higher purity by sacrificing some statistics. In the end both metrics give similar results. The Kalman and Parametric track were treated separately as there wasn't any correlation between the two types of tracks.

The Parametric and Kalman track PID cuts were applied to both the beginning and end of the track over a range of cut values from 0 to 32 in steps of 0.5 independently. The range of cut values was chosen to vary beyond the obvious cut positions, see Figures 6.7 and 6.9. In the end, the ranges used encompassed an optimal point for both types of tracks. The full selection events versus purity space for both types of tracks can be seen in Figure 6.18.

Each cell in these histograms is for a given set of PID cuts, with the z-axis being the value of interest. The optimized point for both sets of criteria and track types is indicated with an X and coordinates (cut track end, cut track begining, value). Each optimized set of cuts is indicated on Figures 6.21 and 6.22 with the total signal events selected and purity. The average cut value of the two optimization criteria is used for the end and beginning of the track for both types of tracks. For the Kalman tracks cut positions of 12.5 and 4.25 are used for the end and beginning of the track respectively. For Parametric tracks cut positions of 3 and 0.75 are used. Kalman tracks tend to have lower signal event rates as well as purities when compared to the Parametric track phase space. The optimization matrices for Parametric and Kalman tracks can be seen in Figures 6.19 and 6.20.

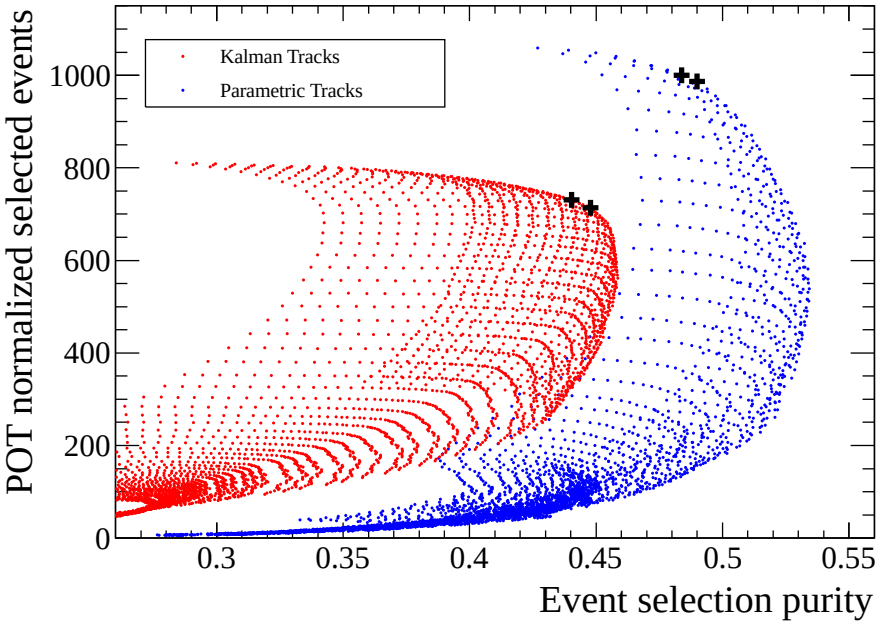

Figure 6.18: The p.o.t. normalized selected signal events versus purity phase space for PID optimization. Each point is for a single PID End + Begining cut combination. This plot shows the possible selection purity and number of signal events selected for these combinations. The optimized cut positions are shown with a +.

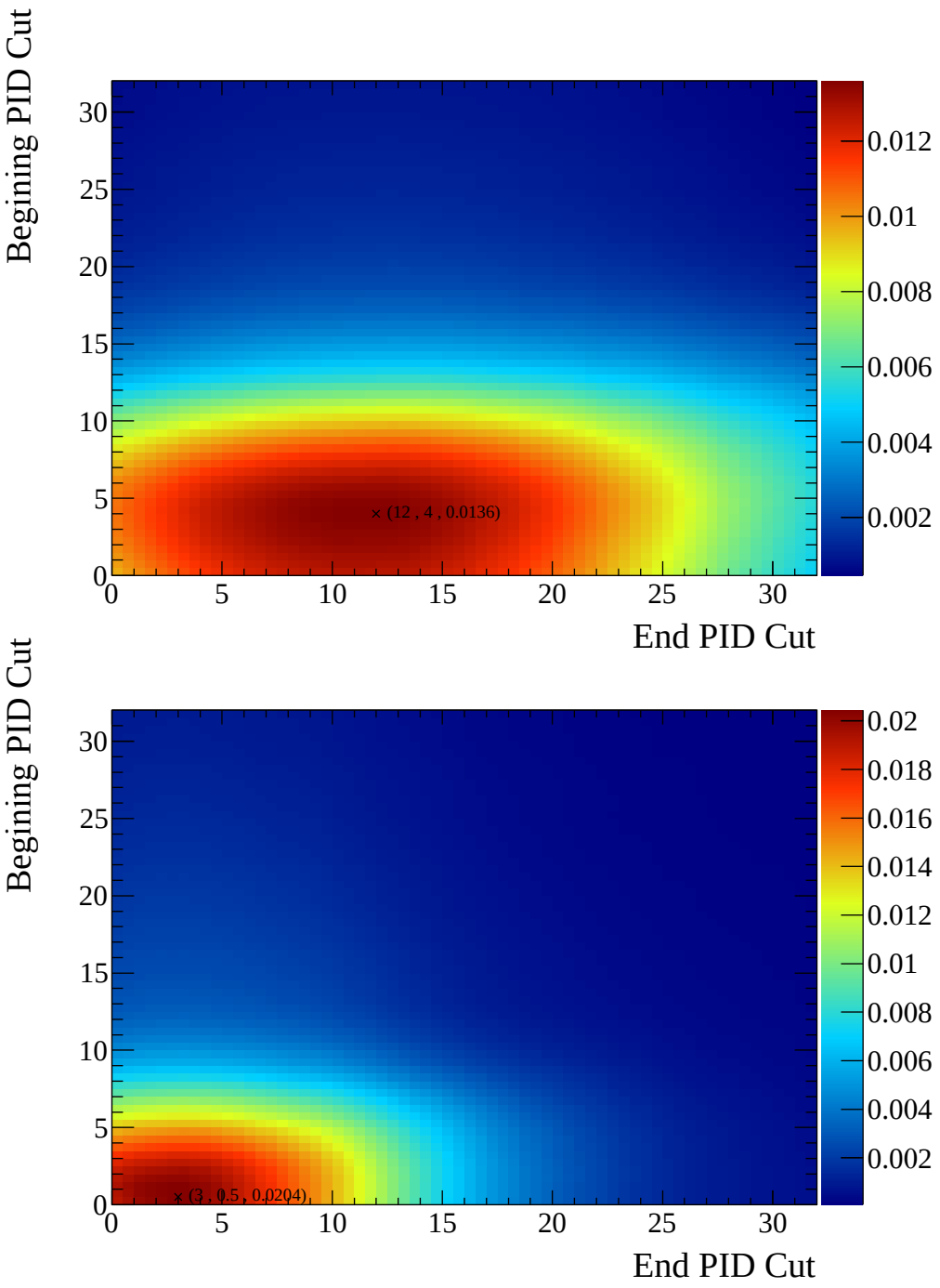

Figure 6.19: Efficiency × Purity: Kalman tracks optimized to be (12,4) (top) and Parametric tracks optimized to be (3,0.5) (bottom). The labeled points are the optimized positions using the Efficiency × Purity metric.

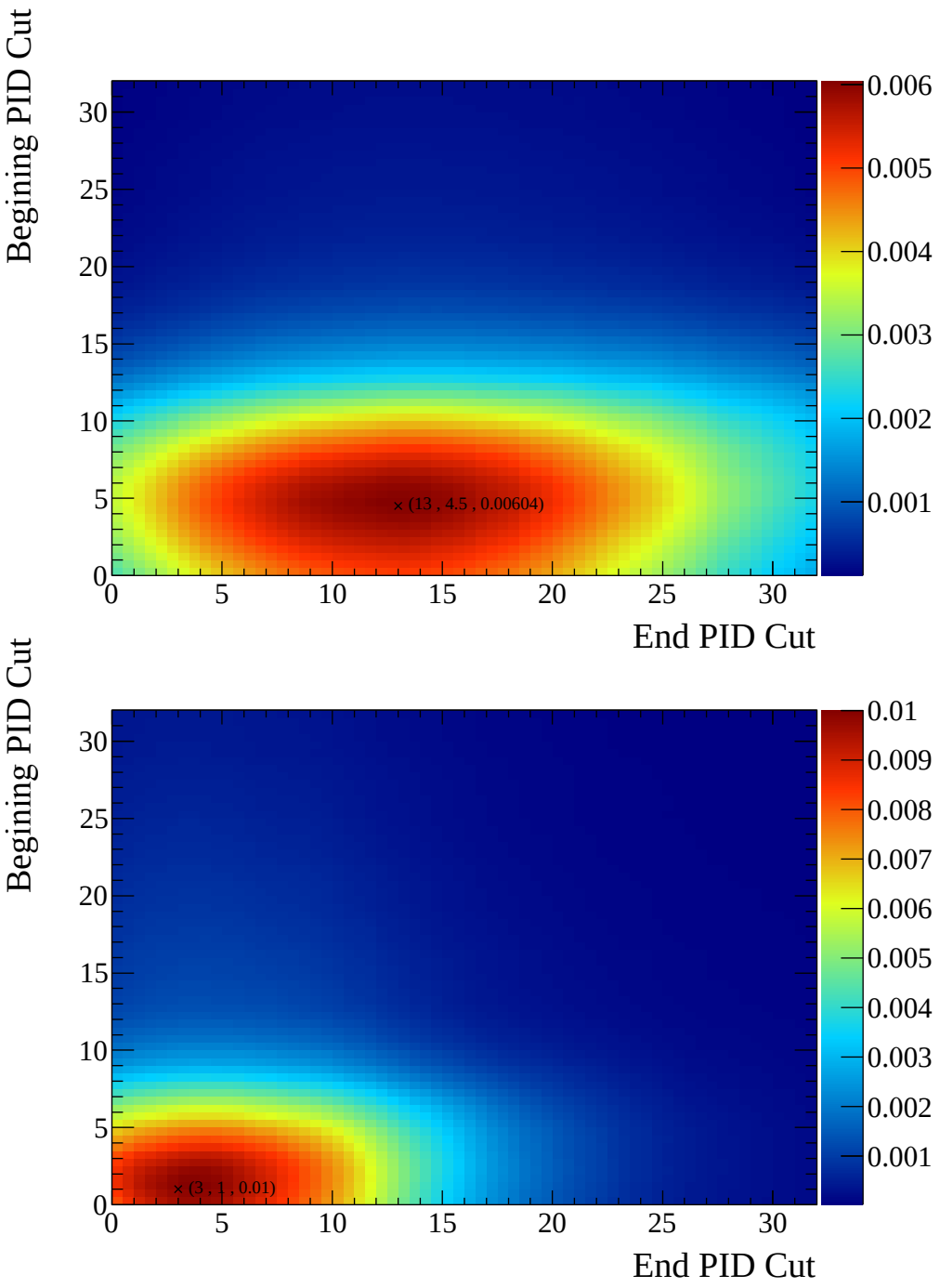

Figure 6.20: Efficiency × Purity × Purity: Kalman tracks optimized to be (13,4.5) (top) and Parametric tracks optimized to be (3,1) (bottom). The labeled points are the optimized positions using the Efficiency × Purity × Purity metric.

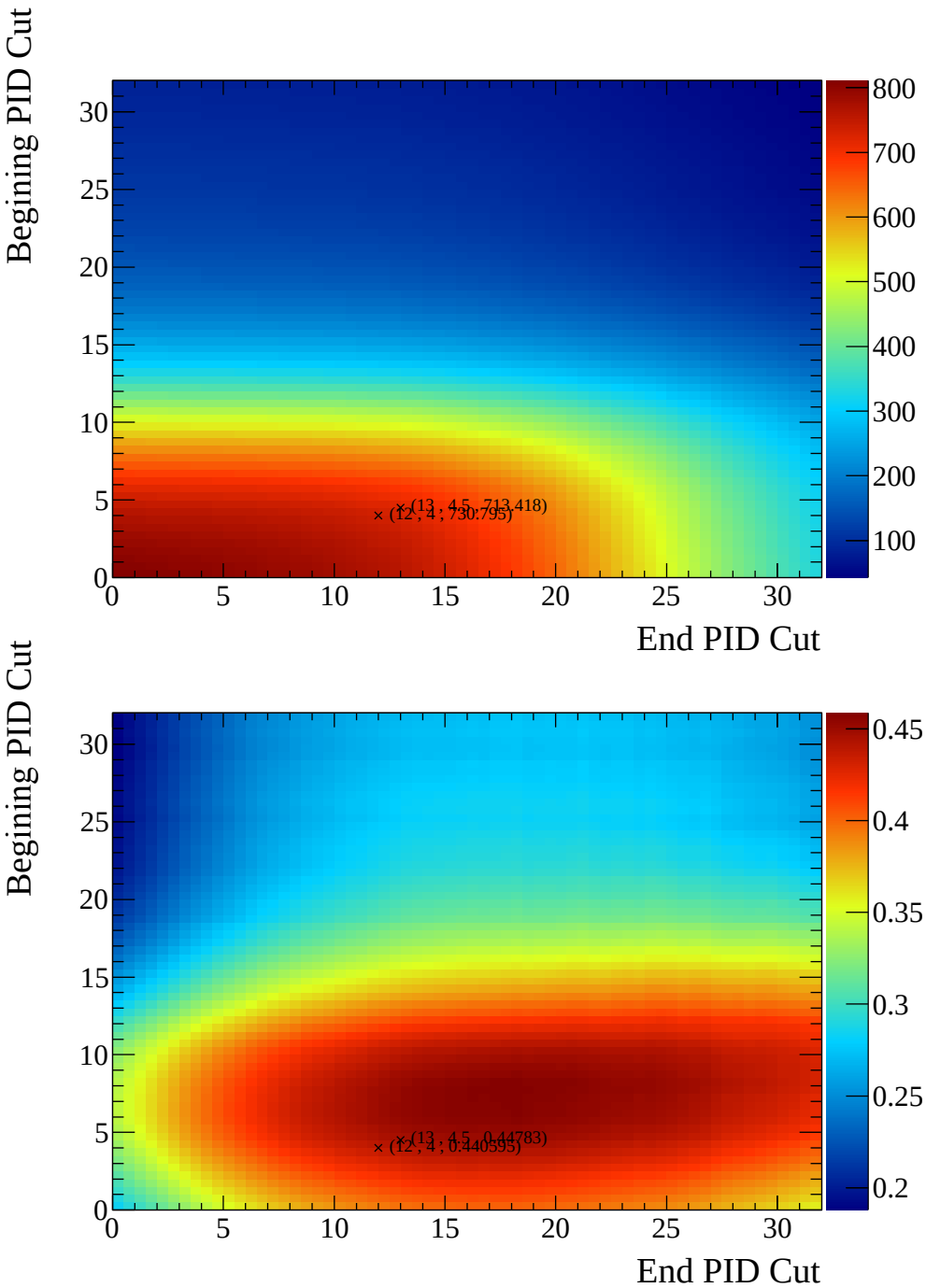

Figure 6.21: Kalman track selection signal events with optimized points (13,4.5,713.418) and (12,4,730.795) (top) and purity with optimized points (13,4.5,0.448) and (12,4,0.441) (bottom) for PID optimization.

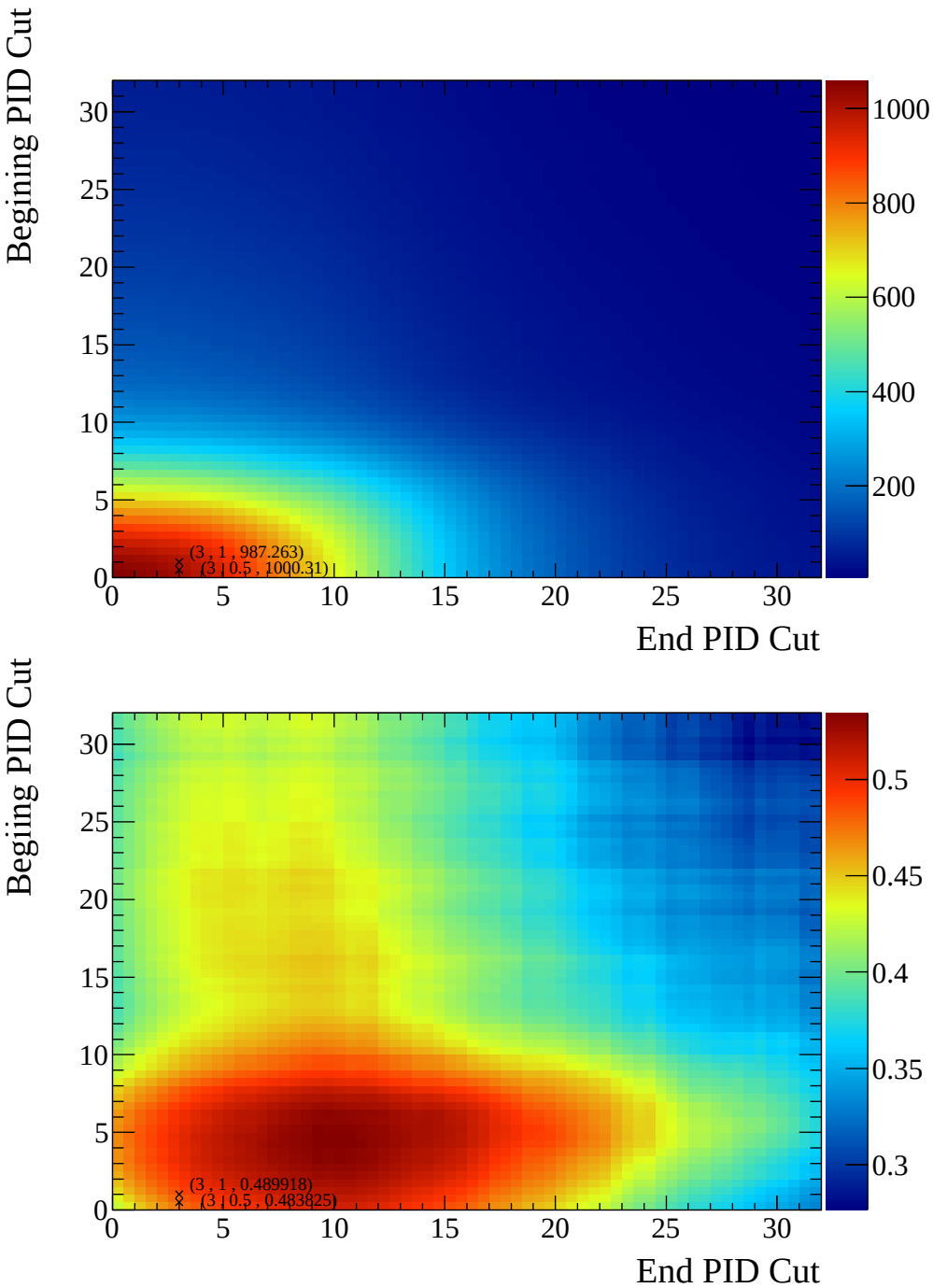

Figure 6.22: Parametric track selection signal events with optimized points (3,1,987.263) and (3,0.5,1000.31) (top) and purity with optimized points (3,1,0.490) and (3,0.5,0.484) (bottom) for PID optimization.

Chapter 7

Systematics

The systematic error analysis provides an estimate of the uncertainty of the final measured cross section due to inputs of the analysis. Systematics errors for this analysis are broken into three general categories: detector and reconstruction, physics model, and beam flux systematics. Each of these categories investigates the effect that the simulation, neutrino models, particle propagation, and initial neutrino flux has on the final cross section result. These effects arise from the fact the MC simulation is not an exact replication of the experimental environment and each piece of the Monte Carlo, while based on as much real data as possible, has uncertainties.

Different techniques will be used to evaluate each source of systematic error. The detector and reconstruction related systematics are typically evaluated by changing event selection cut values such as vertex position for the fiducial volume systematic or the PID algorithm response or by changing the reconstruction algorithm and re-running the analysis. The physics model systematics are typically evaluated by a reweighting technique described in Section 7.2.1, designed to replicate a modified MC without having to re-run. Re-running the MC is very computationally expensive and the number of variables which need to be evaluated makes this process untenable. Finally, the flux systematic is evaluated using a covariance matrix, a matrix providing the information about the size of the correlated errors between neutrino energy bin and varying species, provided by the beam group. The covariance matrix is a function of neutrino species and energy. By drawing random throws from this covariance matrix, the original MC can be reweighted to investigate the effects of the input uncertainties encoded in the covariance matrix while taking into account the correlations (or anti-correlations) between neutrino species and energies.

Table 7.1: Systematics table for flux-averaged cross-section with water in the PØD. The statistical error is included for reference.

Systematic Name	**Error on cross section**
Detector and Reconstruction	
Fiducial Volume	0.72%
PID Algorithm	1.1%
Reconstruction Road Following	1.7%
Michel Efficiency	1.0%
Number of targets	0.7%
Physics	
Cross section model parameters	+14.3%, -16.6%
Pion Absorption	2.3%
Secondary Interactions	2.5%
Outside background scaling factor	6.4%
Beam Flux	
Flux	+17.5%, -21.5%
Total Systematics	$^{+23.9\%}_{-28.2\%}$
Total Statistical	±3.3%

Table 7.1 lists the sources of systematic error considered and the size of the error on the cross section. The evaluation methods used to determing these values are described in the following sections.

7.1 Detector and Reconstruction Systematics

Systematic errors under this category investigate potential differences between MC simulation and data in the areas of detector response and reconstruction performance. The

following systematics are described in detail: fiducial volume selection, particle identification, road following algorithm, Michel tagging efficiency, number of targets.

7.1.0.1 Fiducial Volume

A choice of a fiducial volume, if done poorly, can cause large differences in the event rate seen in simulation versus data as well as missed events. These differences can arise from incorrectly simulated backgrounds, detector material, or detector response. This systematic measures the uncertainty arising from the combination of these potential differences. Even though there is no explicit upstream veto, the fiducial volume cut removes the 15 upstream readout layers from the analysis. In order for the front entering particles to be of concern for the analysis the layer efficiency would have to be very low. The layer efficiency has been measured to be >99%.

When evaluating this systematic a method has to be developed that is as independent of the physics signal model, as much as possible, to avoid being sensitive to its cross section uncertainties. The sample used by this systematic is all single contained tracks. To evaluate this systematic the XY boundaries, Z upstream, and Z downstream cuts were varied for a single contained track sample. For the XY boundary the cut position was allowed to vary by $\pm$ 2,1, and 0 σ where σ corresponds to the resolution in the XY directions, or 32 mm, see Figure 7.1. The Z upstream boundary was allowed to vary by -1, 0, 1, 2 σ where σ=20 mm, which corresponds to the distance between the readout planes in a PØDule. The Z downstream boundary was allowed to vary by -2,-1,0,1 σ where σ=20 mm. For the two Z boundaries the variation was limited from penetrating into the ECal regions because of concerns for the large cross section uncertainties on the lead radiator. All combinations of XY, Z upstream, and Z downstream cuts are used. After each independent variation the fractional change with respect to the number of single contained tracks in nominal MC and data was recorded. After all fiducial volume boundary variations have been evaluated, the difference between the data and MC fractional change is calculated, and an error envelope

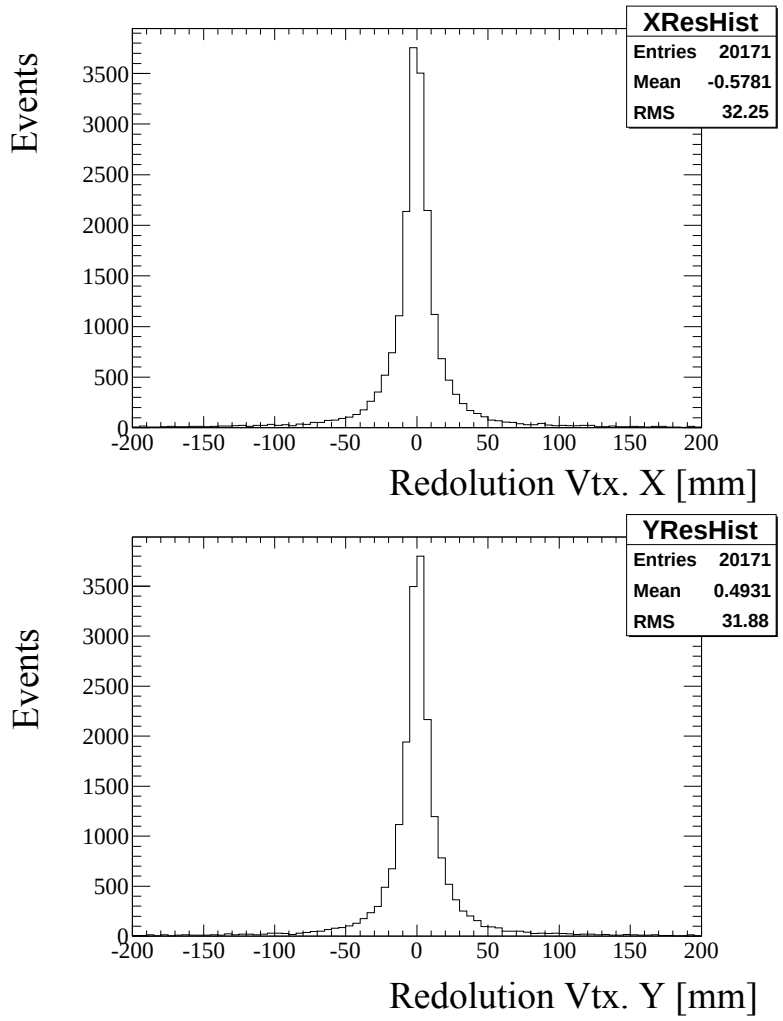

Figure 7.1: Vertex resolutions, X (top) and Y (bottom), for a contained single track sample which starts in the fiducial volume.

large enough to encompass the largest differences is established. The final systematic on the cross section is estimated to be 0.72%.

7.1.0.2 Particle Identification

As the primary background reduction method in this analysis, the PID algorithm needs to be understood well. Since the PID algorithm uses the path length corrected charge deposition of nodes, charge deposition differences between data and MC is a source of PID performance

Table 7.2: PID parameter values derived from data and MC.

Bin number	Muon MPV(data)	Sigma(data)	Muon MPV(MC)	Sigma(MC)
1	78.91	15.91	79.48	18.02
2	64.54	13.60	62.96	12.88
3	55.58	11.15	55.07	11.52
4	51.61	10.84	51.30	10.99
5	49.12	10.45	48.53	10.32
6	47.27	10.34	46.53	10.28

differences. The PID parameters used in the analysis are derived from a stopping sand muons sample derived from data. As a result, a comparison between MC sand muons and data sand muons PID parameter extraction has been investigated. See Section 5.3 for the extraction details. Figure 5.9 shows the data charge distributions fit with a Landau $\otimes$ Gaussian function for a data derived sand muon sample described in Section 5.3. The same procedure was applied to MC sand muon samples.

To try and make the charge distributions as similar as possible, the p.o.t. normalized sum of the beam MC and the sand muon simulation are combined. A comparison between the MC and data derived constants can be seen in Table 7.3. Once these new constants are derived, the same PID algorithm using new constants can provide a second set of optimized PID pulls for the analysis. To investigate the systematic error arising from the charge simulation differences the pull cut values from the MC derived constants are calculated as in Section 6.1.9. The resulting figures optimization values and the corresponding values are seen in Figures 7.2, 7.3, 7.4, 7.5, and 7.6.

Using the same procedure as with the data-derived set of optimized cuts, the MC cuts are the average of the efficiency $\times$ purity $\times$ purity and efficiency $\times$ purity optimizations. Table 7.4 summarizes the optimized cuts for both sets of constants. To understand the size of the effect from differing PID distributions, due to the charge simulation, the two sets of cut values are

Table 7.3: Comparison of MC constants to the Data constants, $1 - \frac{\text{MC}}{\text{Data}}$.

Bin number	Fractional Difference MPV	Fractional Difference Sigma
1	-0.72%	-13.26%
2	2.45%	5.29%
3	0.92%	-3.32%
4	0.6%	-1.38%
5	1.20%	1.24%
6	1.57%	0.58%

Table 7.4: Optimized cut positions for the MC derived PID distribution and data derived PID distribution.

Constant	Kalman PID End	Kalman PID Beg	Para. PID End	Para. PID Beg
MC	11.75	3.5	3	0.75
Data	12.5	4.25	3	0.75

varied between the data derived cut values and MC values, see Table 7.4. For instance, the Kalman tracks have cut values of 12.5 and 11.75 for data and MC constants applied to the end of the track. Cuts ranging from 11.75 to 12.5 are applied to both the MC and data PID distributions for the PID applied to the end of the track. To ensure the full phase space is explored all four cut values are varied independently and a resulting flux-averaged cross section is calculated for each set of cuts and PID distributions. The fractional difference in the measured cross section between the nominal, data derived cuts, and the MC based cuts are used for the systematic. In all, 63 different cut permutations are run (step size is 0.125), with the resulting cross-section distributions seen in Figure 7.7. The fractional difference on a cut set by cut set is seen in Figure 7.8. The sum in quadrature of the mean and RMS is taken as the PID systematic error, 1.1%.

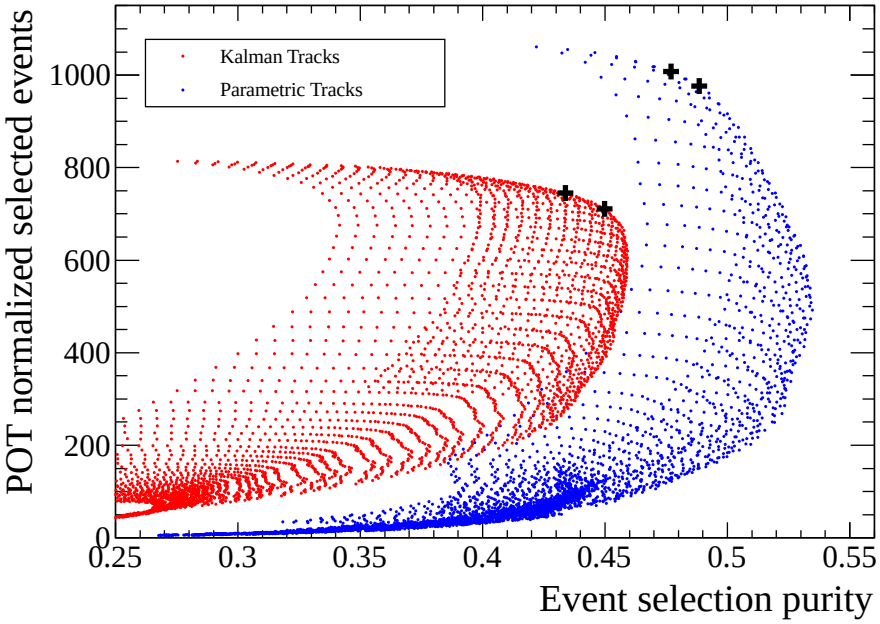

Figure 7.2: Full selected event versus purity phase space for MC Constants. Optmized cut points for both optimization definitions are shown with a +.

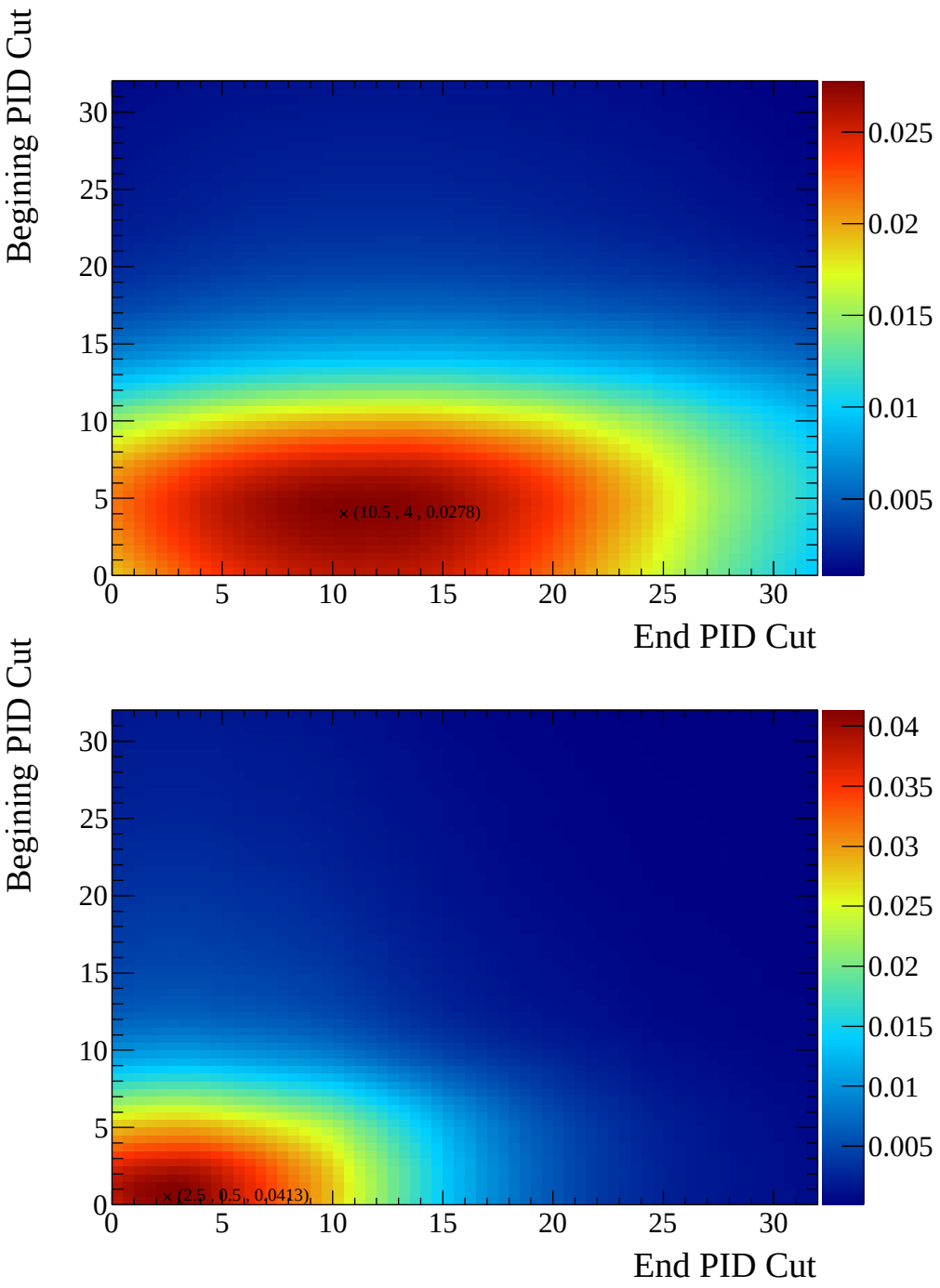

Figure 7.3: Efficiency×Purity: Kalman tracks (10.5,4) (top) and Parametric tracks (2.5,0.5) (bottom) for MC Constants. Labeled points are the optimized cut position using the efficiency×purity metric.

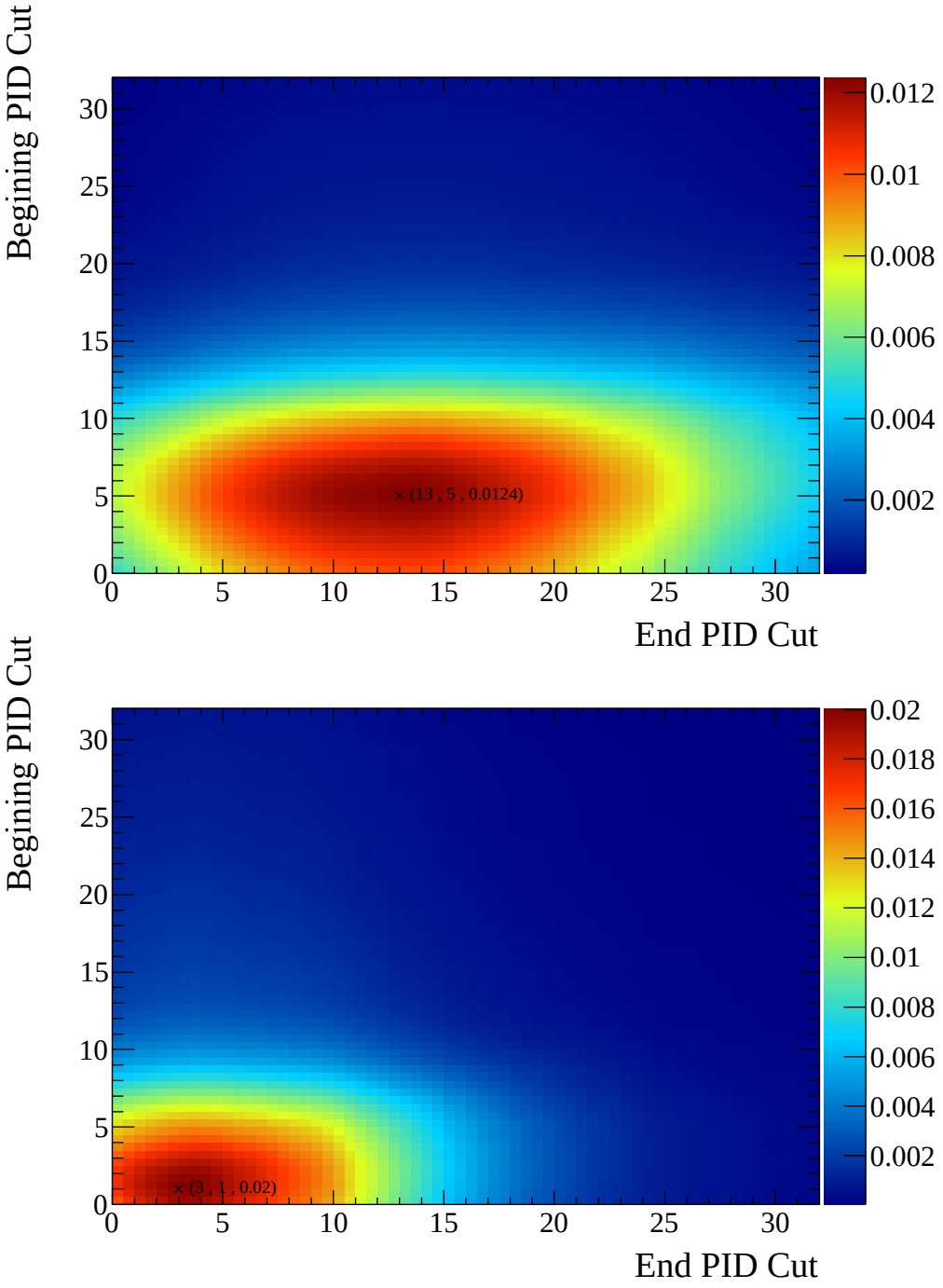

Figure 7.4: Efficiency×Purity×Purity: Kalman tracks (13,5) (top) and Parametric tracks (3,1) (bottom) for MC Constants. Labeled points are the optimized cut position using the efficiency×purity×purity metric.

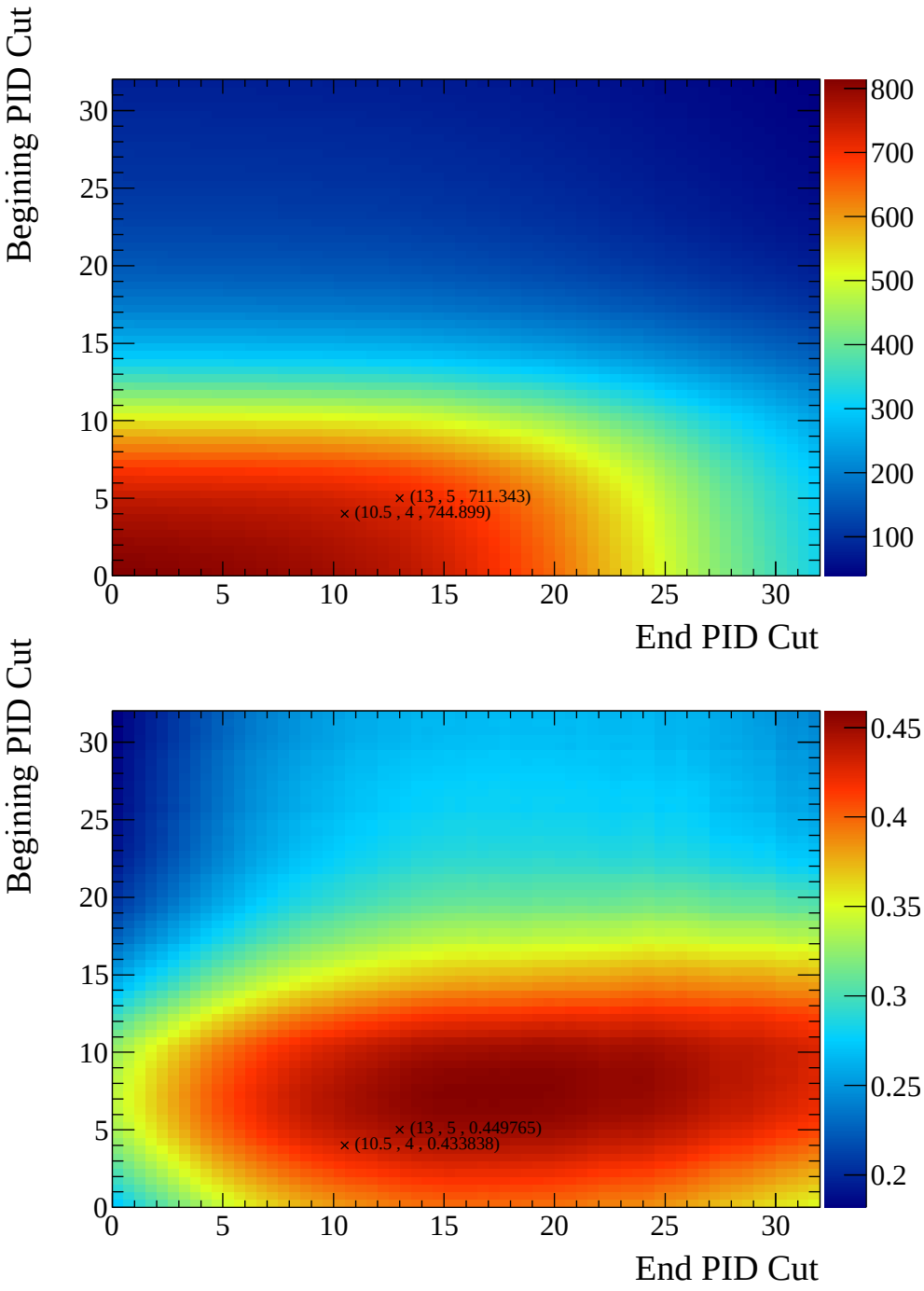

Figure 7.5: Kalman track selection signal events (13,5,711.343) and (10.5,4,744.899) (top) and purity (13,5,0.45) and (10.5,4,0.43) (bottom) for MC Constants.

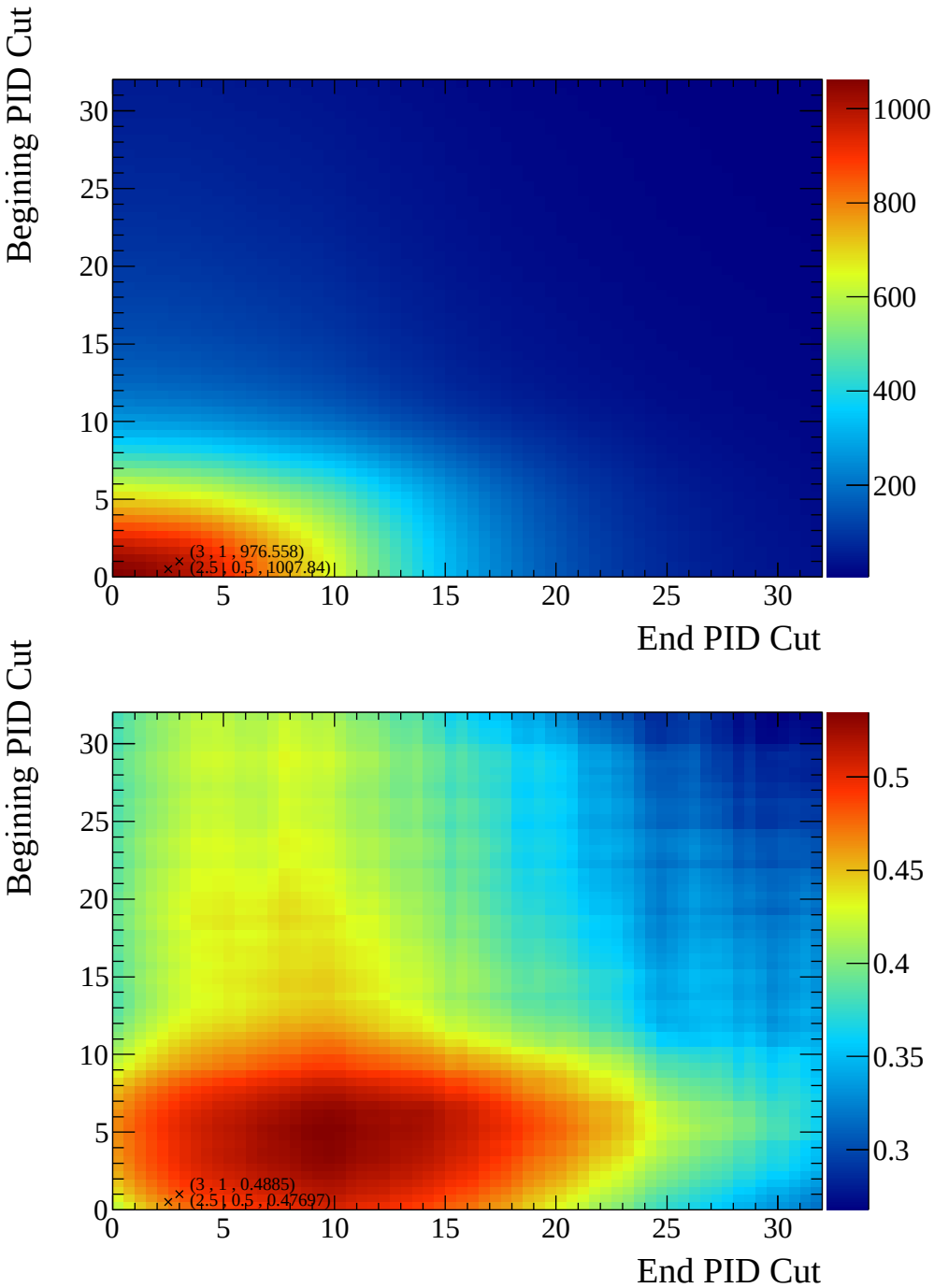

Figure 7.6: Parametric track selection signal events (3,1,976.558) and (2.5,0.5,1007.84) (top) and purity (3,1,0.49) and (2.5,0.5,0.48) (bottom) for MC Constants.

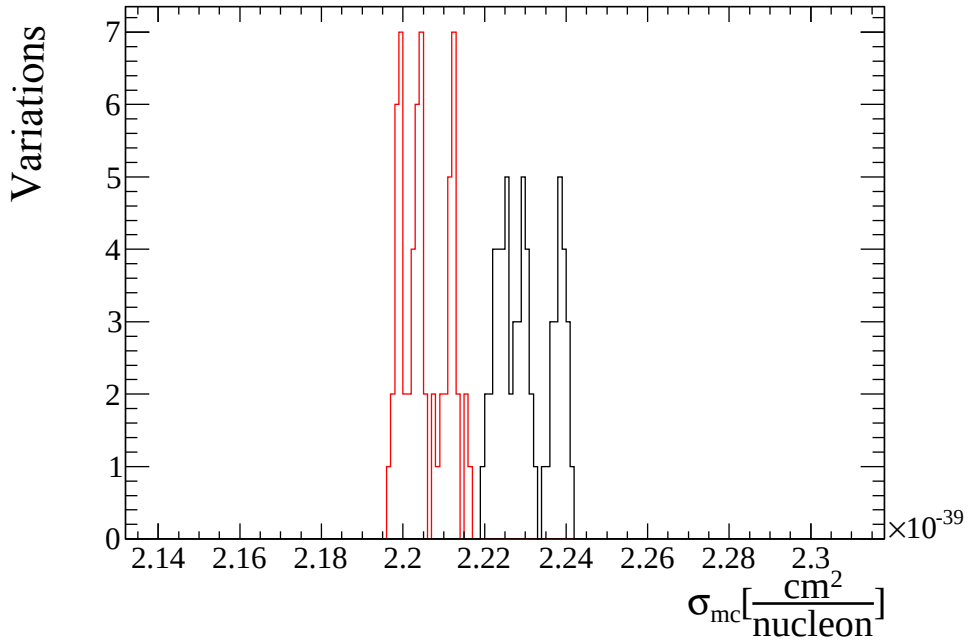

Figure 7.7: Measured cross-section for nominal data derived constants (black) and MC derived constants (red).

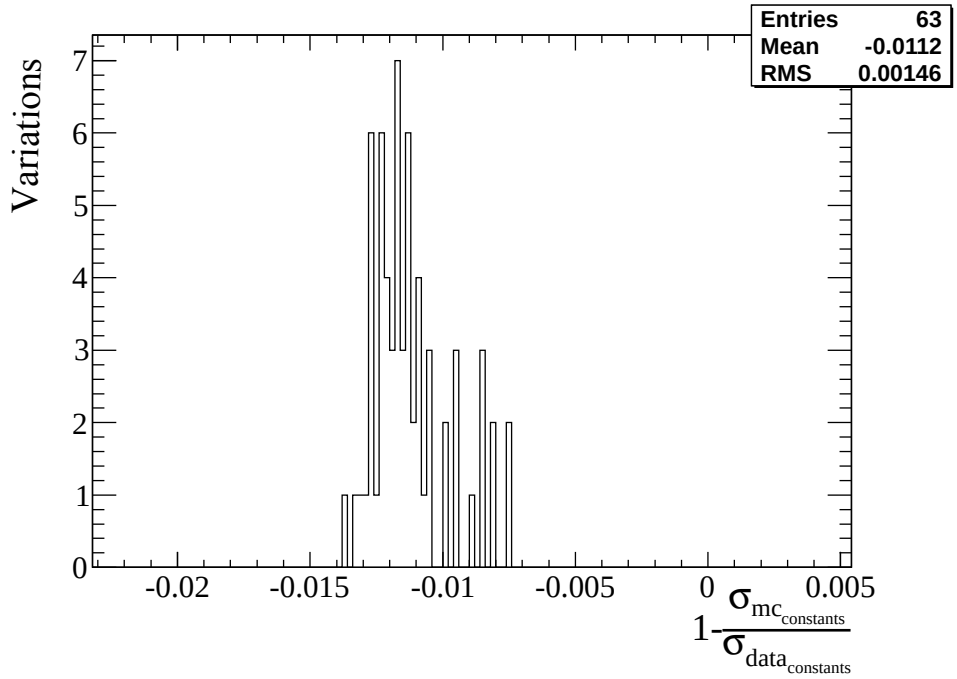

Figure 7.8: Fractional change in cross-section with respect to the nominal data driven method.

7.1.0.3 Reconstruction Road Following Algorithm

Due to the nature of PØD reconstruction, all single tracks are reconstructed as forward going. As a result, a subset of tracks are actually back-to-back particles reconstructed as a single track. In order to ensure the reconstruction performs similarly between data and MC three track reconstruction parameters have been investigated. The PØD tracking algorithm uses a road following algorithm from a Hough Transform seed with a specified cone angle, number of layers allowed to be skipped and road width. The purpose of the road following algorithm is to gather up hits along the path of the seed. The road width specifies how far away a hit can be in a given layer, the angle specifies how much scattering is allowed, and the number of layers allowed to be skipped. Table 7.5 shows the default values and modified values used for this investigation along with the measured systematic. The bar-to-bar distance in the readout plane is 13 mm which means a variation in the road width

Table 7.5: Default road following parameter values and the variation used with the associated systematic error

Variable	Default Value	Modification Value	Systematic
Road Width	80	20	1.19%
Road Angle	0.55	0.1375	0.79%
Layer Skip	2	1	0.84%
		Total Systematic	1.66%

modifies the road width by 1.5 bars or 3 bars for double this variation. The natural unit for the skipped layers parameter is a single layer. The angular variation was chosen to be of the same fractional size as the road width variation, or 25%.

Each default value was varied by $\pm$ 1$\times$ and $\pm$ 2$\times$ the modification value, independently, giving a total of 13 variations including nominal. For this study Run 2 with water in the PØD was used. Each set of data and MC files was rerun with a modified reconstruction and then subjected to the standard analysis cuts and the resulting selection was compared to the nominal set of files.

The reconstruction systematic can be introduced in 2 variables, the background prediction and selection efficiency prediction. To evaluate this systematic a total of 3 different measurements were made; investigating the event selection rates and the relative event rate change between data and MC; directly calculating the background prediction relative to the total event rate change and selection efficiency; calculating the cross section after each reconstruction parameter variation.

Initially, the change in the total number of events was investigated. The total number of events for each $\pm$1$\times$ change results in a $\sim$10% change in the total number of events depending on the reconstruction parameter variation, see Figure 7.9.

The relative change between MC and data gives one measure of this systematic. As can be seen in Figure 7.10 the data and MC event rates diverge by less than 1% for each reconstruction parameter variation. Since the difference in relative change in data and MC

is small it seems the MC is simulating the data event rate well. When investigating the background event rate in MC there is some confidence the total event rate is understood.

With the overall rate event understood, the selection efficiency and background event rates were investigated. Figure 7.11 demonstrates the selection efficiency varies much less than 1% for all variations. Based on the flatness of the selection efficiency the background event rate should vary by ∼10% based on how the overall event rate varies. As can be seen in Figure 7.12 the background event rate varies by ∼10% for ±1x the modification value, as expected.

To understand the effect of the algorithm on the final physics result a cross section calculation was performed for each parameter variation using the full NCE event selection. Each variation will give a different cross section measurement. The resulting distributions for all variations and only the 1x the modification value variations are seen in Figure 7.13.

Based on the overall event selection rate changes between data and MC the values used in Table 7.5 give a total envelope which spans the range of cross-section changes seen in Figures 7.13 and 7.14, or $\sim 0.8\%$ to 1.3%.

7.1.0.4 Michel Tagging Efficiency

Two possible samples could be used to investigate differences in the Michel tagging efficiency between data and Monte Carlo. The first sample, a cosmic sample using the FGD cosmic trigger, could be used to investigate the tagging efficiency, but there are simulation issues which would make the analysis complex. The FGD uses an asynchronous timing structure with respect to the PØD. As a result, there is no guarantee the cosmic event is within the PØD during an active integration window. This in and of itself is not an issue but the integration window simulated in the MC differed significantly from data. During Run 1 and part of Run 2, during the end of the integration window, there was a 50 ns dead period where no TDCs were stored. This was corrected in the DAQ, but the simulation used a value of 70 ns for all run periods. This difference ends up not only affecting the Michel

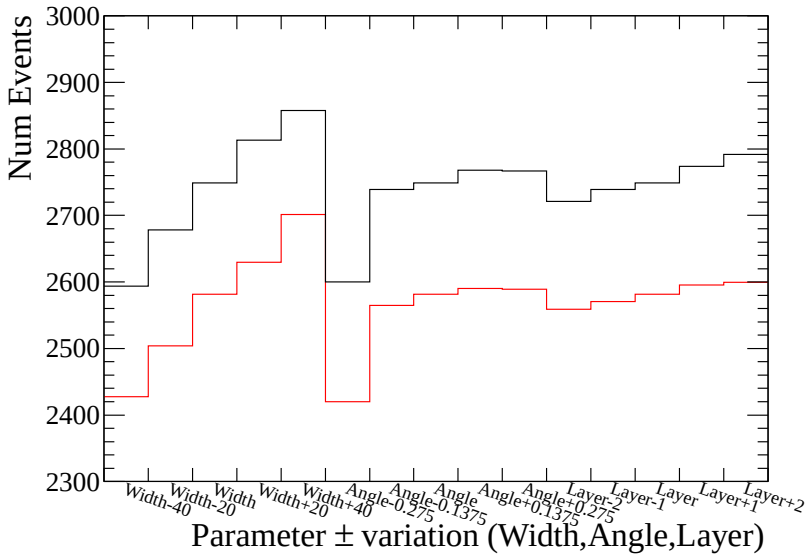

Figure 7.9: Number of selected events for MC (red) and data (black). On the x-axis is the parameter variation for the width, angle and layer parameters.

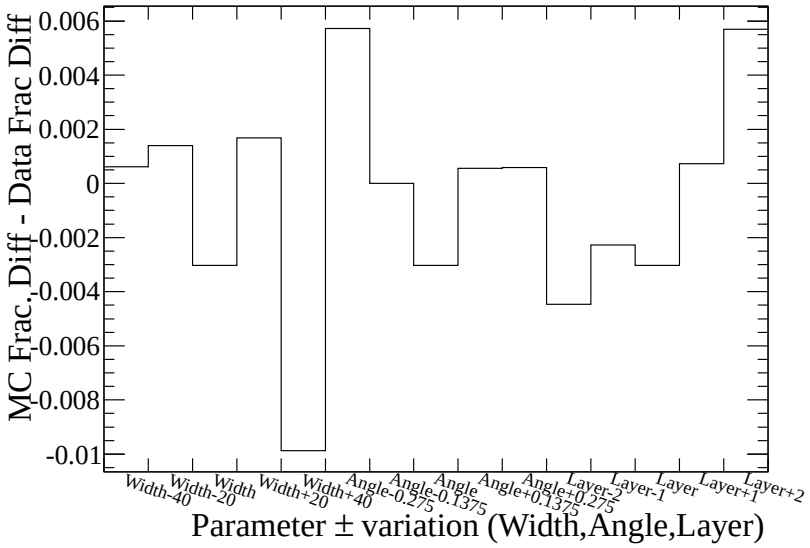

Figure 7.10: Difference in MC and data total event rate response for reconstruction parameter variations. On the x-axis is the parameter variation for the width, angle and layer parameters.

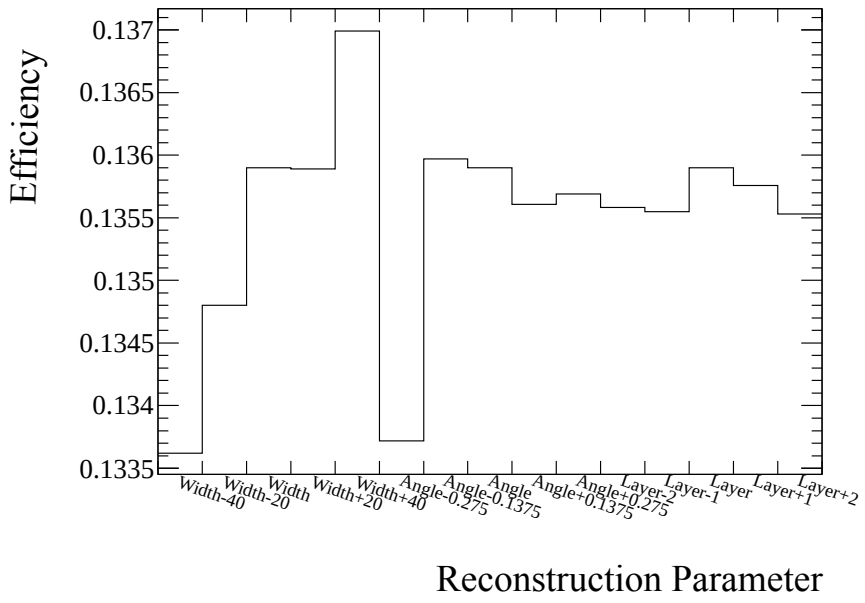

Figure 7.11: Predicted selection efficiency for reconstruction parameter variations. On the x-axis is the parameter variation for the width, angle and layer parameters.

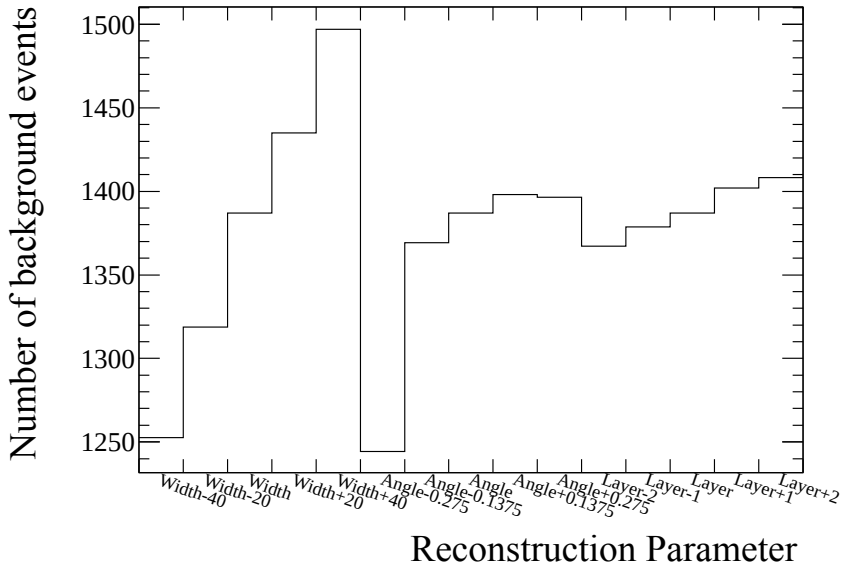

Figure 7.12: Predicted number of background events for reconstruction parameter variations. On the x-axis is the parameter variation for the width, angle and layer parameters.

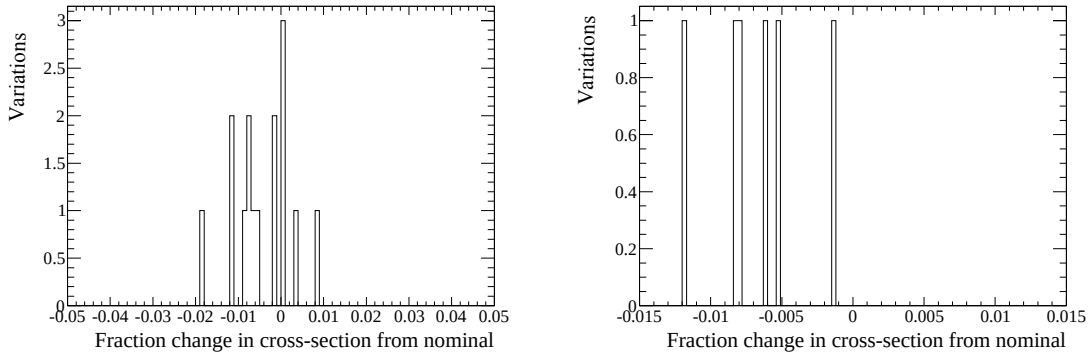

Figure 7.13: Cross-section values for reconstruction parameter variations; all variations (left) and only 1× modification variations (right).

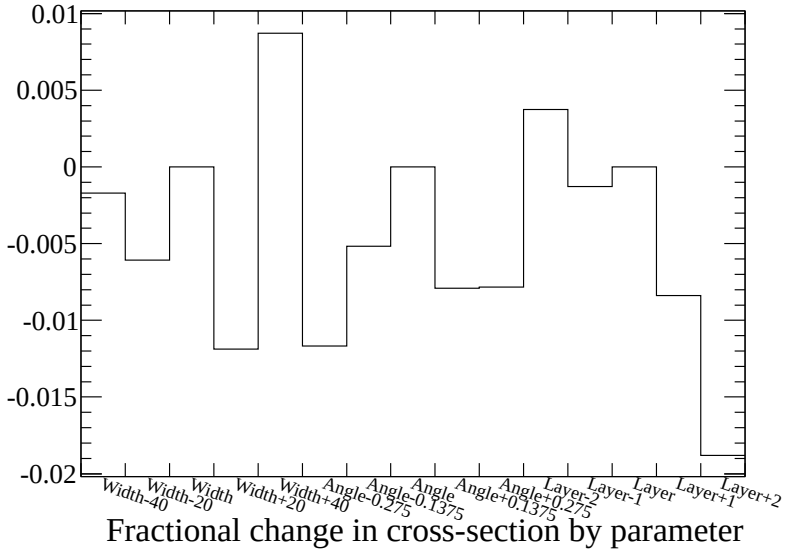

Figure 7.14: Fractional change in the cross-section by parameter variation. On the x-axis is the parameter variation for the width, angle and layer parameters. The final systematic values are pulled from this plot. The 1x variations are used.

tagging efficiency, but also the tracking efficiency as tracks can be truncated in non-trivial ways in the PØD . In principle this could be overcome by requiring the cosmic event be nicely in the middle of the integration window, but the information necessary to calculate the modified time was not available at the higher analysis level files.

Another sample which can be used to evaluate efficiency differences is a sample of sand muons. This was a more appropriate sample, as the events happen in the middle of the integration window and any simulation difference of the TDC dead region between MC and data show up as an efficiency difference.

A sample of contained sand muons was used to understand the magnitude of the efficiency difference. A contained muon-like sample was produced using similar selection criteria to the selection in Section 5.3, with the additional requirement the tracks be muon-like by the NCE analysis PID. To ensure a high purity muon sample a cut of less than 10 on the PID pull applied to the end of the track was used. It was very important to ensure a high purity sample as any particle population differences between data and MC directly shows up as an efficiency difference or cancel a true efficiency difference. For the MC population an equivalent p.o.t. scaled magnet and sand MC were added together. The efficiency difference between MC and data was measured to be 1.33±0.23%, see Table 7.6. For the final cross section result the number of background events removed by the Michel cut (604.34 events) in the MC was increased by 3.1% (43.42%/42.08%) and the new cross section calculated. The fractional change in cross-section was taken as the systematic. The systematic was measured to be 1.0%.

7.1.0.5 Number of Targets

The total number of targets in the detector comes from the total FV mass, 5393.22 ± 0.56 kg multiplied by Avogadro's number to extract the number of target nucleons in the Monte Carlo. The as-built estimations of the target mass are 5460.86± 37.78 and 5480.30± 37.40 for Run 1 and Run 2 respectively [86]. This leads to the Monte Carlo selection being

Table 7.6: Michel tagging efficiency a similar event selection found in Section 5.3 with an additional cut using the NCE analysis PID to ensure a high purity muon-like sample.

Source	Tracks before Michel Cut	Tracks cut by Michel Cut	Efficiency
Run 1+2+Sand MC	148034±384.75	62295.4±249.59	42.08± 0.06%
Run 1+2 Data	10342±101.70	4490±67.01	43.42± 0.22%
Difference			1.33±0.23%

scaled by 1.25%± 0.69% for Run 1 and 1.61%± 0.68% for Run 2. The uncertainty in the total mass and the correction factors lead to a systematic error of 0.7%.

7.2 Physics Systematics

The NEUT Monte Carlo gives a prediction of various interaction modes based on measured cross section values. These cross section values have associated uncertainties which need to be evaluated to understand background variations and signal shape uncertainties. To facilitate this understanding a set of cross section model parameters in NEUT were varied to provide a reweight value for a particular event. A description what reweighting means and the method is found in Section 7.2.1.

These parameter sets were established for the T2K oscillation analyses and as such are focused on CCQE interactions. Some modifications to the parameters were necessary to make them appropriate for the NCE analysis. The "Other NC" category specifically needed special treatment as this normalization parameter scales NCE events in addition to NC multi-pion events. When evaluating the systematic associated with this parameter the true NCE events were forced to a reweight value of 1 while all other events which would have been affected by this parameter were allowed to scale with the nominal reweight value. A new parameter, NCE M_A^{QE} Shape, was added to T2KReweight specifically for this analysis. Unfortunately, due to how NEUT treats the NCE cross section on oxygen the reweighting

infrastructure doesn't treat this target correctly. As will be shown in Section 7.2.2.1, the effect of this parameter is evaluated on two other targets, carbon and copper. The study shows the systematic effect measured is nearly the same for both targets. As a result, until the reweight code is updated to treat the special oxygen case correctly the systematic will be asserted to be the same as carbon and copper.

In addition to uncertainties on the cross-section values in the Monte Carlo there are uncertainties associated with the cascade model which propagates pions from the primary interactions out of the target nucleus. To help understand the uncertainties associated with pion absorption, charge exchange, and scattering, a study was done which looked at parameter variations on the pion cascade model. This type of uncertainty enters this analysis through the signal definition which identifies primary NC pion production as signal if no pions exit the nucleus. An additional parameter investigates pionless delta decay where a delta particle from resonant production is absorbed in the nuclear medium without decaying.

7.2.1 Reweight Method

A full production of MC to produce the final cross section result takes weeks of processing on thousands of CPU cores. To evalute each model parameter, such as M_A^{QE} or M_A^{Res} for instance, the full MC production would have to be run at minimum two extra times per variable change. Even with a single parameter this type of computing becomes prohibitively costly in terms of computing resources as well as personnel resources. To get around this issue a central group of people in the collaboration instead run small MC productions modifying each parameters and develop response functions as a function of various parameters, such as Q^2 or neutrino energy. These response functions tell the analyst how much to reweight each particular event. Initially all events have a weight of 1. Depending on the systematic error variable being evaluated this weight can be changed from 1, either up or down. Having a weight which is not equal to one means the analysis would have picked up some percentage more or less of this particular event if the MC had been rerun.

Some types of systematic error parameters are simple normalization errors which just means the entire pool of events of a certain type, say CCQE resulting from neutrinos with energies lower than 1 GeV, are increased/decreased by 30%. Some error types are shape and normalization errors, such as M_A^{QE}. In this case the total number of CCQE events can be either raised or lowered and the distribution of events as a function of Q^2 will change. Some error types are shape-only errors, such as M_A^{NCE}. In this case the total cross section (number of events) is kept constant but the distribution of events is changed to evaluate how sensitive the selection, and thus efficiency, is to a different distribution of events.

Because there are shape plus normalization and just purely normalization parameters care has to be taken when evaluating errors and these parameters will have corrections or anti-correlations which need to be taken into account accordingly. In addition, some parameters have to be carefully evaluated due to underlying assumptions when making the response functions. Typically, the analyst has to pay attention to parameters which were developed to change the normalization of some type of interaction, say NCE. When evaluating systematic errors you do not want to evaluate the normalization error of your signal events as this is what the measurement is trying to determine!

7.2.2 Cross-section Model Uncertainties

To understand the effect of cross section model uncertainties on the backgrounds and signal shape, various parameters have been modified to understand the systematic effect they have on the final cross section. In Table 7.7 the various parameters are listed with the central values and variation amount. Total error is estimated by adding the listed parameter's effect of the cross section in quadrature with some correlation correction for correlations between M_A^{RES}, NCπ^0 normalization, CC resonant low energy normalization parameters. The total error is estimated to be +14.3%, -16.6%.

Numerous parameters in Table 7.7 are just normalization parameters, but M_A^{QE} and M_A^{RES} are both shape plus normalization. As a result, these two parameters are correlated

Table 7.7: Systematics table of cross-section model uncertainty with central values and 1σ variations

Parameter Name	**Central Value**	**Error**	**Sys. Error**
M_A^{QE}	1.21 GeV^2	0.45 GeV^2	+5.84, -7.47 %
M_A^{RES}	1.16 GeV^2	0.11 GeV^2	+3.64, -4.05 %
Spectral Function	off	on	4.69 %
Fermi Momentum(C)	217 $\frac{\text{MeV}}{\text{c}}$	30 $\frac{\text{MeV}}{\text{c}}$	+0.34, -0.32%
CC Resonant Low Energy Norm.	1.63	0.43	±3.07 %
CC Resonant High Energy Norm.	1	0.4	±0.24 %
CCQE Low Energy Norm.	1.0	0.11	±2.49%
CCQE Medium Energy Norm.	1.0	0.3	±0.09%
CCQE High Energy Norm.	1.0	0.3	±0.02%
CC DIS Norm.	1	0.4	±0.33%
CCν_e Norm.	1.0	0.03	±0.16%
CC Coherent Norm.	1.0	1.0	±0.20%
NCπ^0 Norm.	1.19	0.43	+6.97, -7.64 %
NCOther Norm.	1.0	0.3	±1.08%
NC1π^+ Norm.	1.0	0.3	+3.35, -3.47 %
NC Coherent Norm.	1.0	0.3	±0.57%
NCE M_A^{QE} shape only	1.0	0.37	+1.73, -1.78%
W Width	87.7	45.3	+0.29, -0.58%
Pionless delta decay	0.2	0.2	+8.08, -10.09%
Total			+14.3%, -16.6%

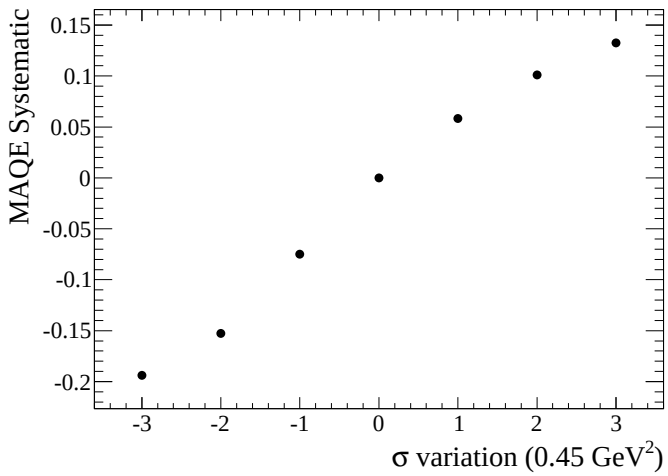

Figure 7.15: M_A^{QE} T2KReweight parameter variation and fractional change in the cross section.

with various other normalization parameters. A correction has been applied based on a covariance matrix provided by the group responsible for the response function production.

To understand how each parameter affects the background and efficiency predictions of the simulation each parameter was varied by up to $\pm$ 3 σ, except for the spectral function which only was varied to "on". After each variation the events were reweighted according to the T2KReweight package and the standard event selection was performed. The efficiency and background prediction were then applied to nominal selection as in Section 8.1 and a flux-averaged cross-section was measured. This cross-section was then compared to the nominal value. The percentage change for the $\pm$ 1 σ variations is calculated for each parameter seen in Table 7.7.

The main purpose of the larger variations was to investigate if there were any large non-linearities as the the parameters were varied. Each parameter varied is shown in Figures 7.15 to 7.33.

It should be noted all external backgrounds were fixed to a reweight value of 1 and scaled by the data driven scaling factor measured in Section 7.2.3.

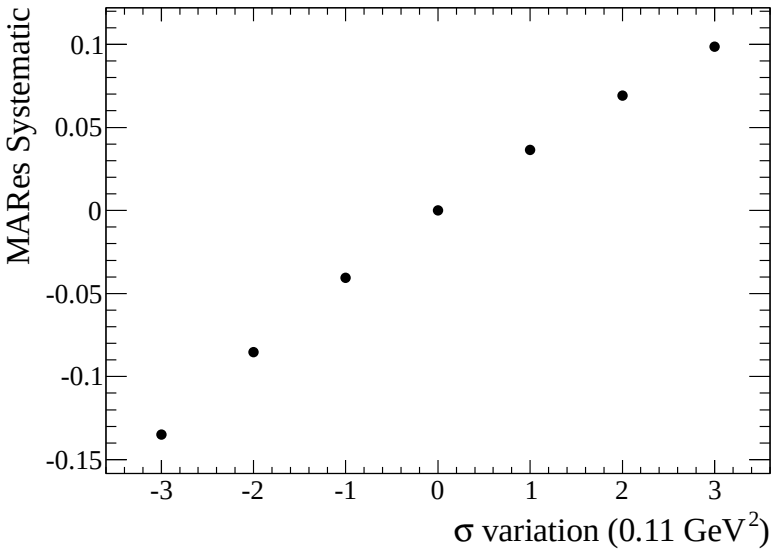

Figure 7.16: M_A^{Res} T2KReweight parameter variation and fractional change in the cross section.

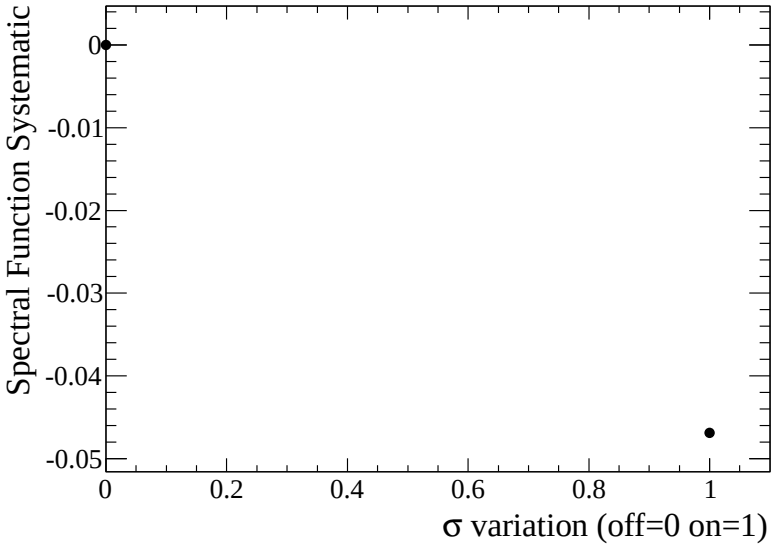

Figure 7.17: Spectral function T2KReweight parameter variation and fractional change in the cross section.

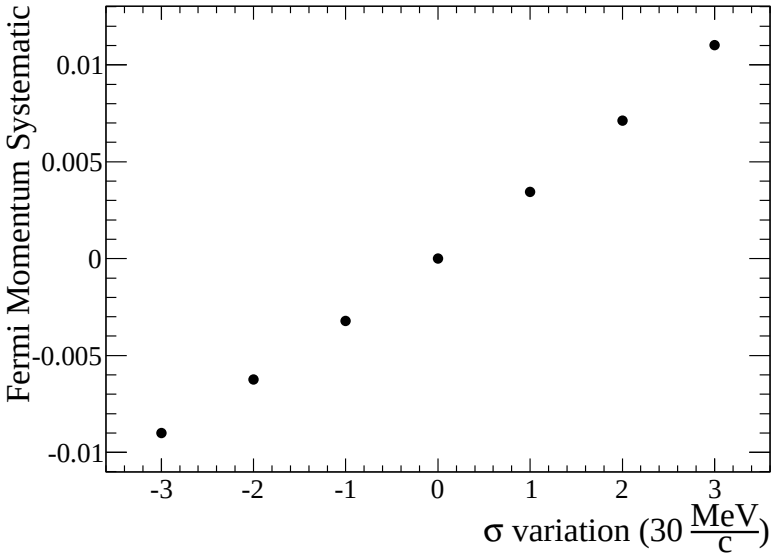

Figure 7.18: Fermi momentum T2KReweight parameter variation and fractional change in the cross section.

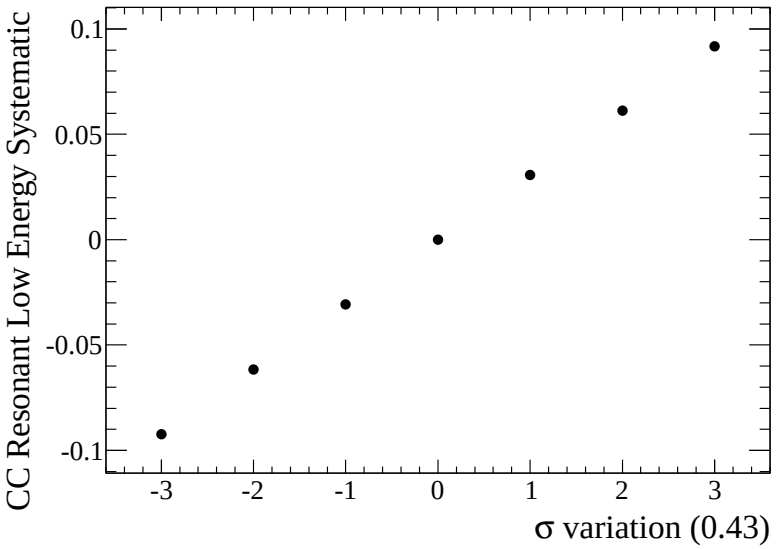

Figure 7.19: CC resonant production low energy normalization T2KReweight parameter variation and fractional change in the cross section.

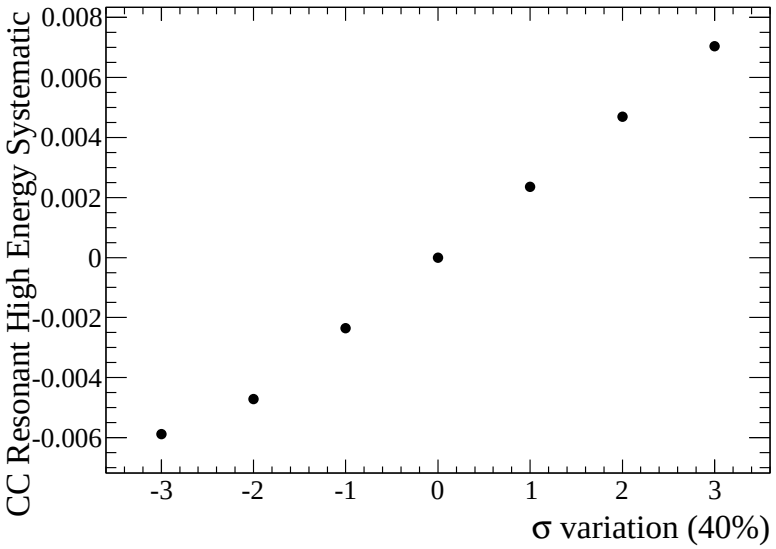

Figure 7.20: CC resonant production high energy normalization T2KReweight parameter variation and fractional change in the cross section.

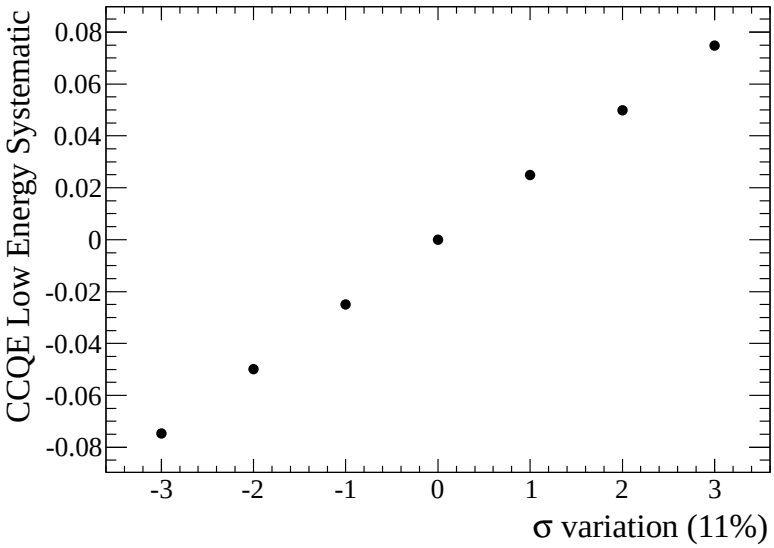

Figure 7.21: CCQE low energy normalization T2KReweight parameter variation and fractional change in the cross section.

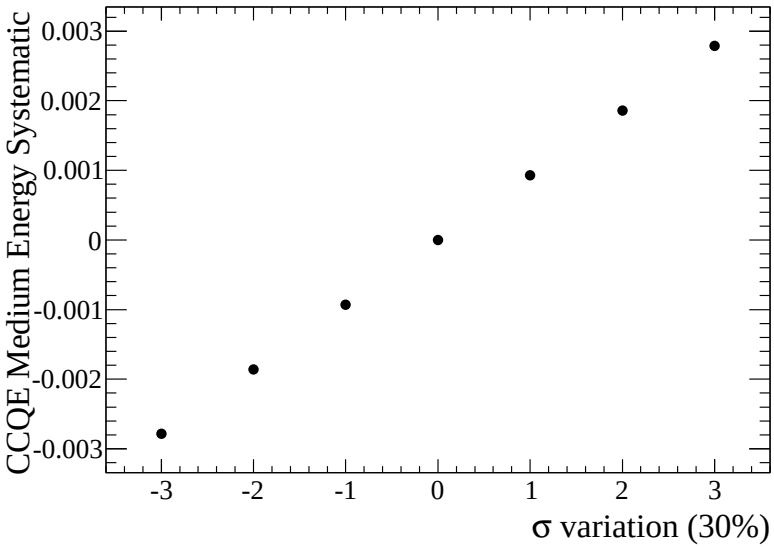

Figure 7.22: CCQE medium energy normalization T2KReweight parameter variation and fractional change in the cross section.

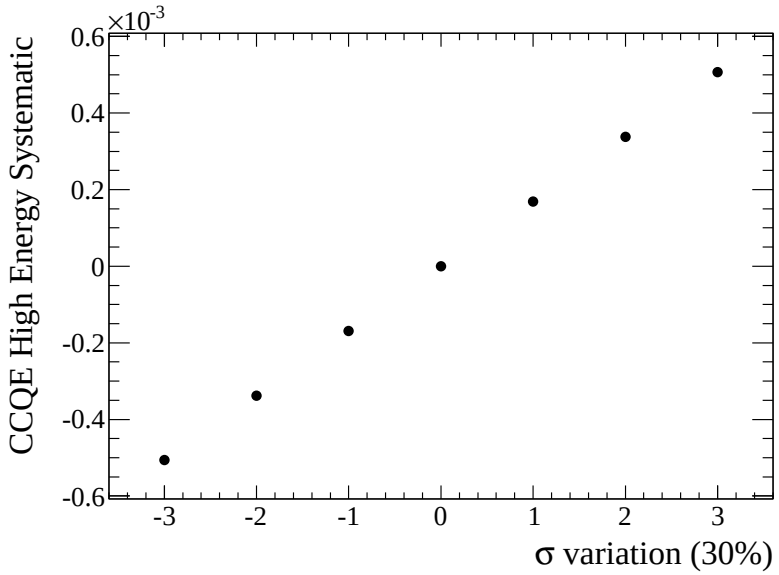

Figure 7.23: CCQE high energy normalization T2KReweight parameter variation and fractional change in the cross section.

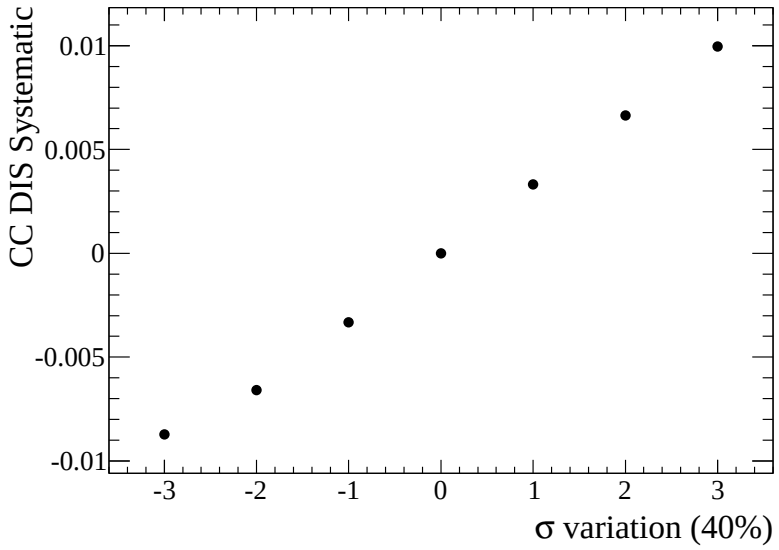

Figure 7.24: CC DIS normalization T2KReweight parameter variation and fractional change in the cross section.

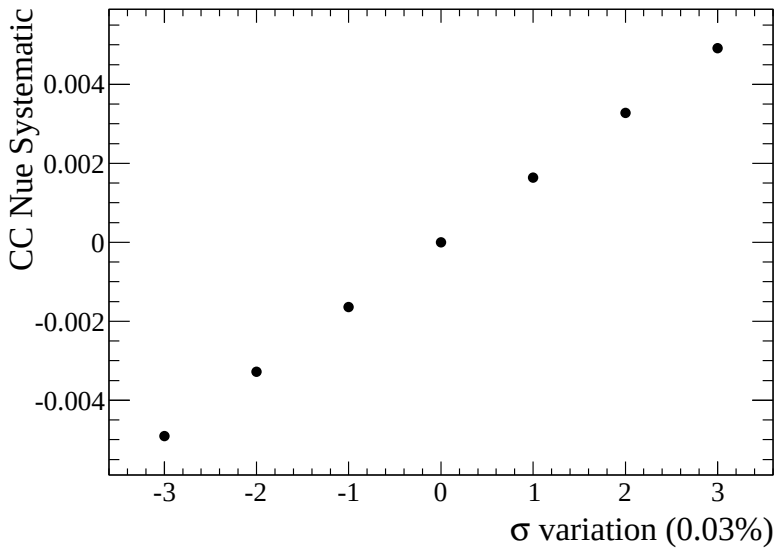

Figure 7.25: CC ν_e normalization T2KReweight parameter variation and fractional change in the cross section.

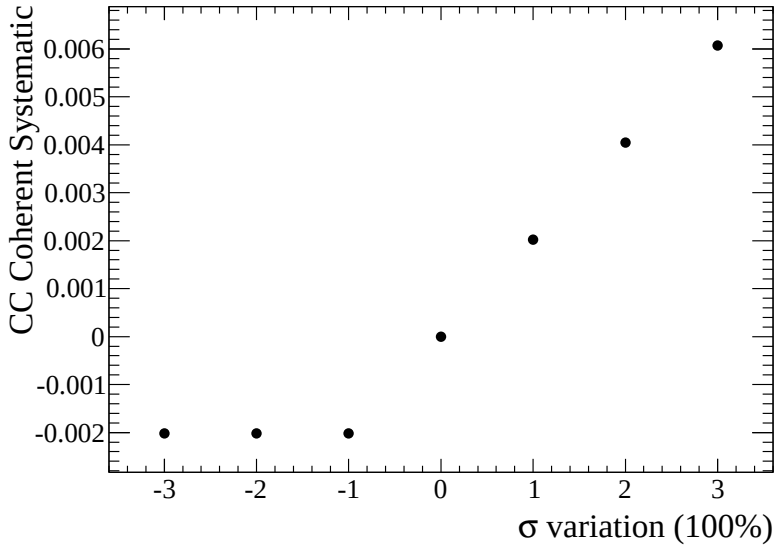

Figure 7.26: CC coherent normalization T2KReweight parameter variation and fractional change in the cross section. The truncation at -2 and -3 sigma is to avoid negative cross sections since the variation for this parameter is 100%.

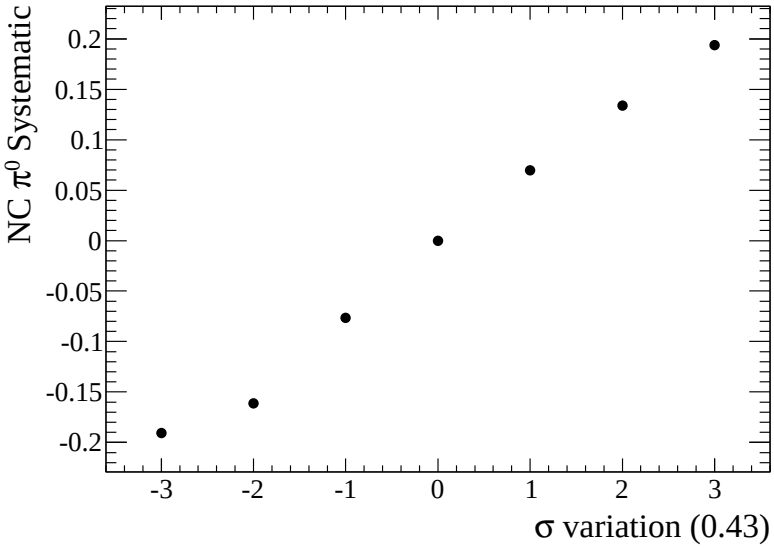

Figure 7.27: NC π^0 normalization T2KReweight parameter variation and fractional change in the cross section.

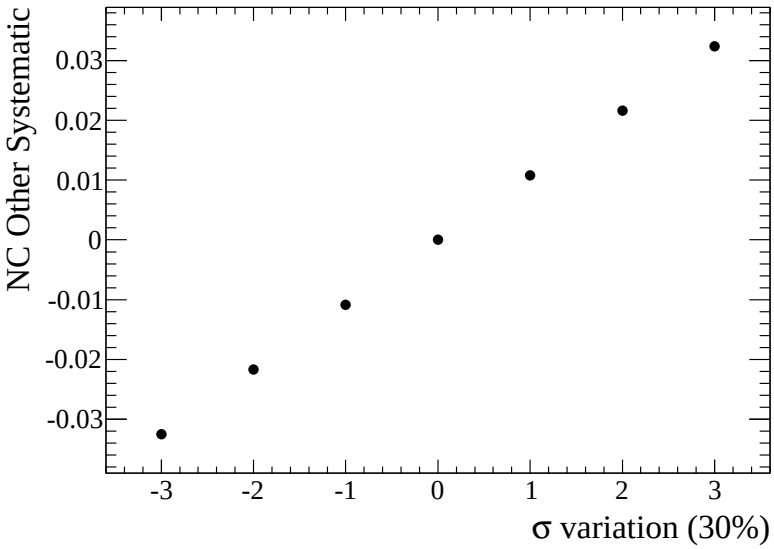

Figure 7.28: Other NC normalization T2KReweight parameter variation and fractional change in the cross section.

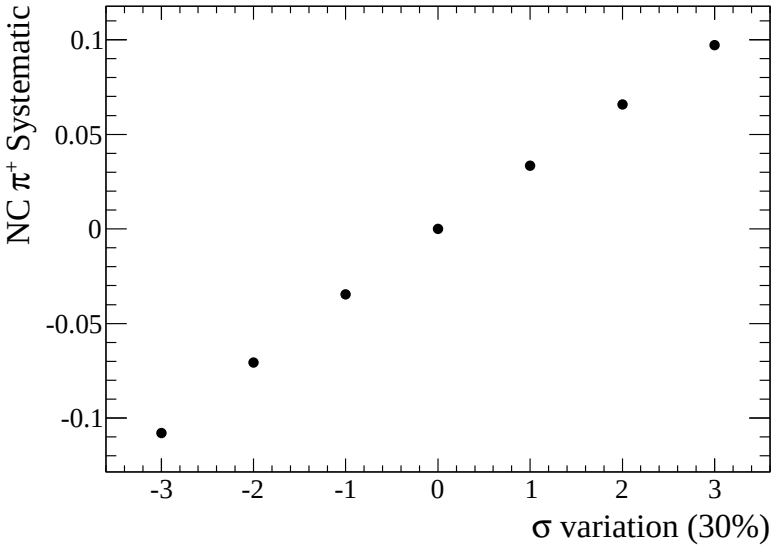

Figure 7.29: NC π^+ normalization T2KReweight parameter variation and fractional change in the cross section.

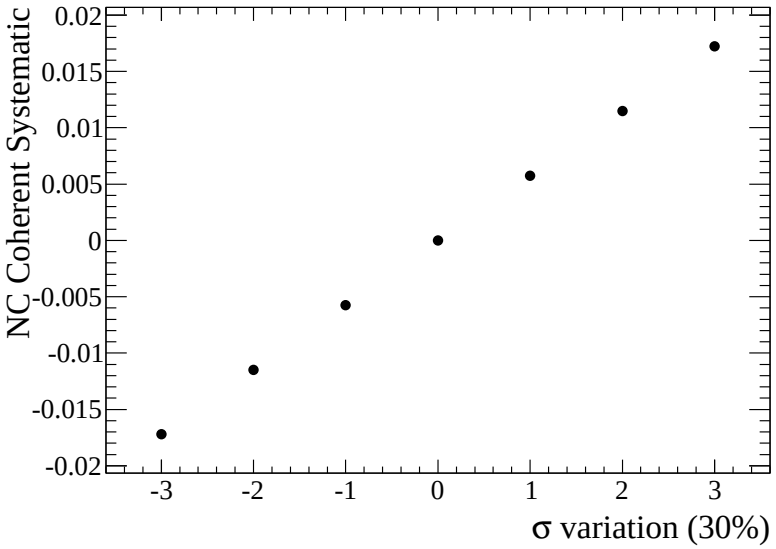

Figure 7.30: NC coherent normalization T2KReweight parameter variation and fractional change in the cross section.

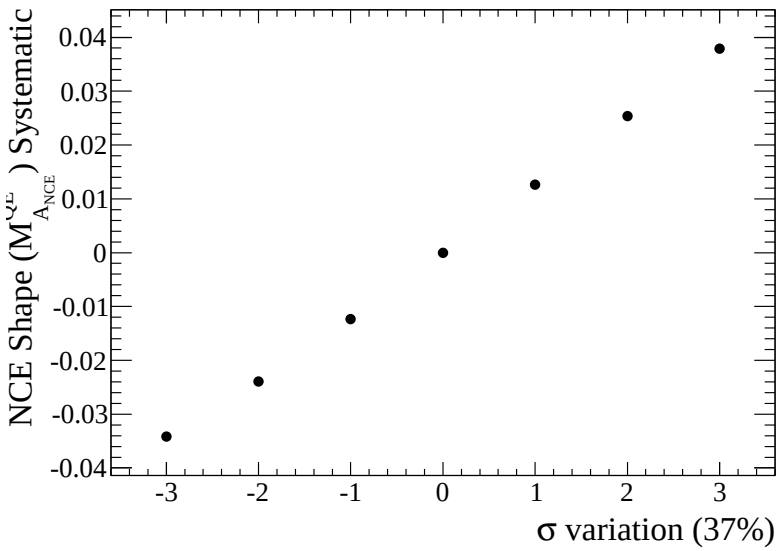

Figure 7.31: NCE M_A^{QE} Shape Only T2KReweight parameter variation and fractional change in the cross section.

7.2.2.1 NCE M_A^{QE} Shape Only

A new reweight parameter was added to T2KReweight to allow for variation of the NCE signal shape to understand possible efficiency systematics. This parameter is able to vary the M_A^{QE} shape correctly for all nuclear targets except for oxygen. Oxygen is a special case in NEUT, because this is the target material in SK, where the cross section is calculated with a spectral function. For all other nuclei the NCE cross section is calculated as a scaled version of the CCQE cross section. The NCE analysis has three primary interaction targets, carbon, oxygen and copper. The carbon and copper systematics were investigated separately with the intention of asserting the oxygen systematic is of the same size as the other two, if carbon and copper show similar systematics.

To understand the size of the systematic the NCE shape parameter was varied for events on carbon and copper separately. For each variation of the shape parameter the carbon cross section was calculated using the nominal flux prediction, exposed p.o.t., and nominal number

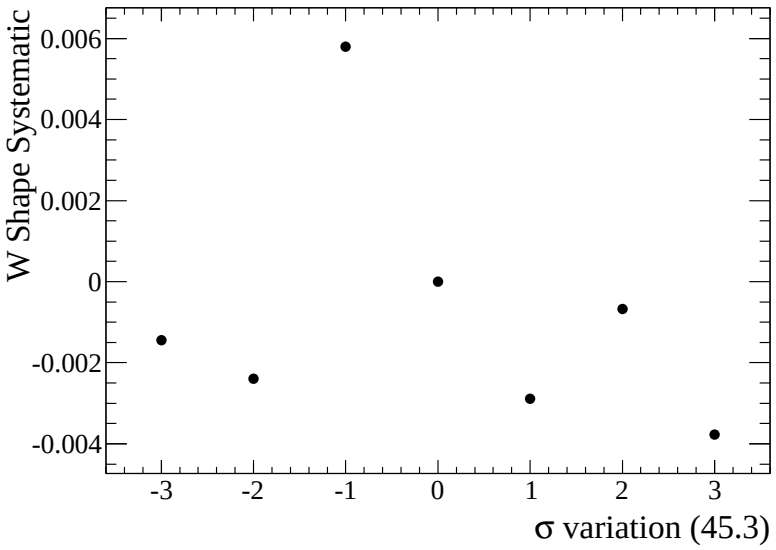

Figure 7.32: W shape T2KReweight parameter variation and fractional change in the cross section.

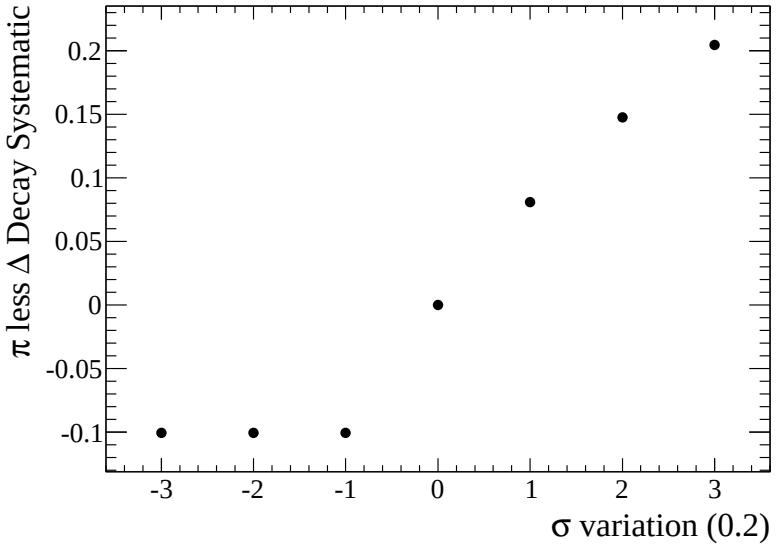

Figure 7.33: Pionless delta decay T2KReweight parameter variation and fractional change in the cross section.

of targets in the fiducial volume and finally corrected by the fraction of the total fiducial volume which is carbon, or 50.93%. The measured cross section was 1.83×10^{-39} cm^2/nucleon. The same procedure was applied to the copper events, 13.86% of the total fiducial volume, where a cross-section of 1.97×10^{-39} cm^2/nucleon was measured. The 8% difference in cross-section comes from the fact carbon has a Z=6 and A=12, while Copper has a Z=29 and A=63 which corresponds to 8% higher neutron fraction. In addition the cross sections are lower than the nominal MC cross section reported in Chapter 8 due to the target normalization used in this study. While the MC provides the exact target of the neutrino interaction the material list of the P0D used for this measurement uses materials such as scintillator (CH_2), water (H_2O). When the number of targets was calculated for this study the fraction of the total fiducial volume mass which was scintillator was used. Because the MC target doesn't include the two hyrogen atoms but the target correction does there is a reduction of the central value of the cross section. Since the fractional change between variations is small the second order effects from the shift in the central value are even smaller.

The systematic measured on carbon was measured to be +1.73%,-1.78%. The systematic on copper was measured to be +1.15%,-1.18%. These systematics are of a similar size and as a result the oxygen systematic will be asserted to be of the same size. The final total systematic is +1.73%,-1.78% to ensure the error spans the largest envelope and target.

7.2.2.2 Pionless Delta Decay

The final state NCE sample is quite sensitive to the pionless delta decay parameter. A large uncertainty of 100% is used for this dial. This variation causes events to either be given a weight of 2 or 0 for a positive or negative variation of the dial (total resonant cross section is preserved by scaling resonant events which do not undergo a pionless delta decay). This results in large flucuations in the number of signal events as many of the signal events come from resonant processes with no resulting pions. Because of these large variations in events,

the efficiency correction for the cross section calculation undergoes a change of 6-8%. The background provides an additional 2% variation.

7.2.2.3 Pion Cascade Uncertainties

This systematic investigates the effect of pion reinteractions in the target nucleus after the initial neutrino interactions. A study was performed looking at pion-carbon scattering to constrain each possible reinteraction mode. The modes investigated are: absorption (FSIABS), low energy quasi-elastic scattering with charge exchange (FSIQE), charge exchange branching ratios (FSICX), high energy quasi-elastic scattering (FSIQEH), high energy charge exchange (FSICXH) and pion production (FSIINEL). A total of 16 parameter sets were chosen to span the "1 sigma" contour of pion reinteraction space. The values used in this study are found in Table 7.8. Figure 7.34 shows graphically the systematic variation in the total cross section. Figure 7.35 shows the calculated systematic for each of the 16 values with respect to the reference nominal value. The nominal value is represented in the first bin and the systematic only uses bins 9 to 24 (last 16 bins). These bins parameter sets were determined to cover the required phase space in the initial study [90]. To calculate the total systematic for pion reinteractions in the target nucleus Equation 7.1 is used.

$$\sigma_{sys} = \sqrt{\frac{1}{16}\sum_{i=0}^{16}(\sigma_i - \sigma_{nom})^2} \tag{7.1}$$

While the final systematic is 2.3%, there should be some concern that the initial study only used pion scattering data for carbon while the PØD has multiple nuclear targets. The most dominant interaction target, not including external backgrounds, according to the MC is carbon(44%) followed by oxygen(28%) and copper(12%). Carbon and oxygen only differ by 4 nucleons which should translate into a similar set of cross sections used in the initial study.

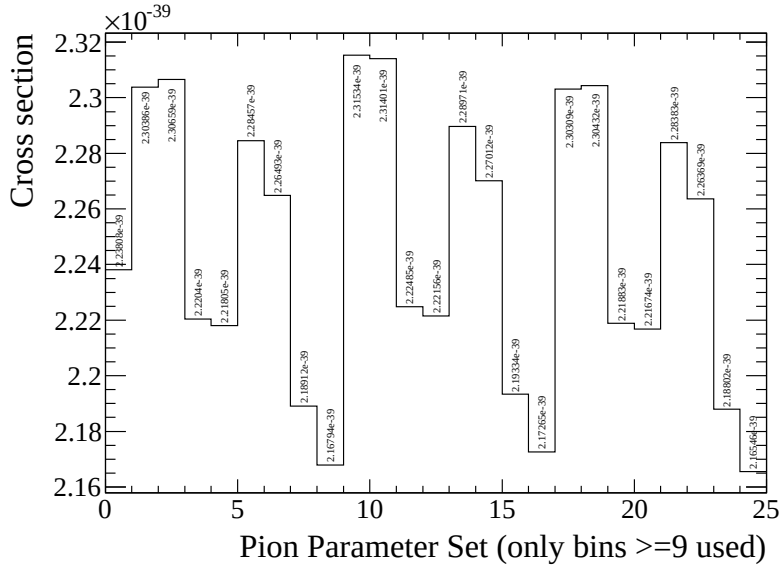

Figure 7.34: Variation in the calculated cross section for all parameter sets. Only the last 16 bins are used in the systematic. The first bin is the nominal cross section.

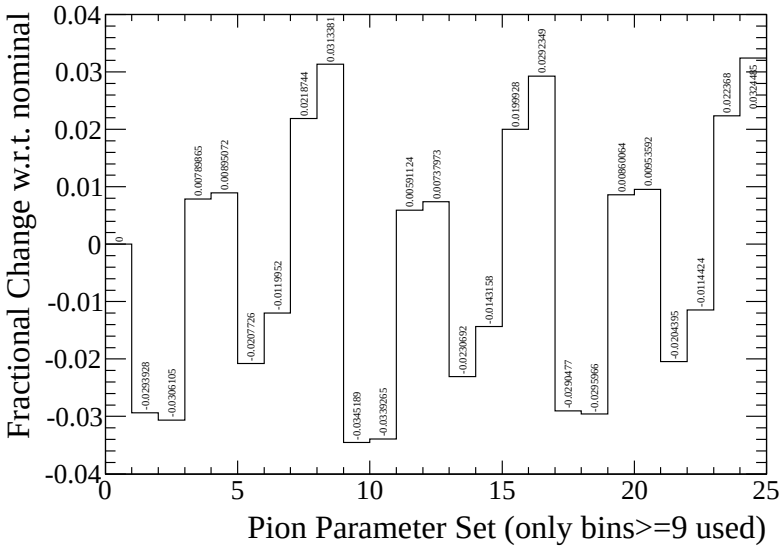

Figure 7.35: Fractional change of the cross section with respect to the nominal cross section. Only the last 16 bins are used in the systematic. The first bin is the nominal cross section.

Table 7.8: Pion FSI parameter sets used for FSI study, found in [90]. These parameters sets correspond to the last 16 bins found in Figure 7.35.

Para. set	**FSIQE**	**FSIQEH**	**FSIINEL**	**FSIABS**	**FSICX**	**FSICXH**
Nom.	1.0	1.8	1	1.1	1.0	1.8
15	0.6	1.1	1.5	0.7	0.5	2.3
16	0.6	1.1	1.5	0.7	1.6	2.3
17	0.7	1.1	1.5	1.6	0.4	2.3
18	0.7	1.1	1.5	1.6	1.6	2.3
19	1.4	1.1	1.5	0.6	0.6	2.3
20	1.3	1.1	1.5	0.7	1.6	2.3
21	1.5	1.1	1.5	1.5	0.4	2.3
22	1.6	1.1	1.5	1.6	1.6	2.3
23	0.6	2.3	0.5	0.7	0.5	1.3
24	0.6	2.3	0.5	0.7	1.6	1.3
25	0.7	2.3	0.5	1.6	0.4	1.3
26	0.7	2.3	0.5	1.6	1.6	1.3
27	1.4	2.3	0.5	0.6	0.6	1.3
28	1.3	2.3	0.5	0.7	1.6	1.3
29	1.5	2.3	0.5	1.5	0.4	1.3
30	1.6	2.3	0.5	1.6	1.6	1.3

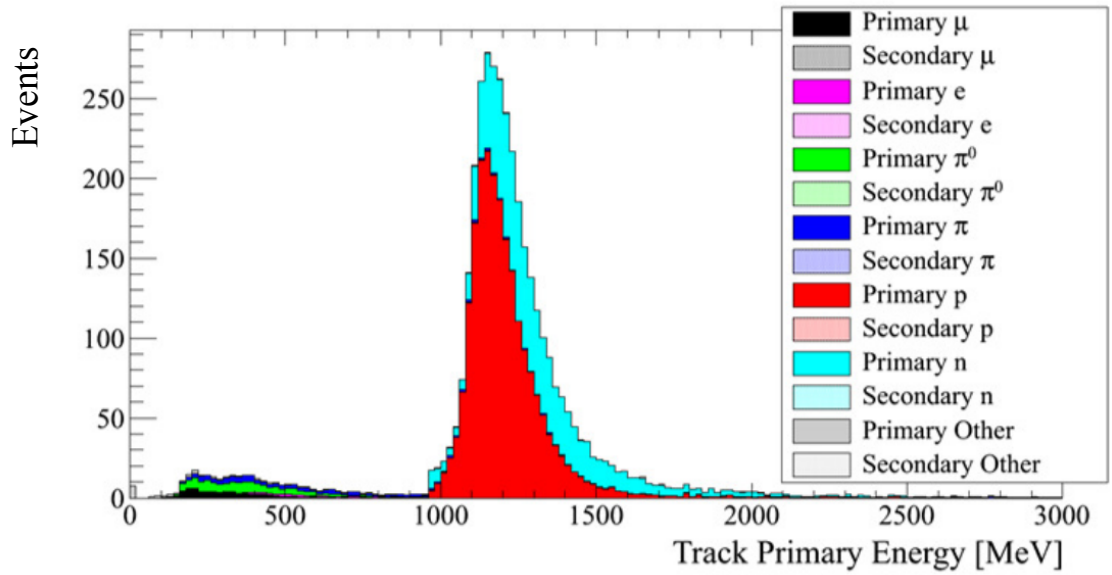

Figure 7.36: Distribution of truth matched primary particles' energy after the full event selection. All particles are matched by the highest charge contributor at the downstream end of the track.

7.2.2.4 Secondary Interactions

The ND280 MC uses the GEANT4 simulation package to propagate the outgoing particle from the target nucleus through the detector materials. As with any simulation package, GEANT uses models which may differ from the measured data for a particular process. This systematic investigates the effect of the difference between the cross section models and data concerning the propagation of the protons and neutrons through the detector.

To understand what energy range is applicable for this study the true primary particle energies have been plotted for the selected NCE events, see Figure 7.36. The particles shown are matched to the dominant charge deposition contributor at the downstream node of the reconstructed track. Based on this distribution the applicable kinetic energies for the protons and neutrons ranges from ∼0.1-1 GeV.

A second investigation into the selected protons looks at how often the protons reinteract in the MC. To look at this, the difference between the primary proton energy and the proton

matched at the end of the track is compared. Only 15% of the primary protons experience any energy loss due to elastic or inelastic scattering. As a result, this systematic study will focus on the more important issue of secondary proton production from neutrons. A difference between the model used by GEANT and data can affect the cross section measured in two ways; the selection's background estimation and the signal efficiency.

The signal definition for this analysis is any neutrino event in which no mesons or leptons (other than a ν_μ) are exiting the nucleus. These events must occur in the fiducial volume. This means if a NCE event produces a neutron in the fiducial volume and the neutron reinteracts within the fiducial volume the event is considered a signal event. A difference in the neutron inelastic cross section between the simulation and data could cause some of these neutron events to either be over predicted or under predicted.

The background estimation is sensitive to differences between the simulation and data in two ways. First, a neutron produced in an NCE interaction outside the fiducial volume can interact inside the fiducial volume to produce an apparent NCE event. Second, any other neutrino interaction in the PØD that produces a neutron can lead to a secondary interaction in the detector that results in a reconstructed proton in the fiducial volume.

The external events which are constrained by the data fit, see Section 7.2.3, do not need to have this study applied to them since the fit constrains the simulation to the data. As a result, these events will be considered a constant background while the two background cases and the signal case will be modified by the data/simulation differences.

To get an estimation of the size of the difference, GEANT validation plots have been used, see [91]. The GEANT collaboration provides a few validation plots comparing data from the Dubna and IHEP experimental databases compared to various cross section models in the GEANT package. Validation was performed on carbon and lead targets. The total neutron cross section on these targets can be seen in Figures 7.37 and 7.38. The inelastic component of the cross section for neutrons can be seen in Figures 7.39 and 7.40. The ND280 MC uses the QGSP_BERT physics list which uses the Bertini intranuclear cascade model in

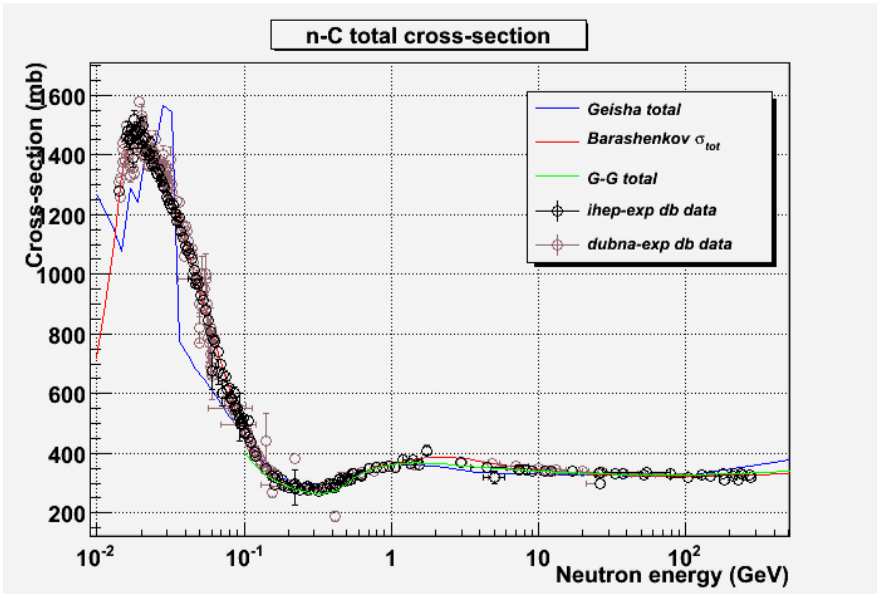

Figure 7.37: GEANT validation plot of neutrons on carbon total scattering cross section. [91]

this energy range. For hadronic inelastic interactions this physics list uses the Barashenkov pion cross section table and the Axen-Wellisch(G4HPW-Axen prod) parameterization for protons and neutrons.

Based on these plots a 10% uncertainty is asserted on the neutron to proton cross section. Table 7.9 shows the p.o.t. -normalized event rate for the three event categories described above and provides the scaled MC external background event rate. Based on the events in Table 7.9 the cross section, using N_{sel} from data and the MC prediction for the efficiency, flux, and background, is recalculated varying the number of events in the signal efficiency (line 1 in Table 7.9) and background prediction(lines 2+3 in Table 7.9) by $\pm 10\%$. In the end the cross section varies by 2.5% which is the systematic assigned.

7.2.3 Outside Background Estimation

About 30% of the background in this measurement comes from external interactions in the magnet and sand which produce neutrons of sufficient energy to produce secondary protons with no other visible signature in the detector. Neutron backgrounds are difficult to

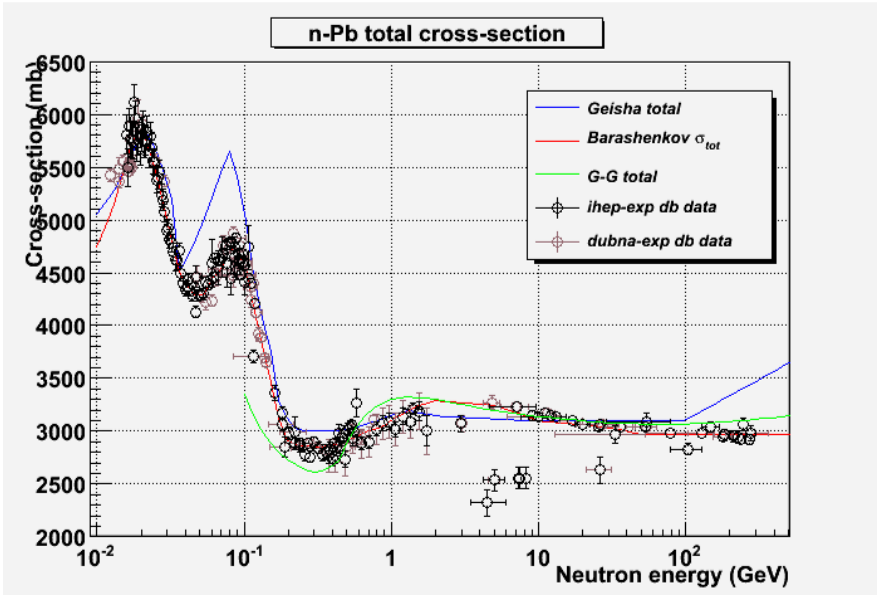

Figure 7.38: GEANT validation plot of neutrons on lead total scattering cross section. [91]

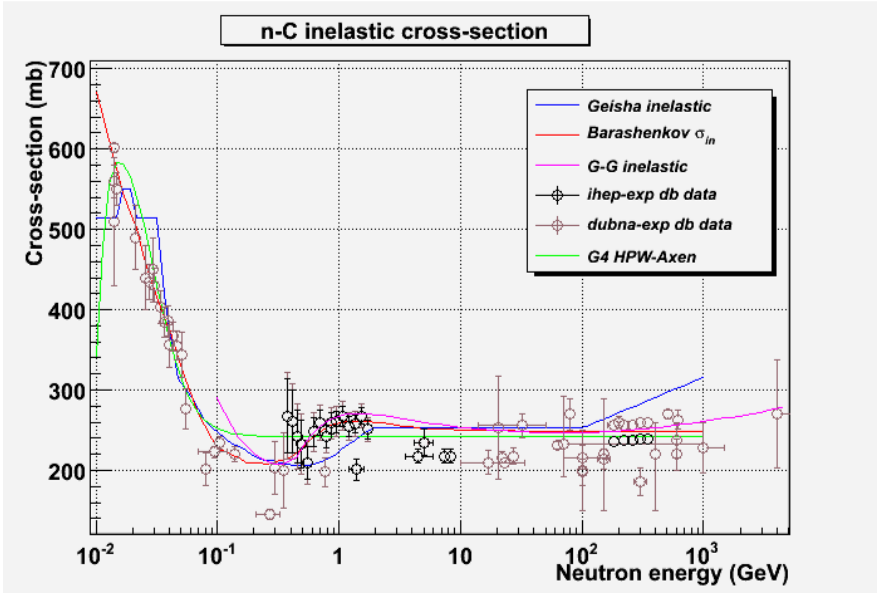

Figure 7.39: GEANT validation plot of neutrons on carbon inelastic scattering cross section. [91]

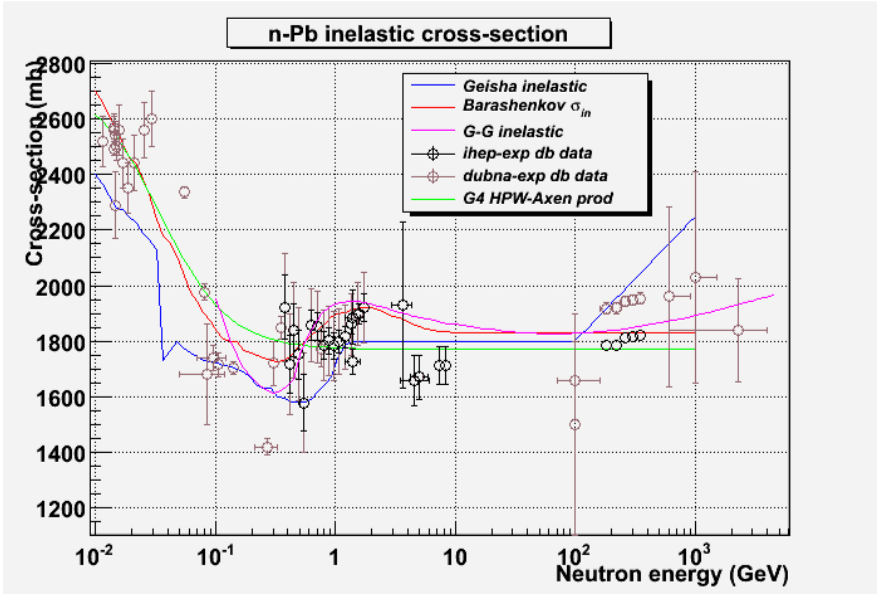

Figure 7.40: GEANT validation plot of neutrons on lead inelastic scattering cross section. [91]

Table 7.9: The p.o.t. normalized event rates for the signal and background categories. Each category has the number of primary neutrons associated with the reconstructed particle.

Category	**Sample**	**Total events**	**Primary neutrons**
Signal efficiency	NCE signal events in FV	1714.69	199.12
Background prediction	NCE outside FV	170.62	127.935
Background prediction	Other bkg neutrino events	1336.48	114.26
Background measured	Data driven background	508.84	N/A

simulate as the overall normalization of nucleons produced in neutrino interactions is not well known. NEUT is known to produce more neutrons when compared to GENIE's prediction, as neutrons are not very important to the simulation in a water Cherenkov detector as the secondary protons are usually below threshold.

The input hits for the clustering algorithm described in Section 5.5 have a 15 PEU threshold applied, instead of the standard PØD reconstruction cleaning algorithm, to avoid the charge simulation issues described in Section 5.6. Figure 7.41 shows a scan of the fitted result for various charge thresholds. The features seen below ∼7 PEU are mostly from dark noise effects but do not affect the result at the 15 PEU level. In addition to a higher threshold, a ±0.5 PEU variation in the MC is introduced to account for time variation of the charge over time in the data. This variation was chosen to be in line with the time variation of the MIP scale in the PØD.

For a cluster to make it into the analysis sample it must pass the following criteria:

1. Good PØD/Magnet data quality and beam spill flags
2. Cluster must be found in integration cycle 4 (first beam bunch)
3. Be downstream of the USEcal to avoid large data/mc shape difference. See Figure 7.42
4. Be upstream of the last 2 PØDules to ensure containment
5. Require the cluster to be 6 bars away from the edge of the PØD
6. The current bunch cannot have any reconstructed tracks or showers

   -There seems to be a difference in MC and data with muon tracks which produce delta rays based on looking at event displays
7. No clusters in the current bunch can be within 6 bars of the edge of the P0D

The analysis only uses events in the first beam bunch to avoid effects from prior bunches with delayed interactions. A selection could instead use a selection criteria where the prior

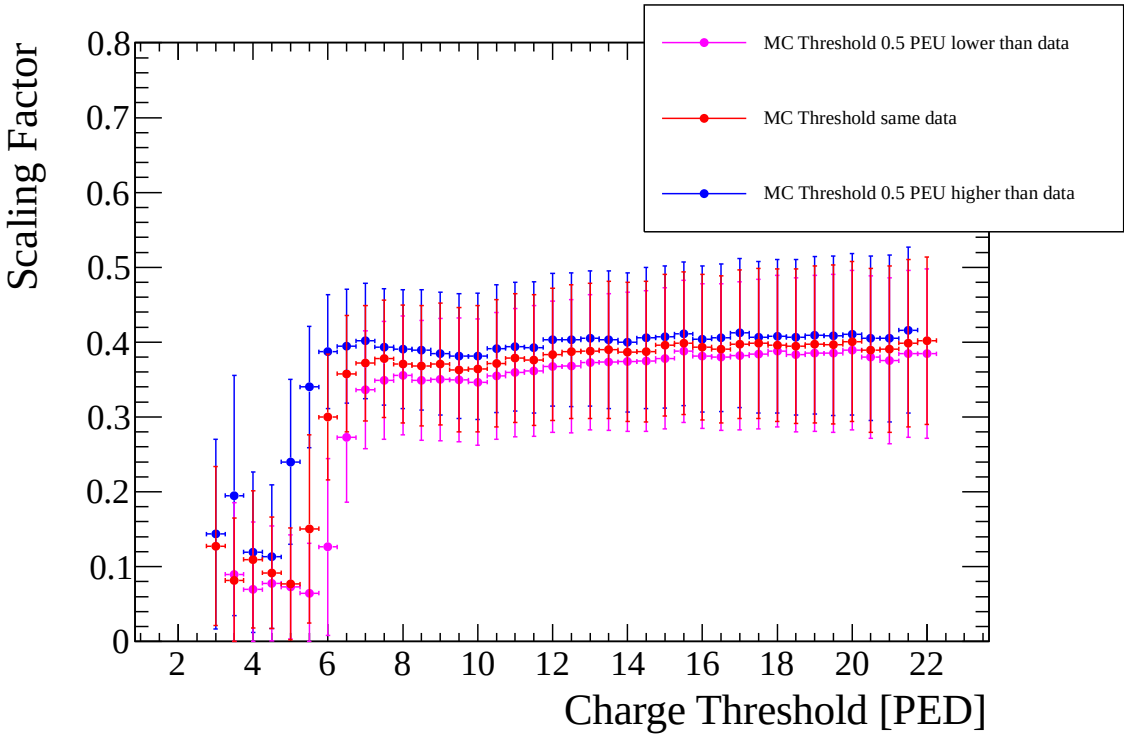

Figure 7.41: Scaling factor fit result with full systematic and statistical errors for various charge thresholds.

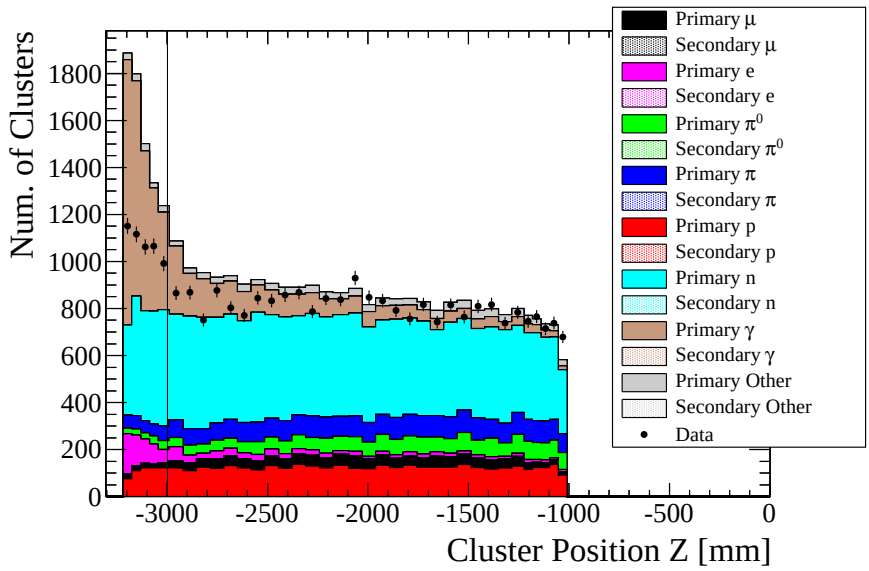

Figure 7.42: Cluster position binned in Z. A large shape difference is visible in the USEcal (Z<-3000 mm). The MC has been normalized to data above 3000 mm to amplify the shape difference in the USEcal.

beam bunches do not have any reconstructed objects, but this could lead to systematic differences between reconstruction efficiencies and cross section models. By only using the first bunch these differences can be minimized. The selection also avoids events where there is activity near the edge of the detector. This is done because the selection uses 2-dimensional clusters, which means a penetrating particle, such as a muon, can produce a hit in the middle of the detector in one view and near the edge in the other view.

To ensure the analysis is scaling the proper particles an analysis of the particle types which cause the external backgrounds in the NCE analysis has been done. The predicted outside background (Table 7.10) in the physics sample is dominated by neutrons, 63%, with a sub-component of charged pions, 16%, protons, 14.3%, pi-zeros, 3.4%, muons, 0.5% and gammas, 2.3%. The cluster sample has a slightly different prediction, see Table 7.11, which is still dominated by neutrons, 44%, with a sub-component of charged pions, 9.3%, protons, 17.3%, pi-zeros, 5.9%, muons, 6% and gammas, 3.9%. The largest difference between the two

Table 7.10: Primary particle breakdown for the external backgrounds in the NCE selection.

Particle Type	Fraction
n	63%
p^+	14.3%
$\pi^\pm$	16%
π^0	3.4%
γ	2.3%
μ^-	0.5%

Table 7.11: Primary particle breakdown for clusters found by the clustering algorithm.

Particle Type	Fraction
n	44%
p^+	17.3%
$\pi^\pm$	9.3%
π^0	5.9%
γ	3.9%
μ^-	6%

samples is the muon component. As a result, the outside muon sample will be considered a background to this measurement.

To extract an outside background scaling factor the cluster Y position histogram, shown in Figure 7.43, is fit, varying each background (NCE, CCQE, other, and outside muons) by a separate normalization uncertainty of 30% for a total of four background scaling factors. The value of 30% was choosen based on the general size of the BANFF cross section normalization uncertainties. In the cases in which the normalizations were defined by neutrino energy the highest uncertainty was used.

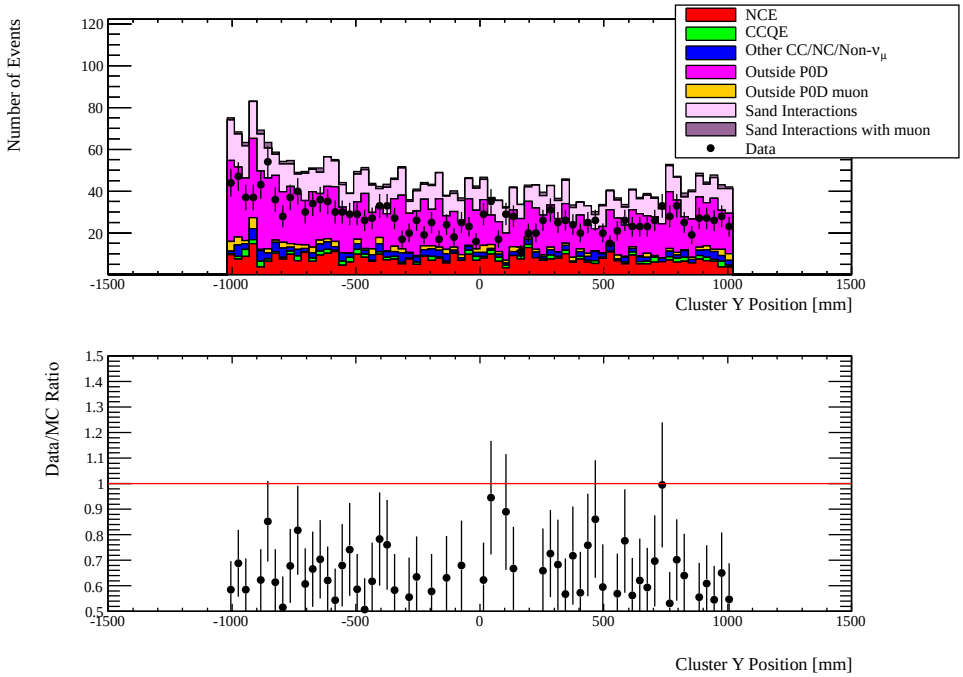

Figure 7.43: Input histogram into the fit. Y position of clusters.

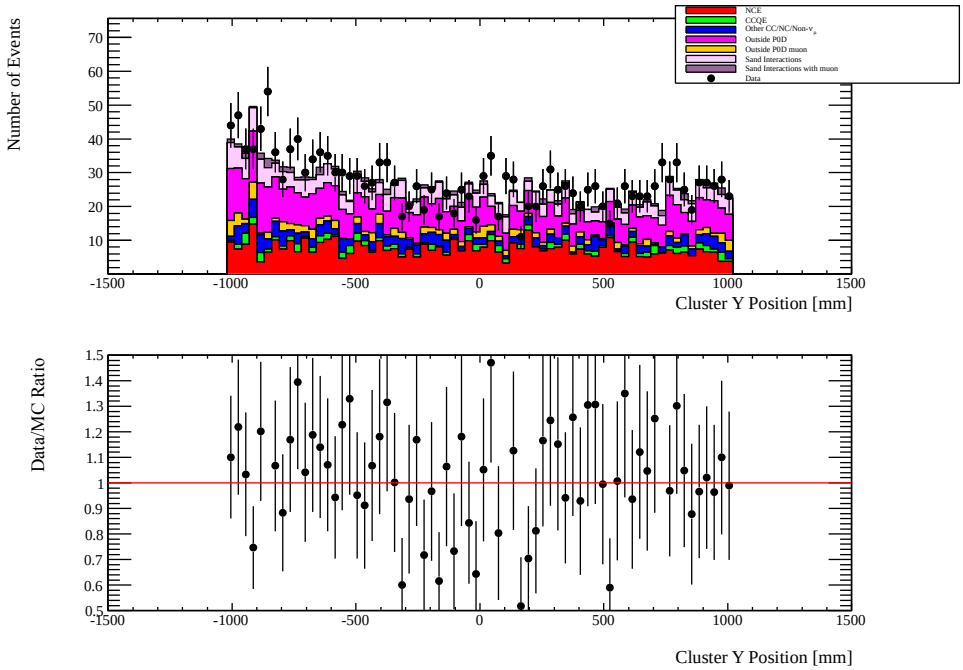

Figure 7.44: Input histogram with scaling factor applied after the fit. Y position of clusters.

A total of 10,000 throws on the normalization parameters were performed and for each throw the χ^2 was minimized for the outside background scaling factor.

$$\chi^2 = \sum_i \frac{(B_i + C \times S_i - \bar{x}_{data,i})^2}{\sigma^2_{data,i}} \tag{7.2}$$

The scaling factor C was fit for each throw with the B_i and S_i being the total background after the four normalization factors are applied and total signal in the ith bin. The $\bar{x}_{data}$ and σ_i variables represent the central value and statistical error for the ith bin in the data.

The extracted outside background scaling factor distribution is seen in Figure 7.45 which when fit with a Gaussian gave a mean scaling factor of 0.396 with a sigma of 0.076. The mean value was applied to the outside background component of the MC and the sigma, in combination with the fit error, was propagated as the error. This resulted in an outside scaled background of 509 ± 122 events, which resulted in a systematic error of 6.4%.

7.2.3.1 Cross Check

A simple cross check has been done to make sure the results of this study do not over correct the MC prediction. A sample of proton-like tracks originating in the USEcal was chosen as a sideband sample to test the effects of the extracted scaling factor. The tracks are selected using the same cuts as the primary analysis with a variation on the Z FV definition. Tracks originating in the most upstream or downstream P0Dule in the USEcal are rejected, which leaves just 5 P0Dules with the lead radiators as targets. Figure 7.46 demonstrates the effect of the scaling factor. The top plot in each plot shows the starting Z position of the track binned by P0Dule and broken down by FSI interaction type, and the bottom plot shows the data to MC ratio. The scaled MC prediction and data agree within the systematic errors of the scaling factor.

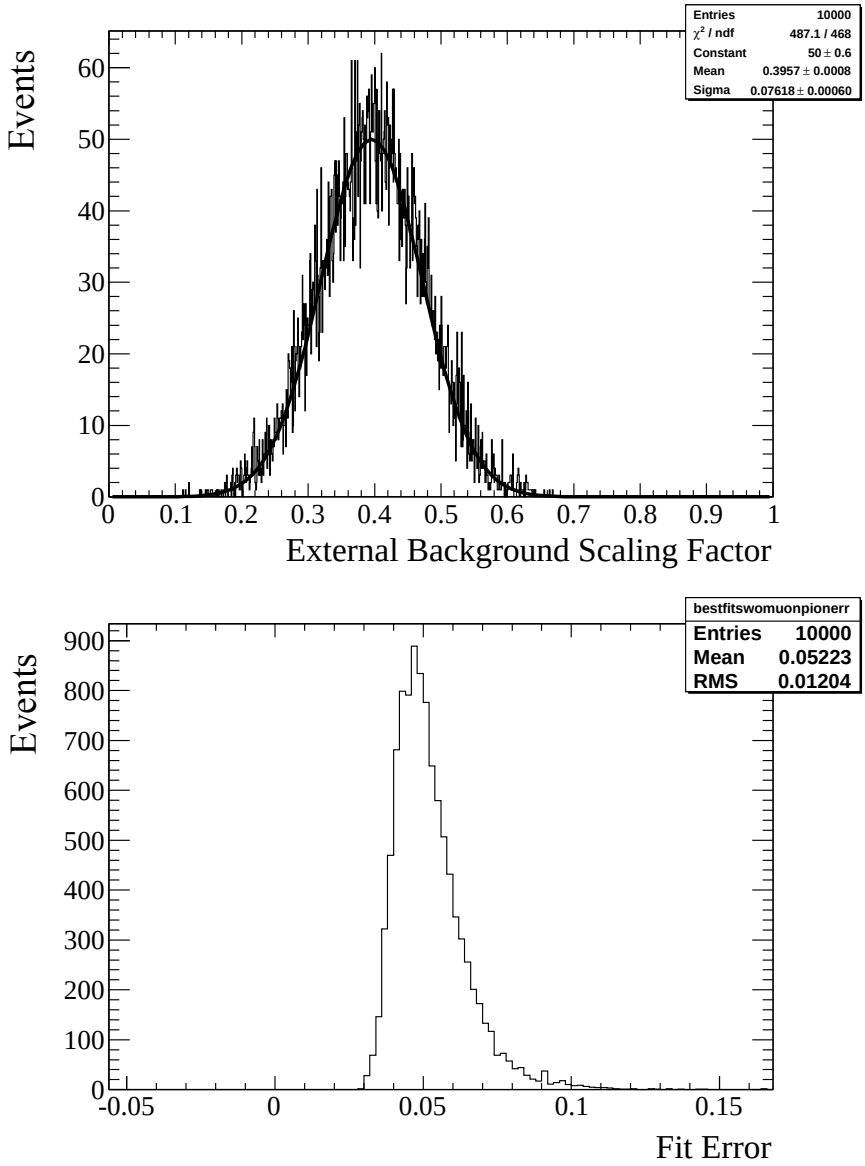

Figure 7.45: Distribution of 10000 throws with the best fit external background scaling factor (top) and fit error (bottom).

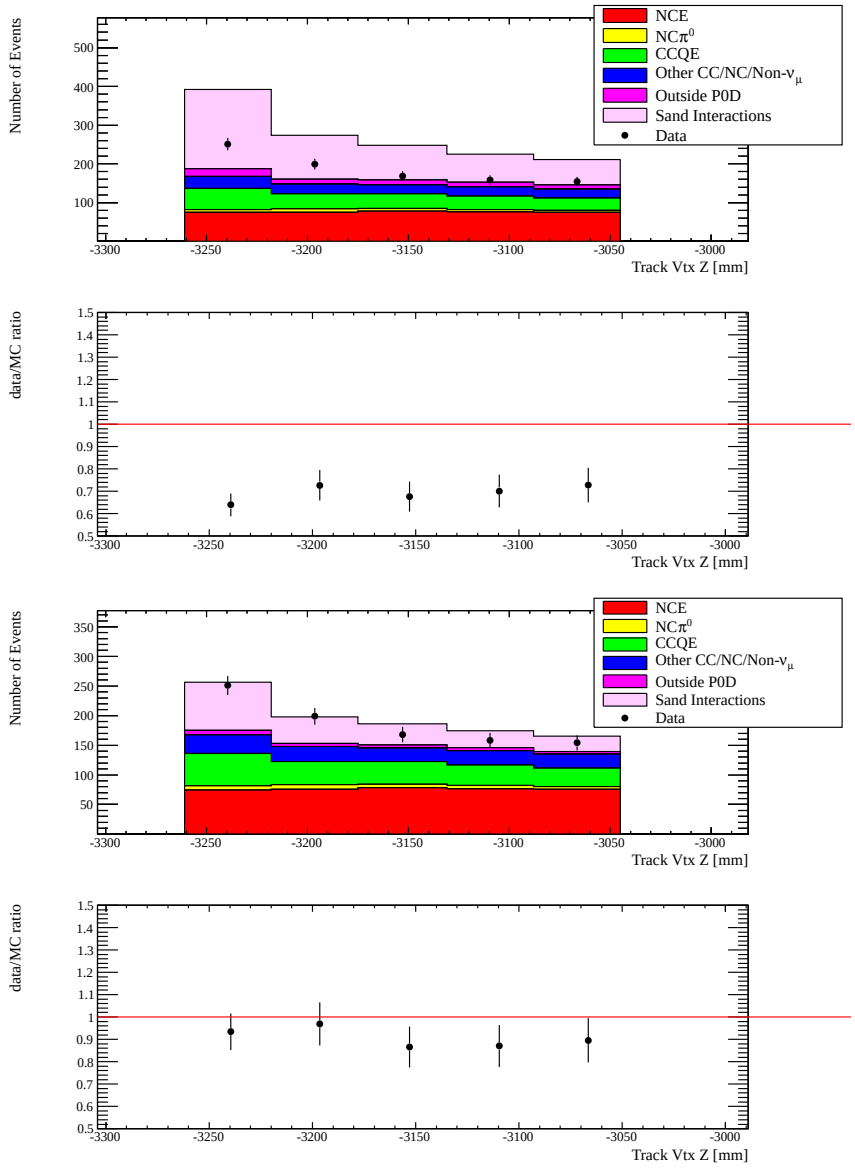

Figure 7.46: Tracks passing the NCE event selection starting in the USEcal without external background scaling (top) and with scaling (bottom).

7.3 Beam Flux

The estimated beam flux in the PØD was based on a reweighted version of the nominal "11a" flux prediction produced by the T2K beam group. The nominal events in the selection are reweighted by an improved prediction "11bv3.2" where the ratio of the "11bv3.2" to "11a" flux predictions to use the best estimations available at the time. Once the events have been reweighted another input from the beam group, in the form of a covariance matrix, was used to develop toy experiments varying the normalization and shape of the flux. For the analysis all four species of neutrinos ($\nu_\mu, \bar{\nu}_\mu, \nu_e, \bar{\nu}_e$) were considered.

To understand the scale of the flux uncertainty, the T2K publication on the beam flux prediction [54] provides the fractional error for the various sources of error and the total error as a function of the neutrino energy and species, see Figure 7.47. For comparison to the analysis the final selection has been binned with the same neutrino energy binning scheme as the flux errors and can be seen in Figure 7.48.

7.3.1 Evaluation Methods

The question answered by this systematic error evaluation is how would the cross section result differ if the real beam flux differed from the best predicted flux in the MC. Two different methods have been proposed for this analysis. This analysis is relatively insensitive to shape variations in the flux due to being a single bin analysis and because the PØD is sensitive to a limited kinematic region. Both methods give the same result when evaluated using only MC inputs.

In each of the methods below N_{sel} is the number of selected events, B is the predicted number of background events, ϕ is the predicted flux, T is the number of targets, and ϵ is the selection efficiency. Parameters denoted with a subscript i are variables modified with systematic variations. The first method attempts to probe the effect of a different flux by

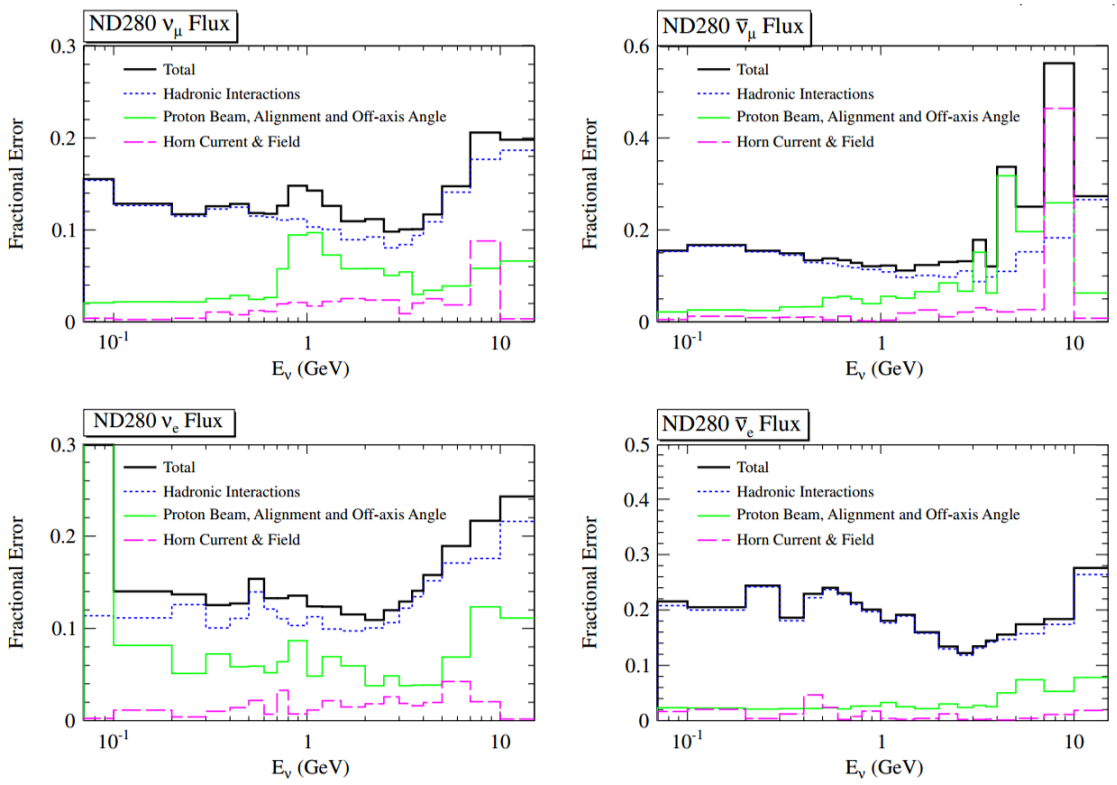

Figure 7.47: T2K beam flux fractional errors at ND280 by neutrino species [54].

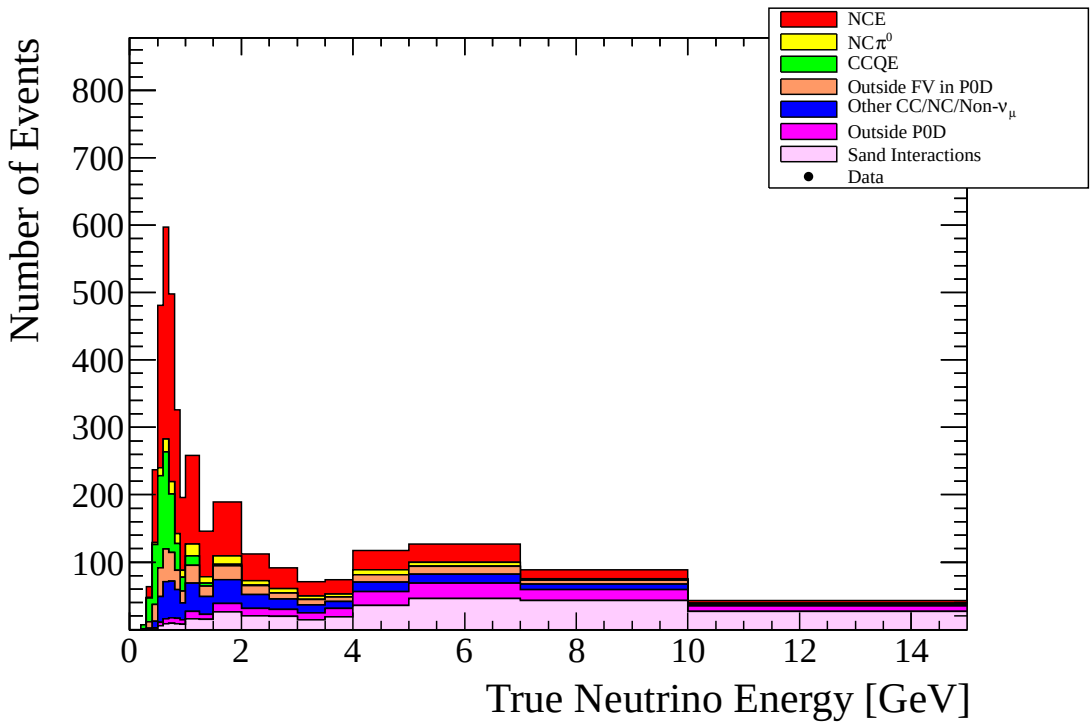

Figure 7.48: NCE Selection binned in neutrino energy.

varying the N_{sel} in the cross section equation, see Equation 7.3.

$$\sigma_i = \frac{N_{sel_i} - B_0}{\phi T \epsilon} \tag{7.3}$$

The idea behind this is that in the real measurement a difference in the flux will appear as a larger or smaller number of selected events. The second method attempts to probe the introduction of a flux variation by looking at how the varied flux would affect the background prediction, the efficiency prediction and total flux prediction while keeping the selected number of events constants, see Equation 7.4.

$$\sigma_i = \frac{N_{sel} - B_i}{\phi_i T \epsilon_i} \tag{7.4}$$

This method has the advantage of being able to accept either the central MC value or the data selected value for the N_{sel} variable. There is some question as to which method is the correct method to apply to the analysis. In practice systematic errors should be calculated the same way for data and toy MC samples. Because of this the second method, Equation 7.4, should be used. In the NCE analysis all the methods giving the nearly the same answer, but future analyses will not necessarily have similar systematic issues. Future analyses should investigate all methods and use the generally accepted systematics evaluation method for cross section measurements in T2K.

7.3.2 Flux systematic

In order to have all the corresponding pieces needed to evaluate the systematic, as described in Section 7.3.1, all selected events in the magnet MC are thrown 10,000 times. For each throw all single reconstructed tracks (potential signal and background events) are thrown together. In addition, all NCE signal events in the FV are thrown at the same time, giving the ability to look at effects the flux might have on the efficiency. For each throw the selected events and denominator of the efficiency can be reweighted from a single throw. The

sand MC is not readily able to be reweighted as header information in the oaAnalysis files appears to be missing information(or some other issue) needed by JReweight, but this sample doesn't need to be thrown as it has been directly measured from data, see Section 7.2.3. As a result, when the systematic is evaluated the external events should remain constant as the event rate measured is directly related to the true beam flux. Any uncertainty in the data measurement has been evaluated as described in Section 7.2.3.

In order to evaluate the flux systematic, using Equation 7.4, ϕ_i is approximated by,

$$\phi_i = \phi_0 \frac{N_{trueNCE_i}}{N_{trueNCE_0}} \tag{7.5}$$

This approximation is valid up to small shape differences that the total NCE sample is sensitive to. A measure of the total NCE sample's sensitivity to shape variations is the variation of the efficiency for each throw compared to the nominal efficiency. This comparison can be see in Figure 7.49, where the shape effect is 1.6%. The other inputs into Equation 7.4 are the background prediction, which for this analysis is a mix of data driven and MC estimations, and efficiency. The fractional change in the total background, which contains a constant background estimated by the data, is seen in Figure 7.50 with an error of 8.1%. Using the second method with N_{sel} coming from MC an estimation on the uncertainty due to the flux is obtained. This method returns an asymmetric error of $+17.5\%, -22.5\%$ as seen in Figure 7.51.

Similar to the result above, the error can be estimated by using the number of selected events in the data instead of the MC prediction. The calculation is the same as in Equation 7.4 with N_{sel} from data. Using these numbers the systematic is evaluated to be +17.5%, -21.5% as seen in Figure 7.52.

For the method described by Equation 7.3, the distribution of total selected events and the fractional change can be seen in Figure 7.53. The total selection varies by 9.5% while the the mean selected events is 3734 and the number of events selected in data, 3936, sits

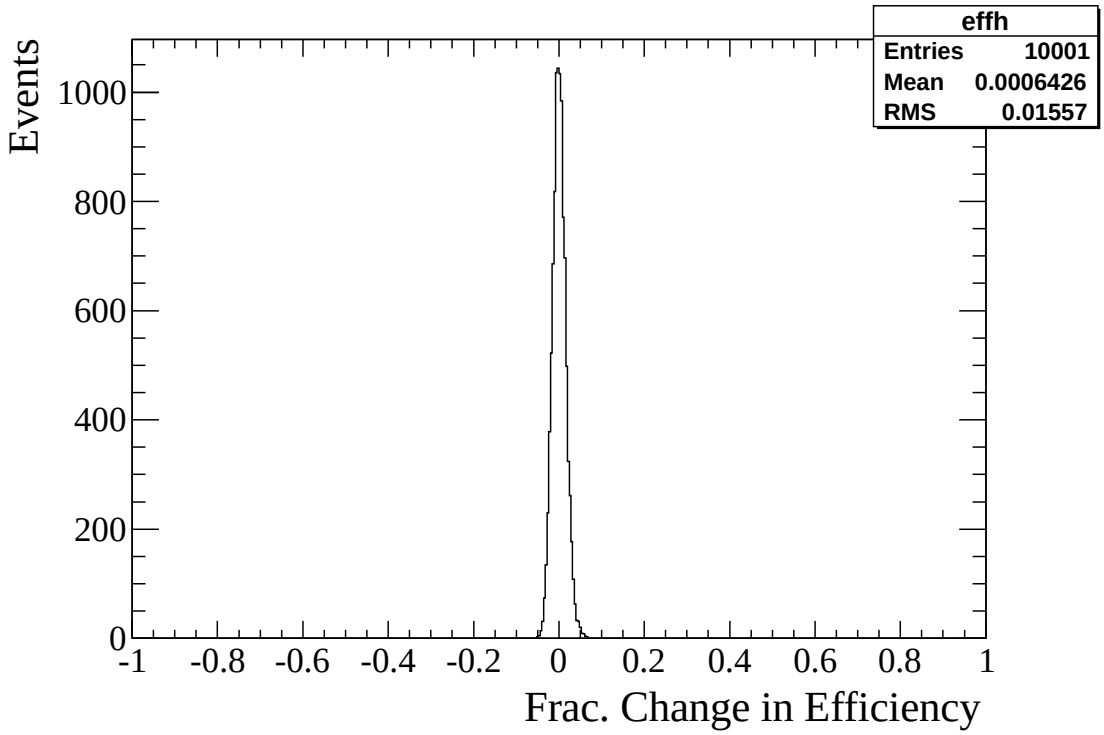

Figure 7.49: Fractional change in the selection efficiency for all beam flux throws.

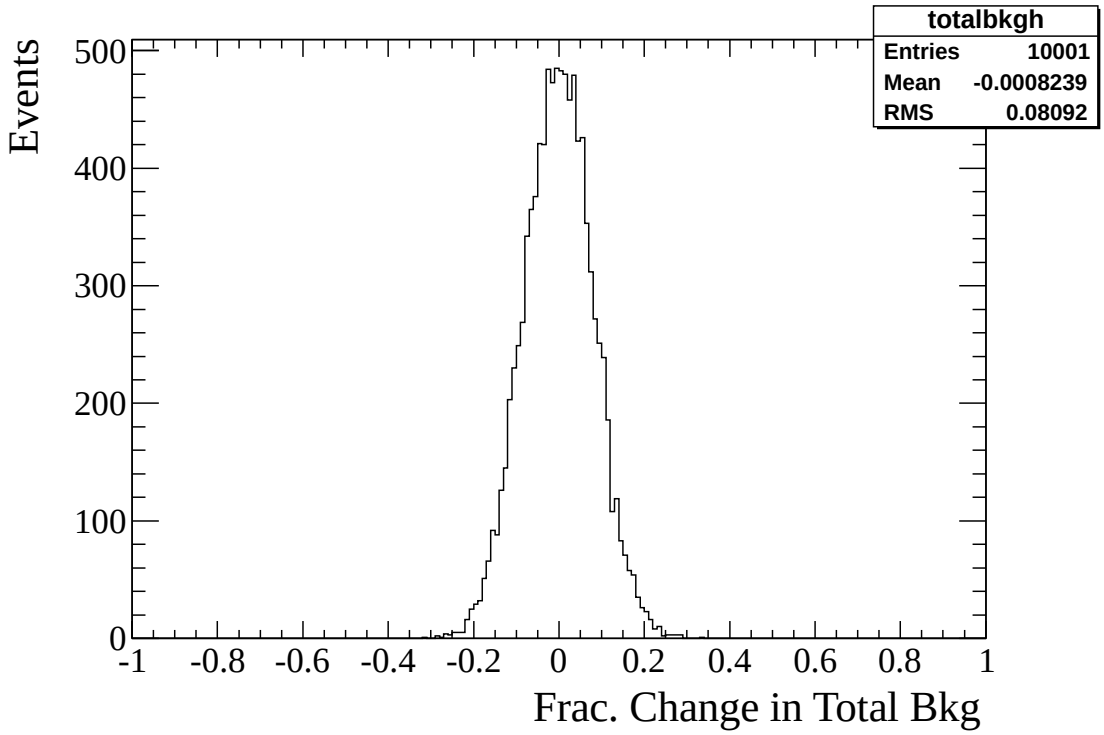

Figure 7.50: Fractional change in the total background for all beam flux throws. The background is partially estimated by the MC and measured by data.

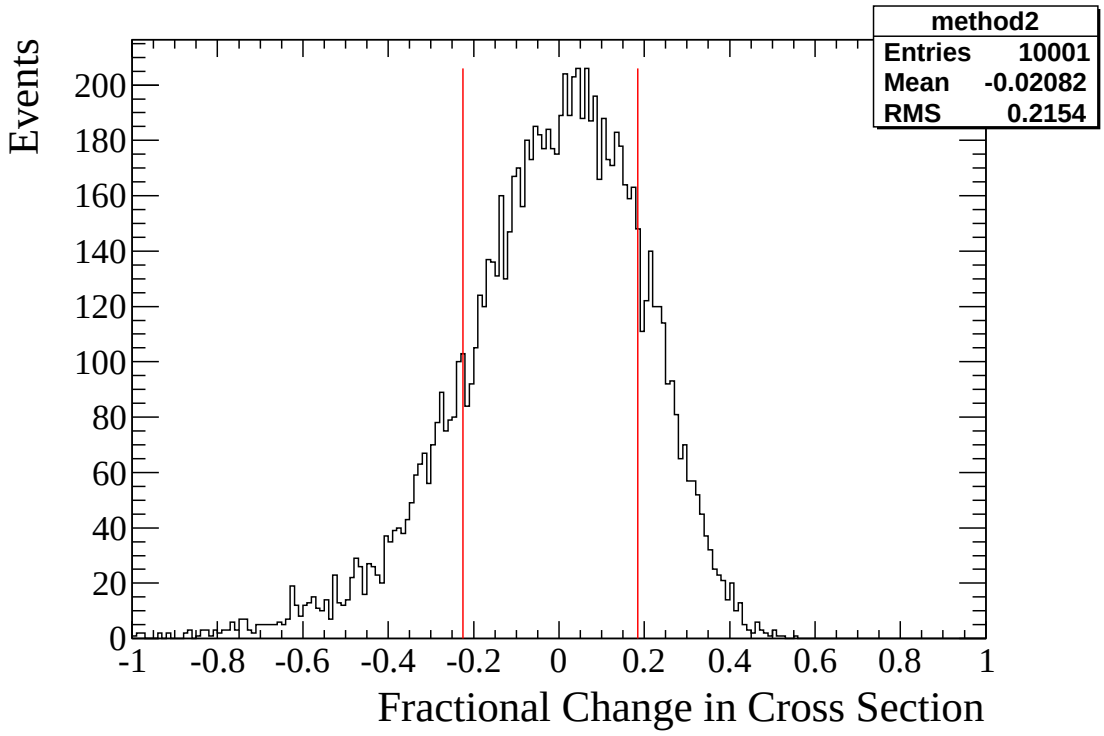

Figure 7.51: Fractional change in cross section measured using variations in the background estimation, the flux, and the selection efficiency. The number of selected event input uses the MC prediction. The estimated error via this method is $-22.5\%, +17.5\%$.

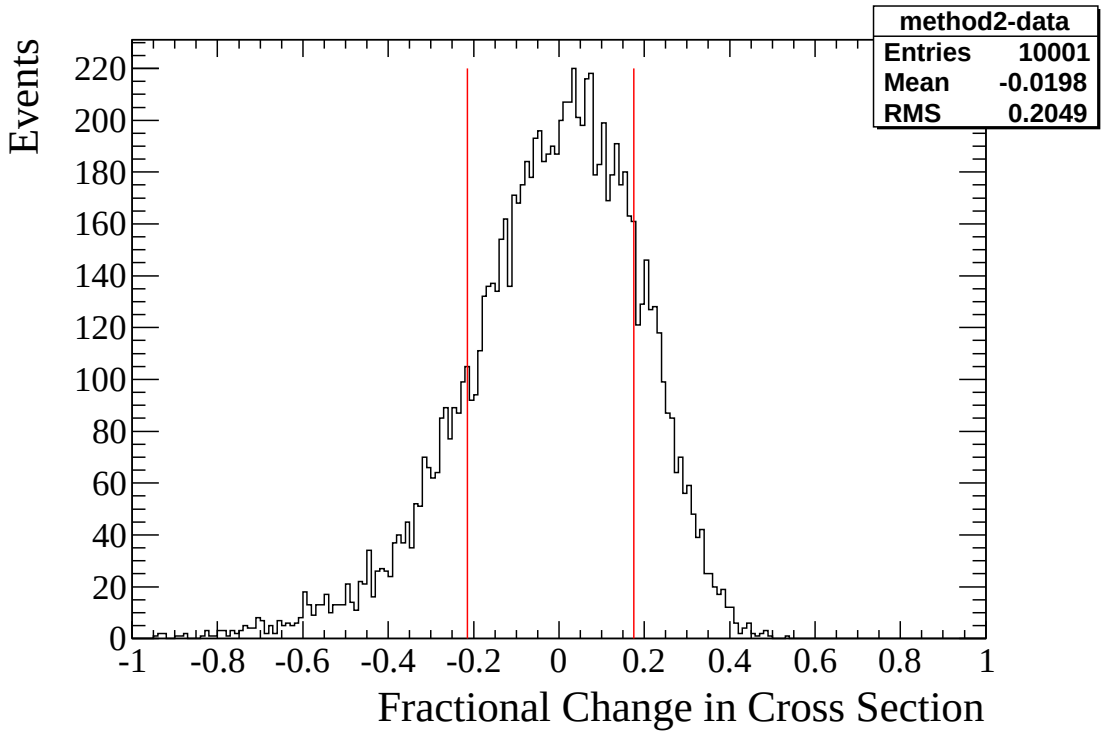

Figure 7.52: Fractional change in cross section measured using variations in the background estimation, the flux, and the selection efficiency. The number of selected event input is from data. The estimated error via this method is +17.5%, -21.5%.

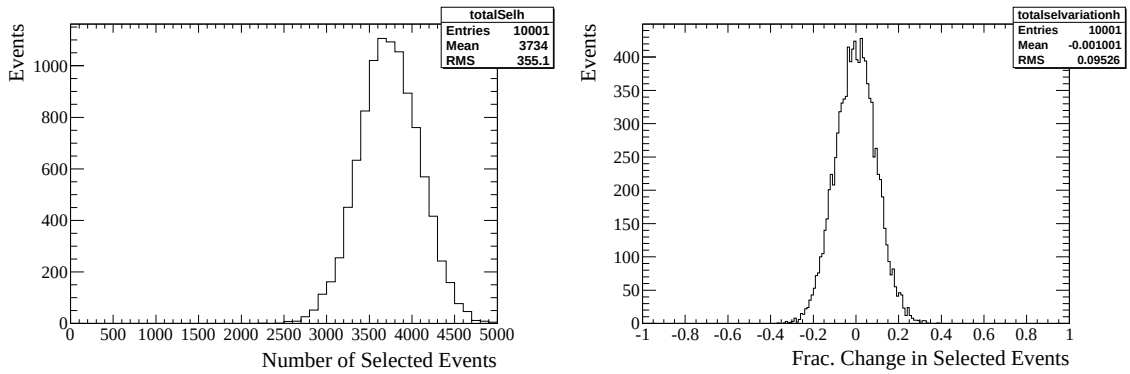

Figure 7.53: Total number of selected events for each flux throw (left) and the fractional change in the number of selected events with respect to the nominal number of selected events (right).

inside the selection event distribution. Using this method the systematic error associated with the flux uncertainty is measured to be 20.7% as seen in Figure 7.54.

The method chosen for this analysis will emulate the method used in the CC inclusive cross section measurement [92] to keep consistency in analysis methods. This method uses the data N_{sel} with Equation 7.4. The final quoted systematic for the beam flux uncertainty is +17.5%, -21.5%.

The size of the evaluated systematic is larger than what would naively be expected. The size of the propagated error is larger than the input flux errors of ∼10–12%. While the flux in the denominator of the cross section extraction varies by this value, the background normalization is also affected by the total flux. This is because the background is the reuslt of the multiplication of flux and cross section of the background. As a result, if the flux changes by 10% so does the unconstrained background prediction. Since the final sample of the NCE analysis is approximately 50% the total flux error is approximately doubled due to the correlation between the flux and predicted background.

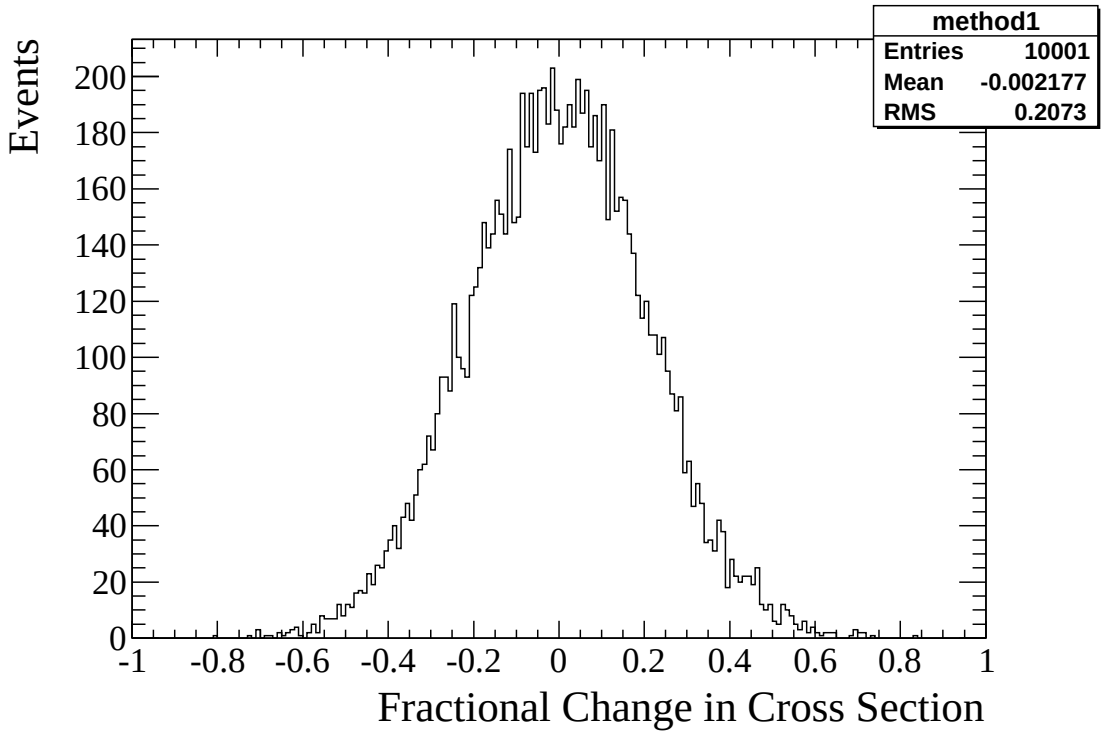

Figure 7.54: Fractional change in cross section measured using variations in the number of selected events. The estimated error via this method is ±20.7%.

Chapter 8

Cross Section Extraction

This chapter constains a description of the cross section extracted from the event selection described in chapter 6. Currently one cross section has been evaluated, the flux-averaged cross section with water in the PØD. In the future, attempts will be made to extract a differential cross section with respect to T_p as well as $\cos\theta$, a flux-averaged cross section with water out of the PØD as well as cross sections on water using combinations of water-in and water-out data.

8.1 Flux-Averaged absolute cross section

The flux-averaged absolute cross section to be extracted from the event selection found in Section 6 uses data with water in the PØD. This cross section is taken with respect to the number of target nucleons in the fiducial volume which averages the result over all the nuclear targets found in the fiducial volume. The primary nuclear targets are carbon, oxygen and copper according to the Monte Carlo. None of the methods used in this analysis are capable of separating specific nuclear targets. This measurement uses Run 1+2 water in data with a total POT of 9.918×10^{19}. The selection efficiency of the sample as a function of the true neutrino energy can be seen in Figure 8.1. From this figure it can be seen the event selection covers the NCE neutrino energy bins except for bins less than 250 MeV. Based on this plot the measurement of a flux-averaged cross section is valid since the event selection has sensitivity in all neutrino energy bins where the NCE process occurs.

The cross section is calculated via Equation 8.1.

$$< \sigma >_{flux} = \frac{N_{sel.} - B_{mc|data}}{\frac{\int \Phi(E_\nu)\mathrm{d}E_\nu}{1\times10^{21} P.O.T.} \times \text{p.o.t.}_{exposure} \times N_{Targets} \times \epsilon_{mc}} \tag{8.1}$$

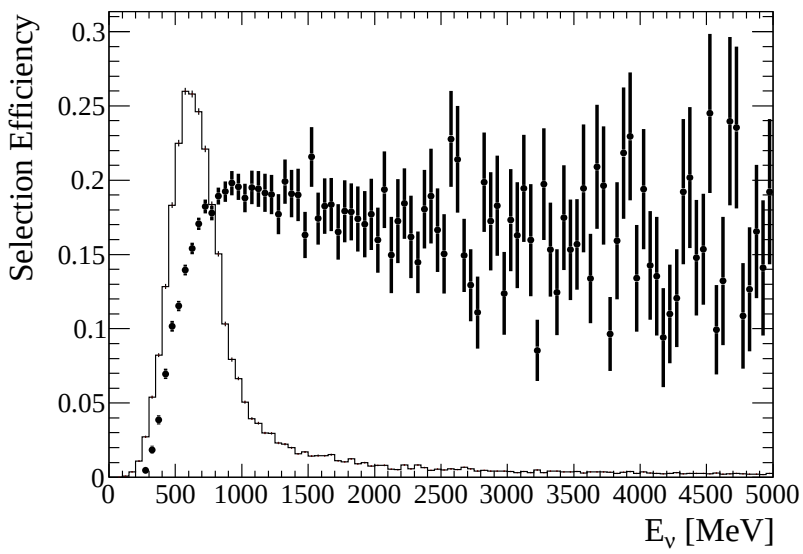

Figure 8.1: The points represent the selection efficiency as a function of true neutrino energy. The overlaid histogram is a scaled histogram of all NCE events in the fiducial volume. The efficiency is the selected number of NCE events divided by the total predicted NCE signal in a given true neutrino energy bin.

Table 8.1: Central values estimated by NEUT MC scaled to exposed 9.918×10^{19} for the FSI topology. The events used in this calculation only come from the MC prediction except for the external events which are scaled by the data constraint. Events are scaled to data p.o.t..

Variable	Central value
$N_{sel.MC}$	3730.63
B_{mc}	2015.94
$\int \Phi(E_\nu)\mathrm{d}E_\nu$	1.91×10^{13}
p.o.t.$_{exposure}$	9.918×10^{19}
$N_{targets}$	3.248×10^{30}
ϵ_{mc}	13.74%
$<\sigma>_{flux} = 2.03 \times 10^{-39} \frac{cm^2}{nucleon}$	

The integrated flux reported by the beam group comes from 11bv3.2 flux files and is reported as a flux per 1×10^{21} p.o.t.. Both the background term, $B_{mc|data}$, and efficiency, ϵ_{mc}, are estimated from the NEUT Monte Carlo version 5.1.4.2 or partially estimated by the data. $N_{Targets}$ comes from the total FV mass.

Since the event selection does not depend on or cut on the neutrino energy no unfolding or equivalent methods are required to correctly account for truth versus reconstruction bin variations when calculating the estimated backgrounds and selection efficiency. The current flux-averaged cross section uses systematic values found in Section 7. The central input values for the FSI defined cross section measurement can be found in Table 8.2. Using these values the flux-averaged cross section is measured to be $<\sigma>_{flux} = 2.24\times10^{-39} \frac{\mathrm{cm}^2}{\mathrm{nucleon}}$. Before the data cross section was calculated various tests were performed, see Section 8.1.1, to ensure the cross section calculation was being done correctly. A simple check with the nominal cuts and NEUT events rates can be found in Table 8.1.

Table 8.2: Run 1+2 water-in cross section final FSI topological cross section.

Variable	Central value
$N_{sel.}$	3936
B_{mc}	2015.94
$\int \Phi(E_\nu)\mathrm{d}E_\nu$	1.91×10^{13}
$\mathrm{p.o.t.}_{exposure}$	9.918×10^{19}
$N_{targets}$	3.297×10^{30}
ϵ_{mc}	13.74%
$<\sigma>_{flux} = 2.24\times10^{-39}\frac{\mathrm{cm}^2}{\mathrm{nucleon}}$	

8.1.1 Cross Section Calculation Validation

In the pursuit of avoiding an incorrect cross section extraction various validations have been performed. The NEUT cross section was calculated using a variety of sources. Using the NEUT cross section tables it is possible to understand the cross section for true NCE events on various materials up to NEUT version differences as the tables are from NEUT 5.0.7 and the version of NEUT used in this analysis is 5.1.4.2. Figure 8.2 is a breakdown of cross sections for various materials. The solid lines correspond to the total NCE cross section per nucleon. The T2K predicted flux can be seen in Figure 8.3. The flux-averaged cross section calculated with both fluxes and the NEUT prediction broken down by the target element can be see in Figure 8.4. Unfortunately, the ROOT file provided did not have all the required information for boron.

A second approach to calculate the cross section is to look at all true NCE and FSI defined NCE interactions in the fiducial volume and calculate the cross section based on those event rates. The advantage this method has over the previous method is it averages over all the materials in the fiducial volume and provides a direct method to understand the predicted FSI defined cross section and true generator level cross section prediction. Using files of

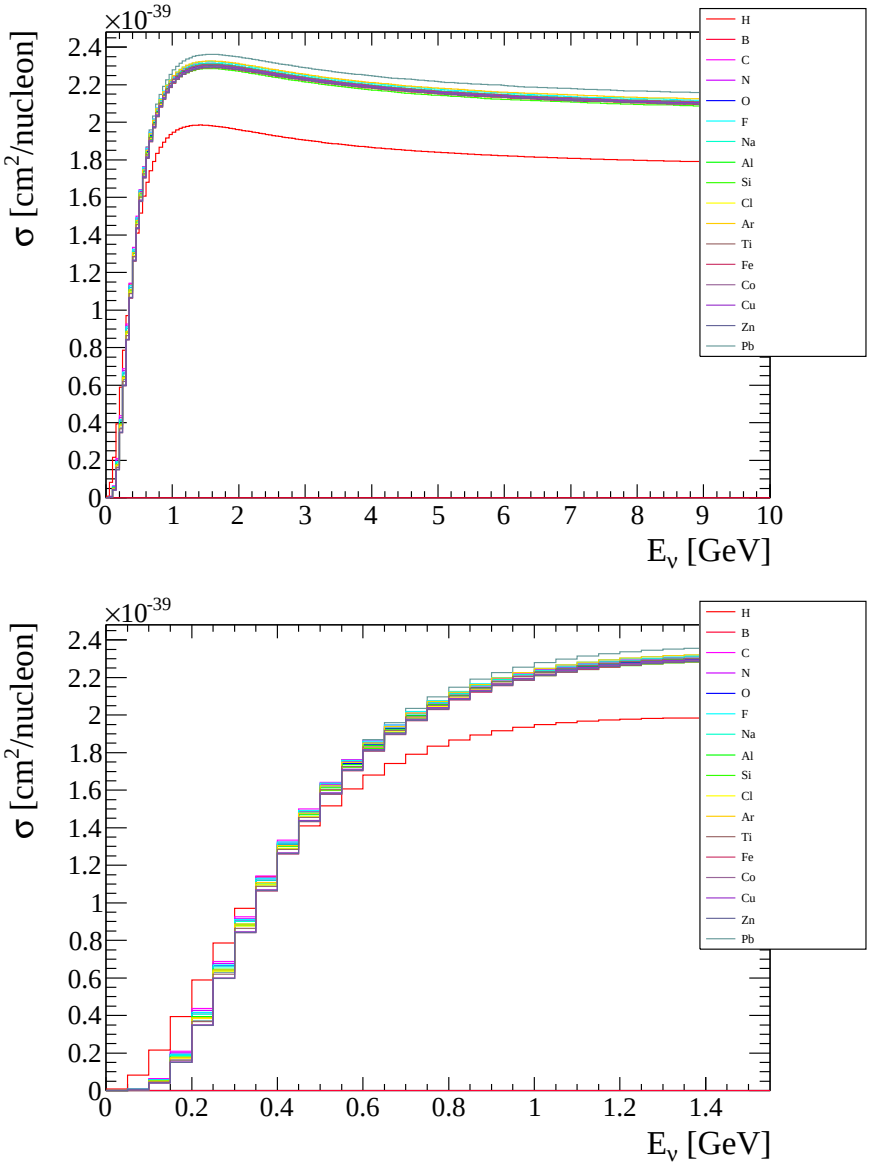

Figure 8.2: NEUT predicted generator level cross section for true NCE interactions with full neutrino energy range (top) and zoomed (bottom).

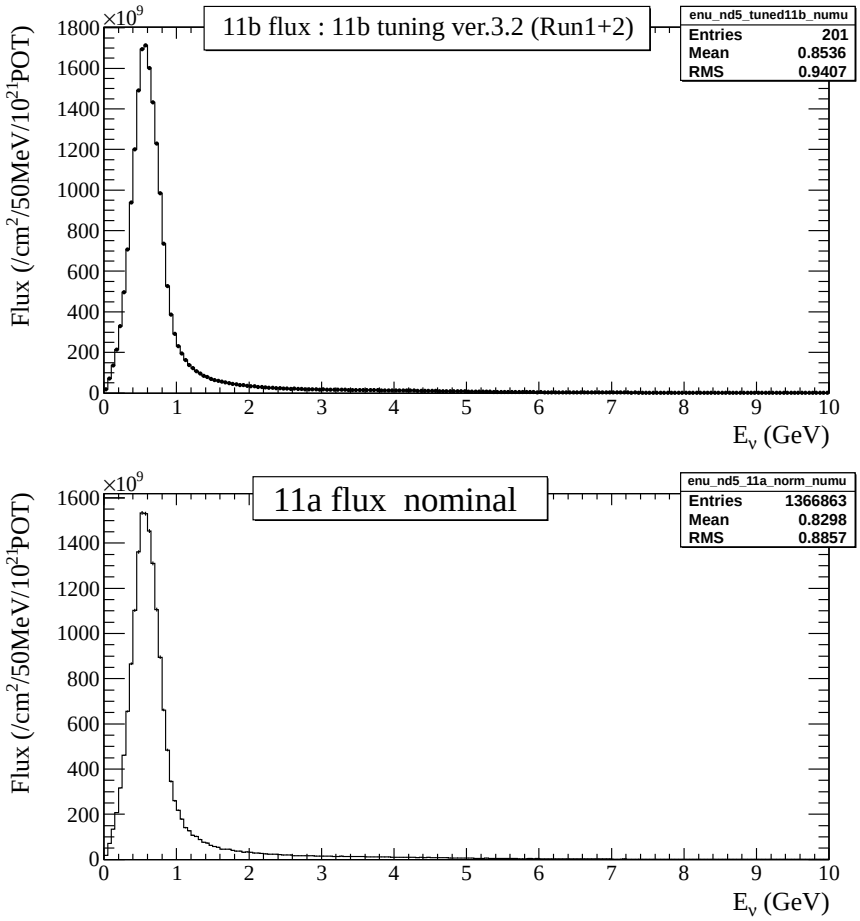

Figure 8.3: Tuned NuMu flux from the 11bv3.2 flux files for Run 1+2 (top) and the nominal 11a flux (bottom).

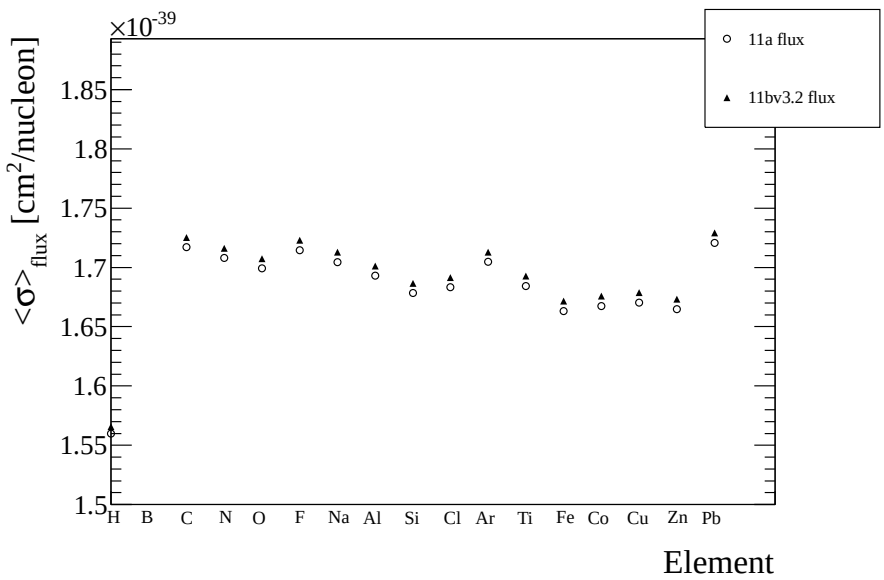

Figure 8.4: Predicted flux-averaged generator level cross section using the nominal and tuned fluxes on various targets. The Boron NEUT prediction was empty.

Run 1 (Run 2) NEUT water in simulation the MC predicts 54548 (72574) true NCE events and 69079 (93472.8) FSI defined NCE events with an exposure of $5.51 \times 10^{20}(7.415 \times 10^{20})$ p.o.t.. Calculating under the nominal flux prediction and the standard FV mass these result in $<\sigma> = 1.75(1.73) \times 10^{-39}$ cm^2/nucleon for true NCE interactions using the 11a flux and $<\sigma> = 2.02(2.03) \times 10^{-39}$ cm^2/nucleon for FSI defined events using the 11bv3.2 flux. The true interaction calculation agrees with the expected value from the NEUT prediction and the nominal flux prediction while the FSI cross section agrees with the NEUT prediction and the 11bv3.2 flux.

To test the software function used to calculate the flux-averaged cross section various PID cuts are implemented, for both MC and data driven PID constants (see Section 7.1.0.2), and the cross section recalculated. This procedure allows for checks in the calculation of the selection efficiency, background prediction, and event yield under numerous event selections. If the software is working correctly the same cross section for either the true NCE or FSI defined events should equal the predicted cross sections described earlier for every cut per-

mutation. The cross section was also calculated for reweight and nominal MCs to ensure the ability to handle these corrections if they change in the future. Under all cut variations the cross section was equal to the expected cross section.

Chapter 9

Conclusion

The analysis described in this dissertation represents the first steps towards a more complete analysis of the NCE neutrino interaction channel at the T2K near detector. The flux averaged cross section result of $<\sigma>_{flux} = 2.24\times10^{-39}\frac{\text{cm}^2}{\text{nucleon}}(1\pm3.3\%(\text{stat.})\ ^{+23.9\%}_{-28.2\%}(\text{sys.}))$ only constrains a portion of the large background and relies on the MC background prediction, which has 10–30% normalization errors. In addition, the analysis efficiency corrects the selected events to regions that the PØD detector and event reconstruction are incapable of measuring, specifically low energy protons ($<\sim$120 MeV). As a result, the final cross section is very model dependent. This means the result depends very heavily on the models and implementation of them in NEUT. Given a different generator the final cross section result could be different. To avoid such a scenario it is best to use as much data as possible and minimize the utilization of the generator predictions.

A future expansion of this analysis should address these issues. Specifically, an analysis of sidebands, such as the events passing all cuts except the Michel decay cut, can constrain many of the backgrounds other than the NCπ^0 background. A direct measurement of the NCπ^0 interaction mode using the PØD should decreases the error currently used in the systematic error analysis. To address the projection of measurable kinematic phase space to the full phase space of the NCE interaction channel the analysis needs to at minimum add a proton kinetic energy threshold cut. By doing this the efficiency correction applied to the final physics sample is valid for the visible events and doesn't depend on the model of the unseen protons. To achieve this two methods can be employed. The first method only accepts events above the kinetic energy threshold in the denominator of the efficiency correction. This essentially makes the analysis a two bin differential cross section measurement with the first bin having zero entries. The second method employs the larger statistics of the final sample and breaks the cross section into a multi-bin differential cross section. This type of

measurement is the most useful since in addition to the overall normalization of the NCE process, the analysis would measure the shape of the cross section.

The analysis can be further expanded in the following ways. The current analysis also only uses $\sim 1/3$ of the total water-in running. The greater statistics will allow for finer binning in the differential measurements. The future analysis should also use the water-out running to produce similar results on a target with different fractional composition of elements. The PØD detector is also able to reliably reconstruct the theta angle of the proton. A differential measurement of this quantity should be a priority to understand the data excess seen in Figure 6.12 around $\cos(\theta) \sim 0.5$ to 0.7. With the larger number of events in the full T2K data set it may be possible to evaluate a double differential cross section to understand this excess as a function of proton kinetic energy.

Ideally, when measuring a cross section it should be compared to previous results. This is of interest because the experimental setups, neutrino beams, reconstruction methods, and background constraints are all different. These differences can also lead to difficulties understanding differences between results. The most recent NCE result was done by MiniBooNE and is described in Section 4.3. Because of the way the MiniBooNE result and the T2K result are constructed there are fundamental differences which make it difficult to compare them equally. The first of these is the difference in signal definition. The MiniBooNE result looks at the generator level NCE as its signal while the T2K result defines the signal as the NCE topology after FSI. Because the two experiments use different neutrino generators, NUANCE for MiniBooNE and NEUT for T2K, this issue is difficult to overcome without applying the same generator to both experiments. Secondly, the acceptances of the detectors are very different. MiniBooNE is a 4π detector which sums over all visible protons while T2K identifies the highest energy proton, typically in the forward hemisphere. In addition, the lower kinetic energy threshold of MiniBooNE can present a problem when comparing results. This results in a different flux averaged absolute cross section when the $\frac{d\sigma}{dQ^2}$ from

MiniBooNE is summed over and compared to T2K. Attempts to mitigate the differences have been done, but will still have differences which are difficult to overcome.

To get an idea of how the MiniBooNE result would perform under NEUT the NEUT NCE cross section can be applied to the MiniBooNE flux prediction to calculate a flux averaged absolute cross section. This results in a flux averaged absolute cross section per nucleon of $<\sigma>_{flux_{\text{MiniBooNE}}} = 1.731 \times 10^{-39} \frac{\text{cm}^2}{\text{nucleon}}$ compared to $<\sigma>_{flux_{\text{T2K}}} = 1.725 \times 10^{-39} \frac{cm^2}{nucleon}$ when using a carbon target. The flux averaged absolute cross section per nucleon for various targets can be seen in Figure 9.1. In addition, Figure 9.2 shows the flux averaged absolute cross section per nucleon using a carbon target with the comparison of the two experimental fluxes which have been normalized in the same manner to fit in the plot. Despite the quite different structure of the flux due to the on-axis versus off-axis nature of the experiments the average cross sections are <1% different from each other when using the NEUT cross section models. This comparison suggests the starting point for the analyses is very similar if both were subjected to the NEUT generator despite the large difference in flux shapes in the experiments.

The MiniBooNE NCE publication [5] presents the differential cross over a truncated Q^2 region, but the dissertation [93] it is based off presents the differential cross section including 0-0.1 Q^2 bins. Integrating this distribution gives the measured MiniBooNE flux averaged total cross section. The correlated error matrices are not given, but assuming a 18.9% fractional error from the dissertation, the MiniBooNE total cross section is measured to be $< \sigma >_{flux} = 1.76 \pm 0.33 \times 10^{-39} \frac{cm^2}{nucleon}$. This result is consistent within error with the T2K result presented.

Another method to compare MiniBooNE to T2K is to apply the ratio of the normalized MiniBooNE flux to T2K flux, Figure 9.3, to the true Q^2 prediction of NEUT using the PØD. This will apply a correction to the Q^2 distribution such that the result is as if the PØD were run in the MiniBooNE beamline. Figure 9.4 shows the Q^2 distribution as a function of the neutrino energy in the T2K beam. Figure 9.5 shows the reweight function applied to

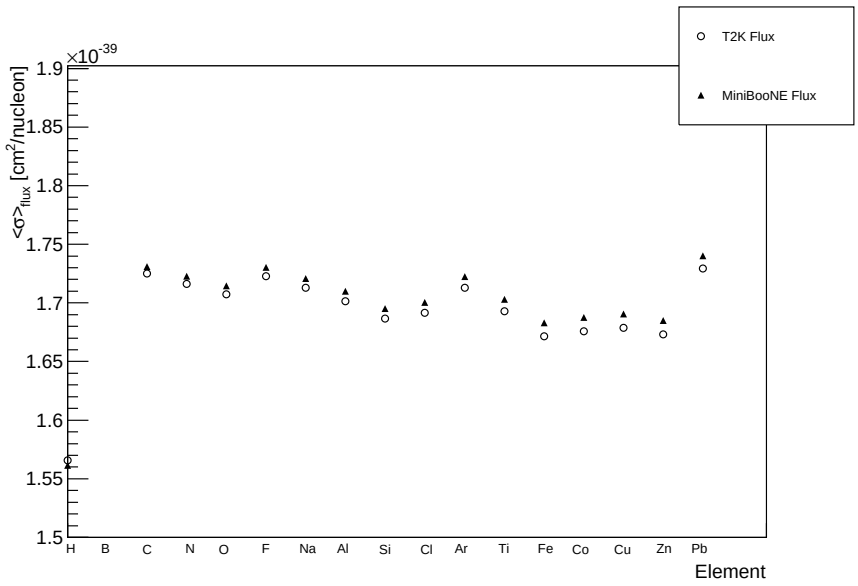

Figure 9.1: Breakdown of the flux averaged absolute cross section per nucleon as predicted by NEUT for different elemental targets using the T2K and MiniBooNE flux predictions. [54] [12].

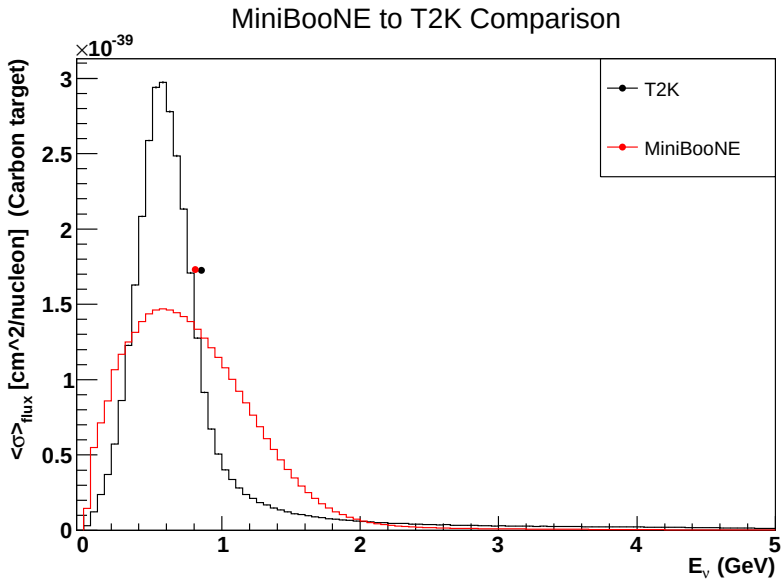

Figure 9.2: The points show a comparison of the flux averaged absolute cross section per nucleon using a carbon target as predicted by NEUT. Scaled T2K and MiniBooNE flux predictions are shown for shape comparisons of the experiment's respective flux. [54] [12]

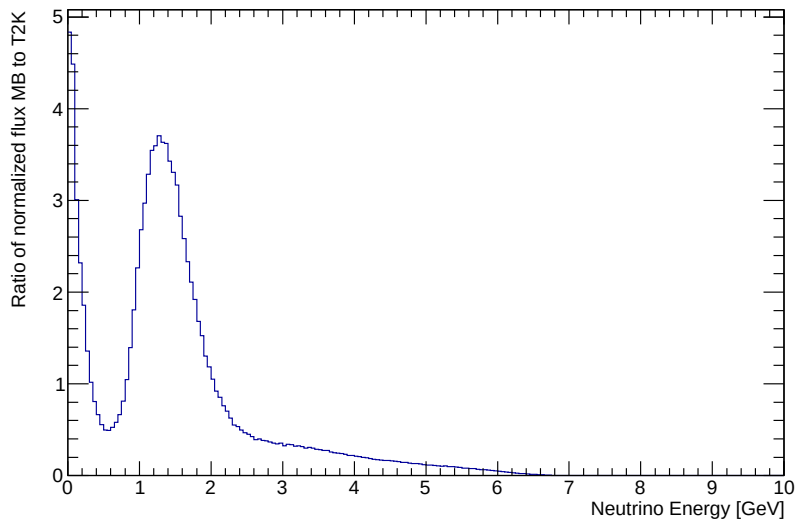

Figure 9.3: Ratio of the normalized MiniBooNE to T2K flux.

the T2K distribution in Figure 9.4 and the resulting changes to the distribution of Q^2 as a function of neutrino energy. A comparison of the Q^2 distribution for the nominal T2K distribution and the reweighted distribution is shown in Figure 9.6. The Q^2 distribution in the T2K beam prefers lower Q^2 while the distribution in the reweighted distribution is more populated in the high Q^2 region. The resulting flux averaged total cross section for the MiniBooNE prediction is $< \sigma >_{flux} = 2.08 \pm 0.42 \times 10^{-39} \frac{cm^2}{nucleon}$ which agrees with the NEUT prediction of $< \sigma >_{flux} = 2.02 \times 10^{-39} \frac{cm^2}{nucleon}$ seen in Table 8.1.

Based on the comparisons shown here the MiniBooNE result and the T2K result agree within error. As the systematic errors in the T2K NCE analysis are reduced it will be interesting to see if this agreement stands. It will also be interesting to see a differential cross section using the T2K result to more directly compare to the MiniBooNE result. The predicted cross section for the PØD in the MiniBooNE beam agrees very well with the value seen in the T2K beam.

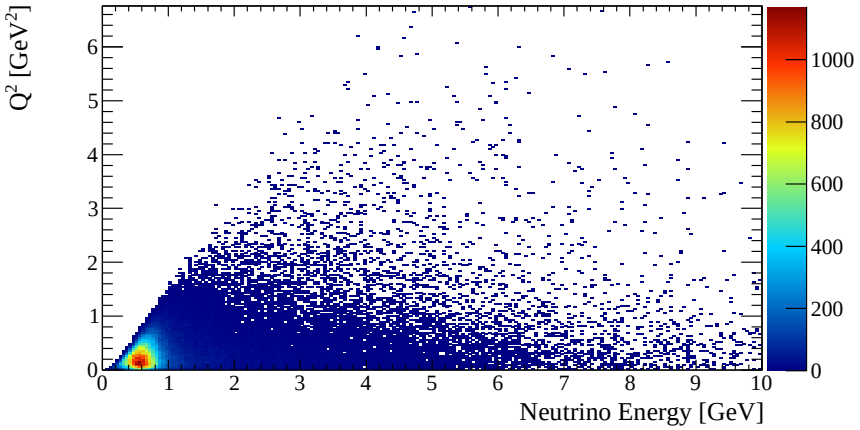

Figure 9.4: Q^2 as a function of the neutrino energy given the T2K flux.

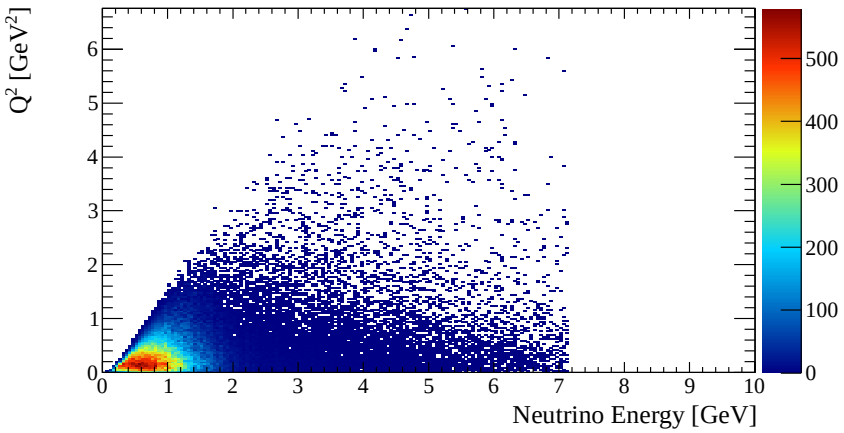

Figure 9.5: Q^2 as a function of the neutrino energy when the ratio of the MiniBooNE to T2K flux is applied.

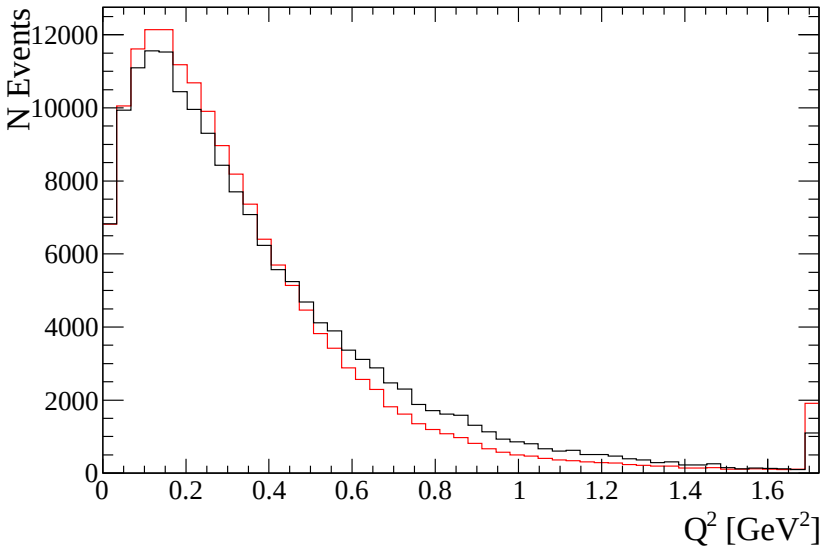

Figure 9.6: Comparison of the T2K Q^2 distribution and the Q^2 distribution when the MiniBooNE to T2K flux ratio is applied.

Bibliography

[1] Sheldon L. Glashow. Partial-symmetries of weak interactions. *Nuclear Physics*, 22(4):579 – 588, 1961.

[2] Steven Weinberg. A model of leptons. *Phys. Rev. Lett.*, 19:1264–1266, Nov 1967.

[3] Abdus Salam. Weak and electromagnetic interactions. In Nils Svartholm, editor, *Elementary particle theory*, pages 367–377. Almquist & Wiksell.

[4] L. A. Ahrens *et al.* (BNL E734 Collaboration). Measurement of neutrino-proton and antineutrino-proton elastic scattering. *Phys. Rev. D*, 35:785–809, Feb 1987.

[5] A.A. Aguilar-Arevalo *et al.* (MiniBooNE Collaboration). Measurement of the neutrino neutral-current elastic differential cross section on mineral oil at $e_\nu \sim 1$GeV. *Phys. Rev. D*, 82:092005, Nov 2010.

[6] P. Adamson *et al.* (MINOS Collaboration). Active to sterile neutrino mixing limits from neutral-current interactions in minos. *Phys. Rev. Lett.*, 107:011802, Jun 2011.

[7] Patrick deNiverville, Maxim Pospelov, and Adam Ritz. Observing a light dark matter beam with neutrino experiments. *Phys. Rev. D*, 84:075020, Oct 2011.

[8] Patrick deNiverville, David McKeen, and Adam Ritz. Signatures of sub-GeV dark matter beams at neutrino experiments. *Phys. Rev. D*, 86:035022, Aug 2012.

[9] G. Garvey, E. Kolbe, K. Langanke, and S. Krewald. Role of strange quarks in quasielastic neutrino scattering. *Phys. Rev. C*, 48:1919–1925, Oct 1993.

[10] G. T. Garvey, W. C. Louis, and D. H. White. Determination of proton strange form factors from ν p elastic scattering. *Phys. Rev. C*, 48:761–765, Aug 1993.

[11] W.M. Alberico, M.B. Barbaro, S.M. Bilenky, J.A. Caballero, C. Giunti, C. Maieron, E. Moya de Guerra, and J.M. Udas. Strange form factors of the proton: a new analysis of the ν ($\bar{\nu}$) data of the BNL-734 experiment. *Nuclear Physics A*, 651(3):277 – 286, 1999.

[12] A.A. Aguilar-Arevalo *et al.* (MiniBooNE Collaboration). Neutrino flux prediction at MiniBooNE. *Phys. Rev. D*, 79:072002, Apr 2009.

[13] G. S. Guralnik, C. R. Hagen, and T. W. B. Kibble. Global conservation laws and massless particles. *Phys. Rev. Lett.*, 13:585–587, Nov 1964.

[14] Peter W. Higgs. Broken symmetries and the masses of gauge bosons. *Phys. Rev. Lett.*, 13:508–509, Oct 1964.

[15] F. Englert and R. Brout. Broken symmetry and the mass of gauge vector mesons. *Phys. Rev. Lett.*, 13:321–323, Aug 1964.

[16] G. Aad *et al.* (ATLAS Collaboration). Observation of a new particle in the search for the standard model higgs boson with the ATLAS detector at the LHC. *Physics Letters B*, 716(1):1 – 29, 2012.

[17] S. Chatrchyan *et al.* (CMS Collaboration). Observation of a new boson at a mass of 125 gev with the CMS experiment at the LHC. *Physics Letters B*, 716(1):30 – 61, 2012.

[18] Lieve radioaktive damen und harren(original in Pauli letter archives). `http://cds.cern.ch/record/83282/files/meitner_0393.pdf?version=1`.

[19] Dear radioactive ladies and gentlemen. `http://microboone-docdb.fnal.gov/cgi-bin/RetrieveFile?docid=953;filename=pauli%20letter1930.pdf;version=1`.

[20] C. L. Cowan, F. Reines, F. B. Harrison, H. W. Kruse, and A. D. McGuire. Detection of the free neutrino: a confirmation. *Science*, 124(3212):103–104, 1956.

[21] G. Danby, J-M. Gaillard, K. Goulianos, L. M. Lederman, N. Mistry, M. Schwartz, and J. Steinberger. Observation of high-energy neutrino reactions and the existence of two kinds of neutrinos. *Phys. Rev. Lett.*, 9:36–44, Jul 1962.

[22] K. Kodama *et al.* (DONUT Collaboration). Observation of tau neutrino interactions. *Physics Letters B*, 504(3):218 – 224, 2001.

[23] Precision electroweak measurements on the Z resonance. *Physics Reports*, 427(56):257 – 454, 2006.

[24] D. Griffiths. *Introduction to Elementary Particles*. Physics textbook. Wiley, 2008.

[25] Yoshinari Hayato. A neutrino interaction simulation program library NEUT. *Acta Physica Polonica B*, 40:2477–2489, 2009.

[26] C.H. Llewellyn Smith. Neutrino reactions at accelerator energies. *Physics Reports*, 3(5):261 – 379, 1972.

[27] R.A. Smith and E.J. Moniz. Neutrino reactions on nuclear targets. *Nuclear Physics B*, 43(0):605 – 622, 1972.

[28] A. A. Aguilar-Arevalo *et al.* (MiniBooNECollaboration). First measurement of the muon neutrino charged current quasielastic double differential cross section. *Phys. Rev. D*, 81:092005, May 2010.

[29] A. A. Aguilar-Arevalo *et al.* (MiniBooNE Collaboration). Measurement of muon neutrino quasielastic scattering on carbon. *Phys. Rev. Lett.*, 100:032301, Jan 2008.

[30] R. Gran *et al.* (K2K Collaboration). Measurement of the quasielastic axial vector mass in neutrino interactions on oxygen. *Phys. Rev. D*, 74:052002, Sep 2006.

[31] B. Pontecorvo. Mesonium and anti-mesonium. *Sov.Phys.JETP*, 6:429, 1957.

[32] Ziro Maki, Masami Nakagawa, and Shoichi Sakata. Remarks on the unified model of elementary particles. *Progress of Theoretical Physics*, 28(5):870–880, 1962.

[33] Raymond Davis. Solar neutrinos. ii. experimental. *Phys. Rev. Lett.*, 12:303–305, Mar 1964.

[34] John N. Bahcall. Solar neutrinos. i. theoretical. *Phys. Rev. Lett.*, 12:300–302, Mar 1964.

[35] J Boger *et al.* (SNO Collaboration). The Sudbury neutrino observatory. *Nuclear Instruments and Methods in Physics Research Section A: Accelerators, Spectrometers, Detectors and Associated Equipment*, 449(12):172 – 207, 2000.

[36] Q. R. Ahmad *et al.* (SNO Collaboration). Direct evidence for neutrino flavor transformation from neutral-current interactions in the sudbury neutrino observatory. *Phys. Rev. Lett.*, 89:011301, Jun 2002.

[37] Y. Fukuda *et al.* (SK Collaboration). Evidence for oscillation of atmospheric neutrinos. *Phys. Rev. Lett.*, 81:1562–1567, Aug 1998.

[38] M. Ahn *et al.* (K2K Collaboration). Measurement of neutrino oscillation by the K2K experiment. *Phys. Rev. D*, 74:072003, Oct 2006.

[39] Yoshitaka Itow. Recent results in atmospheric neutrino oscillations in the light of large. *Nuclear Physics B - Proceedings Supplements*, 235236(0):79 – 86, 2013. The {XXV} International Conference on Neutrino Physics and Astrophysics.

[40] P. Adamson *et al.* (MINOS Collaboration). Measurement of neutrino and antineutrino oscillations using beam and atmospheric data in MINOS. *Phys. Rev. Lett.*, 110:251801, Jun 2013.

[41] K. Abe *et al.* (T2K Collaboration). Measurement of neutrino oscillation parameters from muon neutrino disappearance with an off-axis beam. *Phys. Rev. Lett.*, 111:211803, Nov 2013.

[42] F. P. An *et al.* (Daya Bay Collaboration). Observation of electron-antineutrino disappearance at Daya Bay. *Phys. Rev. Lett.*, 108:171803, Apr 2012.

[43] J. K. Ahn *et al.* (RENO Collaboration). Observation of reactor electron antineutrinos disappearance in the reno experiment. *Phys. Rev. Lett.*, 108:191802, May 2012.

[44] K. Abe *et al.* (T2K Collaboration). Observation of electron neutrino appearance in a muon neutrino beam. *Phys. Rev. Lett.*, 112:061802, Feb 2014.

[45] A. Gando *et al.* (KamLAND Collaboration). Constraints on θ_{13} from a three-flavor oscillation analysis of reactor antineutrinos at KamLAND. *Phys. Rev. D*, 83:052002, Mar 2011.

[46] K. Abe *et al.* (SK Collaboration). Solar neutrino results in Super-Kamiokande-III. *Phys. Rev. D*, 83:052010, Mar 2011.

[47] K. Abe *et al.* (T2K Collaboration). The T2K experiment. *Nuclear Instruments and Methods in Physics Research Section A: Accelerators, Spectrometers, Detectors and Associated Equipment*, 659(1):106 – 135, 2011.

[48] K. Nitta *et al.* (K2K SciBar group). The K2K SciBar detector. *Nuclear Instruments and Methods in Physics Research Section A: Accelerators, Spectrometers, Detectors and Associated Equipment*, 535(12):147 – 151, 2004. ¡ce:title¿Proceedings of the 10th International Vienna Conference on Instrumentation¡/ce:title¿.

[49] B.J. Kim *et al.* (K2K SciFi group). Tracking performance of the scintillating fiber detector in the K2K experiment. *Nuclear Instruments and Methods in Physics Research Section A: Accelerators, Spectrometers, Detectors and Associated Equipment*, 497(23):450 – 466, 2003.

[50] T Ishii *et al.* (K2K MRD group). Near muon range detector for the K2K experimentconstruction and performance. *Nuclear Instruments and Methods in Physics Research Section A: Accelerators, Spectrometers, Detectors and Associated Equipment*, 482(12):244 – 253, 2002.

[51] S. Fukuda *et al.* (SK Collaboration). The super-kamiokande detector. *Nuclear Instruments and Methods in Physics Research Section A: Accelerators, Spectrometers, Detectors and Associated Equipment*, 501(23):418 – 462, 2003.

[52] T2K official plots (not publically available). `http://www.t2k.org/docs/plots`.

[53] Japan proton accelerator research complex. `http://www.http://j-parc.jp/index-e.html`.

[54] K. Abe *et al.* (T2K Collaboration). T2K neutrino flux prediction. *Phys. Rev. D*, 87:012001, Jan 2013.

[55] N. Abgrall *et al.* (NA61/SHINE Collaboration). Measurements of cross sections and charged pion spectra in proton-carbon interactions at 31 GeV/c. *Phys. Rev. C*, 84:034604, Sep 2011.

[56] N. Abgrall *et al.* (NA61/SHINE Collaboration). Measurement of production properties of positively charged kaons in proton-carbon interactions at 31 GeV/c. *Phys. Rev. C*, 85:035210, Mar 2012.

[57] D. Orme *et al.* Development of multi-pixel photon counters for the T2K long baseline neutrino experiment. *Nuclear Instruments and Methods in Physics Research Section A: Accelerators, Spectrometers, Detectors and Associated Equipment*, 623(1):321 – 323, 2010. ¡ce:title¿1st International Conference on Technology and Instrumentation in Particle Physics¡/ce:title¿.

[58] A. Vacheret *et al.* Characterization and simulation of the response of multi-pixel photon counters to low light levels. *Nuclear Instruments and Methods in Physics Research Section A: Accelerators, Spectrometers, Detectors and Associated Equipment*, 656(1):69 – 83, 2011.

[59] M. Otani *et al.* Design and construction of INGRID neutrino beam monitor for T2K neutrino experiment. *Nuclear Instruments and Methods in Physics Research Section A: Accelerators, Spectrometers, Detectors and Associated Equipment*, 623(1):368 – 370, 2010. ¡ce:title¿1st International Conference on Technology and Instrumentation in Particle Physics¡/ce:title¿.

[60] P.-A. Amaudruz *et al.* The T2K fine-grained detectors. *Nuclear Instruments and Methods in Physics Research Section A: Accelerators, Spectrometers, Detectors and Associated Equipment*, 696(0):1 – 31, 2012.

[61] N. Abgrall *et al.* (T2K TPC Collaboration). Time projection chambers for the T2K near detectors. *Nuclear Instruments and Methods in Physics Research Section A: Accelerators, Spectrometers, Detectors and Associated Equipment*, 637(1):25 – 46, 2011.

[62] D. Allan *et al.* The electromagnetic calorimeter for the T2K near detector nd280. *To be published in JINST*, 2013.

[63] S. Aoki *et al.* The T2K side muon range detector (smrd). *Nuclear Instruments and Methods in Physics Research Section A: Accelerators, Spectrometers, Detectors and Associated Equipment*, 698(0):135 – 146, 2013.

[64] S. Assylbekov *et al.* The T2K ND280 off-axis pizero detector. *Nuclear Instruments and Methods in Physics Research Section A: Accelerators, Spectrometers, Detectors and Associated Equipment*, 686(0):48 – 63, 2012.

[65] P Adamson *et al.* The MINOS light-injection calibration system. *Nuclear Instruments and Methods in Physics Research Section A: Accelerators, Spectrometers, Detectors and Associated Equipment*, 492(3):325 – 343, 2002.

[66] W. Lee *et al.* Observation of the reaction $\nu_\mu + p \to \nu_\mu + p$. *Phys. Rev. Lett.*, 37:186–189, Jul 1976.

[67] D. Cline *et al.* Observation of elastic neutrino-proton scattering. *Phys. Rev. Lett.*, 37:252–255, Aug 1976.

[68] J. Horstkotte *et al.* Measurement of neutrino-proton and antineutrino-proton elastic scattering. *Phys. Rev. D*, 25:2743–2761, Jun 1982.

[69] D. Cline *et al.* Observation of elastic antineutrino-proton scattering. *Phys. Rev. Lett.*, 37:648–651, Sep 1976.

[70] M. Pohl *et al.* Study of neutrino proton elastic scattering in the Gargamelle freon experiment. *Physics Letters B*, 72(4):489 – 492, 1978.

[71] H. Faissner *et al.* Measurement of elastic muon-neutrino scattering off protons. *Phys. Rev. D*, 21:555–561, Feb 1980.

[72] A.A. Aguilar-Arevalo *et al.* (MiniBooNE Collaboration). The MiniBooNE detector. *Nuclear Instruments and Methods in Physics Research Section A: Accelerators, Spectrometers, Detectors and Associated Equipment*, 599(1):28 – 46, 2009.

[73] A. Aguilar *et al.* (LSND Collaboration). Evidence for neutrino oscillations from the observation of $\overline{\nu_e}$ appearance in a $\overline{\nu_\mu}$ beam. *Phys. Rev. D*, 64:112007, Nov 2001.

[74] A. A. Aguilar-Arevalo *et al.* (MiniBooNE Collaboration). Measurement of the ratio of the ν_μ charged-current single-pion production to quasielastic scattering with a 0.8∼GeV neutrino beam on mineral oil. *Phys. Rev. Lett.*, 103:081801, Aug 2009.

[75] A. A. Aguilar-Arevalo *et al.* (MiniBooNE Collaboration). Measurement of neutrino-induced charged-current charged pion production cross sections on mineral oil at $E_\nu \sim$ 1GeV. *Phys. Rev. D*, 83:052007, Mar 2011.

[76] A. A. Aguilar-Arevalo *et al.* (MiniBooNE Collaboration). Measurement of ν_μ-induced charged-current neutral pion production cross sections on mineral oil at $E_\nu \mathrm{in} 0.5 - 2.0 \mathrm{GeV}$. *Phys. Rev. D*, 83:052009, Mar 2011.

[77] A. A. Aguilar-Arevalo *et al.* (MiniBooNE Collaboration). Measurement of ν_μ and $\overline{\nu}_\mu$ induced neutral current single π^0 production cross sections on mineral oil at $E_\nu \sim (1gev)$. *Phys. Rev. D*, 81:013005, Jan 2010.

[78] A.A. Aguilar-Arevalo *et al.* (MiniBooNE Collaboration). First observation of coherent production in neutrinonucleus interactions with $E_\nu < 2$ GeV. *Physics Letters B*, 664(12):41 – 46, 2008.

[79] A. A. Aguilar-Arevalo *et al.* (MiniBooNE Collaboration). First measurement of the muon antineutrino double-differential charged-current quasielastic cross section. *Phys. Rev. D*, 88:032001, Aug 2013.

[80] A. A. Aguilar-Arevalo *et al.* (MiniBooNE Collaboration). Measurement of the antineutrino neutral-current elastic differential cross section. *To be published in Phys. Rev. D*, 2013.

[81] A. A. Aguilar-Arevalo *et al.* (MiniBooNE Collaboration). Measurement of the neutrino component of an antineutrino beam observed by a nonmagnetized detector. *Phys. Rev. D*, 84:072005, Oct 2011.

[82] V. *et al.* (NOMAD Collaboration) Lyubushkin. A study of quasi-elastic muon neutrino and antineutrino scattering in the NOMAD experiment. *The European Physical Journal C*, 63(3):355–381, 2009.

[83] J. Beringer *et al.* (PDG Collaboration). Review of particle physics. *Phys. Rev. D*, 86:010001, Jul 2012.

[84] Convoluted landau and gaussian fitting function. `http://root.cern.ch/root/html/tutorials/fit/langaus.C.html`.

[85] Estar, pstar, and astar: Computer programs for calculating stopping-power and 1095 range tables for electrons, protons, and helium ions (version 1.2.3). `http://physics.nist.gov/Star`. National Institute of Standards and 1097 Technology, Gaithersburg, MD. [2012].

[86] PØD geometry and mass. http://www.t2k.org/docs/technotes/073. T2K technical note number 73 by K. Gilje. T2K Internal Only.

[87] Tables of x-ray mass attenuation coecients and mass energy-absorption coecients (version 1.4). http://www.nist.gov/pml/data/xraycoef/index.cfm. By Hubbell, J.H. and Seltzer, S.M. at National Institute of Standards and Technology, Gaithersburg, MD [2012].

[88] Crosscheck of high-energy ν_e event rate with the PØD. http://www.t2k.org/docs/technotes/053. T2K technical note number 53 by M. Day, S. Manly, K. McFarland, P.Rodrigues, I. Taylor. T2K Internal Only.

[89] Measurement of nc1π^0 production with the t2k π^0 detector(PØD). http://www.t2k.org/docs/technotes/056. T2K technical note number 56 by G. Lopez, B. Berger, N. Buchanan, K. Gilje, F. Khanam, C. McGrew, D. Ruterbories, J. Schwerhr. T2K Internal Only.

[90] Cross section parameters for the 2012a oscillation analysis. http://www.t2k.org/docs/technotes/108. T2K technical note number 108 by Patrick de Perio, Mark Hartz, Yoshinari Hayato, Kendall Mahn, Kevin McFarland, Philip Rodrigues, Peter Sinclair, Ryan Terri, and Morgan Wascko. T2K Internal Only.

[91] Hadron inelastic cross section verifications. http://geant4.web.cern.ch/geant4/results/validation-plots/cross-sections/hadronic/inelastic/. GEANT4 Collaboration.

[92] K. Abe *et al.* (T2K Collaboration). Measurement of the inclusive ν_μ charged current cross section on carbon in the near detector of the T2K experiment. *Phys. Rev. D*, 87:092003, May 2013.

[93] D. Perevalov. Neutrino-nucleus neutral current elastic interactions measurement in MiniBooNE. http://www-boone.fnal.gov/publications/Papers/denis_thesis.pdf.